Structural and electronic decoupling of a large organic molecule from a metal surface by a single layer of hexagonal boron nitride

DISSERTATION

zur Erlangung des Doktorgrades (Dr. rer. nat.)
der Mathematisch-Naturwissenschaftlichen Fakultät
der Rheinischen Friedrich-Wilhelms-Universität Bonn

vorgelegt von
CHRISTINE BRÜLKE
aus Bad Honnef

Bonn, 2021

Angefertigt mit Genehmigung der Mathematisch-Naturwissenschaftlichen Fakultät der Rheinischen Friedrich-Wilhelms-Universität Bonn.

1. Gutachter: Prof. Dr. Moritz Sokolowski
2. Gutachter: Prof. Dr. Christian Kumpf
Fachnaher Gutachter: Prof. Dr. Thomas Bredow
Fachfremder Gutachter: Prof. Dr. Carsten Busse

Tag der Promotion: 11.11.2021
Erscheinungsjahr: 2022

Abstract

In the present work, the ability of one single layer of hexagonal boron nitride (hBN) to decouple the organic molecule 3,4,9,10-perylene tetracarboxylic dianhydride (PTCDA) from an underlying Cu(111) surface was investigated. The decoupling was probed by fluorescence (FL) spectroscopy of the PTCDA molecule adsorbed on the hBN surface. An analysis of the topographical and the electronic structure of the system PTCDA/hBN/Cu(111) was performed with spot-profile analysis low energy electron diffraction (SPA-LEED), the normal incidence x-ray standing waves technique (NIXSW), x-ray photoelectron spectroscopy (XPS), and ultraviolet photoemission spectroscopy (UPS). To gain insight into the growth process of the hBN layer, temperature programmed desorption (TPD) was used. The investigation comprises three steps.

First, the structure of the substrate hBN/Cu(111) was analyzed and the growth process of the hBN layer was investigated. The structural analysis revealed the very weak interactions at the hBN/Cu(111) interface. Despite a small lattice mismatch of 2.0% the structure is incommensurate. The hBN layer is slightly buckled with an amplitude of (0.42 ± 0.05) Å, however, compared to the large vertical distance between hBN and the Cu(111) surface of 3.24 Å this buckling is very small and the hBN layer can be considered locally flat. A further indication for weak interfacial interactions is the wide range of azimuthal orientations of the hBN domains. The orientations are determined during the growth process which is separated into three steps. First, hBN domains rotated by 30° relative to the Cu(111) surface grow at surface defects, then the hBN domains on terraces grow aligned with the metal substrate and reach the largest sizes of all hBN domains, and finally, randomly oriented hBN domains fill the remaining gaps between larger domains.

Then, the PTCDA molecule on hBN/Cu(111) was investigated with respect to its geometric and electronic structure. For the PTCDA/hBN interface, too, an incommensurate structure, a large vertical distance, and disorder in the azimuthal orientations of the adsorbate domains were found. Furthermore, the investigations revealed a small desorption energy of PTCDA molecules, a strong resemblance of the C1s XPS spectra of PTCDA/hBN/Cu(111) and PTCDA multilayers, and no differential shifts of orbital energies of PTCDA on hBN/Cu(111) compared to the gas phase of PTCDA. All of these observations point to the very weak interactions between PTCDA and the hBN/Cu(111) substrate. Stronger interfacial interactions have only been found for hBN layers with a higher density of structural defects. Here, the underlying Cu(111) surface could influence the azimuthal orientation of the PTCDA domains.

Finally, the optical properties of PTCDA/hBN/Cu(111) were measured and compared to those of PTCDA/Cu(111) where the first PTCDA layer decouples the higher layers of PTCDA from the metal surface. Raman lines were measured for both systems and compared to PTCDA on other substrates. On both, hBN/Cu(111) and Cu(111), fluorescence from molecules at surface defects and from molecules adsorbed in higher layers (the second and third PTCDA layers on hBN/Cu(111) and on Cu(111), respectively, and higher) was observed at ~18,450 cm^{-1} and at

~18,150 cm^{-1}, respectively. Only on hBN/Cu(111), fluorescence from ordered PTCDA domains in the first layer was found at ~18,300 cm^{-1}. However, the fluorescence intensity of PTCDA on hBN/Cu(111) is low and the life times of the excited states amounts to only $(1.6 - 4.4) \cdot 10^{-14}$ s.

These investigations showed that a single layer of hBN is able to decouple the PTCDA molecule from an underlying Cu(111) surface only to a certain degree. On the one hand, PTCDA on hBN/Cu(111) structurally resembles PTCDA molecules in the gas phase rather than those adsorbed on metal surfaces. On the other hand, the hBN layer does not decouple the PTCDA molecule enough to prevent the quenching of an electronic excitation. Despite the reduction of the charge-transfer at the interface, the fluorescence intensities and quantum yields are small.

Kurzzusammenfassung

In dieser Arbeit wurde untersucht, ob eine einzelne Schicht hexagonales Bornitrid (hBN) die Fähigkeit besitzt, das organische Molekül 3,4,9,10-Perylentetracarbonsäuredianhydrid (PTCDA) von einer Cu(111) Oberfläche zu entkoppeln. Die Entkopplung wurde durch Fluoreszenz (FL)-Spektroskopie an dem auf der hBN-Oberfläche adsorbierten PTCDA-Molekül gemessen. Die Analyse der topographischen und der elektronischen Struktur des Systems PTCDA/hBN/Cu(111) erfolgte mittels Spotprofil-Analyse bei der Beugung niederenergetischer Elektronen (engl. *spot-profile analysis low energy electron diffraction*, SPA-LEED), der Technik des stehenden Wellenfelds unter Normaleinfall (engl. *normal incidence x-ray standing waves technique*, NIXSW), Röntgenphotoelektronenspektroskopie (engl. *x-ray photoelectron spectroscopy*, XPS) und Ultraviolettphotoelektronenspektroskopie (engl. *ultraviolet photoelectron spectroscopy*, UPS). Um einen Einblick in den Wachstumsprozess der hBN Schicht zu erlangen, wurde Temperatur-programmierte Desorption (engl. *temperature programmed desorption*, TPD) eingesetzt. Die Untersuchungen umfassen drei Schritte.

Zunächst wurde die Struktur des Substrats hBN/Cu(111) analysiert und der Wachstumsprozess der hBN-Schicht wurde untersucht. Die Strukturanalyse deckte die sehr schwachen Wechselwirkungen an der Grenzfläche zwischen hBN und Cu(111)-Oberfläche auf. Trotz der nur geringen Gitterfehlanpassung von 2,0 % ist die Struktur inkommensurabel. Die hBN-Schicht ist leicht gewellt mit einer Amplitude von (0,42 ± 0,05) Å. Im Vergleich mit dem großen vertikalen Abstand zwischen hBN und Cu(111)-Fläche ist diese jedoch sehr klein und die hBN-Schicht kann lokal als glatt betrachtet werden. Ein weiterer Hinweis für die schwachen Wechselwirkungen an der Grenzfläche ist die große Spanne von azimutalen Orientierungen der hBN-Domänen. Diese Orientierungen werden während des Wachstumsprozesses festgelegt. Dieser kann in drei Schritte unterteilt werden. Als erstes wachsen hBN-Domänen, die im 30°-Winkel relativ zu der Cu(111)-Oberfläche orientiert sind, an Oberflächendefekten. Dann wachsen hBN-Domänen auf Terrassen. Diese sind an der Cu(111)-Oberfläche orientiert und erreichen die größte Ausdehnung aller Domänen. Schließlich füllen zufällig orientierte hBN-Domänen die restlichen freien Lücken zwischen größeren Domänen.

Im nächsten Schritt wurde das PTCDA-Molekül auf hBN/Cu(111) hinsichtlich seiner geometrischen und elektronischen Struktur untersucht. Auch an der PTCDA/hBN-Grenzfläche wurden eine inkommensurable Struktur, ein großer vertikaler Abstand und Unordnung in der azimutalen Orientierung der Adsorbat-Domänen gefunden. Außerdem deckten die Untersuchungen die geringe Desorptionsenergie der PTCDA-Moleküle auf. Die XPS-Spektren von PTCDA auf hBN/Cu(111) zeigten eine starke Ähnlichkeit zu PTCDA-Multilagen und für die Energien der Molekülorbitale wurden keine differentiellen Verschiebungen im Vergleich zur Gasphase gefunden. All diese Beobachtungen zeigen die sehr schwachen Wechselwirkungen zwischen PTCDA und dem hBN/

Cu(111)-Substrat auf. Stärkere Wechselwirkungen an der Grenzfläche wurden nur dann gefunden, wenn die hBN-Schicht eine höhere Dichte an strukturellen Defekten aufwies. In diesen Fällen konnte die darunter liegende Cu(111)-Oberfläche die azimutale Orientierung der PTCDA-Domänen beeinflussen.

Abschließend wurden die optischen Eigenschaften von PTCDA/hBN/Cu(111) gemessen und mit denen von PTCDA/Cu(111), wo die erste PTCDA-Lage die höheren PTCDA-Lagen von der Metalloberfläche entkoppelt, verglichen. Raman-Linien wurden für beide Systeme gemessen und mit denen von PTCDA auf anderen Substraten verglichen. Auf beiden Substraten, hBN/Cu(111) und Cu(111), wurde Fluoreszenz gemessen von Molekülen, die an Oberflächendefekten adsorbiert sind, und von Molekülen in höheren Lagen (ab der zweiten Lage auf hBN/Cu(111) und ab der dritten Lage auf Cu(111)). Die Fluoreszenz lag bei ~18.450 cm^{-1} bzw. ~18.150 cm^{-1}. Nur auf hBN/Cu(111) wurde Fluoreszenz von geordneten Molekülen in der ersten Lage bei ~18.300 cm^{-1} gemessen. Allerdings ist die Fluoreszenzintensität von PTCDA auf hBN/Cu(111) klein und die Lebenszeiten der angeregten Zustände liegt bei nur $(1,6 - 4,4) \cdot 10^{-14}$ s.

Diese Untersuchungen zeigten, dass eine einzelne hBN-Schicht nur zu einem gewissen Grad in der Lage ist, das PTCDA-Molekül von einer Cu(111)-Oberfläche zu entkoppeln. Einerseits ähnelt das PTCDA-Molekül auf hBN/Cu(111) PTCDA-Molekülen in der Gasphase stärker als solchen, die auf einer Metalloberfläche adsorbiert sind. Andererseits wird das PTCDA-Molekül durch die hBN-Schicht nicht ausreichend entkoppelt, um eine Auslöschung einer elektronischen Anregung zu verhindern. Trotz einer Reduktion der Ladungsübertragung zwischen den Schichten sind die Fluoreszenz-Intensitäten und die Quantenausbeute gering.

Contents

1 Introduction

Two-dimensional materials (2DMs) constitute a special subject in surface science. Since they consist of two surfaces and no bulk, they exhibit unique properties that differ significantly from those of the corresponding bulk materials [1, 2]. In 2010, Geim and Novoselov received the Nobel Prize for the preparation of graphene, a single layer of π-conjugated carbon atoms, by the simple top-down method of mechanical exfoliation, and for measuring its unique electronic properties [3]. Since then, the interest in graphene (with its remarkable properties like extraordinary stability, ballistic transport, and high current density) has risen constantly as it has a multitude of potential applications from electronic and optical devices to chemical sensors and energy storage [4, 5]. In pursuit of new properties of ultrathin materials, the attention of researchers has turned to other materials which can also be produced via mechanical exfoliation: 2DMs now encompass a wide range of materials, such as transition metal dichalcogenides (TMDCs) like MoS_2, TeS_2, or $MoSe_2$ [6, 7], black phosphorous [8, 9], hexagonal boron nitride [10, 11], ultrathin oxides (e.g. MoO_3) [12, 13], and more [14]. Many of these materials can also be prepared via chemical vapor deposition (CVD) [14, 15]. This bottom-up method makes even more materials accessible, e.g. blue phosphorous [16] and the graphene-analogous silicene [17]. In addition, this wide range of different materials with numerous distinct and often tunable properties allows for tailoring of new electronic devices by combing different 2DMs into layered heterostructures [14, 18].

In assembling such heterostructures, it is of paramount importance that the interactions and processes that happen at the interfaces between the layers are understood in detail. For example, in optoelectronic devices like phototransistors and light emitting diodes [18], the preservation of accumulated charges in a semiconductor layer is essential. This is achieved by an insulating layer between the semiconductor and the electrode [19]. Thus, investigating possible charge-transfer processes in layered systems of the type semiconductor/insulator/electrode is of high interest. The general role of the insulator is to provide a sufficient *decoupling* of the semiconductor (e.g. organic molecules as they are used in organic light emitting diodes [20]) and the (metallic) electrode. Here, the term *decoupling* describes the separation of the electronic states of the molecules and the metal. This prevents a charge-transfer between the two, which can be essential for the functionality of the above mentioned devices.

The insulator achieves this decoupling by suppressing the wave functions of the electronic states of the metal and, additionally, spatially separating them from the wave functions of the molecular electronic states. This has also an impact on the excited molecular states and is illustrated in Figure 1.1. In the molecule, an electron is excited from the highest occupied molecular orbital (HOMO) of the electronic ground state S_0 into the lowest unoccupied molecular orbital (LUMO) of the electronic excited states S_1. If these molecular states couple to metallic states, the electron transfers from the S_1 into the unoccupied states of the conduction band of the metal. At the

same time, the electron hole in S_0 is filled by an electron from the metallic valence band. This charge-transfer occurs on a time scale of 10^{-14} s [21, 22]. Due to this quick process, the excitation of the molecule is *quenched*, i.e. lost. A charge-transfer is often even possible from a second molecular layer into the metal without a significant overlap of wave functions via the states of the first layer [23]. An inserted insulating layer prevents the overlap of the wave functions of the above mentioned electronic states, and thus, the charge-transfer. The efficiency of the insulator can range from a complete decoupling to a situation of competing processes for the decay of the excitation, e.g. a non-radiative decay via charge-transfer (quenching) and a radiative decay, like fluorescence. Accordingly, the insulator determines the quantum efficiency and thus the performance of the device. Finding the right insulating material for this task is, hence, of big importance. Previously, thin films (composed of several layers) of insulating materials have been used for this purpose [24–31].
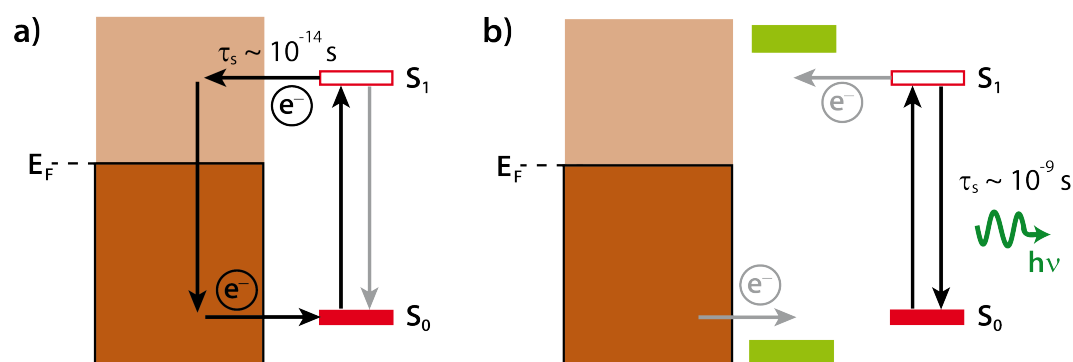
Figure 1.1: *Schematic representation of the electronic states of a metal (brown, with a Fermi energy E_F) and a molecule (red). In the molecule, an electron is excited from the electronic ground state S_0 into the electronic excited state S_1. a) A coupling of the electronic states of molecule and metal leads to a charge-transfer of the excited electron from S_1 into the unoccupied electronic states of the metal. The charge-transfer occurs on a time scale of 10^{-14} s [21, 22]. The excitation decays as the excited electron transfers into the occupied metallic states. The electron hole in S_0 is filled with an electron from the valence band of the metal. b) The electronic states of molecule and metal are separated by a dielectric material with a wide bandgap (green). The charge-transfer between molecule and metal is no longer possible. The excitation can alternatively decay in a radiative process. The life time of the excited electron then typically amounts to 10^{-9} s [23]. The bandgaps of the molecule and the insulating material are on the scale for PTCDA [32] and hBN [33, 34].*

After the discovery of the unique electronic properties of graphene [3], the development of graphene based electronic devices emerged [4]. Some of the advantages of graphene based devices are the high conduction speed, low energy loss, and the compact size of the devices [35]. To preserve the compact size, it is of high interest to keep the other components of such devices, like insulating layers, on a similarly small scale as the graphene, while maintaining their properties [36]. The most prominent 2DM for use in such devices is hexagonal boron nitride (hBN) [36, 37] due to not only its very large bandgap of $5-6$ eV [33, 34, 38, 39], but also its structural similarity with and small lattice mismatch to graphene which make it ideal for combining the two in layered devices [40]. Furthermore, hBN displays very large structural stability mechanically, thermally, and chemically [11] and can be grown in large-scale monocrystalline sheets [41–43]. hBN can be

prepared under UHV conditions via CVD, and displays a wide range of topographical structures depending on the metal substrate it is grown upon [11]. By depositing organic molecules on an hBN layer, as-grown on a metal substrate, a layered system of semiconductor/insulator/electrode is assembled and can be studied.

The objective of the present work was to determine whether a single monolayer of hBN is able to decouple an organic molecule from an underlying metal surface using *fluorescence spectroscopy*. The organic molecule chosen is 3,4,9,10-perylene tetracarboxylic dianhydride (PTCDA) and the metal substrate used here is the Cu(111) surface. The materials and methodology have been chosen for the following reasons:

(i) PTCDA has been extensively studied regarding its structural, electronic, and optical properties on various metallic [44–50] and dielectric surfaces [51–54]. Thus, it is regarded as a model for large, π-conjugated organic molecules and the results of the present work can be viewed in a larger context. Especially the available information regarding PTCDA on the Cu(111) surface are of great importance for the investigations presented here, as a comparison of the properties of PTCDA on hBN/Cu(111) and on bare Cu(111) will reveal the exact changes at the interfaces.

(ii) The interaction between the noble metal Cu and the hBN layer is expected to be rather weak [55] which, in turn, leads to a large vertical distance at the interface. This may help to prevent quenching of the excitation of the molecule [23] in combination with the large bandgap of hBN.

(iii) One possible way to investigate electronic decoupling as described above is photoemission spectroscopy. However, the intrinsic life time of an electron hole amounts to 10^{-14} s [21, 22]. A charge-transfer that is slower than this cannot be observed in a photoemission spectrum. A broadening of the spectrum would only be caused by a shortened life time and, thus, a faster charge-transfer. Fluorescence spectroscopy is sensitive to such a slower charge-transfer. The life time of an excited electron which relaxes back into the ground state in a radiative process typically amounts to 10^{-9} s [23]. Thus, even a small mixing of the electronic states of metal and molecule becomes visible in fluorescence experiments.

The present thesis is divided into three parts. First, hBN on the Cu(111) surface is discussed in detail. The surmised weak interaction and large vertical distance between hBN and metal are expected to be of great importance for the decoupling of organic molecules deposited on top of the hBN. Accordingly, these assumptions had to be verified. Furthermore, the hBN substrate may have a significant influence on the structure of the adsorbed organic layer and thus its optical properties [52, 53]. This thesis reports both the lateral and the vertical structure of the hBN layer which were determined using mainly *spot-profile analysis low energy electron diffraction* (SPA-LEED) and the *normal incidence x-ray standing waves* technique (NIXSW, in this thesis referred to as XSW for brevity). Additionally, a model for the growth process of hBN on Cu(111) is developed based on the results of *temperature programmed desorption* (TPD) experiments.

In the second part, the structure of PTCDA layers on the hBN/Cu(111) substrate is described on the basis of the results from SPA-LEED and XSW. Electronic properties of the system were

examined using various *photoemission spectroscopy* (PES) methods. Both, the structural and electronic properties, deliver information on the influence of the underlying metal substrate on the molecules. The structure and properties of PTCDA on Cu(111) have been studied in detail [46, 56, 57] so that a comparison between the systems clearly shows the effect of the inserted hBN layer. In the third part, the fluorescence (FL) of PTCDA adsorbed on hBN/Cu(111) and on Cu(111) is reported. This allows a direct comparison between the decoupling achieved by the hBN sheet and the first PTCDA layer on the Cu(111) surface whose excitation is expected to be quenched because this was observed for PTCDA on Ag(111) and Au(111) [58].

The present thesis is partly a continuation of the author's Master's thesis [59]. The structural data of hBN/Cu(111) shown in that work will be presented here again since they constitute the basis of the new findings and in order to show the system in a complete picture. The data in the present thesis was partly measured by the author in the home laboratory and was partly measured in collaboration with other scientists. XSW data was measured during several beam times at the Diamond Light Source, Didcot, UK and the data was evaluated by T. Heepenstrick. These results were published in the articles that are included in the Appendices A.1 and A.2. They will be referred to in this thesis, too. The photoemission data (also published in the articles included in the Appendices A.1 and A.2) was measured in the lab of Prof. Dr. F. S. Tautz from the Forschungszentrum Jülich.

The thesis is organized as follows: Chapter 2 will give an overview of the literature on hBN on metal surfaces, PTCDA adsorbed on metal and dielectric surfaces, and large organic molecules on hBN/metal substrates. Chapter 3 concerns the theoretical background of the experimental techniques used in the investigations presented later. Chapter 4 details the experimental procedures. In Chapters 5, 6, and 7, the structure of hBN on Cu(111), the structure and electronic properties of PTCDA on hBN/Cu(111), and the FL of PTCDA/hBN/Cu(111) and of PTCDA/Cu(111) will be given. Finally, Chapter 8 will summarize the results and address some open questions that could be subject to future work.

2 Review of Literature

This chapter gives an overview of topics related to those presented in this thesis, and which are of importance for the understanding of the presented results and for seeing them in a greater context. Chapter 2.1 is an introduction to hexagonal boron nitride grown on different metallic substrates so that the influence of the metal surface on the structure of this 2DM can be understood. In Chapter 2.2, the organic molecule PTCDA will be discussed. Its structural and electronic properties on various metallic and dielectric surfaces will be considered. As reference points, these systems will help in the understanding of the effect the hBN layer has on the interaction between the molecule and the metal surface. Published literature on PTCDA on hBN will be reviewed in Chapter 5.1. Lastly, Chapter 2.3 focuses on the adsorption of molecules on hBN. The templating effect of the hBN layer and the influence of the underlying metal will be introduced.

2.1 Hexagonal Boron Nitride on Metal Surfaces

The bulk material of hexagonal boron nitride (α-BN) is a layered structure of π-conjugated honeycomb lattices made up of alternating boron and nitrogen atoms (see Figure 2.1) [14]. In surface science, the abbreviation hBN commonly refers to one single layer of this material and will be used in the same way in the present thesis. hBN has the same structure as graphene, it is isoelectronic to it, and with a lattice constant of 2.488 Å [60] the two exhibit a lattice mismatch of only -0.1% [61]. Accordingly, hBN is also known as white graphene. It is of comparable mechanical stability [62], resistant against corrosive environments like NaOH solutions [63], and thermally stable up until 1123 K [64]. Like graphene, it can be prepared via mechanical exfoliation from the bulk crystal [10] as in both graphite and α-BN the vertical interactions between the layers are quite weak [65]. The important difference between graphene and hBN are their electronic properties: graphene displays metallic characteristics [3] while hBN has a wide bandgap of $5-6$ eV [33, 34, 38, 39] which makes it an insulating material.

For the use in electronic devices, hBN can be grown on copper foils in an H_2/Ar atmosphere via thermal decomposition of solid ammonia boride $(BH_4)(NH_4)$ [66–68]. It decomposes to borazine $B_3N_3H_6$ [69, 70], an isoelectronic and isostructural inorganic analogue to benzene [71]. This in turn decomposes to hBN on the hot copper foil [11]. While copper foils are most commonly used, hBN has also been prepared on other metal foils [39, 72–74]. The hBN sheets can then be transferred onto other substrates, e.g. SiO_2/Si [60]. Under ultra high vacuum, hBN is grown directly from the precursor borazine which decomposes on the hot metal surface [11]. Since the presence of the metal surface is required for the decomposition of borazine, the growth of the hBN stops after the first layer is completed (self-termination after one monolayer) [75]. The dose and
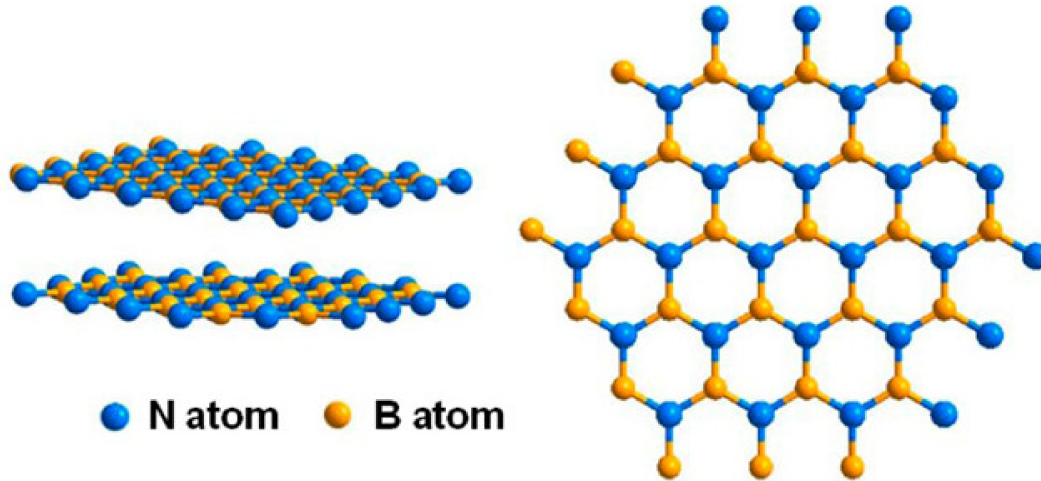
Figure 2.1: *Left: Crystal structure of bulk hexagonal boron nitride (α-BN). The layers of honeycomb lattices are stacked by van-der-Waals forces. Right: Structure model of the π-conjugated honeycomb lattice of a single layer of hexagonal boron nitride, commonly referred to as hBN. Taken from Ref. [14].*

sample temperature necessary for the decomposition is dependent on the metal surface used as the substrate. The substrate also heavily influences the structure of the formed hBN layer [11]. The lattice mismatch between the two and subsequently the strength of interaction at the interface determine the topographical structure of the hBN layer.

The lattice mismatch between hBN and Ni(111) is only -0.5%[1] and the resulting structure at the interface is commensurate [78] with preferred positions of the adsorbate atoms at on-top sites for the nitrogen and on hollow sites for the boron atoms [79, 80]. This leads to the growth of two kinds of incongruent domains (one kind with boron atoms occupying fcc-hollow sites while in the other the hcp-hollow sites are occupied) which differ in their azimuthal orientations by $60°$. The domains display a triangular shape as a termination by only one kind of atom is energetically favorable. Since these two kinds of domains can never coalesce to form a single domain, grain boundaries can be observed in *scanning tunneling microscopy* (STM) images [80], as shown in Figure 2.2. With the adsorbate atoms occupying their preferred adsorption sites, the interaction at the interface is strong on the entire surface which leads to a flat-lying hBN sheet [81].

In the case of a larger mismatch, the hBN layer has to compensate for the deviation from the preferred adsorption sites, as is the case for hBN/Ir(111) [82] with a mismatch of 7.7%. Farwick zum Hagen et al. found a (11.7 x 11.7) on (10.7 x 10.7) superstructure in LEED in which there are areas where the nitrogen and boron atoms are located at the preferred sites and others where this is not the case. In the former case the interaction between hBN and iridium is strong, leading to a small vertical distance between these areas of the hBN sheet and the metal (2.20 Å). However, the rest of the layer does not experience such a strong bonding which leads to a buckling of the layer of about 1.5 Å (peak-to-peak corrugation). The resulting structure is shown in Figure 2.3a.

---

[1]For a better comparison, all lattice mismatches m cited in this thesis are calculated as $m = 1 - a_{\text{hBN}}/a_{\text{metal}}$, using the lattice constants of the metals given in [76] and the bulk lattice constant of hexagonal boron nitride 2.505 Å at 297.5 K [77]. Thus, the values for m may differ from those given in the respective publications. All relevant values are summarized in Table G.1 in Appendix G.
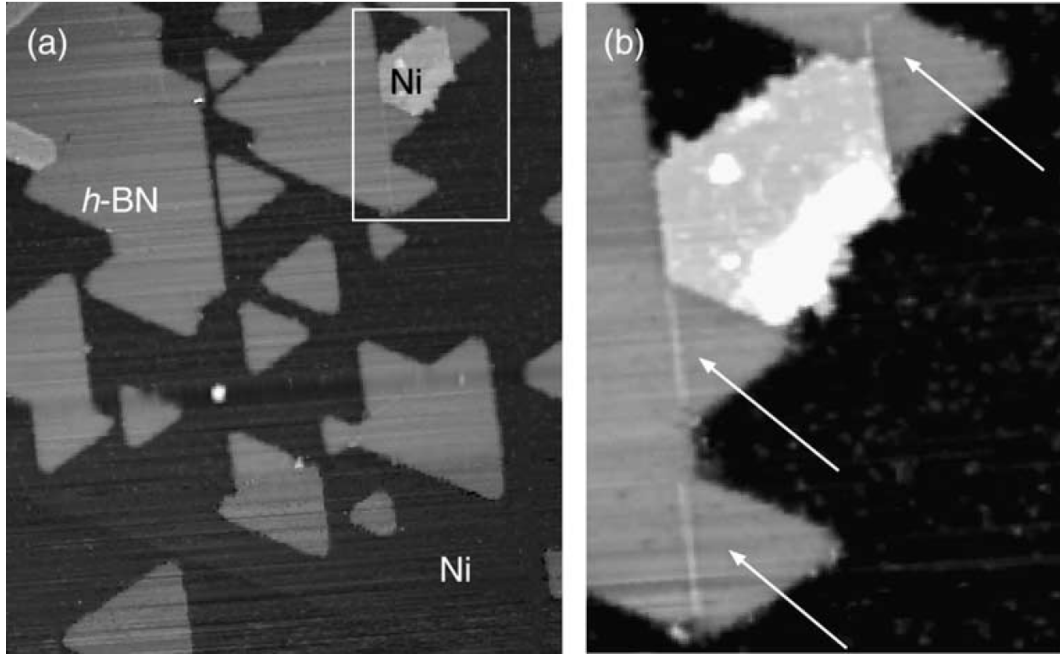
Figure 2.2: *a) STM image of a Ni(111) surface partially covered with triangular hBN domains. Domains of different orientations separated by 60° are incongruent and cannot coalesce. Image size is 0.31 μm x 0.36 μm. b). Zoom-in on the area marked with a white box in a). Arrows indicate the defect lines between two incongruent domains. Taken from Ref. [80].*

Farwick zum Hagen et al. termed the topography of this system "egg-box model" [82]. The areas closer to and the areas further away from the substrate are commonly referred to as "pores" and "wires", respectively, and can be easily observed in STM (cf. Figure 2.3b). Similar structures have been found on Rh(111) [75, 83] and Pt(111) [84] (with lattice mismatches of 6.9% and 9.7%, respectively). For strongly corrugated hBN layers the term "nanomesh" has been introduced in 2004 [75]. Preobrajenski et al. used PES to demonstrate that there is a gradual change in the strength of the buckling of hBN layers on different metals depending on the bonding strength rather than a phase transition going from flat layer to nanomesh [85].

Besides a buckling, a large mismatch can be compensated by a rotation of the hBN domains as has been observed on Pd(111) [86]. In the LEED pattern of hBN/Pd(111) which is shown in Figure 2.3c, three different structures were found: a (11x11) on (10x10) supercell aligned with the substrate, an incommensurate superstructure rotated by 30°, and randomly oriented hBN domains, indicated by a continuous ring in the LEED pattern. An azimuthal rotation by 30°, which reduces the lattice mismatch from 8.9% to $-5.2\%^2$, allows more adsorbate atoms to occupy their preferred adsorption sites. A random orientation, on the other hand, points to such weak interactions at the interface that the metal has no influence on a certain percentage of hBN domains. This is more obvious in the case of hBN/Ag(111) [87], with a lattice mismatch of 13.3%, where in LEED measurements only a continuous ring was observed. Laskowski et al. have shown that elements with full d shells display the weakest binding energies to an hBN layer compared to other transition metals [55]. This means for this case that the Ag(111) surface has no influence on the structure of

---

[2]The definition of the lattice mismatch m refers to the distance between lattice lines $\{h0\}$ and $\{0k\}$, respectively. For rotated domains of hBN, a lattice mismatch can be considered for other lattice lines $\{hk\}$ so that $m = 1 - a_{\text{hBN}}/a_{\text{metal}}^{hk}$.
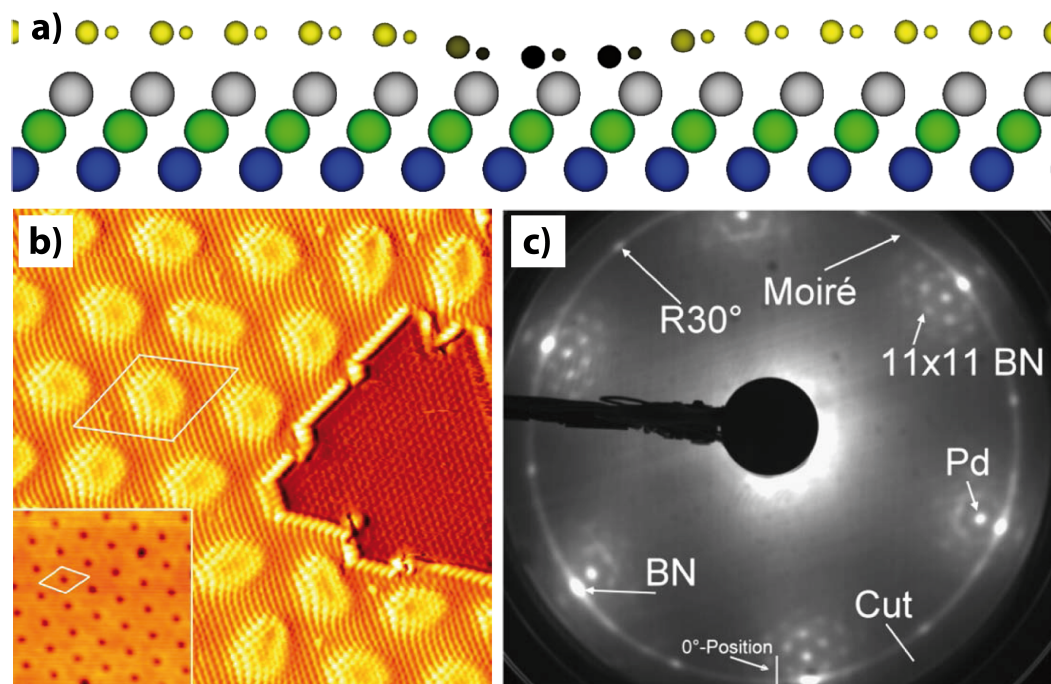
Figure 2.3: *a) Side-view model of a monolayer hBN (atoms color-coded yellow to black according to their vertical distance from the substrate) on Ir(111). The lateral positions of the B and N atoms were chosen according to DFT results for the preferred configuration (nitrogen at on-top sites and boron at hcp sites). The alteration in vertical distance leads to the "egg-box" shape of the hBN layer. Taken from Ref. [82]. b) Atomically resolved STM image of hBN on Ir(111) with a triangular hole exposing bare Ir. White lines indicate the unit cell of the superstructure. Image size is 144 x 144 Å^2. The Moiré pattern clearly shows the locations of the pores and wires of the hBN layer. Taken from Ref. [82]. c) LEED pattern of hBN on Pd(111). The ring of intensity indicates a homogeneous distribution of orientations of hBN domains in most directions. Only orientations in alignment with the substrate and rotated by 30° relative to that are preferred. Taken from Ref. [86].*

the hBN layer or on the azimuthal orientations of its domains. A similarly weak binding energy as on Ag(111) has been calculated for hBN/Cu(111) [55]. Further details regarding this system will be given in Chapter 5.1.

With the interaction strength between metal and hBN being the key factor for the topography and the structure rather than the epitaxial relation to the (111) substrate surface, it comes as no surprise that the growth of hBN on metal surfaces displaying other symmetries than the (111) surfaces is also possible [88–95].

2.2   Bonding of PTCDA on inorganic surfaces

PTCDA (3,4,9,10-perylene tetracarboxylic dianhydride, molecular structure shown in Figure 2.4) is a well-studied large organic molecule that is commonly used as a model for organic semiconductors. It can be evaporated in vacuum which allows the preparation of well-defined structures on surfaces and their investigation using surface science techniques [96]. The bulk material displays two modifications (α and β) with similar lattice constants and the characteristic herringbone arrangement of the PTCDA molecules in the (102) plane [97, 98]. The unit cell in the (102) plane

is rectangular, contains two molecules, and has a *p2gg* symmetry. The stacking of the (102) planes in PTCDA crystals distinguishes the *α*- and *β*-modifications. The second (102) plane is laterally shifted relative to the first along the long axis of the unit cell in the *α*- and along the short axis in the *β*-modification. These shifts amount to 1.9 Å and 1.95 Å, respectively [97].
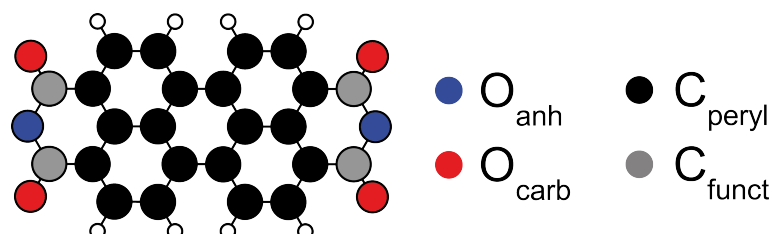
Figure 2.4: *Structure model of the PTCDA molecule. Anhydritic and carboxylic oxygen atoms are depicted in blue and red, respectively. The carbon atoms in the perylene backbone are black, functional carbon atoms in the anhydride groups of the molecule are gray, hydrogen atoms are white.*

The PTCDA molecule has been extensively studied as an adsorption complex on the low index surfaces of the coinage metals. The interactions between metal and PTCDA molecule vary significantly depending on the specific substrate surface which influences both the structure and the electronic properties of the molecule. On all three (111) surfaces, the PTCDA molecules form a herringbone arrangement similar to the (102) plane in the bulk crystal. On Au(111), the structure is incommensurate [49] while on Ag(111), a commensurate arrangement [99] and on Cu(111), a *point-on-line* coincidence [57] have been found. This points to a considerable difference in interaction strengths of the molecule to Au(111) versus Ag(111) and Cu(111).

Indeed, the PTCDA molecules are only weakly physisorbed on Au(111) as no charge-transfer (CT) occurs [46] and the $(22 \times \sqrt{3})$ reconstruction of the metal surface remains unaltered underneath the PTCDA layer [49]. On both Ag(111) and Cu(111), a CT from metal to molecule was found in *ultraviolet photoemission spectroscopy* (UPS) [46]. On the Ag(111) surface, the partially filled former LUMO is shifted just below the Fermi edge giving the molecule itself a metallic character while on Cu(111), the CT from metal to molecule shifts the former LUMO well below the Fermi edge [46]. This increase in interaction is directly felt in the vertical adsorption height of the molecule above the surface. From Au(111), where the PTCDA molecule is positioned at a vertical distance similar to the stacking distance of the (102) planes in the bulk (3.22 Å in the *α*- and 3.25 Å in the *β*-modification [97]), to Ag(111) and Cu(111) the adsorption height decreases [45, 56, 100]. It should be noted that this is in regard to the absolute values for the vertical adsorption heights. When these values are reduced by the respective van der Waals (vdW) radii of the substrates [101], the adsorption height of PTCDA on Cu(111) is larger than on Ag(111). Additionally, on both Ag(111) and Cu(111), the molecule is distorted out of the molecular plane. With the carboxylic oxygen atoms closer to the surface than the perylene backbone and the anhydritic oxygen atoms further away, the molecule forms a saddle-like shape on Ag(111) [100]. On Cu(111), both types of oxygen atoms are further away from the surface than the perylene backbone [56]. These distortions may be linked to a CT from metal to molecule [47]. Figure 2.5 shows the distortion motifs of PTCDA

on the different coinage metal surfaces, the corresponding experimental results are summarized in Table G.2 in Appendix G. More details on the properties of PTCDA on Cu(111) will be given in Chapter 6, as this system is of the highest interest for the work presented in this thesis.
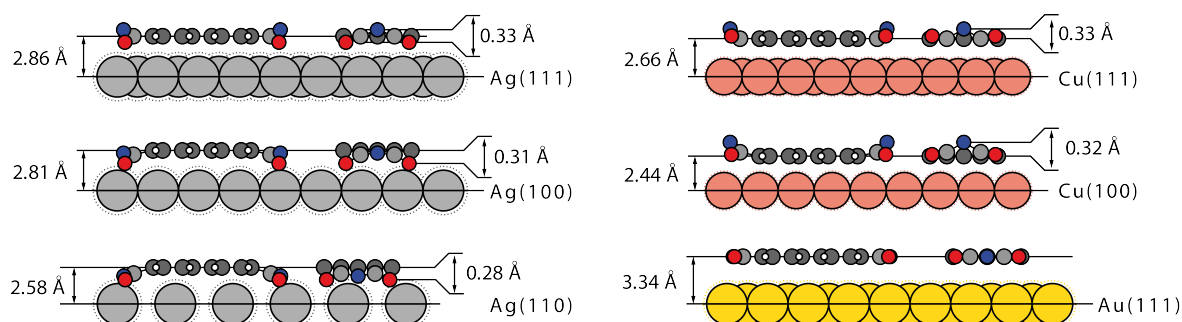
Figure 2.5: *Side-view models along the long and short molecular axes of PTCDA adsorbed on coinage metal surfaces (left: Ag(111), Ag(100), Ag(110), right: Cu(111), Cu(100), Au(111)). Vertical distances taken from Refs. [45, 47, 56, 100, 102], radii taken from Refs. [101, 103, 104]. Covalent radii are drawn at 75% and the vertical distances within the PTCDA molecules are enlarged by a factor of three for better visibility. All radii used in this thesis are summarized in Table G.3 in Appendix G, the results of the XSW experiments and the resulting values for the vertical distances are summarized in Table G.2 in Appendix G.*

An increase in the metal-molecule interactions can also be found when going from the (111) to more open surfaces. The lateral molecular arrangements found on Ag(100), Ag(110), and Cu(100) are T-shape [105], brickwall [99], and L-shape [106, 107] motifs, respectively, all of them displaying commensurability to the surface. Furthermore, the adsorption heights decrease. While on Cu(100), the distortion motif remains the same as on Cu(111) [102], on Ag(100) and Ag(110), the distortion changes from saddle-like to arch-like with both types of oxygen atoms closer to the surface than the perylene backbone [47].

Apart from PTCDA on metal surfaces, the behavior of the molecule on insulating surfaces has also been of large interest. Studies regarding its structure and electronic properties have been conducted on substrates like KBr [108], mica [109], and MgO [110]. Here, the focus will be on PTCDA on thin alkali halide films, namely on NaCl and KCl.

Depending on the growth conditions, PTCDA forms two structurally distinct monolayer phases on NaCl, a commensurate structure with a quadratic unit cell and a T-shape arrangement of the molecules (Q-phase) and herringbone arrangement of the molecules in a rectangular unit cell (HB*-phase) [111]. The Q-phase is the thermodynamically more stable phase. The multilayer also grows in a herringbone arrangement (HB-phase), its structure, however, differs from that of the HB*-phase. On KCl, PTCDA forms a commensurate brickwall structure [112]. DFT calculations [113] have shown that a single PTCDA molecule on a KCl or NaCl terrace prefers an adsorption site in which the perylene backbone is positioned above a Cl^- anion at a distance of 2.72 Å and 2.54 Å, respectively, while the oxygens atoms are located close to the cations in the surface. This leads to a distortion of the molecule similar to the situation on Ag(100) and Ag(110) but with an even more pronounced downward shift of the carboxylic oxygen atoms. The distortion of the molecule is bigger on NaCl than on KCl which can be attributed to the difference in lattice

constants of the substrates. If the molecules are located at step sites on the surface, the interaction of the molecule with the step edge lifts up one anhydride group of the molecule, making the distortion asymmetric [114].

2.3 Molecules adsorbed on hexagonal boron nitride

Large organic molecules adsorbed on metal-supported hBN layers show distinctly different behaviors compared to when they are adsorbed on bare metal surfaces. The hBN provides a level of electronic decoupling from the metal and at least reduced CT which can lead, for example, to the formation of molecular assemblies driven by intermolecular interactions rather than being dictated by the substrate [11]. However, there is still an influence of the underlying metal surface on the organic molecules since the properties of the hBN layers themselves are determined by them.
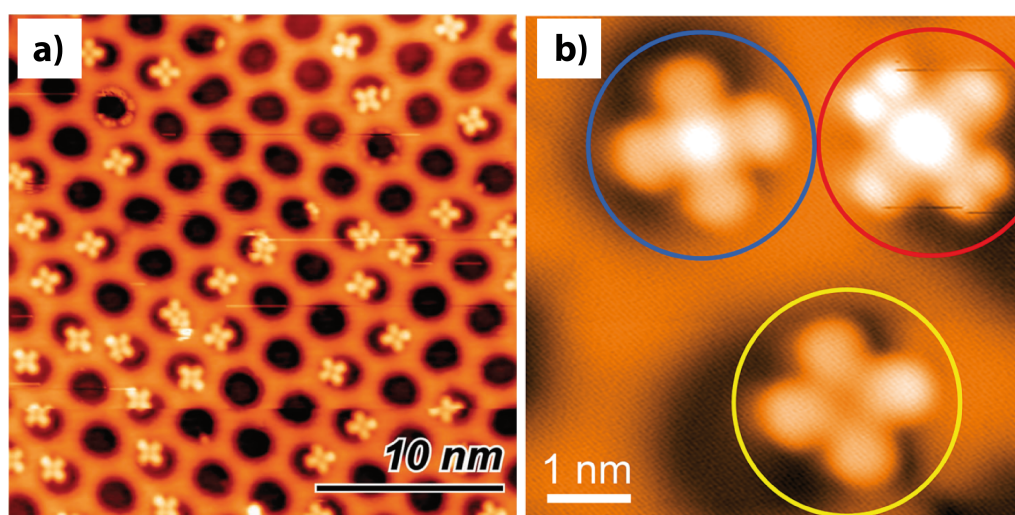
Figure 2.6: *a) STM image of CuPc molecules adsorbed on hBN/Rh(111), measured at 20 K. The molecules adsorb in the black hBN pores on off-center sites. Taken from Ref. [115]. b) High resolution STM image of MnPc adsorbed on hBN/Rh(111), measured at 4.9 K. The molecules adsorb on off-center positions in the hBN pores. Subtle differences in adsorption sites lead to a variation in the STM signatures of the molecules. Taken from Ref. [116].*

As described in Chapter 2.1, hBN on Rh(111) forms a nanomesh made up of pore and wire regions, with the pore regions being located considerably closer to the metal surface than the wires. Upon deposition of small amounts of large organic molecules, these molecules preferably adsorb in the pore regions, however, rather at the rim of the pores than their centers (off-center pore sites), and with specific orientations relative to the substrate [115–118] (cf. Figure 2.6a). This is attributed to dipole-rings which are a result of the different work functions of wires and pores [117]. Only when the coverage exceeds the pore areas, molecules adsorb on wire regions so that large crystalline islands form [119, 120]. The hBN layer is able to decouple the molecules from the underlying metal and has itself only a very small influence on the electronic molecular structure, demonstrated by *scanning tunneling spectroscopy* (STS) [118]. This influence, that is signified by a position-dependent shift of the frontier orbitals in STS and/or a change in the appearance of the molecules in STM (as seen in Figure 2.6b), is actually dependent on the specific adsorption site of the molecule within

the pore as this governs the interactions and possible charge-transfer characteristics [115, 116, 118]. A similar behavior has been found on hBN/Ir(111) where cobalt phthalocyanines adsorb first at off-center pore sites before adsorbing on the wires where their electronic properties (namely the positions of the frontier orbitals) differ significantly from the molecules in the pores due to the work function modulation of the hBN substrate [121].

The interactions of the molecules with an hBN/metal substrate can differ so drastically from the molecule/metal interface that, e.g. on-surface dehalogenation reactions could be induced and analyzed in detail which is impossible on metals where the reaction occurs immediately upon adsorption and too fast for observation [122, 123].

The behavior of large organic molecules on hBN/Cu(111) will be summarized in Chapter 6.1. Specifically, studies on PTCDA on hBN/Rh(110) [124], on hBN/Pt(111) and hBN/Rh(111) [125], and on hBN/SiO$_2$ [126] will be discussed in Chapters 6 and 7.

3 Theoretical Background

The goals of the present thesis have been outlined in the Introduction. Here, the experimental techniques used to answer the questions posed to the specific sample systems of hBN/Cu(111), PTCDA/hBN/Cu(111), and PTCDA/Cu(111) will be introduced. Only aspects that are important in the context of the present thesis will be summarized briefly. For more in-depth explanations of these techniques, refer to the literature cited in this chapter.

3.1 Low Energy Electron Diffraction

For structural investigations of the sample systems, *low energy electron diffraction* (LEED) was used which has become a standard technique in surface science since its discovery in 1927 by Davisson and Germer [127]. All LEED measurements presented here were done with an apparatus specifically designed for SPA-LEED. Detailed information on LEED and SPA-LEED can be found in Refs. [128–133].

The LEED pattern that arises due to the angular dependence of the constructive interference of electrons is commonly explained using the *Ewald construction* as shown in Figure 3.1a. The positions of diffraction spots are given by the wave vector $\vec{k}^{hk}$. With kinetic energies E_{kin} of $20 - 500$ eV, the depth of penetration of the electrons into the material amounts to only a few atomic layers ($5 - 10$ Å). Since the depth of penetration is so small, there is no periodicity perpendicular to the surface and the corresponding wave vector component $\vec{k}^{hk}_{\perp}$ can have arbitrary values which delivers *diffraction rods* rather than *diffraction spots* in reciprocal space. The wave vector component parallel to the surface $\vec{k}^{hk}_{\parallel}$ has to meet the conditions

$$\vec{k}^{hk}_{\parallel} = h \cdot \vec{a}^* + k \cdot \vec{b}^* \tag{3.1}$$

with

$$|\vec{k}^{hk}_{\parallel}| = \vec{k}_0 \cdot \sin(\vartheta) \tag{3.2}$$

and

$$|\vec{k}_0| = \frac{2\pi}{\lambda_{\text{el}}} \, , \tag{3.3}$$

where h and k are the Miller indices, ϑ is the diffraction angle (see Figure 3.1), and λ_{el} is the de Broglie wavelength [134] of the electrons. $\vec{a}^*$ and $\vec{b}^*$ are the reciprocal unit cell vectors of the surface. They are defined as

$$|\vec{a}^*| = \frac{2\pi}{|\vec{a_0}|}, |\vec{b}^*| = \frac{2\pi}{|\vec{b_0}|} , \tag{3.4}$$

where $\vec{a_0}$ and $\vec{b_0}$ are the distances between rows of atom parallel to the surface. For quadratic and rectangular surfaces unit cells, they correspond to the vectors of the unit cells $\vec{a}$ and $\vec{b}$, for hexagonal surfaces $\vec{a_0}$ (and $\vec{b_0}$, respectively) is given by

$$\vec{a_0} = \vec{a} \sin \alpha , \tag{3.5}$$

with $\alpha = 120°$. $\vec{k_0}$ is the radius of the Ewald sphere. Thus, only those diffraction spots are present in the LEED pattern whose *diffraction rods* intersect with the Ewald sphere. This entails that at lower electron energies diffraction spots of higher order will not be observed (c.f. Figure 3.1b).
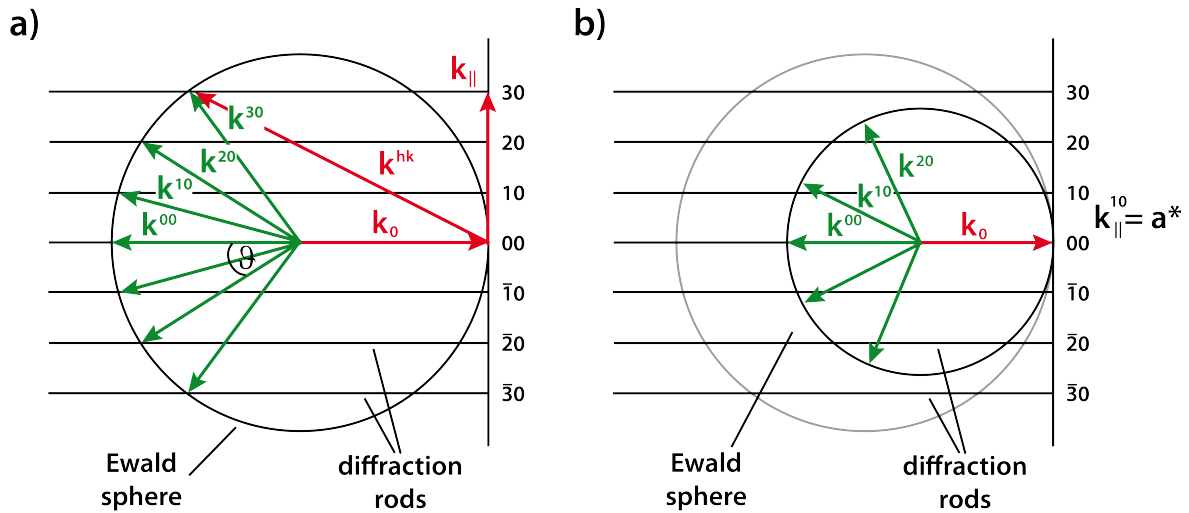
Figure 3.1: *a) Ewald construction corresponding to the conventional LEED set-up. The radius of the Ewald sphere $\vec{k_0}$ (red) depends on the energy of the electrons according to Eq. (3.3). Only diffraction rods that intersect with the Ewald sphere cause spots to appear in the LEED pattern. ϑ is the diffraction angle. b) Ewald construction for electrons with 50% of the energy as in a) (for comparison, the original Ewald sphere is shown in gray). With the smaller Ewald sphere, less diffraction spots can be observed in the LEED pattern and those spots that are present are positioned at larger distances from each other on the screen. As per Ref. [131].*

While the arrangement of the diffraction spots contains information about the symmetry, size, and orientation of the surface unit cell, the shapes of the spot profiles deliver information about the surface morphology, namely the surface roughness due to steps or domain boundaries. Deviations from the ideal surface like point defects, steps, and domain boundaries result in a broadening of the profiles. The broadening of the profiles due to steps depends on the energy of the incident electrons. Electrons that are diffracted at the upper and the lower level of a step, respectively, interfere destructively for certain energies. The phase shift of the two electron waves is described with the scattering phase S (cf. Figure 3.2a) and is defined via the step vector $\vec{g}$ and the diffraction vector $\vec{k}$:

$$S = \frac{\vec{g} \cdot \vec{k}}{2\pi} = \frac{\begin{pmatrix} g_x \\ g_y \\ g_z \end{pmatrix} \cdot \begin{pmatrix} k_x \\ k_y \\ k_z \end{pmatrix}}{2\pi} . \tag{3.6}$$

The effect of the step is maximal when S = half-integer (anti-phase condition). If S = integer, the electrons interfere constructively and they are not sensitive to the steps (in-phase condition). Thus, from the width of the profiles Δk_x measured at anti-phase conditions, the width of terraces T_{terrace} may be determined, while Δk_x measured at in-phase conditions is correlated to the transfer width T_{transfer}, a measure for the general spatial coherence of the surface and the instrument itself:

$$T_x = |\vec{a_0}| \cdot \frac{|\vec{k}^{01}|}{\Delta k_x} = \frac{2\pi}{\Delta k_x} . \tag{3.7}$$
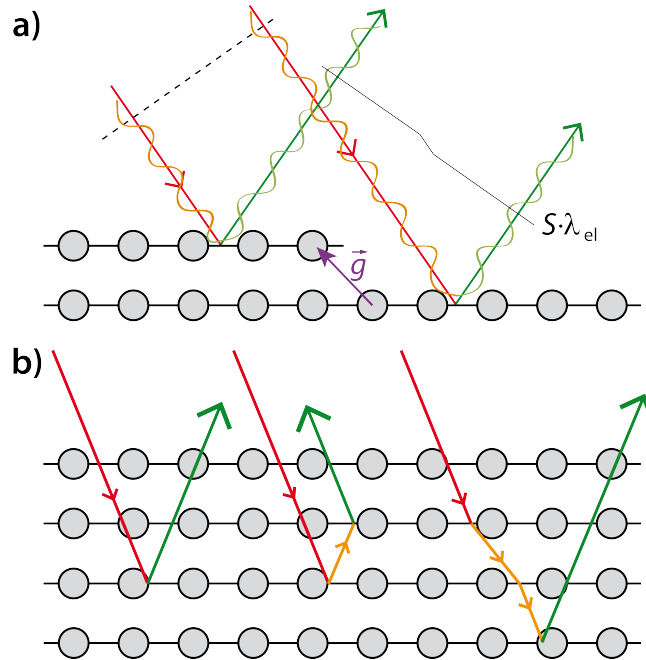
Figure 3.2: *a) Illustration of the scattering process at a step edge. In-phase incident electrons (red) get scattered at the upper and the lower level of a step edge, resulting in two diffracted waves (green) with a difference in path length of $S \cdot \lambda_{\text{el}}$ (the phase shift is indicated). As per Ref. [130]. b) Illustration of a single scattering process (left) compared to multiple scattering processes (middle and right). In multiple scattering processes, the incident electrons (red) do not only get scattered once leading to the outgoing, diffracted electron wave (green), but several scattering processes can be occurring in the first few layers of the crystals (orange) that lead to different outcomes for the diffracted beam. As per Ref. [131].*

Besides the surface morphology, electron diffraction allows access to the overall geometry of the surface including the adsorption sites of adsorbate atoms via the spot intensities. In the present thesis, this will be utilized in a simple kinematic approximation which is detailed in Appendix B. However, the spot intensities observed in experiments are also influenced when multiple scattering processes occur (as depicted in Figure 3.2b). Then, additional spots can be observed in the

LEED pattern of an incommensurate adsorbate as the additional scattering events alter the paths of the electrons. This, too, will be relevant for the present thesis.

3.2   Optical Spectroscopy

As introduced in Chapter 1, optical spectroscopy allows the investigation of slow CT due to a small mixing of electronic states of substrate and adsorbate and is thus an appropriate method for the systems investigated in the present thesis. The techniques employed here are FL and Raman spectroscopy. Reviews of these methods can be found in Refs. [135–142]. Both techniques can be used to probe the molecular vibrations of an adsorbate on a surface, however, FL spectroscopy concerns the excitation and relaxation of electrons in the probed substance leading to emission of photons and Raman spectroscopy is based on inelastic scattering of visible light.

3.2.1   Fluorescence Spectroscopy

The relationship of electronic and vibrational excitation in FL spectroscopy can be explained with the *Franck-Condon principle* and is commonly visualized with the Morse potential which describes the important phenomena for a single normal coordinate (see Figure 3.3a). The incidence of light on a substance may excite an electron from the HOMO of the ground state S_0 to the LUMO of the first electronic excited state S_1. The time-frame of molecular vibrations is 10^{-10} to 10^{-12} s and is much slower than the electronic transition which occurs within 10^{-15} s so that, in accordance with the *Born-Oppenheimer approximation*, the movement of the nuclei can be neglected and we speak of "vertical transitions". The probability for a specific transition increases with the overlap of the nuclear wave functions of the initial and the final state which affects the intensities of the FL vibrational peaks. This is shown in Figure 3.3b where the relative intensities of the vibrational peaks reflect the wave function overlap of the vibronic states in S_0 and S_1 in Figure 3.3a. In an FL process in condensed matter, the excited molecule relaxes non-radiatively into the vibrational ground state of S_1 where the excitation decays under emission of a photon into S_0. Thus, FL spectroscopy is in some sense the reversal of absorption spectroscopy.

The total intensity of the FL is described by the quantum yield η which is the ratio between emitted and absorbed photons and is connected to the life time of the excited state τ_S according to Eq. (3.8) in which k_r and k_{nr} are the rate constants of the radiative and non-radiative excitation decay processes and τ_r is the natural life time of the FL:

$$\eta = \frac{k_r}{k_r + k_{nr}} = k_r \cdot \tau_S = \frac{\tau_S}{\tau_r} \, . \tag{3.8}$$

τ_S has an essential influence on the shape of FL spectra as it determines the natural line width $\Delta\nu_{nat}$ of an FL peak [143] according to
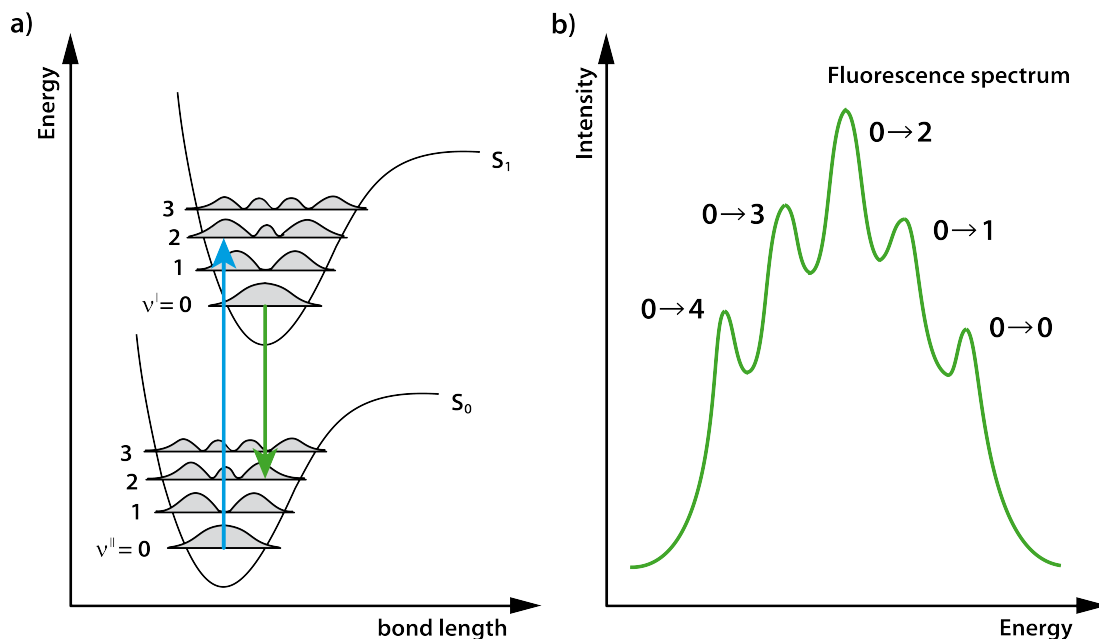
Figure 3.3: *a) Illustrations of the energetic transitions leading to FL. The absorption of laser light transfers an electron from the ground state S_0 into the first electronic excited state S_1 (blue). S_1 is shifted to larger bond lengths relative to S_0. In a non-radiative process the electron transfers from a vibronic exited state ($v' > 0$) in S_1 into the vibronic ground state. There, the excitation decays (green) emitting a photon which is detected as fluorescence. The transition probability depends on the overlap of the wave functions of the vibronic levels and influences the intensities of the signals in the spectrum. b) Fluorescence spectrum for the transitions depicted in a). The 0-2 transition shows the highest intensity as the involved wave functions have the largest overlap. As per Ref. [137].*

$$\Delta \nu_{\text{nat}} = \frac{1}{2\pi \tau_{\text{S}}} \ . \tag{3.9}$$

However, the line width of a given FL peak $\Delta \nu$ is determined by more factors. Factors that influence every molecule individually cause inhomogeneous line broadening. Besides the natural line broadening, temperature and saturation broadening increase the widths of FL peaks [144]. Inhomogeneous line broadening is a consequence of probing an ensemble of molecules. It is caused by the statistical distribution of energies of electronic transitions due to variations in the environment of individual molecules in the ensemble.

Non-radiative decay leads to a loss of FL intensity (quenching) and can be a result of a variety of processes. Significant for the present work is the quenching by interfacial CT between adsorbate molecules and the substrate as depicted in Figure 1.1. If the rate constants of the non-radiative decay processes of the excitation are significantly larger than that of the radiative decay, no FL can be observed. For similar time constants, both competing processes may be present.

3.2.2   Raman Spectroscopy

Raman spectroscopy observes light inelastically scattered by a material (for the purpose of this thesis, large organic molecules). The interaction of the electromagnetic wave with the molecules can lead to an energy transfer (corresponding to the energy of a vibration) from the photons to the molecule or vice versa (if the molecules are in a vibrationally excited state). These different interactions manifest as Stokes and Anti-Stokes lines in the Raman spectrum (see Figures 3.4a and b). However, not all molecular vibrations can be observed in the Raman spectrum because only such vibrations are Raman-active that lead to a change of the polarizability of the molecule.
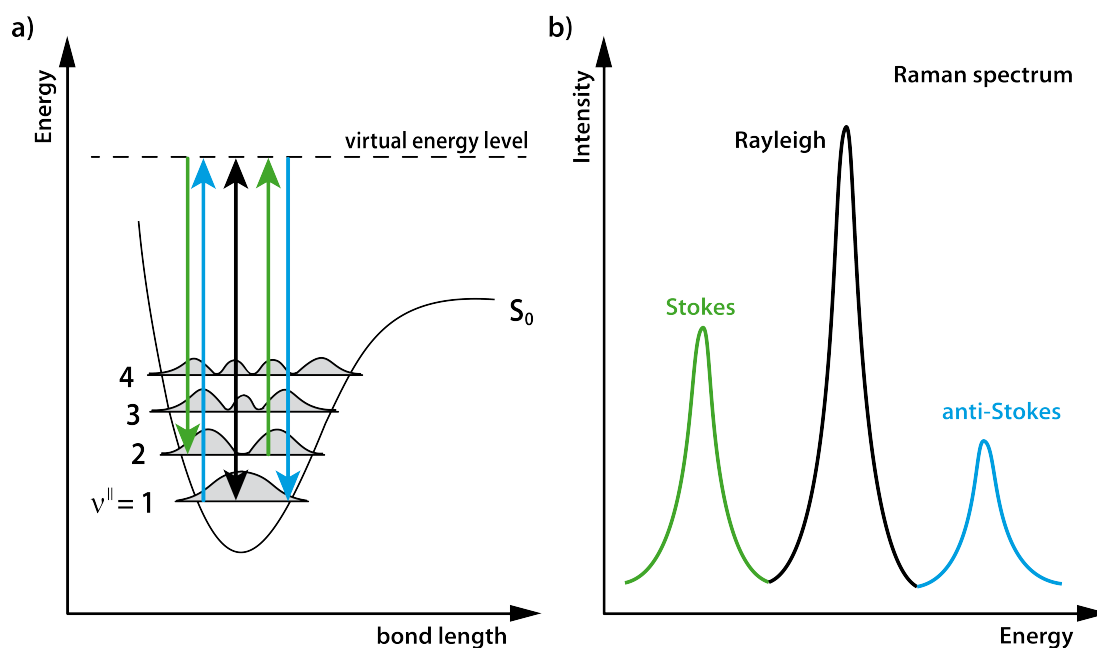
Figure 3.4: *a) Schematic representation of the Raman scattering process. The interaction with light leads to the transition of an electron to a higher or lower vibronic level within S_0 via a virtual energy level. b) Schematic illustration of a Raman spectrum. Elastically scattered photons occur in the spectrum as a Rayleigh peak (black). Electrons that get excited into a higher vibronic state cause Stokes lines in the spectrum (green), while an energy loss of electrons in higher vibronic states leads to anti-Stokes lines (blue). For the latter process to be even possible, higher vibronic states have to be occupied. Since the population of these is lower than the population of the ground state, the intensity of the anti-Stokes lines is smaller than that of the Stokes lines. As per Ref. [137].*

If the energy of the incident light is close to an electronic transition of the molecule, the Raman effect gets enhanced because the change in the electronic configuration of the molecule greatly changes its polarizability so that the Raman scattering is much stronger. The related technique is called *resonance Raman spectroscopy*.

Surface enhanced Raman spectroscopy

Surface enhanced Raman spectroscopy has become a powerful tool among the surface science methods. The effect of *surface enhanced Raman scattering* (SERS) is commonly observed on rough surfaces of noble metals [145] or near metallic nanocrystals [146]. There is a chemical and an electromagnetic mechanism that both contribute to the enhancement of Raman signals.

The chemical mechanism is based on the intrinsic chemical characteristics of the investigated system [146]. A CT between molecule and substrate, if present, will lead to a change in the polarizability of the molecule and thus to an enhanced Raman signal. It is also possible that the intrinsic electronic structure of the adsorbed molecule allows for a resonance Raman effect which causes an enhancement of the signal by a factor of 10^2 - 10^3 [146].

The electromagnetic mechanism is related to the surface roughness. In a theoretical study, García-Vidal and Pendry [147] showed that the interaction of the incident light with localized surface plasmon polaritons, which are trapped in the crevices between surface defects, creates a large local E field. This leads to an enhancement of the Raman signal by a factor of 10^5 - 10^6. Thus, the contribution of the electromagnetic mechanism is much more significant than that of the chemical mechanism. The SERS effect caused by the electromagnetic mechanism is a highly localized effect and the spectrum will be governed by those enhanced Raman signals coming from the surface area with the highest roughness.

3.3 Temperature Programmed Desorption Spectroscopy

Temperature programmed desorption (TPD) is an experimental method that allows insight into the interaction between the substrate and the adsorbate. In the context of the present thesis, TPD is used to investigate the desorption process of borazine on Cu(111) in order to understand the growth of hBN layers. Furthermore, the determination of molecular coverages on the surface is essential for the interpretation of optical spectra of PTCDA on hBN/Cu(111) and Cu(111). Details on the TPD technique can be found in Refs. [128, 129, 148–150].

In a TPD experiment, the temperature of the sample is increased with a constant heating rate β while simultaneously the desorbed molecules are detected with a mass spectrometer. To avoid detecting molecules that desorb from the sample holder, a Feulner cup can be used [151] (depicted in Figure 3.5). The aperture at the bottom of the cup allows the detection of the desorbed molecules while slits in the sides allow the ionization chamber of the mass spectrometer to be pumped and, additionally, monitoring of the amount of deposited molecules during sample preparation. With a constant pumping speed and a large ratio of pumping speed to volume (as provided by the Feulner cup) the recorded ion current is proportional to the number of particles desorbed per time [152] and thus the integral of the measured ion current is proportional to the amount of molecules desorbed from the surface. This way, for systems where the adsorbate desorbs completely upon heating of the sample (e.g. hexaazatriphenylene–hexacarbonitrile desorbs from Au(111) intact while the desorption from Ag(111) is not possible [153]), the exact coverage for every preparation can be determined.

The spectrum can be described with the *Polanyi-Wigner* equation which connects the desorption rate r (the change of the number of adsorbed molecules on the surface N with time t or surface temperature T_S) with the coverage-dependent desorption energy $E_{des}(\theta)$ [150, 152]:

$$r = -\frac{dN}{dt} = -\beta \frac{dN}{dT_S} = \theta^n \cdot \nu_0 \cdot \exp\left(\frac{-E_{des}}{k_B T_S}\right) . \tag{3.10}$$
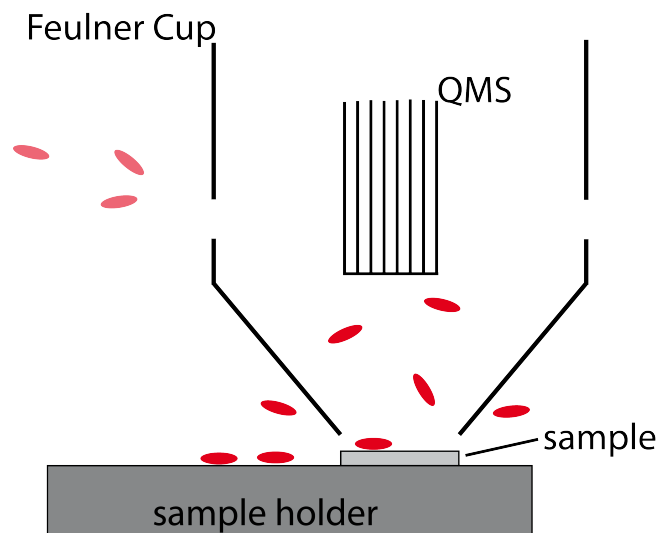
Figure 3.5: *Schematic depiction of a Feulner cup. The Feulner cup encloses the ionization chamber of the mass spectrometer. An aperture at the bottom and slits on the sides allow the detection of molecules desorbing from the sample or those that are evaporated during deposition, respectively. At the same time, the Feulner cup blocks molecules that desorb from the sample holder from entering the detector.*

The pre-factor ν_0 contains the partition functions of the initial state of the adsorbed molecules and of their transition states during desorption; n is the order of the desorption process [129] and can have values of 0, 1, or 2. A 1st order desorption describes the desorption of the complete molecule from the surface, a 2nd order desorption requires a preceding step like a recombination, and desorption of 0th order refers to the desorption of multilayers which is independent of the coverage. The order of desorption determines the shape of the desorption spectrum [128]. Additionally, the shape of the spectrum may be influenced by lateral interaction between the adsorbate molecules [154] which leads to a shift of the spectrum to higher or lower temperatures. Several different methods for the analysis of TPD spectra have been reported. An overview of the most common methods has been published by de Jong et al. [150].

3.4   Photoemission Spectroscopy

Photoemission spectroscopy (PES) experiments delivered crucial information about the vertical structure and electronic properties of the systems hBN/Cu(111) and PTCDA/hBN/Cu(111). These experiments were, however, not the main focus of the present thesis, thus, the methods *x-ray photoemission spectroscopy* (XPS), *normal incidence x-ray standing waves* (NIXSW, in this thesis referred to as XSW for brevity), and *ultraviolet photoemission spectroscopy* (UPS) will be summarized only briefly. Detailed reviews on these techniques can be found in Refs. [128, 138, 155–161].

The basic principle for PES is the photoelectric effect: irradiation of a solid material with photons leads to an emission of electrons, as long as the photonic energy is larger than the work function of the sample. Thus, depending on the energy of the photons, different electrons can be extracted

from the material. The kinetic energy E_{kin} of the electrons that leave the sample upon irradiation with the energy hν is given by *Einstein's photoelectric equation*:

$$E_{\text{kin}} = \text{h}\nu - (E_{\text{B}} + \Phi) \,, \tag{3.11}$$

where E_{B} is the binding energy of a core level with respect to the Fermi level E_{F} and Φ is the work function. This is schematically shown in Figure 3.6. The electrons get detected by a hemispherical analyzer and from E_{kin}, E_{B} can be determined.
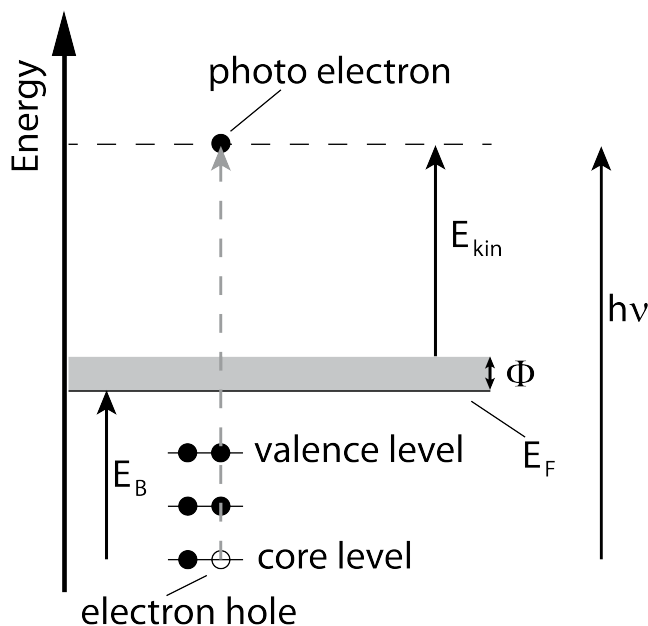
Figure 3.6: *The irradiation of a sample by light leads to the removal of an electron from an orbital, out of the sample, and into the vacuum. For this, the energy of the light hν has to be large enough to overcome the binding energy E_{B} of the electron and the work function Φ. Excess energy is converted into the kinetic energy E_{kin} of the electron. As per Ref. [128].*

For the probing of core level electrons, monochromatic high-energy x-rays are used to irradiate the sample (XPS). The binding energy of the core levels is characteristic for each element, yet also dependent on the chemical environment of the atom. The chemical environment changes the energies of the initial and final state of electrons and, thus, causes shifts of E_{B}. In the spectrum, this manifests as the "chemical shift" of the XP peaks. Thus, XPS allows not only the identification of the atomic species on the surface but also the analysis of their chemical environment.

The probing of valence electrons, on the other hand, allows the analysis of the actual chemical bonds in the adsorbate molecules. Here, the sample is irradiated with ultraviolet light (UPS). Since the ionization cross section of valence orbitals is significantly larger for low photon energies, these electron transitions can be probed more effectively by UPS compared to XPS [162]. The specific molecular orbitals that bond to the substrate can be identified by "fingerprinting": The UP spectrum of the adsorbed molecule is compared to the spectrum of the molecule in the gas phase. An energetic shift of the peaks points to the changed orbitals due to the adsorption on a surface. Furthermore, the work function of the probed surface can be determined from UP spectra.

Besides the investigation of the electronic structure of an adsorbate, PES in the special form of XSW can also be used for measuring its vertical structure. The XSW technique allows the determinations of the vertical distances of adsorbed atoms relative to the Bragg planes of the substrate. For this, it employs XPS measurements as a function of the energy of the photons. If the energy of the incident x-ray beam (normal to the surface) corresponds to the Bragg energy E_{Bragg} of the probed sample according to

$$E_{\text{Bragg}} = \frac{hc}{\lambda} = n \cdot \frac{hc}{2d_{hkl} \cdot \sin \theta_{\text{B}}} \, , \tag{3.12}$$

with d_{hkl} as the lattice plane spacing of the {hkl} lattice planes and θ_{B} as the Bragg angle with respect to the lattice planes, we speak of a Bragg reflection. For a Bragg reflection, the incident and the reflected waves combine to a standing wave which extends into the crystal and into the vacuum above the surface. The periodicity of the x-ray wave field is well-defined, corresponds to the periodicity of the Bragg planes and causes the emission of photoelectrons from the sample. Those species that are positioned at a maximum of the standing wave emit more electrons than those that are not. Thus, a scanning of the energy around the Bragg energy ($\pm$ 5 eV), which leads to a shift of the maxima of the standing wave, allows the detection of XP spectra in which the intensities for different atomic species on the surface depend on their respective vertical distances from the surface.

For an XSW spectrum, the integrals of the XP peaks of the individual species are plotted as a function of incident energy. The intensity I of the resulting *yield curve* can be described by

$$I \sim 1 + R + 2\sqrt{R} \cdot F_{\text{C}} \cdot \cos \left(\nu_{\text{C}} - 2\pi P_{\text{C}} \right) \, , \tag{3.13}$$

in which R is the reflectivity of the substrate and ν_{C} describes the phase relationship between incident and reflected electromagnetic wave.[1] The results gained from the yield curve are the coherent position P_{C} and the coherent fraction F_{C}. For the ideal case of a single adsorption height, F_{C} would be 1 and P_{C} would describe the adsorption height in units of the distance between the Bragg planes of the crystal from which the standing wave originates. However, in real cases F_{C} is always < 1 because of thermal vibrations which render both the atomic positions and the standing wave slightly incoherent. P_{C} can then be interpreted as corresponding to average adsorption heights.

The vertical distance d_{C} of the adsorbate atoms from the surface can be calculated as

$$d_{\text{C}} = (P_{\text{C}} + n) \cdot d_{\text{hkl}} \, , \tag{3.14}$$

where n is an integer and and d_{hkl} is the distance between the Bragg planes of the substrate. For the Cu(111) surface, this distance is 2.087 Å [163]. This corresponds to a Bragg energy of 2.972 keV. For the calculations of d_{C} in the present thesis, $n = 1$ is used. Hence, the experiment requires the use

---

[1]Eq. (3.13) only holds for the dipole approximation. For a correct interpretation, nondipolar corrections have to be considered.

of synchrotron radiation. The experiments shown in this work were carried out at the Diamond Light Source in Didcot, England, at beam line I09.

4 Experimental

All experiments presented in this thesis were carried out under ultra-high vacuum (UHV) conditions. The experimental set-ups, sample preparation, and general procedures will be described in this chapter.

4.1 Experimental Set-up

Different UHV set-ups were employed for the experiments in the present work. The set-ups for the SPA-LEED, TPD, and optical experiments will be given below. The set-up of the STM chamber is described in detail in Ref. [107]. UPS data were measured as part of a cooperation with Dr. Serguei Soubatch and Dr. François Posseik from the group of Prof. Dr. F. Stefan Tautz from the Forschungszentrum Jülich. The XPS and XSW experiments were conducted at beamline I09 at Diamond Light Source in Didcot, UK. A detailed description of the experimental details and of the data analysis can be found in Appendix A.1.

4.1.1 The UHV chamber

The SPA-LEED, TPD, and optical experiments were carried out in a UHV chamber with a base pressure p of 2.3×10^{-10} mbar, which was reached after a 48 h bake-out at 150°C. The chamber is pumped with five pumps: a rotary oil pump, a diffusion pump, a turbo molecular pump, an ion getter pump, and a titanium sublimation pump. A schematic representation of the chamber is shown in Figure 4.1. All experiments were done on Cu(111) single crystals with a diameter of 8 mm, bought from Mateck.

The crystal was mounted on a home-build sample holder, which is detailed in Ref. [166]. The sample holder is attached to a long travel manipulator with a continuous-flow helium cryostat that allows cooling of the sample down to 6 K. The crystal could be heated up to 1100 K via thermal irradiation from a tungsten filament and electron bombardment. High temperatures were measured by a type-K thermocouple and low temperatures (< 70 K) were measured via a Si-diode (DT-670B-SD, Lake Shore, Cryotronics). The diode was positioned on the sample holder, approximately 70 mm removed from the sample.

The chamber was equipped with a sputter gun with a separate argon line (IQE11/35, Specs) for cleaning the sample. For the deposition of the adsorbates, two different evaporators were used. The liquid borazine for the preparation of hBN layers was stored in and evaporated from a glass container which was held at a temperature of −5°C by a removable Peltier cooling system. For
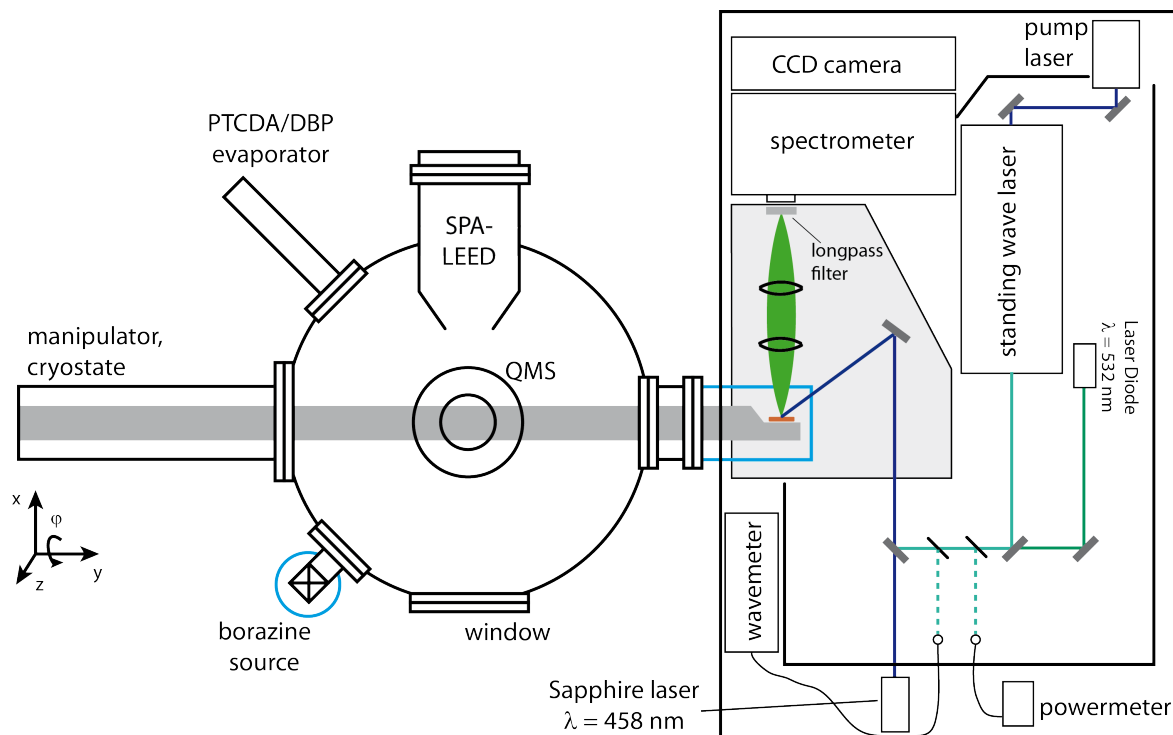
Figure 4.1: *Experimental set-up of the UHV chamber and the optical table. Not true to scale. For detailed description, see text. As per Refs. [164, 165].*

a detailed description of the handling, cleaning procedure, and storage of borazine, refer to Appendix F. The organic molecules were evaporated from glass crucibles in home-build Knudsen cells.

For monitoring the molecular flux and checking the purity of the adsorbed species, a quadrupole mass spectrometer (QMG422, Pfeiffer Balzers) was used. For conducting TPD experiments, the quadrupole mass spectrometer (QMS) was equipped with a Feulner cup [151]. For the optical experiments, the sample could be transferred into a glass head (quartz glass, VP63Q, Vacom) at the far end of the chamber. The set-up for the optical experiments will be detailed in the next section. Between the main body of the chamber and the glass head, a home-build incident light microscope (for details see Ref. [166]) could be installed that could image the sample under UHV through a 1.75 mm thick glass window with all optical components outside the vacuum.

Structural investigations were carried out with a SPA-LEED apparatus (Omicron). The channeltron aperture was expanded to 300 μm (from 100 μm) which allows a higher counting rate but reduces the instrumental resolution. However, the higher counting rate is desirable for the investigation of large organic molecules since a smaller electron current on the sample reduce possible radiation damage. Additionally, the deflection voltages of the SPA-LEED controller were modified (50 V instead of 150 V) in order to stabilize the more frequently used lower voltages. The lowest possible acceleration voltage E_{kin} for the electrons was 20 eV. For measurements with even slower electrons, the E_{kin} and the voltage of the entrance lens (which is internally dependent on E_{kin}) were controlled by home-build external potentiometers (see Appendix B.2).

For TPD experiments, the sample was moved directly beneath the Feulner cup at a distance of ~0.5 cm. The ion getter pump and the titanium sublimation pump were disconnected from the chamber by a large plate valve in order to ensure a constant pumping rate in the chamber (cf. Chapter 3.3). The sample was then heated with a rate of 1 Ks^{-1} with a temperature control (Eurotherm). The TPD spectra were recorded via Labview [167] with a program written by N. Humberg [168] and modified by B. Wolff [169].

Some SPA-LEED experiments were carried out in a different UHV chamber (with a base pressure of 3.0 $\times$ 10^{-10} mbar), equipped with the above mentioned evaporators, a QMS (QMS 200 Prisma, Pfeiffer Balzers) and a SPA-LEED apparatus from Omicron. Its channeltron aperture was modified in the same way as described before (300 μm instead of 100 μm) but the deflection voltages were not modified.

4.1.2 Optical set-up

In the glass head, the sample was illuminated by a monochromatic laser beam that was focused on the sample by a mirror. The incident angle was approximately 45° relative to the surface normal. The diameter of the laser spot on the sample was about 0.5 mm. The fluorescence and Raman scattered light from the sample was collected and parallelized by an achromatic lens (N-BAF10/SF10, f = 100 mm, $\varnothing$ = 50.8 mm) and focused by a second achromatic lens (N-BK7/SF2, f = 200 mm, $\varnothing$ = 50.8 mm) onto the entrance slit of the spectrometer. The spectrometer (Spectra Pro 2300i, f = 0.3 m, Acton) contained three different gratings (300, 600, and 1200 grooves per millimeter) and was equipped with a nitrogen-cooled CCD camera (Spec-10:100-BR(LN)), operated at −110°C. In order to block external stray light from entering the spectrometer, the glass head, the lenses, and the entrance slit of the spectrometer were enclosed by black oxidized aluminum plates.

For the excitation, three different lasers were used. Most experiments were conducted using an optically pumped semiconductor laser (Sapphire LP UBB CDRH, Coherent) with 458 nm and 50 mW. Secondly, a laser diode (Laser Components) with 532 nm and 10 mW was employed. To block the laser light from entering the spectrometer, long pass filters were positioned in front of the entrance slit (cut-off at 475 nm when using the Sapphire laser and cut-off at 532 nm when using the laser diode). Lastly, a combination of a tunable standing wave laser (Cr-599, Coherent) and an optically pumped semiconductor laser (Genesis CX, Coherent) with 480 nm and up to 4 W was used. The dye used in the standing wave laser was Coumarin 498 and the laser was tunable (using a three-plate birefringent filter, line width 1 cm^{-1}) between 494 and 515 nm with an output of up to 60 mW. About 10% of the laser light were redirected to a power meter (PM120, Thorlabs) and a wavelength meter (High Finesse Angstrom WS/6), respectively, to monitor both attributes of the tunable laser light. In front of the entrance slit of the spectrometer a long-pass filter with cut-off at 520 nm was used.

The acquisition of the spectra was controlled with the software WinSpec32 [170]. For the wavelength calibration of the spectra, reference spectra of a calibration lamp (Hg(Ar)-lamp, Newport)

were recorded for each grating used per experimentation day. For the conversion of the wavelength scale to the wavenumbers scale, the relative spectral intensity was corrected by applying a factor λ^2. The FL spectra were mostly recorded with an exposure time of 2 seconds and 50 accumulations. All pixels of the CCD in the vertical direction were binned. The entrance slit of the spectrometer was usually set to 0.1 mm. With this set-up, spectra with resolutions of 48, 24, and 12 cm^{-1} (for the gratings with 300, 600, and 1200 grooves per millimeter, respectively) were recorded. The spectrometer resolution was checked by measuring the light of a Hg lamp and determining the full width at half maximum (FWHM) of the peak that was positioned at ~18,300 cm^{-1} where the fluorescence observed in the experiments presented in the present thesis are located.

4.2 Preparation procedures

4.2.1 The Cu(111) surface

All experiments presented in this thesis were carried out on the (111) surface of a copper single crystal. The clean metal substrate was prepared in iterative cycles of two steps. First, contaminations were removed from the sample at room temperature by ion bombardment with Ar$^+$ ions at an argon pressure via the background of 2.2×10^{-5} mbar. The ions were accelerated onto the surface with 1000 eV. In a second step, the sample was annealed in order to heal the roughened surface. After preparation, the quality of the Cu(111) surface was verified via SPA-LEED. A well-prepared surface showed sharp spots and high spot-to-background intensity ratios.

Two different crystals in two separate UHV chambers were used for the experiments presented here. Diverging preparation conditions for the two crystals are summarized in Table 4.1. An additional third crystal was employed for the PES measurements at the Diamond Light source. The structural investigations of hBN/Cu(111) and PTCDA/hBN/Cu(111) were conducted with crystal A in the second UHV chamber (base pressure 3.0×10^{-10} mbar, see Chapter 4.1). In the main chamber (see detailed description above), FL measurements, structural investigations of PTCDA/Cu(111), and the line profile analysis of hBN/Cu(111) were carried out on crystal B. From the analysis of the full-half widths of spot profiles recorded at 78 eV (corresponding to in-phase conditions for the specular spot) the transfer width T_{transfer} of the crystals was determined (cf. Eq. 3.7). For crystal B, segregations of impurities from the bulk occurred when the same preparation conditions were used as for crystal A, namely when the sample was annealed at temperatures >1040 K or for a time >30 minutes. They were identified by additional sharp spots of complicated superstructures in LEED. These patterns are shown in Appendix D. Accordingly, the preparation conditions were adjusted in order to prevent the segregations (cf. Table 4.1).

Table 4.1: *Preparation conditions for the two Cu(111) crystals used in the experiments presented here. The ion current on the sample during sputtering I_S, the impact angle of the ions on the sample relative to the surface normal during sputtering ϕ_S, the sputtering time $t_{sputtering}$, and the annealing temperature $T_{annealing}$ are summarized. Additionally, the transfer widths $T_{transfer}$ are given.*

	I_S	ϕ_S	$t_{sputtering}$	$T_{annealing}$	$T_{transfer}$
crystal A	$7\ \mu A$	$0°$	30 minutes	1070 K	430 Å
crystal B	$3-4\ \mu A$	$+/-45°$	15 minutes each	1000 K	450 Å

4.2.2 hBN on Cu(111)

Before the preparation, the quality of the borazine was controlled with the QMS. In storage, borazine decomposes to hydrogen and BN polymers. A large percentage of hydrogen in the gas dosed into the chamber falsifies the presumed amount of borazine molecules in the chamber and thus prevents the preparation of a high quality hBN layer. Details of the cleaning procedure of borazine are given in Appendix F. The borazine was considered suitable for hBN preparation when the signals for H_2 ($m/z = 2$)[1] and borazine ($m/z = 80$) showed a ratio of $\leq$ 1:1.

The hBN layers were prepared on the clean Cu(111) surface. The final annealing step of the preparation of the clean Cu(111) surface before borazine deposition was omitted for crystal B. The sample was heated up to 1010 K (for crystal B that showed segregation) or 1070 K (for crystal A) and the borazine was dosed into the chamber to $(1.6 \pm 0.1) \times 10^{-6}$ mbar via the background for 30 minutes. This amounts to a dosage of ~2000 L. During borazine deposition, the ion getter pump was switched off in order to prevent hBN from growing on its hot filaments. After 30 minutes, the borazine valve was closed and then the sample was cooled down with a rate of $1-2$ Ks^{-1}.

4.2.3 Molecules on hBN/Cu(111) and Cu(111)

3,4,9,10-perylene tetracarboxylic dianhydride (PTCDA) and 5,10,15,20-tetraphenylbisbenz[5,6]-indeno[1,2,3-cd : $1', 2', 3' - lm$]perylene (DBP) were evaporated from glass crucibles. Their molecular flux was monitored with the QMS. The evaporation temperature was adjusted so as to achieve a constant growth rate of 1 monolayer per minute (typically 850 K for PTCDA and 770 K for DBP). These rates were calibrated by B. Wolff in TPD experiments [169, 171]. A monolayer (ML) is defined as one completed closed layer of flat lying molecules. During deposition, the sample was turned towards the crucible and was held at a constant temperature (either 20 K or 300 K for PTCDA and 20 K for DBP).

Borazine was evaporated from its glass container. The molecules were deposited on Cu(111) at a sample temperature of 100 K. The doses amounted to $0.5-8.5$ L with a borazine pressure of up to 4×10^{-8} mbar via the background. During the borazine deposition, the ion getter pump was switched off in order to prevent hBN from growing on its hot filaments.

---

[1]m is the mass of the molecule and z is its charge.

The desired coverages were achieved by on-line integration of the QMS signal via *Labview* [167] (m/z = 392 for PTCDA and m/z = 80 for borazine, which correspond to the unfractured molecules with a single charge, and m/z = 402 for the unfractured DBP molecule with a double charge). The exact coverages were determined after every experiment via TPD with a margin of error of $\pm$ 0.05 ML for PTCDA, $\pm$ 0.10 ML for DBP and $\pm$ 0.1 ML for borazine. The underlying calibration for the PTCDA coverages [169] are true for both the hBN/Cu(111) and the Cu(111) surface due to the large structural similarity of the monolayer structures (see Chapter 6).

5 Hexagonal Boron Nitride on Cu(111)

This chapter presents the lateral and vertical structure of a monolayer of hBN adsorbed on the Cu(111) surface. Most of the results have been published and can be found in Appendix A.1. They will be summarized here and supplemented with investigations of incomplete layers of hBN. The structural information of the incomplete layer of hBN and desorption experiments of borazine on the Cu(111) surface will be used to develop a model for the growth process of hBN on Cu(111). Both the structure and the growth of hBN on Cu(111) will be discussed in the context of other publications that appeared during the time of the present work. As an introduction, some of the relevant publications in this field will be summarized.

5.1   Literature Overview

hBN can be grown under UHV conditions on single crystalline metal surfaces from the precursor borazine [11]. Borazine is an inorganic analogue to benzene, an aromatic cyclic molecule composed of boron and nitrogen instead of carbon [71]. When the borazine molecules come into contact with the hot metal surface they decompose, losing their hydrogen atoms, and form the hBN sheet. The surface temperature that is required for the hBN growth depends on the metal surface. In general, less reactive surfaces require higher temperatures and higher doses of borazine than more reactive surfaces [11]. The growth of hBN is self-terminated after one monolayer [75].

hBN on Ni(111) forms a commensurate structure [78] due to the small lattice mismatch of only -0.5%. The lattice constants of Cu(111) ($a_{Cu} = 2.556$ Å [76]) and Ni(111) ($a_{Ni} = 2.492$ Å [76]) differ by only 2.5% and the nominal lattice mismatch of hBN/Cu(111) amounts to 2.0%. In this regard unsurprisingly, the first study about hBN/Cu(111) [172] also found a commensurate structure, indicating a stretching of the hBN layer in order to match with the Cu(111) surface. However, the binding energy of hBN to Cu(111), according to theoretical calculations [55], is significantly smaller (by a factor of $1.4-3.8$, depending on the theoretical method employed) than that to the Ni(111) surface. Furthermore, photoemission experiments have shown a strong chemisorptive bond between hBN and Ni(111) due to a hybridization of the $3d$ metal states and the π-orbitals of hBN, while on Cu(111), only a much weaker hybridization was found [172]. The binding energy of hBN/Cu(111) is rather comparable to hBN/Ag(111), where the metal has no influence on the structure of the hBN layer [87] (cf. Chapter 2.1). Such a weak bond makes a stretching of the hBN layer to overcome the (even small) lattice mismatch and, thus, to conform to the Cu(111) lattice rather unlikely. Furthermore, it was shown in STM that hBN domains can grow across Cu step edges which indicates weak interactions at the interface, too [173].

Joshi et al. [174] conducted an experimental STM study on hBN/Cu(111). As described for other metal substrates in Chapter 2.1, the authors observed Moiré patterns composed of wire regions and pores ("moirons")[1]. At high bias voltages, they found a multitude of Moiré patterns with varying periodicities, moiron sizes, and orientations. Figure 5.1 shows four of these Moiré patterns next to each other. These different patterns are caused by *incommensurate* hBN domains that vary in their azimuthal orientations relative to the Cu(111) substrate. The lattice mismatch between Cu(111) and the hBN layer was 1.8% (at 6 K), the periodicities of the Moiré patterns were in the range of 5 nm to 14 nm, and the minute rotations of the domains were between 0 and 3° relative to the substrate lattice vector $\vec{a}_1$. Roth et al. confirmed the structural parameters in LEED [176]. Near the domain boundaries, distortions of the Moiré patterns were observed [174].
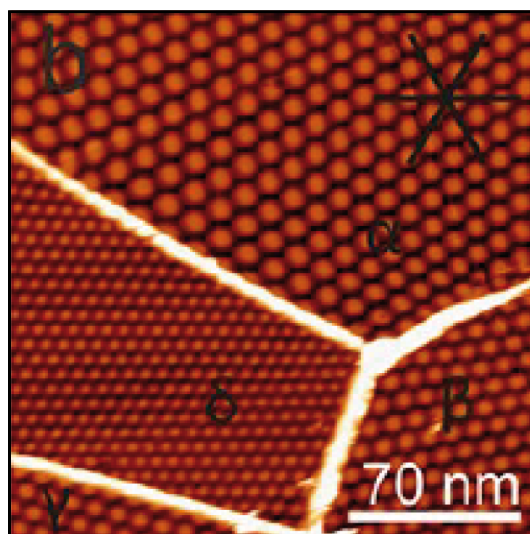
Figure 5.1: *STM image of hBN/Cu(111) measured at 6 K with U_{bias} = + 4 V and I_t = 0.6 nA. Four different Moiré patterns (labeled $\alpha - \delta$) are separated by domain boundaries. The domains differ in periodicity and azimuthal orientation of their respective Moiré patterns. The lines in the top right corner indicate the high-symmetry directions of the Cu(111) surface. Taken from Ref. [174].*

The apparent heights of the Moiré patterns strongly depended on the bias voltage which led the authors to the conclusion that the surface was merely electronically corrugated and not topographically. This has been corroborated by DFT calculations [177] which give a vertical distance between the hBN layer and the Cu(111) surface of 3.006 Å, with a maximum amplitude of the hBN layer of 0.013 Å. Note that other theoretical studies have found other values for the vertical distance between hBN and Cu(111), covering a wide range between 2.65 Å and 3.341 Å [55, 178–181]. The probable reason for these discrepancies are the different theoretical approaches toward the weak vdW interactions at the interface.

The electronic corrugation is also apparent in the change of work function from 4.1 eV in the wire regions to 3.8 eV in the moirons [174] (a reduction of the work function of bare Cu(111) of 4.94 eV [182]). This is in agreement with the lateral work function change of hBN on other metal

---

[1]The round areas of the Moiré patterns termed "pores" in other studies are called "hills" by Joshi et al. while the equivalents of the "wires" are called "valleys" [174]. Due to the bias dependence of the apparent heights, this terminology is not robust. To avoid confusion when talking about hBN/Cu(111) in this work, the term "moiron" [175] will be used for the regions equivalent to what is called "pores" in other studies. The areas between the moirons will be referred to as "wires".

substrates as summarized in Chapter 2.3. The lateral shift in adsorption positions of boron and nitrogen atoms is the suspected reason for this as the adsorption sites of the atoms changes from the preferred registries (N: on-top, B: hollow sites, as on Ni(111)) to less favorable registries [174, 177].
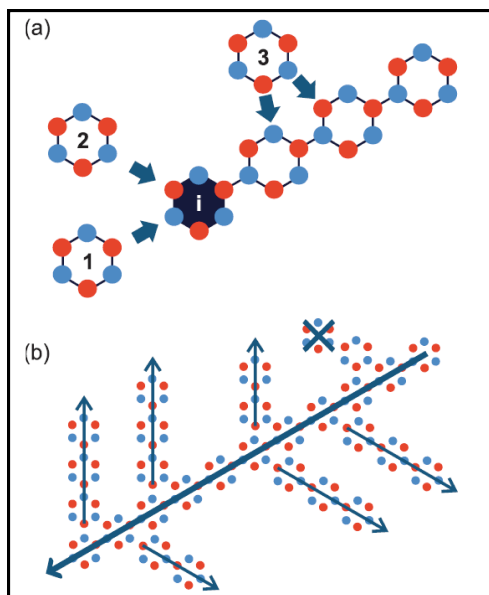
Figure 5.2: *Schematic illustration of the model for the hBN growth process on Cu(111) by Felter et al. Taken from Ref. [183]. a) The hBN domain can grow via the BN ring "i" by the attachment of borazine molecule 1 forming a bond from a red to a blue atom or borazine molecule 2 forming a bond from blue to red. An additional possibility is the attachment of molecule 3, forming two bonds. The preference of molecule 1 attaching to a domain over molecule 2 is explained by Felter et al. with the difference in dehydrogenation energy between the B−H and N−H bonds. b) Growth of the main branch occurs via bond formation with molecule 1. After molecule 3 attaches, further growth via the channel of molecule 1 leads to the formation of side branches in an angle of 120°.*

As mentioned above, the required growth conditions for hBN (sample temperature and borazine dose) correlate with the reactivity of the metal surface and the hBN growth is self-terminated after one monolayer. Both factors point to a catalytic reaction of the borazine molecules with the metal surface which is required for the hBN formation. However, this assumption has not been proven, yet. The first study on the growth process of hBN was conducted by Felter et al. [183]. They investigated the growth of hBN on Cu(111) in *low energy electron microscopy* (LEEM) experiments and proposed a model for the growth process of hBN domains. In the context of the present thesis, this is of very high interest as Felter's findings can assist in the interpretation of the structural data of hBN/Cu(111) presented here. Felter observed dendritic growth of domains with three main branches separated by 120°, from which minor branches grew outward, bend backwards, again in an angle of 120° (see Figure 5.2). In their model, this dendritic growth is caused by the formation of single B−N bonds, with a preference for one of the atoms as part of the domain and the other atom being the attacking reactant. The differentiation between BN-rings attaching themselves to domains via a boron or a nitrogen atom was explained by a difference in dehydrogenation energy due to the different bond strengths of hydrogen to the two atoms [184]. Thus, this growth mode was termed "dehydrogenation limited aggregation". Importantly, the B−N bonds form between *intact* BN rings of the borazine. Importantly, the B−N bonds within the molecules do not break

upon adsorption of the molecule on the surface so that the (possibly dehydrogenated) BN-rings may be diffusing on the metal surface. As shown in Figure 5.2, this allows the growth of domains in three straight directions (main branches, via molecule 1) while the growth in 60° relative to the main branch is inhibited (molecule 2). If the main branch can no longer grow, the addition of a BN ring on the side via the formation of *two* B−N bonds widens the main branch (molecule 3). From there, the minor branches grow by the formation of single bonds, as before.

5.2   The Structure of hBN on Cu(111)

5.2.1   The lateral structure

A LEED pattern of hBN/Cu(111) is shown in Figure 5.3a. It exhibits two features that are characteristic for this surface: a continuous ring of intensity passing in proximity to the first order diffraction spots of the Cu(111) surface and satellite structures composed of lines around those Cu spots and the specular spot (see Figures 5.3c and d).

The radius of the ring is ~2% larger than the distance of the Cu(10) spots from the specular spot, in agreement with the nominal mismatch of 2.0%. The ring is the result of a superposition of the first order spots of hBN domains with different azimuthal orientations on the Cu(111) surface and will be referred to as "hBN ring" in the following. The intensity of the hBN ring is not homogeneous. Approximately 90% of the intensity is accumulated in the $\overline{\Gamma M}$ direction with a spread of 4.4°. These sections of the ring will be referred to as "arcs". On the rest of the ring, the highest intensity can be observed in the $\overline{\Gamma K}$ direction. Increased intensities in certain directions indicate preferential azimuthal orientations of the hBN domains. A similar arrangement of the hBN domains has been observed on Pd(111) [86] where LEED spots from the hBN layer have been observed in the $\overline{\Gamma M}$ and $\overline{\Gamma K}$ directions, connected by a ring (cf. Chapter 2.1). There, the orientation of domains in $\overline{\Gamma K}$ direction was explained by a reduction of the lattice mismatch from 8.9% in $\overline{\Gamma M}$ direction to −5.1% in $\overline{\Gamma K}$ direction.[2] In the same way, the occurrence of these two orientations of hBN domains on Pt(111) [84, 185] can be understood. However, this explanation is not convincing for Cu(111) because such a rotation of the domains by 30° *increases* the lattice mismatch to −13.1%. Instead, the origin of the domain orientation may have kinetic reasons and occur during the growth process. This aspect will be discussed in further detail in section 5.3.

The satellite structure in the diffraction pattern

The satellite structure may have two different origins. Due to a buckling of the hBN layer, a superstructure is present on the surface that causes additional spots in LEED as it has been observed, e.g., for hBN/Pt(111) [84] or hBN/Ir(111) [82]. A second reason for additional spots in LEED is multiple scattering (cf. Chapter 3.1). Indeed, a combination of both is possible as well. First, the contribution of multiple scattering will be discussed.

---

[2]The definition of the lattice mismatch m given in Chapter 2.1 refers to the distance between lattice lines $\{h0\}$ and $\{0k\}$, respectively, which corresponds to the vector of the unit cell of the metal substrate a_{metal}. For rotated domains of hBN, a lattice mismatch can be considered for other lattice lines $\{hk\}$ so that $m = 1 - a_{\text{hBN}}/a^{hk}_{\text{metal}}$.
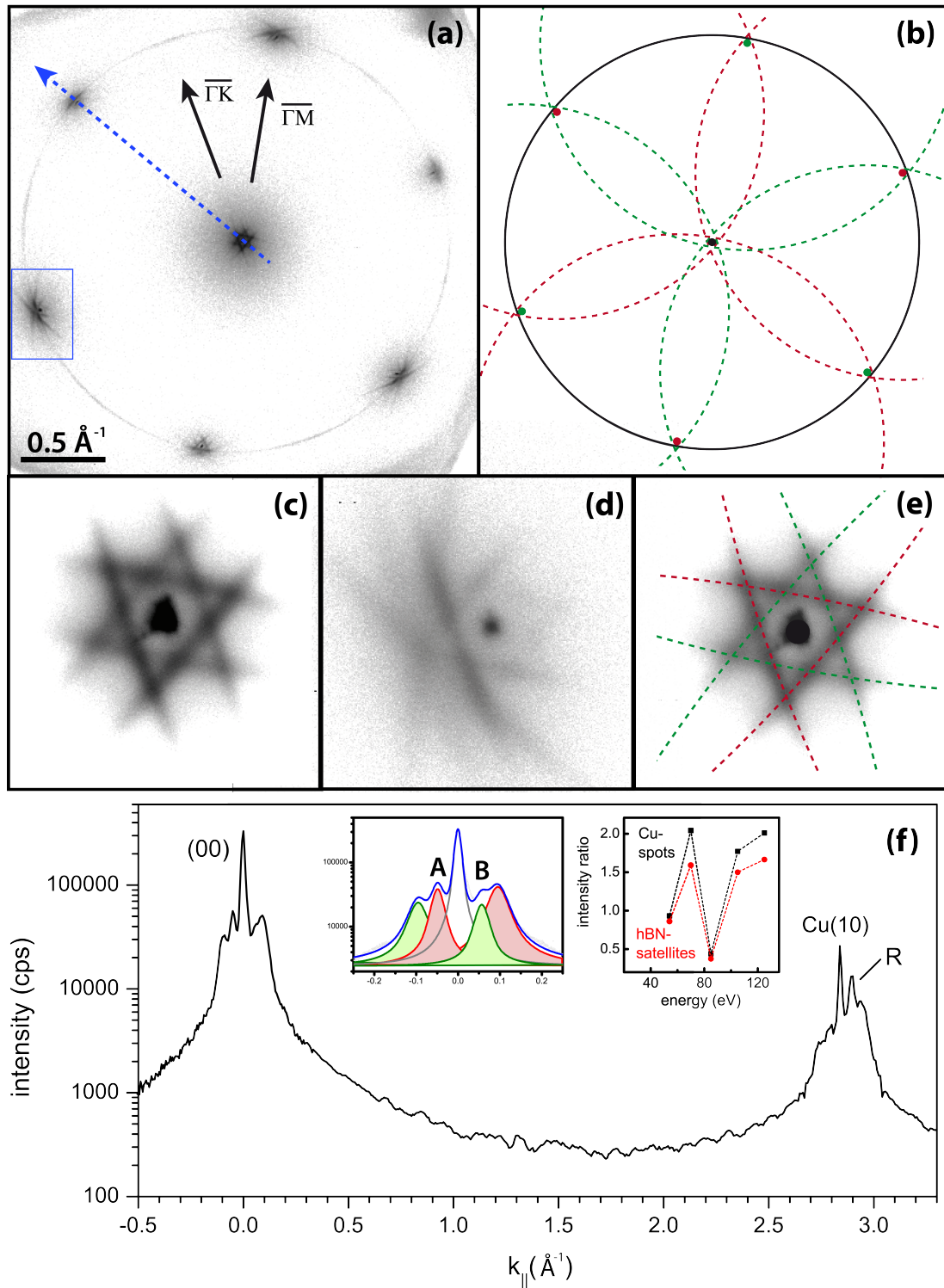
Figure 5.3: *For figure caption, see next page.*

Figure 5.3: *a) SPA-LEED pattern of hBN/Cu(111). The ring of intensity is caused by the azimuthal disorder of the orientations of the hBN domains. The LEED pattern was recorded with an electron energy of 70 eV at 110 K. The lines around the specular spot and the first order Cu spots are caused by multiple scattering. b) Simulation of a). The hBN ring is represented in black. Red and green refer to the symmetry inequivalent Cu spot and the hBN rings that originate from them due to multiple scattering. c) Zoom-in on the specular spot with the satellite structure around it. The lines correspond to the arcs of the hBN ring in a) in $\overline{\Gamma M}$ direction. The star-pattern is formed by two triangles, the intensities of the lines forming these two triangles differ. d) Zoom-in on the Cu first order spot marked in a) with the satellite structure around it. e) The specular spot with the satellite structure as in c), overlaid with the simulation in b). The different intensities of the two triangles stem from the different intensities of the parental Cu first order spots. f) Line scan along the blue line in a), crossing the specular spot (00), a Cu first order spot Cu(10), the hBN ring R, and several lines of the satellite structures and their intersections. The left inset shows a zoom-in on the specular spot, the profile is fitted with five Pseudo-Voigt functions. The colors refer to the parental Cu spots of the satellite lines. The line scans were measured at 110 K with an electron energy of 70.3 eV and converted to the k-scale and deskewed using Eq. (5.2). The right inset shows that the intensity ratio of two satellite lines (I_S^A/I_S^B, red) behaves as a function of electron energy in the same manner as the intensity ratio of the respective parental Cu spots (I_{Cu}^A/I_{Cu}^B, black). LEED patterns were previously shown in Ref. [59].*

Figure 5.3b shows a simulation of the LEED pattern. The hBN ring is represented in black, the symmetry inequivalent first order Cu spots are differentiated by color (red and green). Electrons that are scattered at the Cu(111) surface *and* the hBN layer can be observed in LEED as rings that are centered around the Cu spots. These rings are represented in the figure by the colors of their respective parental Cu spots. The zoom-in on the specular spot (Figure 5.3c) shows the formation of a star-like satellite pattern around it which is composed of two triangles of different intensities.

The comparison of the LEED pattern with the simulated satellite structure in Figure 5.3e shows not only that the arrangement of lines fits well (the lines around the specular spot correspond to the arcs of the original hBN ring in $\overline{\Gamma M}$ direction), but also that the different intensities of the lines are related to the intensities of the different parental Cu spots. These differences in intensities of the satellite lines can be seen more clearly in line scans across the specular spot (see inset in Figure 5.3f). The satellite structure around the Cu spots (Figure 5.3d) can be explained in the same manner as those around the specular spot. Here, multiple scattering of higher orders has to be taken into account (for details, see Appendix A.1).

To prove the multiple scattering, the intensities of the lines of the satellite structure around the specular spot I_S in relation to the intensities of the respective parental Cu spots I_{Cu} as a function of the electron energy were investigated using line scans as shown in Figure 5.3f. The ratios I_S^A/I_S^B and I_{Cu}^A/I_{Cu}^B (inset in Figure 5.3f) show that the intensities of the lines of the satellite structure are linked to the intensities of the Cu spots which proves the multiple scattering.

For the determination of a possible contribution from a buckling of the hBN layer to the satellite structure, the contribution by multiple scattering has to be eliminated. This can be achieved at low electron energies. Then the Cu first order spots contribute no longer to the LEED pattern (cf. Figure 3.1). Horn-von Hoegen et al. [186] have investigated the buckling of Ge films on Si(111) using the kinetic approximation for LEED. A detailed description of a similar approach for the analysis of LEED measurements at low energies to determine the buckling of the hBN layer is

given in Appendix B. This analysis delivers an estimation for the buckling of the hBN layer of (0.42 ± 0.05) Å. This amounts to 13 % of the vertical distance between hBN and Cu(111) surface.

The hBN lattice

Further details about the structure of hBN/Cu(111) can be gained from line scans across the LEED pattern. Figure 5.3f shows a scan along the blue line in Figure 5.3a. This scan allows the determination of the lattice constant of the hBN layer. However, the LEED pattern (and thus the line scan) is skewed. For an exact analysis, the measured line scans do not only need to be converted from a voltage-scale to a $\vec{k}_{\parallel}$-scale, but they also need to be deskewed. The distortion of the LEED pattern is assumed to be described by a polynomial of second order as

$$\vec{k}_{\parallel} = s_0 \cdot U_X + s_1 \cdot U_X^2 \ , \tag{5.1}$$

with U_X as the x-axis of the line profile as measured (in Volts) and s_0, s_1 as instrument-, energy-, and direction-specific parameters. From the discussion of the multiple scattering it is known that the distance between the specular spot and the satellite line is the same as between a Cu(10) spot and the hBN ring. Thus, the peak positions on the voltage scale of the Cu(10) spot U_C, the hBN ring U_h in $\overline{\Gamma M}$ direction, and the satellite line U_S in the same direction (cf. Figure 5.3f) can be used in Eq. (5.1) to describe the reciprocal lattice constant of the Cu(111) surface a_{Cu}^* [76]:

$$s_0 \cdot U_h + s_1 \cdot U_h^2 - s_0 \cdot U_S - s_1 \cdot U_S^2 = s_0 \cdot U_C + s_1 \cdot U_C^2 = a_{Cu}^* \ . \tag{5.2}$$

From Eq. (5.2), s_0 and s_1 can be calculated and used to deskew and convert the line scans which results in Figure 5.3f. The lattice constants of hBN on Cu(111) at 100 K and at 300 K are given in Table 5.1. They deviate from the lattice constants in the bulk crystal at the respective temperatures by only 0.35% and 0.19% [77], respectively, and both agree with the lattice constant of the free standing hBN layer within 0.5% [60]. A comparison of the hBN lattice constants on Cu(111) with those in the bulk at the respective temperatures (cf. Table 5.1) shows, that the surface has an influence on the structure of the hBN. The thermal expansion coefficient of hBN is negative between 70 and 300 K [77]. Thus, the lattice constant in the bulk decreases going from 100 K to 300 K. On Cu(111), on the other hand, the hBN lattice constant *increases*, thus following the thermal expansion of the substrate.

Due to the mismatch and the azimuthal rotation of the hBN domains on the Cu(111) lattice, Moiré patterns form. Their lattice constants L can be calculated as

$$L = a_{Cu} \cdot \left(1 + \frac{1}{(1-m)^2} - \frac{2}{1-m} \cdot \cos \phi \right)^{-\frac{1}{2}} \ , \tag{5.3}$$

wherein ϕ is the rotational angle of the hBN domains [175]. They are given in Table 5.1 as well and are in good agreement with the sizes of the Moiré pattern of $5-14$ nm measured by Joshi et al. in STM [174]. Here, the large impact even minute rotations of domains have on the size of the Moiré

Table 5.1: *Lattice constants a_{hBN} for hBN on Cu(111) at different sample temperatures T_S. a_{hBN} follows from the experimentally determined lattice mismatch m and the lattice constant a_{Cu} of the Cu(111) surface. a_{Cu} is calculated from the lattice constant of Cu(111) at 25°C (2.556 Å) and its thermal expansion coefficient 16.7×10^{-6} K^{-1} [76]. For comparison, the lattice constant of an hBN layer in the bulk a_{hBN}^{bulk} is given [77]. Using Eq. (5.3), the range of Moiré lattice constants L for azimuthal orientations of the hBN domains ϕ between 0° and 2.2° is calculated.*

T_S	a_{Cu}	m	a_{hBN}	a_{hBN}^{bulk} [77]	L
300 K	2.556 Å	(2.2 ± 0.2) %	(2.500 ± 0.004) Å	2.50468 Å	$5.7 - 11.3$ nm
100 K	2.548 Å	(2.0 ± 0.1) %	(2.497 ± 0.003) Å	2.50583 Å	$5.8 - 12.5$ nm
6 K	2.544 Å	1.8 % [174]	2.498 Å	2.50579 Å	$5.9 - 13.9$ nm

lattice becomes clear. This can also be seen in the structure model in Figures 5.4a and b. There, the Moiré unit cells for $\phi = 0°$ and 2.2° are shown. By this small rotation, the lattice constant of the Moiré structure is reduced from 50 hBN lattice constants to 23.

5.2.2 The vertical structure

The vertical structure of the hBN layer was investigated in XSW experiments. XP spectra showed only one single line for both nitrogen and boron at binding energies of (397.97 ± 0.03) eV and (190.35 ± 0.01) eV, respectively. This is in good agreement with the binding energies of both elements in hBN layers on Cu surfaces [93, 187]. The results of the XSW experiments are summarized in Table 5.2. The vertical distances from the Cu(111) surface amount to $d_C(B) = (3.25 \pm 0.02)$ Å and $d_C(N) = (3.22 \pm 0.03)$ Å. These distances refer to the extended Bragg planes. However, the relaxation of the top-most Cu layer is 0.02 Å inwards for the clean surface [188]. After the adsorption of a weakly bonded adsorbate, the relaxation is proposed to be also small so that the extended Bragg planes are assumed to have the same distances with an error of ± 0.02 Å which is within the error margins of the vertical distance between hBN and Cu surface. Figure 5.4d shows a side-view model of hBN/Cu(111). The mean height of the hBN layer of (3.24 ± 0.03) Å, which almost matches the interlayer distance in the hBN bulk of 3.33 Å [77], exceeds even the sum of the vdW radii of adsorbate and substrate.

Since only one species for both boron and nitrogen was observed in XPS, the hBN layer could be considered flat. However, the XSW results actually include one prominent indication for a variation in the vertical distances of boron and nitrogen from the substrate: the coherent fractions. For a flat, unbuckled layer, $F_C = 1$ would have been expected for both atoms. Instead, the coherent fractions are 0.57 ± 0.02 for boron and 0.80 ± 0.04 for nitrogen. A periodic buckling of the hBN sheet is expected to result in an equal reduction of F_C for both atoms. Yet, F_C of boron is smaller by 0.23 than F_C of nitrogen. This is unexpected for a 2DM with strong lateral bonds. First, this difference will be considered. Then, the lowering of $F_C(N)$ from 1 to 0.80 will be discussed.

There are several possible explanations for the difference in coherent fractions of boron and nitrogen. *(i)* There is an actual variation in the vertical position of the boron atoms and/or a split position. *(ii)* The spatial distribution of the 1s orbital is larger for boron than nitrogen which leads
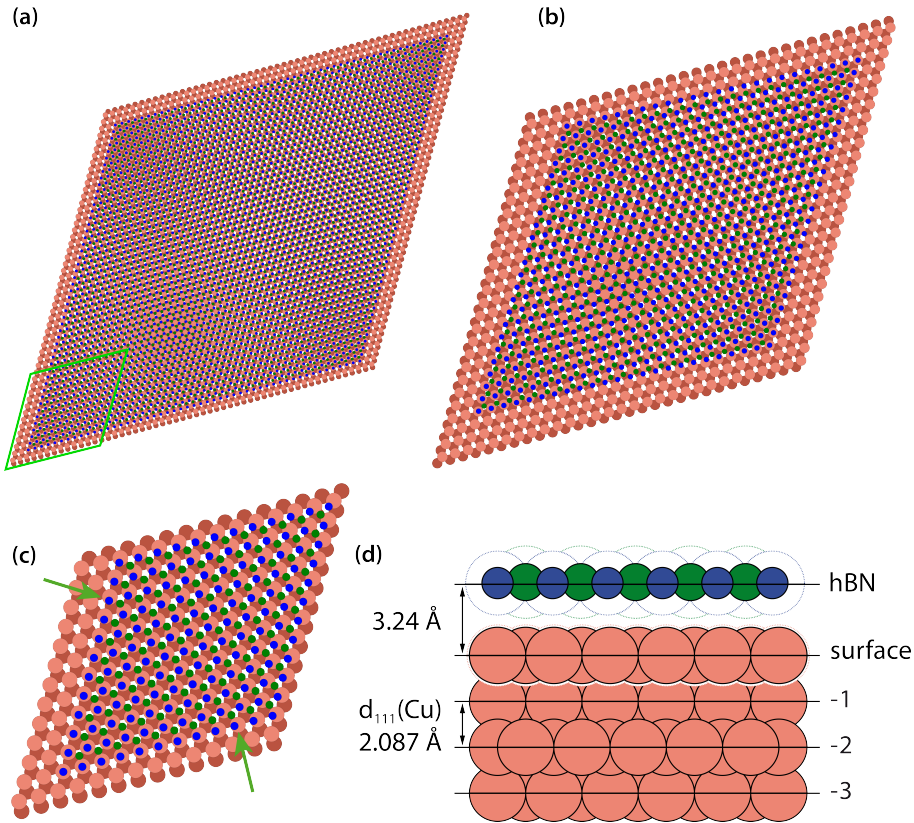
Figure 5.4: *Structure models of hBN/Cu(111). a) Lateral structure of an hBN domain aligned with the Cu(111) substrate. 50 × 50 BN unit cells are required for a complete Moiré cell with a lattice constant of 11.3 nm at 300 K. b) Lateral structure of an hBN domain rotated by 2.2° relative to the Cu(111) substrate. Only 23 × 23 BN unit cells are required for a complete Moiré cell, resulting in a lattice constant of 5.7 nm at 300 K. c) Zoom-in of the area of the hBN domain in a) (marked in green). The first nitrogen atom (blue) of the hBN layer is positioned on top of a Cu atom. In the first 9 hBN unit cells, the nitrogen atoms remain on on-top positions (indicated by green arrows). After that, the positions of the nitrogen atoms shift towards hollow sites. d) Vertical structure of hBN/Cu(111) as a side-view along the [11$\bar{2}$] direction. Black lines indicate the (extended) Bragg planes of Cu(111) and the mean height of the hBN layer. The full spheres correspond to covalent radii of boron and nitrogen [104] and the metallic radius of copper [103]. Dotted spheres indicate vdW radii [101]. All radii used in this thesis are summarized in Table G.3 in Appendix G.*

to a wider spread of the vertical distance of the boron atom from the Cu(111) surface on different lateral positions. *(iii)* There are disordered BN fragments with excess boron compared to nitrogen.

A large variation in the vertical distance of only the boron atoms (explanation *(i)*) seems unlikely in light of the strong lateral interaction within the hBN layer. For example, a 50 : 50 split position which reduces the coherent fraction by 0.23 would result in vertical positions of ± 0.27 Å (12%) (see Appendix A.1) removed from the mean height of the hBN layer and thus from the neighboring N atoms. Factors *(ii)* and *(iii)*, on the other hand, appear more reasonable. The 1s orbital of boron has a larger spatial distribution than the 1s orbital of nitrogen. However, this difference cannot alone account for the large difference in F_C of 0.23 (Appendix A.1). Thus, explanation *(ii)* may only partially cause this difference. Accordingly, explanation *(iii)* must also play a role.

The presence of a boron-rich defect species of BN on the surface may be caused by occasional breaking of borazine rings, either upon adsorption on the surface or during storage in the borazine

source[3]. Atomic nitrogen desorbs after recombination to N_2 from the Cu(111) surface already at $620-770$ K [189] which explains the depletion of nitrogen from the defect species. Yet, it is unclear why this boron-rich defect species was not observed in XPS (see Figure 3 in Appendix A.1).

Now, the reduction of F_C from 1 (for the flat layer) to 0.80 will be discussed. Again, there are several possible explanations: *(i)* surface defects lead to a (vertical) distortion of the hBN layer, *(ii)* a variation in the heights of differently azimuthally oriented, flat hBN domains, and *(iii)* a buckling of the hBN layer.

(ad i) The distortion of the Moiré patterns at the domain boundaries found in STM [174] may also indicate a *vertical* distortion of the hBN layer in these regions. However, the sharpness of the Cu spots, the hBN ring, and the satellite lines in LEED images (Figure 5.3) indicate a high structural quality of the hBN layer that was investigated in the present thesis. From line profiles, domain widths of the Cu(111) surface and the hBN layer were determined to be 450 Å and 200 Å, respectively. Thus, domain boundaries or other defects are not considered to be abundant enough to distort the layer enough for the coherent fraction to be reduced by 0.2.

(ad ii) Due to the weak interfacial interactions, a broad minimum in the interfacial interaction energy can be expected which may lead to small differences in vertical distance of the different hBN domains from the surface. However, in DFT calculations of the vertical interfacial distances and interaction energies of hBN/Cu(111) [190] no such variations were found. The calculated mean heights of hBN domains aligned with the substrate and of hBN domains rotated by $30°$ differed by 0.16 Å. The resulting reduction of F_C is estimated to be 0.12 which is not enough to account for the measured coherent fraction on its own. Furthermore, rotated hBN domains constitute a minority as estimated from the intensity distribution in the hBN ring (see above).

(ad iii) The buckling of the hBN layer presented in this thesis was estimated by measuring line profiles of the diffraction spots recorded in SPA-LEED (see Appendix B for details). The results suggest a buckling of (0.42 ± 0.05) Å. It is estimated that F_C is reduced to 0.66 due to a sinosoidal buckling with this amplitude while a split position with this height difference would lead to an F_C of only 0.33.

The results regarding the vertical structure of hBN/Cu(111) will now be compared to a study conducted in parallel to this thesis by Schwarz et al. [190]. These results are also included in Table 5.2 for comparison. Qualitatively, these results are mostly in agreement with the results of the present thesis.

From the coherent fractions, the authors determined a peak-to-peak corrugation of the hBN layer on Cu(111) of 0.6 Å (thus, an amplitude of 0.3 Å). In addition, they used *non-contact atomic force microscopy* (nc-AFM) to investigate the surface and found a peak-to-peak amplitude of 0.40 Å (thus, an amplitude of 0.20 Å).[4] However, since these amplitudes are smaller than the covalent radii of both nitrogen and boron [104] and spread out over a lateral scale of nanometers (the diagonal of the Moiré unit cell which crosses both moiron and wire amounts to 19.57 nm and 9.87 nm for

---

[3]For information on the decomposition of borazine in storage, see Chapter 5.3.1.

[4]The authors have closely examined the influence of electrostatic forces on the tip and the resulting height profiles.

Table 5.2: *XSW results for hBN on Cu(111). The binding energies of the 1s levels E_B, coherent fractions F_C, and coherent positions P_C of boron and nitrogen are given. The vertical distances from the Cu(111) surface d_C were calculated according to Eq. 3.14. For details on the evaluation, see Appendix A.1. The results from Ref. [190] for the majority and minority species B_0N_0 and $B_{def}N_{def}$ are included for comparison. Additionally, the amplitude of the buckling of the hBN layer as determined by SPA-LEED (for B and N) and by nc-AFM (for B_0 and N_0) [190] are given.*

	E_B	F_C	P_C	d_C	amplitude
N	(397.97 ± 0.03) eV	0.80 ± 0.04	0.54 ± 0.01	(3.22 ± 0.03) Å	
B	(190.35 ± 0.01) eV	0.57 ± 0.02	0.56 ± 0.01	(3.25 ± 0.02) Å	(0.42 ± 0.05) Å
N_0	398.0 eV	0.71 ± 0.02	0.62 ± 0.02	(3.37 ± 0.04) Å	
B_0	190.4 eV	0.65 ± 0.03	0.63 ± 0.02	(3.39 ± 0.04) Å	0.20 Å
N_{def}	398.5 eV	0.40 ± 0.03	0.58 ± 0.03	(3.30 ± 0.06) Å	
B_{def}	191.0 eV	0.34 ± 0.07	0.56 ± 0.04	(3.26 ± 0.09) Å	

$\phi = 0°$ and $2.2°$, respectively), Schwarz et al. considered neighboring atoms to be, in effect, coplanar and saw this long-scale buckling as the reason that the values of the coherent fractions are below 1. Thus, the buckling of the hBN layer was considered locally negligible and only able to reduce F_C on the large scale. The same argument holds even for an amplitude of 0.42 Å, which was found in the present thesis, so that the same conclusion can be drawn.

A similar situation as for hBN/Cu(111) investigated in the present thesis has been found for the weakly interacting graphene/Ir(111) interface [191]. There, only one carbon species was observed in XPS with a mean vertical distance of the graphene layer from the Ir(111) surface of 3.38 Å, which is close to the interlayer distance in graphite. Yet, a peak-to-peak corrugation of 0.35 Å was found in a combined XSW and DFT study. For the strongly interacting interfaces graphene/Ru(111) [192] and hBN/Ir(111) [82], on the other hand, the findings were significantly different. Two different species were found in XPS in either case, with minimum vertical heights of the respective 2DMs of 2.17 Å and 2.20 Å and peak-to-peak amplitudes of 1.47 Å and 1.50 Å(thus, amplitudes of ~1.25 Å).

Despite the similarities in the results of the two studies on hBN/Cu(111), there are also some significant differences.
1) The mean vertical distance found by Schwarz et al. amounts to 3.38 Å. The difference to the distance found in the present work of 3.24 Å exceeds the error margins.
2) Schwarz et al. found a second species of BN in XP spectra which was considered to be a minority phase. This species was not observed in the present investigation.

The shift in binding energy between Schwarz's majority and minority phases is comparable to that between the two different areas of the strongly buckled hBN/Ir(111) [82], yet their height difference on Cu(111) is much smaller than that found for the buckled hBN layer on Ir(111) (0.1 Å instead of 1.5 Å). Thus, the authors excluded a similarly strongly buckled hBN layer on Cu(111) and rather interpreted this second (defect) species as BN polymers with a B-N ratio deviating from 1:1. This corresponds to explanation *(iii)* for the observed difference between the coherent fractions of boron and nitrogen in the present thesis. However, it remains unclear why Schwarz et

al. observed the defect species in XPS while this was not the case for the hBN layers investigated here. These differences may be related to differences in preparation conditions or sample quality in the two studies. This may also be the reason for the significant difference in the mean vertical distance found by the two groups.

In conclusion, the hBN layer is located at a large vertical distance from the Cu(111) surface of (3.24 ± 0.03) Å. The buckling of the hBN layer amounts to (0.42 ± 0.05) Å which, in comparison to the interfacial distance and the lateral scale of the buckling, is small. Accordingly, the hBN layer is considered locally flat, however, the buckling on the large scale of the Moiré unit cell reduces the coherent fractions determined in XSW experiments. An additional reduction of the coherent fractions can be caused by different vertical distances of domains with different azimuthal orientations. The difference of coherent fractions between boron and nitrogen is explained by the different spatial distributions of the $1s$ orbitals and the presence of a boron-rich defect species of BN on the surface.

5.3   The Growth of hBN on Cu(111)

One open question that remains is why the hBN domains adopt the different azimuthal orientations that were found for hBN/Cu(111). The clearly preferred orientation of the domains is along the $\overline{\Gamma M}$ direction, followed by the $\overline{\Gamma K}$ direction. Additionally, a small quantity of domains is randomly distributed in their azimuthal orientations. This cannot be explained by a matching of the hBN lattice with the Cu(111) surface. Instead, the determination of the orientations of the domains may already occur during the growth process. Accordingly, incomplete layers of hBN/Cu(111) were investigated with SPA-LEED.

Furthermore, the growth of hBN on Cu(111) will be investigated since the growth of hBN on any metal surface is not well studied, yet. Especially the presumably catalytic process in which the borazine molecules decompose to form the hBN layer, is not understood. To shed light on this, TPD experiments of borazine on Cu(111) were used to determine the adsorption energy which may constitute a first step in the understanding of the growth of hBN layers.

5.3.1   Incomplete layers of hBN/Cu(111)

The growth model proposed by Felter et al. [183] already explains why the preferred orientations of the hBN domains are separated by 120°. But the ring in LEED shows a sixfold symmetry. How can this be understood?

DFT calculations [179] have shown, that on Cu(111), the preferential adsorption site of the nitrogen atoms of hBN is on-top of the Cu atoms. Boron preferably adsorbs on fcc sites, however the energetic difference to hcp sites is negligible small. The same preferences has been found for other surfaces (Ni(111) [78, 79, 179, 193], Ir(111) [82], Rh(111) [179]). With these two preferred adsorption sites of $N_{top}B_{fcc}$ and $N_{top}B_{hcp}$, two equivalent domains can form which are azimuthally rotated by 60° relative to each other. For the commensurate hBN/Ni(111) interface, this was shown in STM

experiments where triangular domains with these two different orientations were observed [80]. Yet, since hBN on Cu(111) is not commensurate, both boron and nitrogen atoms occupy all adsorption sites inside the Moiré unit cell, as shown in Figure 1 of Ref. [177]. Nevertheless, since this preferential alignment with the Cu(111) surface was observed in LEED in the present study, too, it is reasonable to assume, that the same growth mechanism governs the orientation of the domains here. As Felter et al. have shown, domain nuclei form on surface terraces and their orientation determines the orientation of the whole domain [183]. Figure 5.4c shows that the shift in adsorption sites due to the lattice mismatch happens only gradually. For the first nine hBN unit cells, the nitrogen atoms clearly occupy the on-top adsorption sites. This equals an area of ~500 Å^2, enough to anchor the hBN domain in a preferred orientation, which will not change during the growth process.

To conclude, the preferential orientation of the hBN domains on Cu(111) in $\overline{\Gamma M}$ direction is caused by the adsorption of the hBN nuclei on the preferred adsorption sites $N_{top}B_{fcc}$ or $N_{top}B_{hcp}$, which separates them azimuthally by 60°. This is followed by a dendritic growth of the domains in three main directions, separated by 120°. The vast majority of hBN domains form like this, as shown in LEEM [183] and LEED.

The two types of domains ($N_{top}B_{fcc}$ and $N_{top}B_{hcp}$) cannot coalesce, which was shown by the defect lines at the boundaries of these two kinds of domains of hBN/Ni(111) [80]. But also for the incommensurate structure hBN/Cu(111) it is very unlikely that two domains meet and perfectly coalesce, as this would require very specific adsorption sites of the atoms at the domain edges. In fact, the dendritic growth, leading to triangular island, predestines the surface for the formation of defects in the hBN layer, leaving bare patches of Cu(111). These get filled by new, small domains of hBN. Since the occupation of preferential adsorption sites is hindered by the neighboring hBN domains, an azimuthal alignment at the Cu(111) surface is not possible for these domains and they become azimuthally disordered and lead to the continuous ring in the LEED pattern. This has been shown by a combination of LEEM and μLEED measurements by Felter et al. [183].

As pointed out in Chapter 5.2.1, the LEED intensity of the ring (and thus the distribution of domain orientations), even with exception of the $\overline{\Gamma M}$ direction, is not homogeneous. There is a small preference in the $\overline{\Gamma K}$ direction, corresponding to an azimuthal rotation of the hBN domains by 30° relative to the aligned domains. For simplicity, these domains will now be referred to as R30°-domains. The LEEM measurements [183] showed that from the beginning of the domain growth, there is no change in the orientation of the domains. Thus, it is very likely that the orientation of the domains is determined *in the moment* of the formation of the nucleus rather then caused by a diffusion and rotation of hBN domains *after* the formation of the nucleus. Once an R30°-nucleus has formed, the growth in the six preferred directions occurs the same way as was described in Chapter 5.1 for aligned domains, because the dehydrogenation limited aggregation is only driven by the intrinsic properties of hBN [183]. The remaining question is why the R30°-nuclei form. A rotated domain has an increased lattice mismatch *m* compared to the aligned domains (see Chapter 5.2.1) so that the occupation of preferential adsorption sites is not possible. However, this may explain the wider azimuthal spread of the R30°-domains (6.1°) compared to the aligned domains.

The weakened interactions between hBN and Cu(111) due to the deviation from the preferred adsorption sites allows for a wider range in the azimuthal rotations of the nuclei.

Furthermore, the preference of R30°-domains is not connected to a filling of Cu(111) areas left bare during the growth of aligned hBN domains. Figure 5.5a shows the LEED pattern of hBN/Cu(111) that was prepared with a third of the borazine dose that was commonly used for a full monolayer. There is no continuous ring, only the arcs in the $\overline{\Gamma M}$ and $\overline{\Gamma K}$ directions are present. This means that the R30°-domains appear earlier in the growth process than the randomly oriented domains.

Figure 5.5b shows a LEED pattern of hBN/Cu(111) that was prepared in the same way as the surface of Figure 5.3a. Yet, it is strikingly different. There is *only* intensity in $\overline{\Gamma K}$ direction with a wide azimuthal spread of $\pm 21°$. The domains are only 50% of the size of the domains that yield Figure 5.3a (which was derived from the FWHM of the ring in the radial direction) and the high background indicates disorder on the surface. The preparation that yielded the LEED pattern in Figure 5.5b was the last in a series of experiments, all identically conducted over the course of four weeks, but that yielded hBN layers which very gradually decreased in quality. The LEED patterns changed from resembling Figure 5.3a for a complete monolayer, over patterns as shown in Figure 5.5a for an incomplete layer, finally arriving at Figure 5.5b. Presumably, the borazine$-H_2$ ratio had continuously decreased over this time.[5] With the same dose of gas let into the chamber but a decreased borazine percentage in this gaseous phase, the hBN coverage decreased until, at the lowest coverage, only R30°-domains grew.
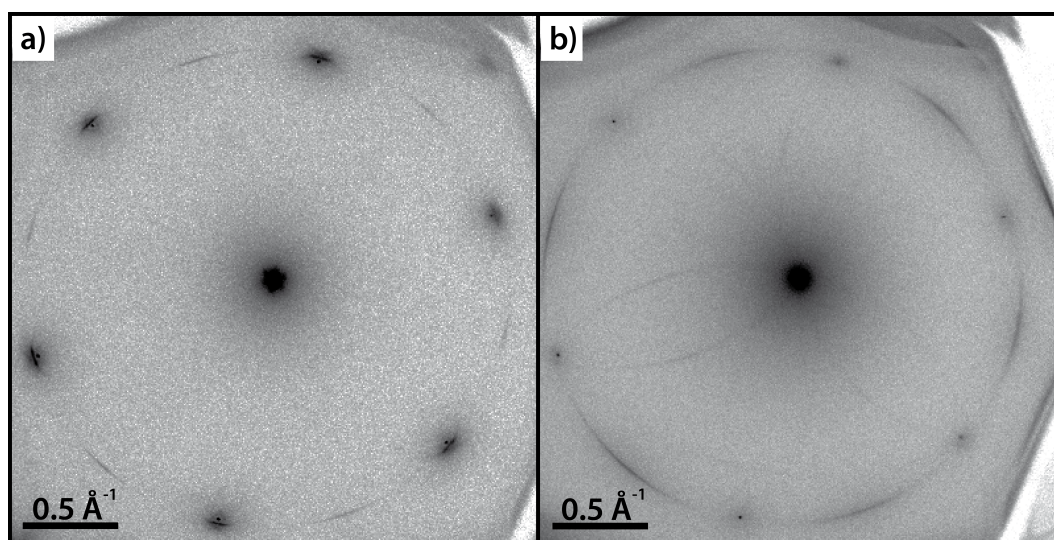
Figure 5.5: *SPA-LEED patterns of incomplete layers of hBN on Cu(111). a) The hBN ring is not continuous, intensity is only present in $\overline{\Gamma M}$ and in $\overline{\Gamma K}$ direction (where the ring intensity is the highest for a full monolayer). The satellite structures are weak in intensity, but present. b) The only intensity on the hBN ring is observed in $\overline{\Gamma K}$ direction. The well-known satellite structures are absent. Between the specular spot and the first order Cu spots are long, curved lines of intensity due to multiple scattering. They correspond to the arcs of the ring in $\overline{\Gamma K}$ direction. The LEED patterns were recorded with an electron energy of 70 eV at 110 K.*

---

[5]At the time of these experiments, the author of this thesis was not yet aware of the decomposition of borazine to BN polymers and H_2 even at low temperatures. Thus, the composition of the borazine gas was not regularly checked via QMS so that the gaseous phase probably contained large amounts of H_2 which increased over time.

This means that at the very beginning of the hBN growth, R30°-domains form *before* the aligned domains form. Since the full monolayer is predominantly composed of aligned domains, something has to change during the growth process so that the preferred domain formation switches from R30° to aligned. A possible explanation is that R30°-domains nucleate at surface defects. A saturation of defects at low coverages would then inhibit further formation of more R30°-domains and allow the formation of aligned domains on Cu terraces. The attachment to defects may also inhibit the growth of the R30°-nucleus in at least one direction, leading to a smaller size of the R30°-domains. Note, that Felter et al. did not observe any preference of R30°-domains over any other azimuthal orientation which is indicated by the higher intensity of the hBN ring in the LEED pattern in that direction. However, this is likely correlated with the smaller illuminated surface area of μLEED compared to SPA-LEED [183].

On the basis of the described results, the growth model of hBN/Cu(111) by Felter et al. [183] can be expanded. A summary of the proposed growth process is depicted in Figure 5.6.
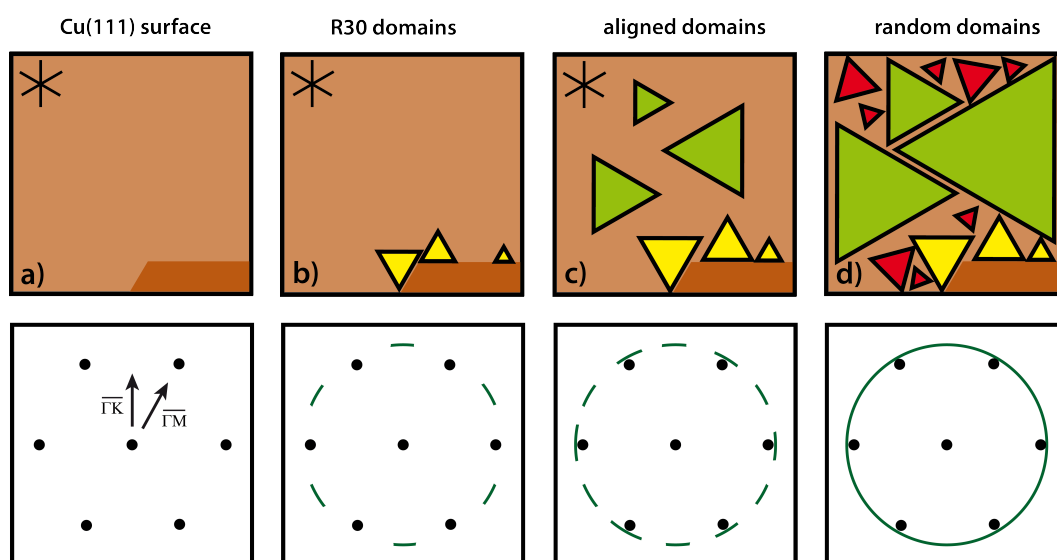
Figure 5.6: *Schematic overview of the different hBN domains on the Cu(111) surface (top row) during the growth process of hBN with the corresponding LEED patterns (bottom row). The mirror planes of the clean Cu(111) surface (a) are indicated in the top left corners of the pictures in the upper row. During borazine deposition, the first hBN nuclei form at defects, e.g. at step edges, which grow to become R30°-domains (yellow), leading to intensity in the $\overline{\Gamma K}$ direction in the LEED pattern (b). After saturation of the defects, nuclei form on terraces with the B and N atoms occupying their preferred adsorption sites. This starts the formation of aligned domains (green) and the appearance of LEED spots in $\overline{\Gamma M}$ direction (c). When the surface is almost completely covered, randomly oriented domains (red) begin to form in the gaps between the larger hBN domains and the hBN ring in the LEED pattern appears (d).*

When the hot Cu(111) surface (Figure 5.6a) is exposed to borazine, first R30°-nuclei form at surface defects. Following the dendritic growth model by Felter et al. [183], they increase in size (yellow domains in Figure 5.6b). However, their growth is hindered in (at least) one direction due to the attachment to the surface defects. Furthermore, the large lattice mismatch of -13.2% leads to a wide spread in the azimuthal orientation of the domains of 6.1°. After the saturation of the surface defects, nuclei form on the terraces. Due to the possibility of occupying their preferred adsorption sites, the nuclei anchor to the Cu(111) surface so that aligned domains form (green domains in

Figure 5.6c, due to the rather weak interfacial interactions an azimuthal spread of 4.4° remains). Since the aligned domains can grow freely in all directions, they grow to the largest sizes of all hBN domains. However, they are not able to coalesce. When the surface is almost completely filled with aligned and R30°-domains, nuclei form in the remaining gaps where the preferred adsorption sites cannot be occupied. This results in the random distribution of orientations of the new domains (red domains in Figure 5.6d). They constitute the minority and remain of the smallest size because they form only when the monolayer is already almost completely closed. The formation of these nuclei is the least probable due to the very weak interaction strength between the Cu(111) surface and the borazine molecule.

5.3.2 Borazine adsorption on Cu(111)

Desorption spectra of borazine

While the growth model presented in the previous section explains the steps in which the different kinds of hBN domains form on the Cu(111) surface, it is yet unclear how and why the hBN nuclei form and why the R30°-nuclei form before the aligned. To gain insight into these questions, the adsorption of the precursory borazine molecule on the Cu(111) surface was investigated.
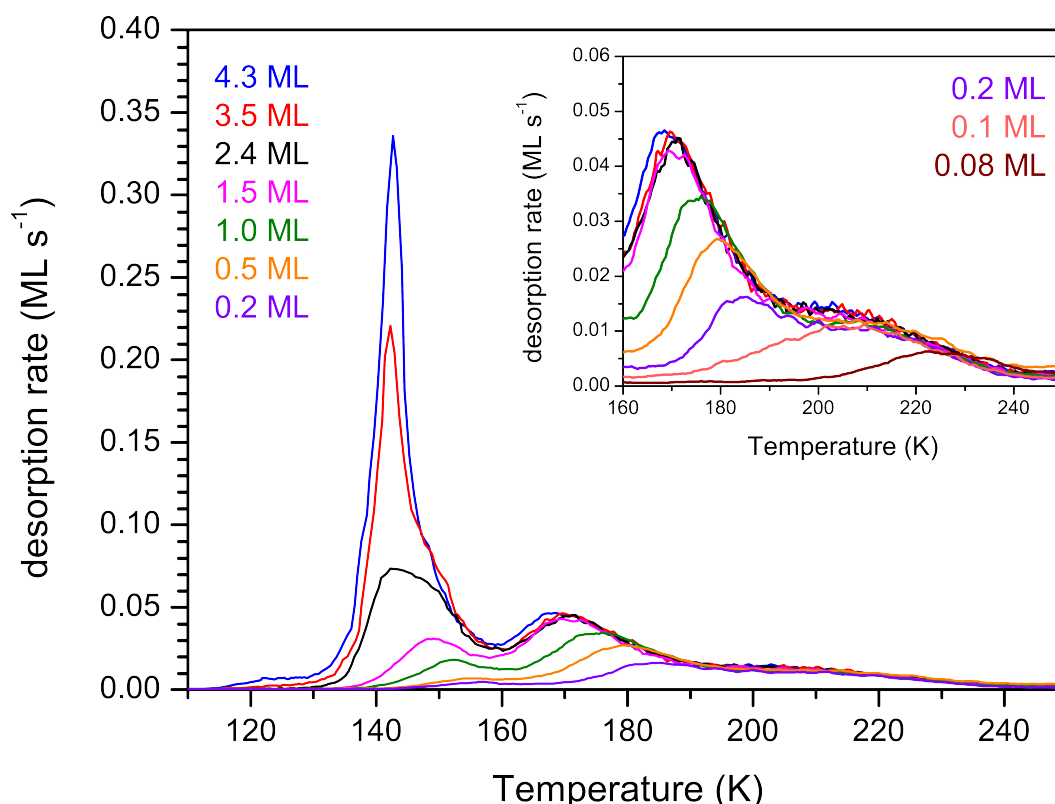
Figure 5.7: *TPD spectra of borazine on Cu(111) (m/z = 80). The molecules were deposited at a sample temperature of 100 K and the sample was heated with a rate of 1 Ks^{-1}. The initial borazine coverages are between 0.08 and 4.3 ML. Two peaks can be clearly distinguished at 143 K and 170 K and are assigned to the multilayer and monolayer desorption, respectively. The inset shows that at temperatures between 190 and 240 K desorption from surface defects occurs which amounts to ~10% of the monolayer. Spectra are smoothed.*

Figure 5.7 shows TPD spectra of $0.08 - 4.3$ ML borazine on Cu(111). The borazine was deposited at a sample temperature of 100 K and was completely desorbed at a temperature of 250 K. This is the first indication of the very weak bond between borazine and Cu(111). The complete desorption of borazine has been verified via SPA-LEED where the LEED pattern of the clean Cu(111) surface was observed after the desorption experiments.

Two peaks can be clearly distinguished at ~143 K and ~170 K which are assigned to multilayer and monolayer desorption, respectively, as will be discussed below. Additionally, at temperatures of $190 - 240$ K, a very broad peak of very low intensity can be observed. This signal has previously been assigned to borazine desorption from defects on the Cu(111) surface [194].

Desorption of borazine multilayers from Cu(111)

The determination of the desorption energy E_{des} of borazine on Cu(111) will first be approached via the multilayer peak at 143 K. Using a Menzel-Schlichting plot [195] (an Arrhenius plot on an inverted reciprocal temperature scale), E_{des}^{multi} of the multilayers can be gained from a leading edge analysis of the spectra of 3.5 and 4.3 ML. This is shown in Figure 5.8a. The fits of the leading edges result in $E_{des}^{multi} = (0.60 \pm 0.01)$ eV for 3.5 ML and $E_{des}^{multi} = (0.53 \pm 0.01)$ eV for 4.3 ML. This discrepancy of more than 10% between the two experimental values will be addressed below. For comparison, the sublimation enthalpy of borazine is 0.60 eV [196].
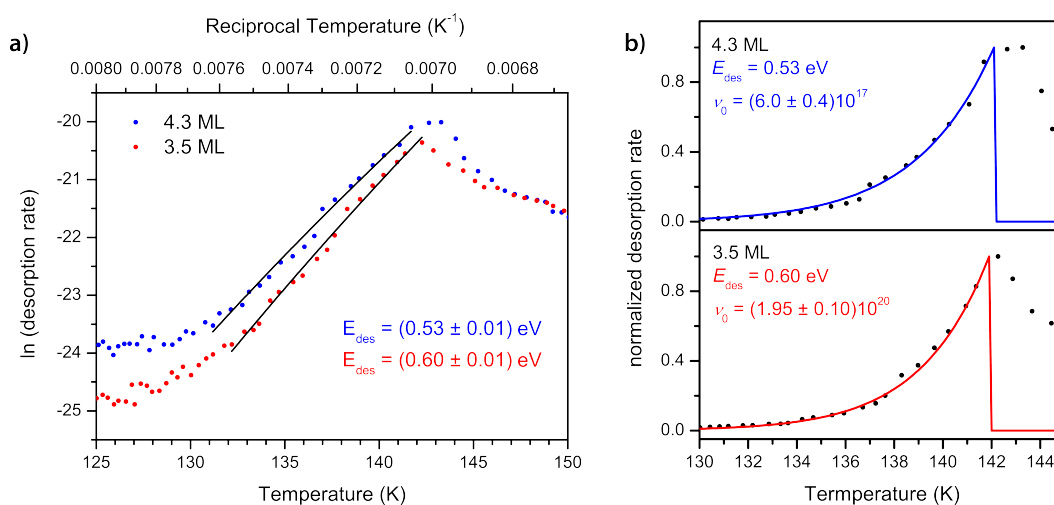
Figure 5.8: *a) Menzel-Schlichting plot of 4.3 ML (blue) and 3.5 ML (red) borazine on Cu(111) ($\beta = 1\ Ks^{-1}$). The leading edges are fitted linearly (black). From the slopes of the fits, the desorption energies of the borazine multilayer E_{des}^{multi} were determined as (0.53 ± 0.01) eV for 4.3 ML and (0.60 ± 0.01) eV for 3.5 ML, respectively. b) Calculated TPD spectra for zeroth order desorption for 4.3 ML with $E_{des}^{multi} = 0.53$ eV (top, blue) and for 3.5 ML with $E_{des}^{multi} = 0.60$ eV (bottom, red). Experimental data points are shown for comparison (black). The calculated spectra are fitted to the experimental data by the leading edges which delivers a pre-exponential factor of $(6.0 \pm 0.4) \cdot 10^{17} \frac{particles}{s\ cm}^2$ for 4.3 ML and $(1.95 \pm 0.10) \cdot 10^{20} \frac{particles}{s\ cm}^2$ for 3.5 ML, respectively. The spectra were divided by the peak maxima; the peak maxima correspond to 0.34 MLs^{-1} (blue) and 0.22 MLs^{-1} (red).*

The pre-exponential factor ν_0 of the *Polanyi-Wigner* equation (Eq. 3.10) can be determined by calculating the TPD spectra using the values for E_{des}^{multi} gained from the Menzel-Schlichting plots

and comparing them to the experimental spectra as shown in Figure 5.8b. For this, the program *Octave* [197] with a self-written script by the work group *Organische Filme* of Prof. M. Sokolowski from the University of Bonn based on the integration of Eq. (3.10) [198] was used. For the computation, the number of molecules in a full monolayer was used which was calculated with an estimation of the molecular density on the surface (see Table 5.3). This was obtained from LEED pattern of borazine on the Cu(111) surface which will be shown below. The pre-exponential factors used to calculate the TPD spectra of 3.5 and 4.3 ML shown in Figure 5.8b are $\nu_0 = (1.95 \pm 0.10) \cdot 10^{20} \, \frac{\text{particles}^2}{\text{s cm}}$ and $(6.0 \pm 0.4) \cdot 10^{17} \, \frac{\text{particles}^2}{\text{s cm}}$, respectively. The large difference of three orders of magnitude is a result of the discrepancy between $E_{\text{des}}^{\text{multi}}$ for the two layers. This will be discussed below.

Borazine monolayers on Cu(111)

The high-temperature peak at ~170 K is symmetrical and eventually saturates when the borazine coverage is increased. Thus, this peak is assigned to the monolayer desorption. Note that the multilayer peak starts to grow before the monolayer peak is saturated. This indicates a Stranski-Krastanov growth of the borazine molecules (islands on a wetting layer) which, again, points to a weak interaction between the molecules and the Cu(111) surface. Accordingly, the coverages given here are nominal thicknesses based on the estimation of the molecular density on the surface obtained from LEED and shown below.

The maxima of the monolayer peaks shift to lower temperatures with increasing coverage. This shift can be an indication for either second order desorption or repulsive lateral interactions between the molecules in the monolayer [129]. A second order desorption would entail a recombination step before the molecule desorbs. This is rather unlikely. Breaking the hydrogen bonds of borazine to form hBN requires a temperature ~1000 K so that a breaking up of the molecule at only 100 K is not possible. Instead, the shift of the peak indicates repulsive lateral interactions between the borazine molecules in the monolayer.

Similarly, repulsive lateral interactions have been found for benzene on Ag(111) in TPD experiments where a shift of the monolayer peak to lower temperatures with increasing coverage was observed [199], too. Further similarities can be found in the structures of these systems. Figure 5.9 shows LEED patterns of two different preparations of ~2 ML borazine on Cu(111). (Observing a LEED pattern at lower coverages (~1 ML) was not possible.) In both cases, there is a high background which indicates some disorder on the surface. In Figure 5.9b, the LEED signals are even smeared out to such a high degree that the identification of individual spots is impossible which points to very small, azimuthally disordered domains of borazine. However, the distance of the specular spot to the ring of intensity is the same as the distance to the more distinguishable spots in Figure 5.9a. A simulation of the LEED pattern (shown in Figure 5.9c) reveals that the first order LEED spots are extinct. The lattice constant of the hexagonal unit cell was determined as (14.9 ± 0.8) Å. Due to the very broad spots, the margin of error is rather large. The LEED pattern in Figure 5.9a shows some similarity to that of benzene on Ag(111) [200] and also to that of
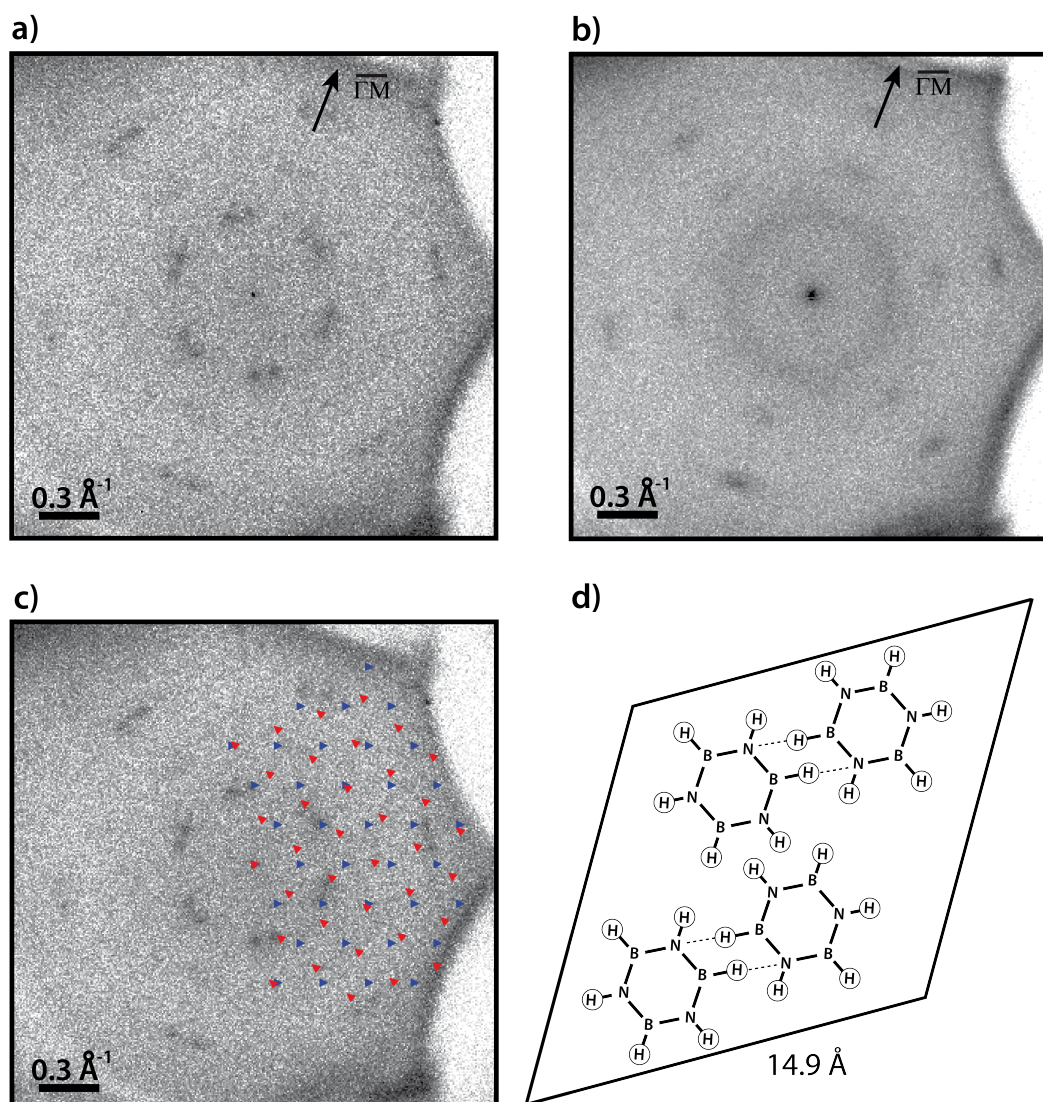
Figure 5.9: *a) SPA-LEED pattern of ~2 ML borazine on Cu(111). The LEED spots are very broad and not easily distinguishable which indicates small domains of borazine. The pattern has a hexagonal symmetry and resembles the LEED patterns of benzene on Ag(111) [200] and cyclo-hexane on Pt(111) [201]. b) LEED pattern of a different preparation of ~2 ML borazine on Cu(111). The LEED spots are azimuthally smeared out completely so that individual spots cannot be iden-tified at all. This points to very weak adsorbate-substrate interactions. The high background in both patterns speaks for a high amount of disorder on the surface. c) The LEED pattern from a) overlaid with a simulation. Different colors refer to different rotational domains. The first order LEED spots are extinct. d) Structure model for the unit cell of borazine on Cu(111), based on the structure model for cyclohexane on Pt(111) by Firment at al. [201]. The structural parameters are given in Table 5.3. Dotted lines indicate hydrogen bonds. For details, see text. The LEED patterns were recorded with an electron energy of 30 eV at 100 K.*

cyclohexane on Pt(111) [201] which display hexagonal patterns of doublets of beams. Table 5.3 summarizes the structural parameters of these two systems in comparison to borazine/Cu(111)[6].

Table 5.3: Structural parameters of benzene/Ag(111) [200], cyclohexane/Pt(111) [201], and borazine/Cu(111). c_1 is the vector of the hexagonal surface unit cell, A is the area of the unit cell, and N is the number of molecules per unit cell. The footprint f of the molecules and their packing densities on the surfaces ρ are given. For the calculation of f, see Figure G.1 in Appendix G. T_{obs} is the temperature at which LEED patterns could be observed.

	c_1	A	f	N	ρ	T_{obs}	
benzene/Ag(111)	13.2 Å	150.9 Å^2	39.280 Å^2	4	0.027 Å^{-2}	<125 K	[200]
cyclohexane/Pt(111)	12.7 Å	139.7 Å^2	42.545 Å^2	4	0.029 Å^{-2}	140−200 K	[201]
borazine/Cu(111)	14.2 Å	175.4 Å^2	40.636 Å^2	4	0.023 Å^{-2}	100 K	

The comparison in Table 5.3 shows that these three molecules that share a similar footprint (for the calculation, see Figure G.1 in Appendix G) order on (111) metal surfaces in unit cells of similar sizes. For both, benzene/Ag(111) and cyclohexane/Pt(111), structure models of flat lying molecules with 4 molecules per unit cell were proposed [199, 200]. Borazine and benzene are isostructural and isoelectronic and on their respective surfaces, their monolayer desorption peaks are found at similar temperatures around 170−180 K [199]. Thus, the same model of flat lying molecules will be assumed here for borazine/Cu(111). The corresponding structure model is depicted in Figure 5.9d. In this structure model, pairs of borazine molecules can form hydrogen bonds between nitrogen atoms and hydrogen atoms which are bonded to boron atoms. Two of the pairs can be arranged in the unit cell so that an interaction between boron atoms and hydrogen atoms bonded to nitrogen atoms becomes possible.

This results in almost identical packing densities in all three systems in Table 5.3. Another common behavior of benzene/Ag(111) and borazine/Cu(111) is that the LEED patterns could only be observed at low temperatures.[7] After heating of the sample to 125 and 115 K, respectively, the LEED spots irreversibly vanished, pointing to a rearrangement of the molecules from an ordered layer to disorder. However, for both systems, distinct multi- and monolayer peaks were observed in TPD at temperatures *above* 125 and 115 K, respectively. Thus, a dewetting and formation of clusters most likely does *not* occur. Instead, the formation of an unordered phase akin to an amorphous crystal can be imagined.

---

[6]For the monolayer of benzene/Ag(111), two different LEED patterns were observed depending on the preparation conditions. The parameters given here refer to the preparation at low dosage (-1 L) and low temperature (100 K).

[7]The authors [200] did not present the LEED patterns for the monolayer of benzene/Ag(111), only described it. The LEED patterns for the multilayers, however, were shown and are similarly blurry as the LEED pattern of ~2 ML borazine/Cu(111) in Figure 5.9a.
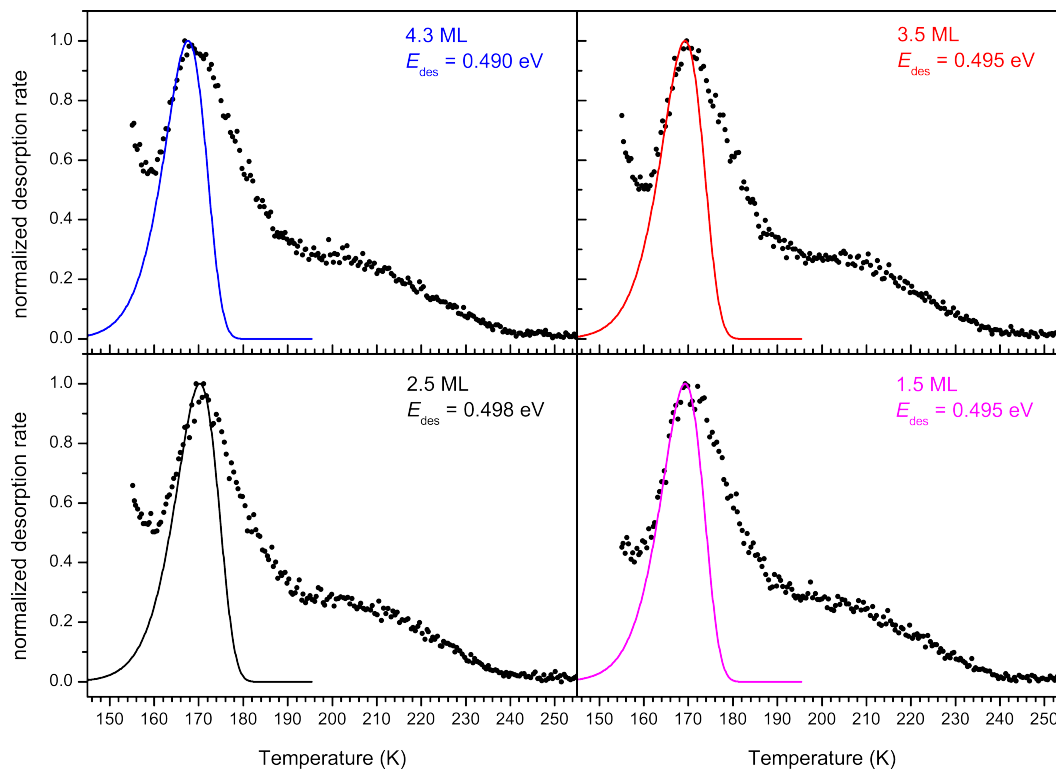
Figure 5.10: *Monolayer desorption peaks of borazine for coverages of 1.5−4.3 ML. At these coverages, the monolayer desorption peak is saturated and the monolayer is complete. The molecules were deposited at a sample temperature of 100 K and the sample was heated with a rate of 1 Ks^{-1}. Black points are the measured data, solid lines are calculated monolayer first order desorption peaks for the respective coverages, calculated with $\nu_0 = 1 \cdot 10^{13}$ s^{-1}. The resulting desorption energies $E_{\mathrm{des}}^{\mathrm{mono}}$ are given. The calculated peaks are fitted to the experimental data by the leading edges. The desorption from surface defects at 190−240 K changes the trailing edge of the monolayer desorption peak. The spectra were divided by the peak maxima; the peak maxima correspond to 0.4 MLs^{-1}.*

For the determination of the adsorption energy of the monolayer of borazine on Cu(111), the strong similarity to benzene/Ag(111) is utilized. The monolayer peaks are calculated and compared to the experimental spectra using the pre-exponential factor of $\nu_0 = 1 \cdot 10^{13}$ s^{-1} of benzene/Ag(111) [199]. Figure 5.10 shows calculated monolayer spectra in comparison to the measured spectra for coverages of 1.5−4.3 ML for which the monolayer peak is saturated and is constantly positioned at 170 K. The calculated spectra are fitted to the leading edges of the experimental spectra since the desorption peak from molecules at defects at higher temperatures changes the trailing edges of the peaks. The desorption energy of the borazine monolayer gained from these calculations amounts to $E_{\mathrm{des}}^{\mathrm{mono}} = (0.495 \pm 0.005)$ eV.

This desorption energy is smaller than the desorption energy of the multilayer which is surprising since the monolayer desorption occurs at a higher temperature. Nevertheless, the same behavior has been observed for benzene/Ag(111) as well. Table 5.4 summarizes the desorption energies of these two systems. First of all, the desorption energies of the monolayers are smaller than that of the multilayers in both systems. The difference amounts to 12% for benzene/Ag(111) and 6.6% for borazine/Cu(111) (compared to $E_{\mathrm{des}}^{\mathrm{multi}} = 0.53$ eV; for $E_{\mathrm{des}}^{\mathrm{multi}} = 0.60$ eV, the difference is 18%). This decrease in E_{des} can be attributed to the repulsive lateral interactions between the molecules

in the monolayer discussed above [199]. Furthermore, $E_{\text{des}}^{\text{multi}}$ of benzene/Ag(111) deviates from the sublimation energy ΔH_{sub} of benzene by 10%. This matches well with the desorption energy determined for 4.3 ML borazine/Cu(111) of 0.53 eV which deviates from the sublimation energy of the molecule by 12% ($E_{\text{des}}^{\text{multi}}$ = 0.60 eV for 3.5 ML is in perfect agreement with ΔH_{sub}).

From the similarities between benzene/Ag(111) and borazine/Cu(111) which have been pointed out above, the conclusion of very similar interactions in the multilayers of these two systems can be drawn. The observations for the respective monolayers point to very weak interactions between these and the respective metal surfaces. Thus, an influence of the substrates on the second and higher molecular layers can be assumed to be even weaker so that the comparison between benzene multilayers and multilayers of the benzene-analogous borazine is legitimate. Based on this comparison, a decision can be made regarding the two different results for the desorption energy of borazine multilayers on Cu(111) presented above. Assuming that the similarity between the two system also holds in regard to the desorption energy of multilayers, $E_{\text{des}}^{\text{multi}}$ = 0.53 eV is determined for borazine/Cu(111), rather than the value of 0.60 eV determined for 3.5 ML. [8]

Table 5.4: *Desorption energies of benzene on Ag(111) [199] and of borazine on Cu(111) for the monolayer $E_{\text{des}}^{\text{mono}}$ and the multilayer $E_{\text{des}}^{\text{multi}}$. The pre-exponential factors ν_0 and the sublimation enthalpies of the respective molecules ΔH_{sub} are included.*

	borazine/Cu(111)	benzene/Ag(111)
$E_{\text{des}}^{\text{multi}}$	(0.53 ± 0.01) eV	0.42 eV [199]
ν_0 (multi)	$(6 \pm 1) \cdot 10^{17} \frac{\text{particles}^2}{\text{s cm}}$	—
$E_{\text{des}}^{\text{mono}}$	(0.495 ± 0.005) eV	0.37 eV [199]
ν_0 (mono)	$1 \cdot 10^{13}\ s^{-1}$	$1 \cdot 10^{13}\ s^{-1}$
ΔH_{sub}	0.60 eV [196]	0.46 eV [202]

Borazine molecules at surface defects desorb at $190-240$ K. For a rough estimation of their desorption energy $E_{\text{des}}^{\text{def}}$, a similar approach as for the complete monolayer was employed. A TPD spectrum was calculated using $\nu_0 = 1 \cdot 10^{13}\ s^{-1}$ and E_{des} was changed so that the position of the desorption peak could be reproduced. This delivers $E_{\text{des}}^{\text{def}}$ = 0.59 eV as a very rough estimate due to the significant broadness of the experimental desorption peak. This broadness may be explained by the different kinds of surface defects that act as adsorption sites for the borazine molecules and/or by the different characters of bonds formed between the molecules and these defects.

These findings may be compared to literature about borazine on other substrates. On Au(111) [203], the multilayer desorption peak was observed at 140 K which agrees well with the peak position of 143 K on Cu(111). The monolayer desorption peak was found at higher temperatures compared to Cu(111). With increasing coverage, it shifted from 243 K to 206 K, pointing to the same repulsive lateral interactions as observed in the present work. $E_{\text{des}}^{\text{mono}}$ was determined to be 0.52 eV (assuming $\nu_0 = 1 \cdot 10^{13}\ s^{-1}$) which reflects the higher desorption temperature for the monolayer on Au(111) compared to Cu(111). *High resolution electron energy loss spectroscopy* has shown that on

---

[8]A calculated multilayer desorption peak with $E_{\text{des}}^{\text{multi}}$ = 0.53 and $\nu_0 = 5 \cdot 10^{17}\ s^{-1}$ agrees well with the experimental spectrum for 3.5 ML. Thus, the large difference between values for ν_0 (multi) presented above is resolved as well.

Au(111), too, the borazine molecules lie flat on the surface.

The behavior of borazine on Rh(111) [204] and Pt(111) [203] is very different from that on Cu(111) and Au(111) [203]. On these two surfaces, multilayer desorption was observed at 176 K (in agreement with the noble metal surfaces) and 150 K, respectively. A monolayer desorption, however, was *not* observed. Instead, the borazine molecules were dehydrogenated between 300 and 400 K and at higher temperatures (~600 K) hBN lattices formed. This process shows the much stronger interactions between the borazine molecule and the transition metal surfaces compared to the noble metal surfaces with a complete *d* shell as it has also been found for hBN [55].

Borazine adsorption and growth of hBN

The formation of hBN on any metal surface requires elevated temperatures. This process can be viewed as an activated adsorption [129] where borazine molecules adsorb on the surface in a physisorbed precursor state and have to overcome an activation barrier ΔE_A in order to contribute to the growth of the hBN layer. Figure 5.11 shows an energy diagram for activated desorption. The temperature dependent sticking factor plays an important role in the growth process of hBN[9]. On the one hand an elevated temperature is required for the hBN growth, but on the other hand, an elevated temperature causes increased desorption of the borazine molecules.

The value of the desorption energy gained from the TPD experiments presented above can be used to access ΔE_A. Using the desorption energy for borazine monolayers on Cu(111), ΔE_A can be estimated via the sticking factor *s* at the sample temperature T_S of 1070 K, the growth temperature of hBN. *s* is the ratio of the rate constants for the adsorption of molecules from the precursor state k_{ad} and the sum of the rate constants of all processes, in the current case of adsorption and desorption:

$$s = \frac{k_{ad}}{k_{ad} + k_{des}} \approx \frac{k_{ad}}{k_{des}} = e^{-\frac{\Delta E_A - E_{des}}{k_B T_S}} \quad . \tag{5.4}$$

For the growth of hBN on Cu(111), a high borazine dose *D* of 2000 L is required. The resulting impingement density of molecules is much higher than the molecular density of a closed monolayer. Accordingly, s $\ll$ 1 which will be shown below, and thus follows that $k_{ad} \ll k_{des}$.

The sticking factor can also be expressed as the amount of molecules that stick on the surface N^{stick} as the fraction of all molecules that hit the surface per time unit N^{hit}:

$$s = \frac{N_{BN}^{stick}}{N_{BN}^{hit}} = \frac{A^{-1}}{Zt} \quad . \tag{5.5}$$

A^{-1} is the number of molecules per surface area. Since one hBN unit cell contains one BN unit, the number of BN units N_{BN} will be considered for simplicity so that $A^{-1} = a_{hBN}^2 \cos(60°)$, with a_{hBN} as the lattice constant of the hBN layer, as it was used previously in this chapter. When the

---

[9]Here, the term *sticking factor* refers to the transition from precursor state of the borazine molecule on the surface to the hBN layer. For the transition of the molecule from gas phase to precursor state, a sticking factor of 1 can be assumed due to the low sample temperature and the small borazine dose of 1.8 L necessary to achieve monolayer coverage.
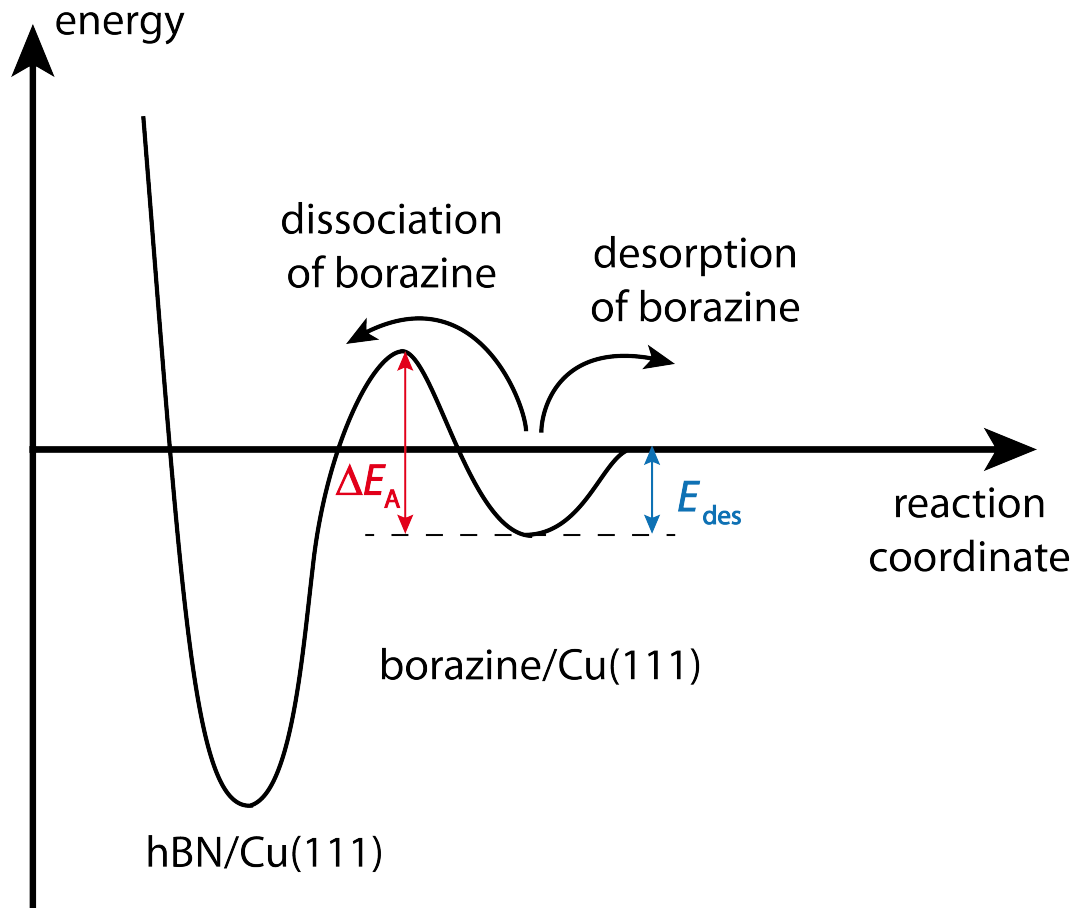
Figure 5.11: *One-dimensional representation of the energy diagram of the activated adsorption of borazine molecules. The precursor state of borazine on the surface and the hBN layer formed after dissociation of the borazine molecules are represented as energy wells. They are separated by the activation barrier ΔE_A. At an elevated temperature, borazine molecules can either cross this activation barrier and form hBN or desorb from the surface which requires the desorption energy E_{des}. As per [129].*

BN units instead of the complete borazine molecule are considered, the collision rate Z needs to reflect this, too. Thus, a factor 3 is included because a borazine molecule contains 3 BN units:

$$Z = \frac{3p}{\sqrt{2\pi m k_B T_G}} \, , \tag{5.6}$$

where T_G is the temperature of the borazine gas. Thus follows

$$Zt = \frac{3D}{\sqrt{2\pi m k_B T_G}} \tag{5.7}$$

and

$$s = \frac{\sqrt{2\pi m k_B T}}{3 D a_{hBN}^2 \cos(60°)} = 2.256 \cdot 10^{-3} \, , \tag{5.8}$$

with a borazine dose $D = pt = 2000$ L at a temperature $T_G = 298$ K.

Now, using Eq. 5.4, the barrier for the activated adsorption of borazine on the Cu(111) surface ΔE_A at $T_S = 1070$ K can be calculated as

$$\Delta E_A = E_{des} - k_B T_S \ln(s) = 1.06 \pm 0.01 \text{ eV} .\tag{5.9}$$

Following the model for the hBN growth by Felter et al. [183] (see Chapter 5.1), ΔE_A corresponds to the dissociation energies of the B−H and N−H bonds in the borazine molecule. Auwärter et al. [184] calculated these bond energies to be 4.72 eV and 5.38 eV, respectively. These values refer to the molecule in the gas phase and not on a metal surface. There, the energy required to break these bonds is reduced, presumably because the metal activates the chemical bonds.

The model of the activated adsorption of borazine on the metal surfaces for the formation of hBN explains why the desorption of borazine molecules in the monolayer was not observed in TPD on either Rh(111) or Pt(111) [203, 204]. Eq. 5.4 shows that the term $\Delta E_A - E_{des}$ is the deciding factor for the sticking factor. The borazine molecule in the precursor state on the surface can be assumed to be similarly weakly bound on Rh(111) and Pt(111) as on Cu(111). Thus, the activation barrier needs to be considered.

If $\Delta E_A > E_{des}$, s increases with increasing temperature according to Eq. 5.4, i.e. the formation of hBN is more favored with respect to the desorption of the borazine molecule. On Rh(111) and Pt(111), the desorption of the borazine monolayer was not observed and instead, the hBN layer was formed [203, 204]. This points to a smaller activation barrier ΔE_A for the formation of hBN on Rh(111) and Pt(111) compared to Cu(111).

A similar conclusion can be drawn for the activation barriers of borazine molecules adsorbed at defects or on terraces on the Cu(111) surface. According to the growth model introduced in Chapter 5.3.1, first, hBN nuclei form at Cu defects which grow into R30°-domains. After the saturation of the defects, aligned domains grow from hBN nuclei which form on Cu(111) terraces. Thus, the activation energy for the formation of hBN nuclei from molecules adsorbed at defects must be smaller than that for molecules adsorbed on terraces.

In summary, the desorption of borazine molecules adsorbed on the Cu(111) surface in multilayers, monolayers and at surface defects can be clearly distinguished in TPD spectra. Their desorption energies were determined to be (0.53 ± 0.01) eV, (0.495 ± 0.005) eV, and (0.59 ± 0.01) eV, respectively. The smaller desorption energy for borazine monolayers compared to that of multilayers is explained by repulsive lateral interactions in the monolayer. The larger desorption energy of molecules at surface defects leads to a preference of the formation of hBN nuclei at surface defects over those on Cu(111) terraces that are aligned with with the metal substrate.

5.4   Conclusion

The interface of hBN/Cu(111) can be considered to be of a physisorptive nature, which is revealed by several structural parameters. hBN/Cu(111) is incommensurate despite only a small lattice

mismatch which leads to a lattice constant of (2.500 ± 0.004) Å which is similar to that of the bulk material and the free standing hBN layer. The azimuthal orientations of the hBN domains on the Cu(111) surface are widely distributed and their vertical distance to the top-most Cu layer of (3.24 ± 0.03) Å exceeds the sum of the vdW radii of adsorbate and substrate. The influence of the Cu(111) surface on the hBN layer is reflected only in the thermal expansion of the hBN following that of the substrate, the preferential orientation of domains in alignment with the metal surface, and a small buckling of the layer. The buckling of (0.42 ± 0.05) Å can be considered small on the scale of the Moiré pattern and the hBN layer can be viewed as locally flat. The LEED pattern of hBN/Cu(111) can be explained by a combined effect of this minute buckling of the hBN layer and multiple scattering effects.

The azimuthal orientations of the domains are determined during the growth process. Based on SPA-LEED and TPD experiments, the growth model for hBN/Cu(111) by Felter et al. [183] was expanded. The growth process of hBN begins with the formation of domains rotated by 30° relative to the Cu(111) surface, whose orientation may be influenced by surface defects. At surface defects, the desorption energy of borazine molecules is higher and the activation barrier for the formation of hBN is lower compared to borazine molecules adsorbed on Cu(111) terraces. After the saturation of surface defects, hBN domains form on Cu(111) terraces where their orientation is determined by the preferential adsorption sites $N_{top}B_{fcc}$ or $N_{top}B_{hcp}$ of the nuclei. These domains, which grow in alignment with the Cu(111) surface, make up the majority of hBN domains. The desorption energy of borazine on terraces amounts to (0.495 ± 0.005) eV with repulsive lateral interactions between the molecules. In the last step of the growth process, hBN domains of random orientation fill the gaps between the large, aligned domains.

6 Electronically decoupled PTCDA on hBN/Cu(111)

In this chapter, the decoupling of PTCDA from the Cu(111) surface by a single layer of hBN will be discussed based on the lateral structure of PTCDA monolayers, the vertical structure of the adsorption complex PTCDA/hBN/Cu(111), and the electronic structure of PTCDA which was investigated using PES methods. These results have been published in Appendix A.2. The results of the SPA-LEED investigations of the lateral structure will be discussed in detail here and compared to the structure of other PTCDA films on metal substrates. Furthermore, the influence of the quality of the hBN layer on the PTCDA layer will be reported. The results on the vertical and electronic structure of PTCDA on hBN/Cu(111) will be summarized more briefly.

6.1 Literature Overview

The adsorption of PTCDA on Cu(111) leads to a CT from metal to molecule which shifts the former LUMO below the Fermi energy [46]. The CT is presumably the reason for the vertical distortion of the molecule [47, 56] which was already described in Chapter 2.2 and illustrated in Figure 2.5. The PTCDA molecule displays a boat-shape as both the anhydritic and the carboxylic oxygen atoms are shifted upwards and are located above the perylene backbone of the molecule. STM experiments showed that on Cu(111), PTCDA grows in a layer-by-layer mode for the first few layers before nanocrystals begin to form [205]. The formation of nanocrystals has also been shown in desorption experiments [206], beginning in the fifth layer. In TPD spectra, the desorption of the second PTCDA layer was clearly distinguishable from that of the multilayer. Additionally, at higher temperatures, the desorption of nanocrystals was observed. A desorption of the first layer which is directly adsorbed to the Cu(111) surface, was not found. This is due to the chemisorptive bond between PTCDA and the metal surface [46] which does not allow the desorption of intact molecules.

Two lateral structures with herringbone arrangements of PTCDA on Cu(111) were observed by Bauer (α- and β-phase) [57] and by Wagner et al. (structures '1' and '2') [207], respectively. While Bauer's β-phase and Wagner's structure '2' exhibit distinct similarities, the α-phase and the structure '1' were not found in the respective other study. This may be ascribed to differences in substrate quality and preparation conditions, or to the different methods employed (SPA-LEED vs. STM). A detailed comparison of the results of the two studies can be found in Appendix A.3 and in Ref. [57]. In the scope of the work presented here, the results by Bauer were reproduced, and

thus act as a reference point. The structural details of the α- and β-phases of PTCDA on Cu(111) can be found in Table 6.1.

In Chapter 2.3, the trapping of organic molecules in the pores of metal-supported hBN layers was introduced. The same was reported for some molecules on hBN/Cu(111). For example, a trapping of adsorbed molecules in areas of low local work function (corresponding to the moirons[1]) was observed for the deposition of small amounts of tetracyanoquinodimethane (TCNQ) and free-base porphine (2H-P) [208]. But this is not the only scenario which was observed. Quaterphenylene dicarbonitrile (QDC) does not get trapped on hBN/Cu(111) and instead forms self-assembled molecular domains [209]. For the aforementioned molecules, a trapping has only been observed at larger coverages. This difference has been assigned to an effect of presence or lack of inter-molecular interactions [11]. When these are strong, self-assembly can occur; if the variation of the molecule-substrate interaction is relevant and its length scale is of the order of the size of the molecules, individual molecules get trapped in the moirons. For domains of 2H-P [208] and QDC [209] at higher coverages, a shift of the positions of the frontier orbitals depending on the adsorption sites of the molecules has been observed which is an effect of the electronic superstructure of hBN/Cu(111) [174].

Concerning PTCDA, a trapping of molecules has been observed on hBN/Rh(111) [125]. After deposition of submonolayer coverages of PTCDA at 300 K, the molecules preferably adsorbed in pores with three preferred orientations, following the symmetry of the substrate. These molecules can function as nuclei for tiny domains with many defects. Annealing above 370 K leads to the formation of highly ordered, densely packed domains with a herringbone arrangement of the molecules. A similar structure has been observed for PTCDA/hBN/Pt(111) [125], however, this structure formed immediately after deposition at 300 K. Additional annealing extended these domains and reduced defects.

On hBN/Rh(110), [124] a long-range ordered herringbone structure of PTCDA which is commensurate to the hBN layer was observed after deposition at room temperature. An influence of the stripe-like Moiré superstructure of hBN on Rh(110) on the molecular structure was not found. The apparent height of the PTCDA molecules above the hBN layer measured in STM was slightly higher than 3 Å.

In contrast to these herringbone arrangements of PTCDA on hBN, a T-shape arrangement of the molecules in a quadratic unit cell was found on exfoliated hBN on Si/SiO$_2$ [126]. Here, PTCDA was deposited at room temperature from an ethanolic solution.

In summary, PTCDA and the Cu(111) surface form a chemisorptive bond which strongly influences the structure of the molecule. For some molecules, an hBN layer was able to structurally decouple these from an underlying Cu(111) surface which depended on the strength of inter-molecular compared to the interfacial interactions. PTCDA on hBN layers has been shown to still be influenced by the underlying metal, however, this was the case for more reactive transition metal substrates.

---

[1]or pores, see Chapter 5.1

6.2 The impact of an hBN layer on the lateral structure of the PTCDA/Cu(111) interface

For a deposition of submonolayer coverages of PTCDA on hBN/Cu(111) at sample temperatures between $260-300$ K, no trapping of molecules was observed in STM experiments. Instead, ordered domains with a herringbone arrangement formed (cf. Figure 1 in Appendix A.2). For detailed structural analysis from the submonolayer- to the multilayer-regime of PTCDA on hBN/Cu(111), SPA-LEED experiments were conducted.

6.2.1 The lateral structure

A LEED pattern of PTCDA on hBN/Cu(111) is shown in Figure 6.1a. The sharp spots of the Cu(111) substrate, the hBN ring, and the satellite structures of the hBN layer are clearly visible. The LEED pattern is assigned to a PTCDA coverage of ≤ 1 ML[2]. Between the hBN ring and the specular spot, there are several more rings of intensity. The rings of the highest intensities are found at a distance of $0.6-0.9$ Å from the specular spot. These rings stem from the first PTCDA layer on hBN/Cu(111). Similar to the hBN ring, these rings show a modulation in intensity along the rings.
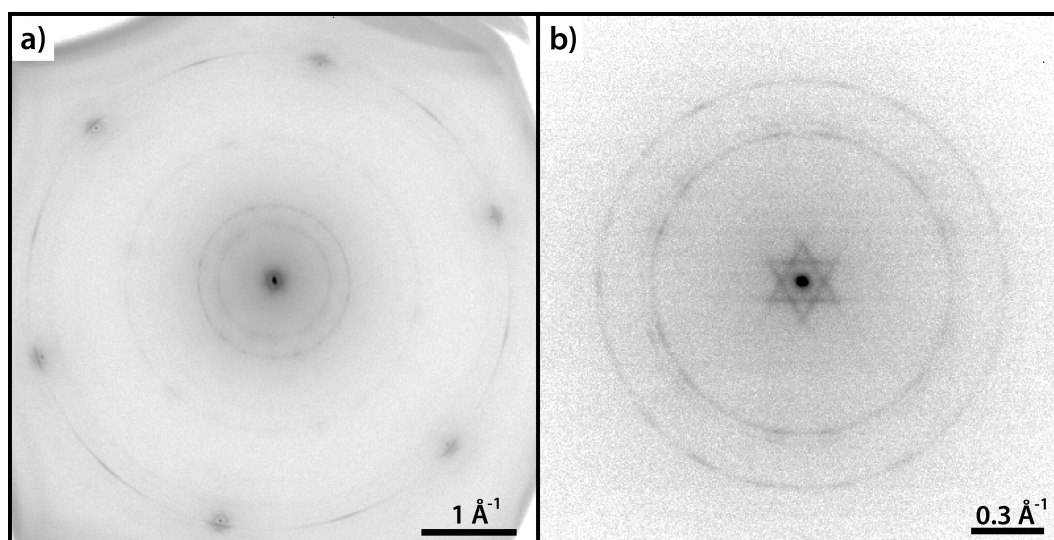
Figure 6.1: *LEED patterns of the first layer of PTCDA on hBN/Cu(111). a) Overview LEED pattern measured with an electron energy of 70.7 eV at a sample temperature of 110 K. The Cu spots and the hBN ring are clearly visible. Modulated rings of intensity between the specular spot and the hBN ring are caused by the PTCDA layer. b) Zoomed-in LEED pattern measured with an electron energy of 60 eV at a sample temperature of 140 K. Three rings of intensity with radii between 0.6 and 0.9 Å show different patterns of modulation in their intensities. The LEED pattern was recorded for a different preparation of PTCDA on hBN/Cu(111) than a).*

---

[2] An exact determination of the coverages for the LEED pattern shown in Figures 6.1a, b, and 6.2a via TPD was not possible for these experiments because TPD was not available at the UHV chamber used for recording these LEED patterns. The coverages given are based on the high intensities of the substrate spots and the extinction of certain PTCDA diffraction spots. This is explained in detail in the main text of Chapter 6.2.1 and is corroborated by other experiments that combined LEED and TPD.

Table 6.1: *Overview of the PTCDA lattice parameters in the (102) planes of the two bulk configurations α and β and on different substrates. The vectors of the unit cells $\vec{b}_1$ and $\vec{b}_2$, the angle γ between the two, and the areas of the unit cells A are given. φ is the enclosed angle between the vector $\vec{b}_1$ and the substrate lattice vector $\vec{a}_1$. ρ is the packing density of the molecules. Additionally, the superstructure matrices **M** are given. The matrix for PTCDA/hBN/Cu(111) refers to the Cu(111) surface at 100 K, the matrix for PTCDA/hBN/Rh(100) refers to the hBN layer with a periodicity of 2.51 Å [210]. The matrices given for PTCDA/Ag(111) and PTCDA/hBN/Rh(110) are not those reported in Refs. [99] and [124], respectively, but have been set up according to the rules given in [211].*

	Bulk (α) [97]	Bulk (β) [97]
b_1 (Å)	11.96	12.45
b_2 (Å)	19.91	19.30
γ (°)	90	90
A (Å^2)	238.12	240.3
ρ (Å^{-2})	8.4×10^{-3}	8.3×10^{-3}

	Ag(111) [99]	Cu(111) (α) [57]	Cu(111) (β) [57]
b_1 (Å)	12.61	12.4 ± 0.2	11.8 ± 0.2
b_2 (Å)	18.96	19.5 ± 0.3	19.9 ± 0.5
γ (°)	89.0	90.0 ± 0.9	90.0 ± 1.3
A (Å^2)	238.7	242 ± 7	235 ± 10
ρ (Å^{-2})	8.4×10^{-3}	8.3×10^{-3}	8.5×10^{-3}
ϕ (°)	7.6	2.5 ± 0.7	10.3 ± 1.0
M	$\begin{pmatrix} 3 & -2 \\ 6 & 7 \end{pmatrix}$	$\begin{pmatrix} 4.98(9) & 0.25(7) \\ 4.06(11) & 8.79(15) \end{pmatrix}$	$\begin{pmatrix} 5.01(8) & 0.95(9) \\ 3.03(15) & 8.82(20) \end{pmatrix}$

	hBN/Cu(111)	hBN/Rh(110) [124]	hBN/Pt(111) [125]
b_1 (Å)	12.07 ± 0.3	13.3	12.81
b_2 (Å)	19.33 ± 0.9	20.57	20.84
γ (°)	90(3)	91.3	90.2
A (Å^2)	233(2)	273.6	266.96
ρ (Å^{-2})	8.6×10^{-3}	7.3×10^{-3}	7.5×10^{-3}
ϕ (°)	9 ± 1	74.3	n.d.
M	$\begin{pmatrix} 5.12(5) & 0.9(1) \\ 3.0(3) & 8.64(9) \end{pmatrix}$	$\begin{pmatrix} 9 & 7 \\ 2 & -4 \end{pmatrix}$	n.d.
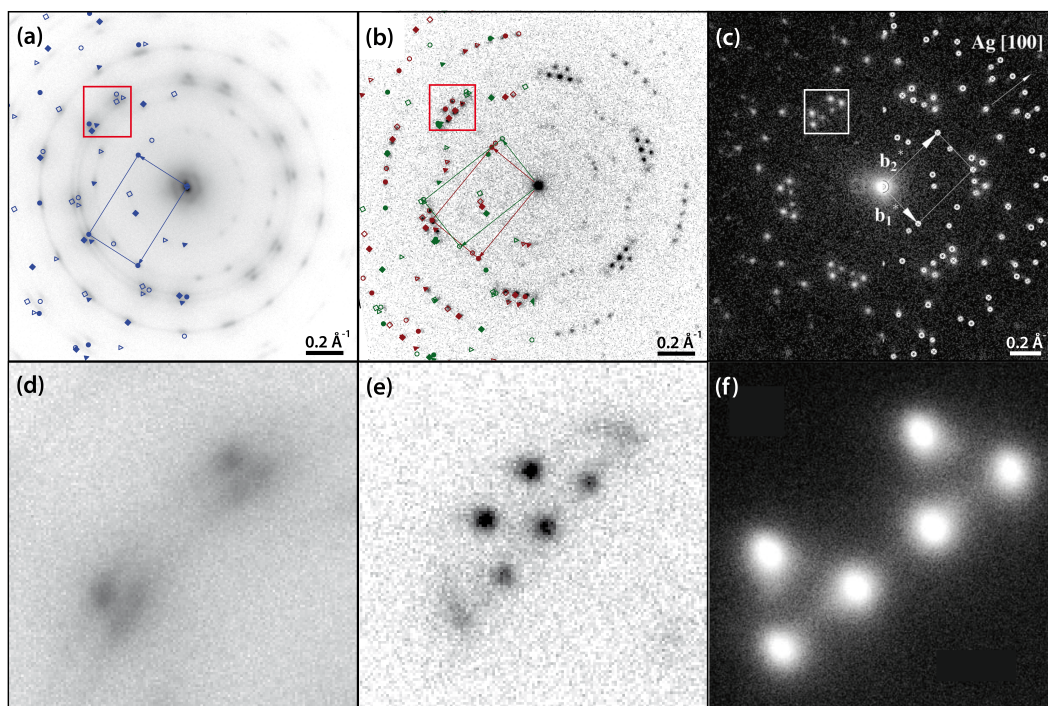
Figure 6.2: *LEED patterns of a) 2 ± 0.5 ML PTCDA/hBN/Cu(111), recorded at a sample temperature of 110 K with an electron energy of 30.4 eV, b) 1.55 ML PTCDA/Cu(111), recorded at a sample temperature of 100 K with an electron energy of 78 eV, and c) 1 ML PTCDA/Ag(111), taken from Ref. [50], recorded at a sample temperature of 300 K with an electron energy of 20 eV. The LEED pattern of PTCDA/Cu(111) corresponds to what was reported in Ref. [57]. In all cases, the characteristic double triangle arrangement of spots are marked with red or white boxes and the LEED patterns are overlaid with the corresponding simulations. Different symbols refer to symmetry inequivalent domains. Red and green symbols in b) refer to the α- and β-phases of PTCDA/Cu(111). The intensities of the spots in the LEED pattern of PTCDA/hBN/Cu(111) in a) are azimuthally smeared out as opposed to the sharp spots in b) and c). d)-f) Zoom-ins on the double triangles in a)-c). On hBN/Cu(111) (d) and Ag(111) (f), it is formed by two triangles made up of six spots. On Cu(111) (e), five spots form two corner-connected triangles.*

The modulation of intensity can be seen more clearly in Figure 6.1b which shows a zoom-in on the PTCDA rings of highest intensity. (Note that this LEED pattern was recorded for a different preparation of PTCDA on hBN/Cu(111).) The modulation is caused by an azimuthal smearing of the PTCDA diffraction spots. At the positions of the spots, a maximum in intensity remains. As for hBN/Cu(111) (cf. Chapter 5.2.1), the presence of rings in the LEED pattern indicates azimuthal disorder of the PTCDA domains. This can either be an indication for very weak interfacial interactions so that there is no influence of the substrate on the azimuthal orientation of the PTCDA domains or a consequence of the azimuthal disorder of the hBN domains which would cause azimuthal broadening although the PTCDA domains grew epitaxially on hBN/Cu(111).

For different preparations of PTCDA on hBN/Cu(111), different LEED patterns were measured. All of them showed the discussed rings, however, their shapes ranged from complete homogeneity in the intensities, to a modulation as shown in Figure 6.1b, to distinct spots with only a small

amount of intensity remaining on the rings (see Figure 6.2a). The much more homogeneous azimuthal distribution of the PTCDA intensity compared to that of the hBN shows that the azimuthal broadening of the PTCDA intensity is due to a rotation of the PTCDA domains relative to the hBN layer. This indicates very weak interfacial interactions between PTCDA and hBN. The azimuthal order that was occasionally observed has to be related to a change in adsorbate-substrate interactions and, thus, may be related to the quality of the hBN layer. This correlation will be discussed in detail in Chapter 6.2.2.

A LEED pattern of 2 ± 0.5 ML PTCDA with more distinct PTCDA spots is shown in Figure 6.2a. Such a LEED pattern allowed the determination of the structure of the PTCDA monolayer on hBN/Cu(111). The structure was analyzed in an iterative process of deskewing the LEED pattern and simulating the spot positions, using the programs *ImageJ* [212] with a Plug-In written by N. Rohbohm [213] and *Spotplotter* [214]. The resulting simulation of the LEED pattern is overlayed on Figure 6.2a and the derived structural parameters are given in Table 6.1.[3] Apart from the degree of modulation of the ring intensities, there is a second important difference between the LEED patterns of different preparations of PTCDA/hBN/Cu(111). In Figure 6.1b, the first order spots {$h0$} and {$0k$} are systematically extinct, while in Figure 6.2a, these spots are clearly visible. Both, the extinction and the presence of these spots, have been observed for different modulations of the ring intensities. Thus, the extinction is not related to this. Instead, the extinction is related to the PTCDA coverage as will be discussed in the next section.

PTCDA on hBN/Cu(111) compared to metallic substrates

The spot pattern of PTCDA/hBN/Cu(111) shows an obvious similarity to PTCDA films on metal surfaces [49, 57, 99]. For comparison, LEED patterns of 1.55 ML of PTCDA/Cu(111) (which are in agreement with those given in Ref. [57]) and 1 ML PTCDA/Ag(111) (taken from Ref. [50]) are shown in Figures 6.2b and c (including an overlay of the simulated LEED patterns) and the corresponding structural parameters are included in Table 6.1. The two different phases of PTCDA on Cu(111) (α and β) are indicated in red and green in Figure 6.2b.

The most prominent difference between the three LEED patterns is the azimuthal smearing of the spot intensities for PTCDA/hBN/Cu(111). The arrangement of the spots, on the other hand, is rather similar for all three substrates. The characteristic LEED feature of PTCDA layers in a herringbone arrangement is marked in the patterns by red or white boxes and will be referred to as *double triangle*. Figures 6.2d−f show zoom-ins on these respective *double triangles*. On Ag(111) [50, 99] (and on Au(111) [49]), this feature is made up of six diffraction spots, arranged in two adjacent triangles. On Cu(111) [57], two of these spots overlap, so that the *double triangle* is effectively formed by only five spots and the two triangles are connected by one corner. On hBN/Cu(111), the *double triangle* consists of two triangles, formed by six spots, as is the case for PTCDA/Ag(111). Thus, PTCDA/hBN/Cu(111) can unambiguously be distinguished from PTCDA/Cu(111).

---

[3]Table 6.1 includes a matrix for PTCDA/hBN/Cu(111) referring to the Cu(111) surface at 100 K. The matrix referring to the hBN layer at 100 K is $\begin{pmatrix} 5.22(5) & 0.9(1) \\ 3.1(3) & 8.81(9) \end{pmatrix}$.

On Cu(111), the same extinction of the first order spots {h0} and {k0} was observed for 1 ML of PTCDA as for PTCDA on hBN/Cu(111). For both systems, these first order spots were present for the second layer of PTCDA (in agreement with the findings presented in Ref. [57]). The extinction is an effect of the glide planes in the *p*2*gg* space group of the PTCDA herringbone structure. Strictly, the glide planes are only present if the substrate surfaces are not taken into account for the PTCDA monolayer. This is possible due to the large discrepancy in periodicity of the PTCDA layer and the substrate [57] to a certain extend. However, this is not the case with an additional second PTCDA layer, which is shifted laterally with respect to the first layer [97]. Then, the symmetry is lifted and the glide planes vanish because of the second PTCDA layer. Thus, the LEED patterns of two PTCDA layers on hBN/Cu(111) and on Cu(111) contain the first order PTCDA spots, as seen in Figures 6.2a and b. The change in symmetry upon adsorption of a second PTCDA layer confirms the layer-by-layer growth mode for the first two layers that was found previously for PTCDA/Cu(111) [57] and shows that the same is true for at least the first two layers of PTCDA/hBN/Cu(111).

Note that the same extinction was observed for 1 ML PTCDA/Au(111) [49] but *not* for 1 ML PTCDA/Ag(111) [50]. This is caused by the deviation of the angle γ between the two lattice vectors of the PTCDA structure from 90° on Ag(111). Thus, already in the monolayer, the *p*2*gg* symmetry is broken and the first order spots are not extinct.

In the following, the structures of the PTCDA films presented in Figure 6.2 will be compared to the PTCDA bulk modifications and the influence of the different substrates on the lattices of the films will be discussed. All PTCDA structures on the three substrates hBN/Cu(111), Cu(111) [57], and Ag(111) [99] show a strong resemblence to the PTCDA structures in the two bulk modifications [97], with a deviation in the unit cell areas of not more than 7%. The smallest deviation between the bulk and a PTCDA monolayer is that of PTCDA/Ag(111) (the unit cell areas differ by only 0.24% for the α-modification and −0.67% for the β-modification). The ratio of the two lattice vectors $\vec{b}_1$ and $\vec{b}_2$ shows that PTCDA/Ag(111) rather resembles the β-modification than the α-modification (with deviations by 4.48% and 10.45%, respectively). To achieve the commensurate structure of PTCDA/Ag(111), lattice mismatches between the β-modification and the Ag(111) surface of -1.8% and 1.2% in the two directions are overcome by stretching and compressing the two vectors accordingly.

On Cu(111), the α-phase corresponds to the β-modification in the bulk and, vice versa, the β-phase resembles the α-modification, in both the area of the unit cell and the lengths of the lattice vectors. Both phases exhibit a *point-on-line* (*pol*) coincidence with the Cu(111) surface. Although the individual lattice mismatches between the PTCDA bulk modifications and the respective phases on the Cu(111) surface in either direction is smaller than the lattice mismatch between PTCDA in the β-modification and on Ag(111) (0.1−1.4% in both phases on Cu(111)), the deviation in the unit cell areas is larger (−1.3% for the β-phase and 7.0% for the α-phase) and no true commensurability was found for PTCDA/Cu(111).

A direct comparison of PTCDA/hBN/Cu(111) with the two bulk modification shows, that there is resemblance to both of them. The unit cell areas deviate by −2.15% (to the α-modification) and −3.04% (to the β-modification), the ratios of the lattice vectors differ by 3.80% and −3.31%, respectively. Each of the lattice vectors of PTCDA/hBN/Cu(111) agrees with one of the vectors of the

bulk modifications within 1%. The structure is incommensurate and the domains show azimuthal disorder.

These observations reflect the interaction strength at the PTCDA/substrate interfaces. The *pol*-coincidence between PTCDA and Cu(111) instead of true commensurability despite a smaller lattice mismatch than PTCDA/Ag(111), which *is* commensurate, show the weaker interactions for PTCDA/Cu(111). The stronger interaction between PTCDA and Ag(111) allows a sufficient stretching/compressing of the PTCDA lattice which leads to the commensurate structure. This agrees with the larger interfacial distance for PTCDA/Cu(111) compared to PTCDA/Ag(111) [56, 100].

The interaction strength between PTCDA and hBN/Cu(111) seems to be even smaller due to the incommensurate structure and the azimuthal disorder which is indicated by the rings in the LEED patterns. Accordingly, a weaker CT (if any) and a larger interfacial distance compared to PTCDA/Cu(111) and PTCDA/Ag(111) can be expected.

Remarkably, the structural parameters that were extracted from a PTCDA/hBN/Cu(111) structure with exceptionally high azimuthal order strongly resembles the β-phase of PTCDA/Cu(111), with a difference in the area of the unit cells of only 0.85% and almost the same orientation relative to the Cu(111) lattice ($\pm 1°$). The preferential azimuthal orientations point to increased interfacial interactions and the structural resemblance to PTCDA/Cu(111) indicate that this interfacial interaction involves the Cu(111) substrate. This would require defects in the hBN layer which reveal the bare Cu(111) surface where these interactions then are possible. A LEED pattern with a higher azimuthal order, as in Figure 6.2a, thus indicates the presence of more defects in the hBN layer than a LEED pattern with more homogeneity of the rings (cf. Figure 6.1b). Consequently, as mentioned before, the quality of the hBN layer plays a decisive role here. This will be discussed further in Chapter 6.2.2.

PTCDA on hBN/Cu(111) compared to other hBN-substrates

Now, PTCDA films on metal-supported hBN layers will be discussed. The structures of PTCDA on hBN/Rh(110) [124] and hBN/Pt(111) [125] differ much more from the structures of the bulk modifications compared to hBN/Cu(111) (see Table 6.1). The areas of the unit cells are much larger than those in the bulk modifications (by $11-15\%$) which results in a significantly smaller density of molecules on the surfaces. On hBN/Rh(110), a commensurate structure was found which is achieved by a stretching of the lattice vectors $\vec{b}_1$ and $\vec{b}_2$. While the angle ϕ between the PTCDA lattice and the substrate lattice is very large compared to the other angles ϕ given in Table 6.1 at 74.3°, the angle between the PTCDA lattice and the Moiré superstructure of hBN/Rh(110) (which is made up of stripes) is only 1.9°. Thus, the strong electronic corrugation of the hBN/Rh(110) substrate may be the reason for this PTCDA structure that so significantly deviates from those that have been discussed before. Accordingly, a much stronger interfacial interaction can be assumed here. On hBN/Pt(111), similar interactions may be in effect since the corrugation of hBN on Pt(111) [84] and its influence in the electronic structure of PTCDA [125] have been observed. However, the azimuthal orientation of the PTCDA structure, and thus the superstructure matrix were not determined for this interface.

These observations proof the expectation that weak interactions at the hBN/metal interface also facilitate the decoupling of the organic molecule on top of the hBN layer. On Pt(111) and Rh(110), where the hBN layer is strongly modulated by the metal [84, 124], the PTCDA structure shows a strong influence of the substrate. Contrastingly, on hBN/Cu(111), where the interfacial interactions are weak and the hBN layer is mostly flat, the PTCDA structure is bulk-like and shows no epitaxial relationship to the substrate.

Despite the stronger interfacial interaction between PTCDA and the substrates hBN/Pt(111) and hBN/Rh(110), the domains formed by molecules are still in a herringbone arrangement, equivalent to the situation on the hBN/Cu(111) substrate. Contrastingly, on hBN/SiO$_2$ [126], the PTCDA molecules are arranged in a T-shape, leading to a quadratic unit cell, as it was observed on NaCl/Ag(100) [111] (Q-phase, cf. Chapter 2.2). On NaCl, the Q-phase is commensurate and forms due to attractive interactions between the molecules and the adsorbate. It remains unclear why a T-shaped arrangement is found on hBN/SiO$_2$. The interaction between the PTCDA molecules and the hBN layer itself are, in principle, expected to be at least similar on SiO$_2$ and Cu(111) as no significant periodic corrugation (topographical or electronic) occurs on either substrate (the exfoliated hBN layer was deposited on SiO$_2$) so that the bulk-like herringbone arrangement of PTCDA can be expected. A possible explanation for the formation of the Q-phase may lie in the preparation conditions. PTCDA was not deposited on hBN/SiO$_2$ via vapor deposition but from an ethanolic solution which was dried in N$_2$ stream [126]. The growth of PTCDA domains from the liquid phase is most likely influenced by the solvent molecules and different kinetic mechanisms may be present, which then leads to the formation of the Q-phase.

6.2.2 The importance of the hBN quality

Now, the influence of the quality of the hBN layer on the structure of an adsorbed PTCDA layer will be discussed. The LEED pattern of PTCDA/hBN/Cu(111) in Figure 6.2a shows PTCDA spots which are exceptionally *not* smeared out and thus supported the structural analysis. This pattern could not be *reliably* reproduced. Instead, patterns as the ones shown in Figures 6.1b and 6.3a were often observed. A correlation to a change in the preparation conditions of the PTCDA layer or the coverage could not be found. The discernible difference for the different kinds of LEED patterns was, however, the quality of the hBN layer. For an easy comparison, Figure 6.3 comprises a LEED pattern with homogeneous PTCDA diffraction rings (a) and the LEED pattern of azimuthally oriented domains that was previously shown in Figure 6.2a (b). Figures 6.3c and d show the LEED patterns of the respective hBN layers before PTCDA deposition. Both show the hBN ring of the azimuthally disordered hBN domains, with a preferential orientation in $\overline{\Gamma M}$ direction and the satellite structures around the specular spot and the Cu first order spots. In both patterns, the rings are sharp, however, while the ring in Figure 6.3c is continuous, the ring in Figure 6.3d only shows intensity in the $\overline{\Gamma M}$ and $\overline{\Gamma K}$ directions (gaps in ring intensity are exemplary indicated by green arrows). Furthermore, the satellite structures, while present in Figure 6.3d, too, are not as pronounced and clear as in Figure 6.3c because the lines that form these structures are shorter.
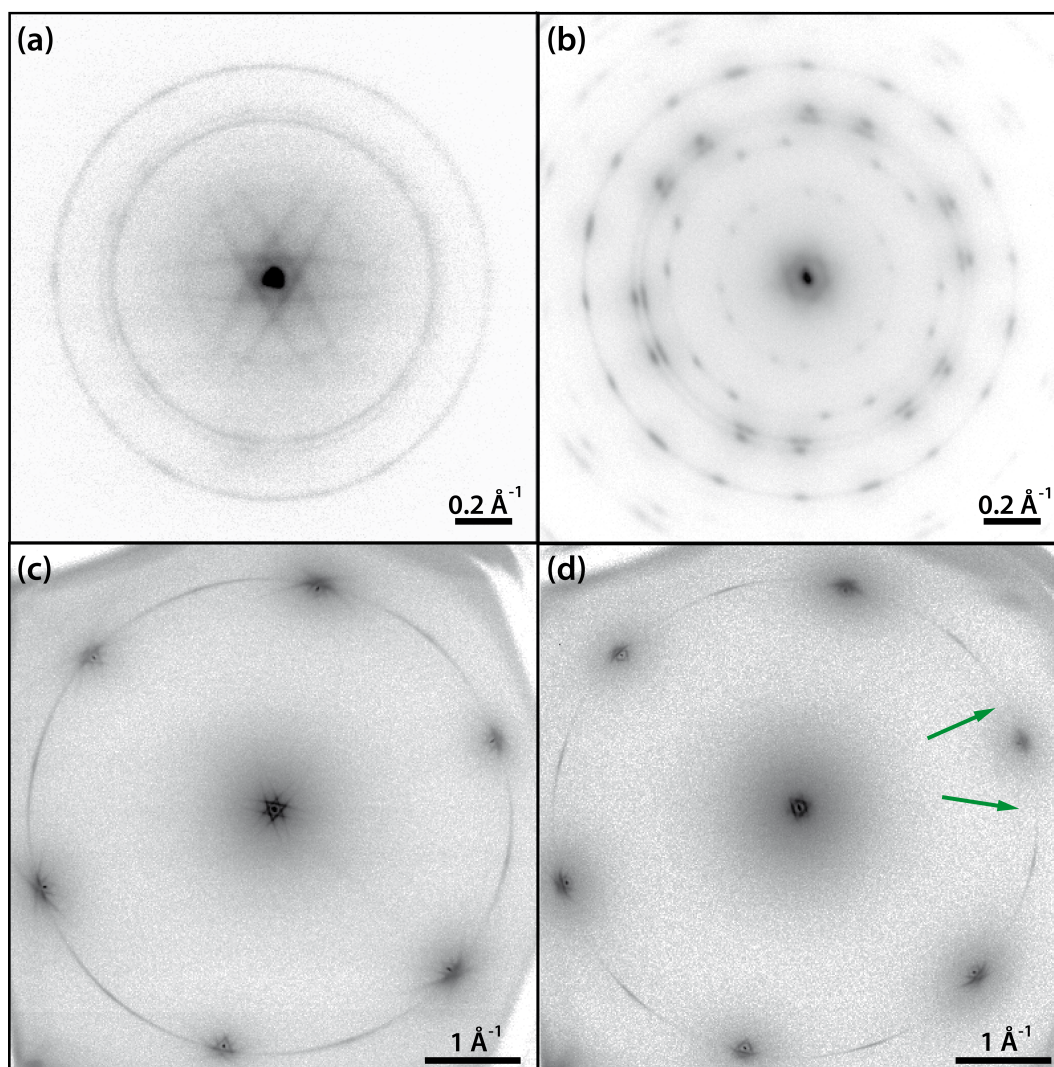
Figure 6.3: *LEED patterns of PTCDA/hBN/Cu(111) (a and b) and of the respective hBN/Cu(111) surfaces before PTCDA deposition (c and d), recorded at a sample temperature of $110-160\,K$ with electron energies of $31 \pm 0.5\,eV$ (a and b) and $70.6\,eV$ (c and d). a) The intensities of the diffraction rings of PTCDA are homogeneous and indicate complete azimuthal disorder of the PTCDA domains. b) Same LEED pattern as in Figure 6.2a. The maxima of intensity on the diffraction rings of PTCDA show the preferential orientation of the domains. c) The diffraction ring of the hBN layer is continuous, with maxima in the intensity in $\overline{\Gamma M}$ and $\overline{\Gamma K}$ direction. The satellite structures are comprised of sharp long lines. d) The diffraction ring of the hBN layer shows intensity only in $\overline{\Gamma M}$ and $\overline{\Gamma K}$ direction. Two gaps in the ring are exemplary indicated by green arrows. The satellite structures are less pronounced as the lines that form these structures are short compared to c).*

In Chapter 5.3, the intensity of the ring between the $\overline{\Gamma M}$ and the $\overline{\Gamma K}$ direction was attributed to small hBN domains that fill the gaps where larger, aligned domains could not coalesce. Due to the inability of the atoms of these small domains to occupy their preferred adsorption sites (at least in parts of the hBN domain) the interaction between these domains and the Cu(111) surface is even weaker which leads to the azimuthal disorder of these small domains. The absence of intensity of the hBN ring in the indicated directions thus means, that these small domains are not present on the surface and the gaps between larger hBN domains are not filled. There are small patches of the bare Cu(111) surface left.

In the previous section (Chapter 6.2.1), the stronger interaction of PTCDA with the Cu(111) surface as opposed to the hBN/Cu(111) surface has been discussed in relation to the lateral structures of the PTCDA layers. It can also be derived from TPD experiments. While the thermal desorption of intact PTCDA molecules in the first layer was not observed on Cu(111) [206], on hBN/Cu(111) the first PTCDA layer desorbs completely at $550-570$ K (cf. Appendix A.2 and Ref. [169]). The complete thermal desorption of PTCDA from hBN/Cu(111) was confirmed in LEED, where the same LEED pattern of hBN/Cu(111) was observed before the deposition and after the desorption of PTCDA. For the deposition of PTCDA molecules on an incomplete layer of hBN on Cu(111), a LEED pattern as the one shown in Figure 6.2b of PTCDA/Cu(111) was observed. This is explained as follows. At a sample temperature of 300 K during PTCDA deposition, the molecules have enough energy for diffusion on the surface since ordered PTCDA structures form. Consequently, on the incomplete hBN layer, the molecules diffuse from hBN domains to bare Cu(111) areas where the interaction energy is stronger, and they form the α- and β-phases of PTCDA/Cu(111).

Now, a surface where the Cu is *almost* completely covered like the hBN/Cu(111) surface of Figure 6.3d is considered. The gaps between the large hBN domains are filled, but smaller bare Cu patches remain [173]. The PTCDA molecules will diffuse to these small bare patches and pin to the metal. The pinning then determines the azimuthal orientation of the PTCDA domains. This model explains why the angles ϕ of the β-phase of PTCDA/Cu(111) and of the azimuthally oriented PTCDA/hBN/Cu(111) agree so well ($10.3 \pm 1.0°$ and $9 \pm 1°$, respectively). However, the oriented domains of PTCDA that produce the LEED pattern shown in Figure 6.3b are in fact PTCDA domains on hBN/Cu(111) and not PTCDA domains that grow on uncovered Cu(111) areas. This conclusion can be derived from the difference in the *double triangle* patterns (shown in Figure 6.2) as discussed in Chapter 6.2.1. Thus, while the PTCDA domains pin to the Cu(111) surface at defects in the hBN layer, they continue to grow onto the hBN which determines their lateral structure. For a *completely closed* hBN layer, on the other hand, no pinning of the PTCDA domains can occur. In this case, the domains are azimuthally completely disordered (as seen in Figure 6.3a). Intrinsically, there is no preferred orientation of PTCDA domains on hBN/Cu(111), confirming the weak interfacial interactions.

## 6.3   PTCDA decoupled from the Cu(111) surface by a layer of hBN

The weak interfacial interactions between PTCDA and hBN/Cu(111) are further confirmed by the vertical structure of the molecule that was measured in XSW experiments and its electronic structure as determined from PES experiments. These investigations were published (see Appendix A.2) but are not the main focus of this thesis. Thus, only the results are summarized briefly here.

The vertical structure of PTCDA on hBN/Cu(111) is shown in Figure 6.4a. The vertical distance between PTCDA and hBN is at (3.37 ± 0.03) Å even larger than the distance at the hBN/Cu(111) interface of 3.24 Å. Both oxygen species are bend downwards toward the surface so that the molecule resembles the situation on Ag(100) and Ag(110) [47] in distortion motif. However, the largest downwards shift (of the carboxylic oxygen atoms) amounts to only 0.08 Å, which corresponds to only 2.4% of the vertical distance. Figure 6.4b puts these values in a broader context. Here, the adsorption heights for the chemically discernible species in the PTCDA molecule are given for several substrates as vdW corrected heights. The corrected heights show a clear trend as a function of both the work function of the substrates and the adsorption energy E_{ads} of the PTCDA molecule on these surfaces. The work function of hBN/Cu(111) was determined in a UPS experiment to be 0.5 eV smaller than that of Cu(111) and amounts to a value of 4.44 eV [4].

E_{ads} of PTCDA on hBN/Cu(111) was determined via TPD experiments (see Appendix A.2) as (2.10 ± 0.09) eV. This is even less than E_{ads} of the physisorbed molecule on the Au(111) surface of (2.5 ± 0.1) eV [215]. Figure 6.4b shows that the PTCDA/hBN/Cu(111) interface constitutes an extreme case regarding the vertical distance of the molecule from the surface. The corrected heights of the carbon atoms in the perylene backbone and both oxygen species equal the sum of the vdW radii of the involved atoms. Only the functional carbon atoms are positioned at a slightly smaller distance which can be attributed to the downwards pull of the oxygen atoms. Thus, while the molecule is not fully planar, the minute distortion of 0.08 Å can be explained by attractive local vdW interactions and/or electrostatic interactions between the partially negatively charged oxygen atoms with mirror charges in the Cu substrate. The latter would indicate a transparency of the hBN layer for such interactions. In light of the equivalence of the vertical distances and the exact sum of the vdW radii, this seems rather unlikely. Furthermore, XSW experiments showed that the adsorption of PTCDA molecules on hBN/Cu(111) has no influence on the vertical height of the hBN layer itself, again indicating weak interactions.

PES experiments show a stronger resemblance between PTCDA in the PTCDA bulk and PTCDA on hBN/Cu(111) compared to PTCDA on metal surfaces. The differential shift of the electronic states in the C1s XPS spectrum of the first layer of PTCDA on hBN/Cu(111) is the same (within the error) as that of the PTCDA multilayer on Ag(100) [57] while the PTCDA monolayers on either Ag(100) [47] or Cu(100) [102] display a significantly different shift of the electronic states (for

---

[4]The reduction of the work function agrees qualitatively with the findings by Joshi et al. [174], however they find work functions of 3.8 eV in the moirons and 4.1 eV in wire regions. This discrepancy may be related to the same effect of small difference in sample preparation that causes the different finding in XSW experiments (see Chapter 5.2) or to the different methods used to measure the work functions (STM vs. UPS). The work function of the bare Cu(111) surface of 4.94 eV is taken from Ref. [174].
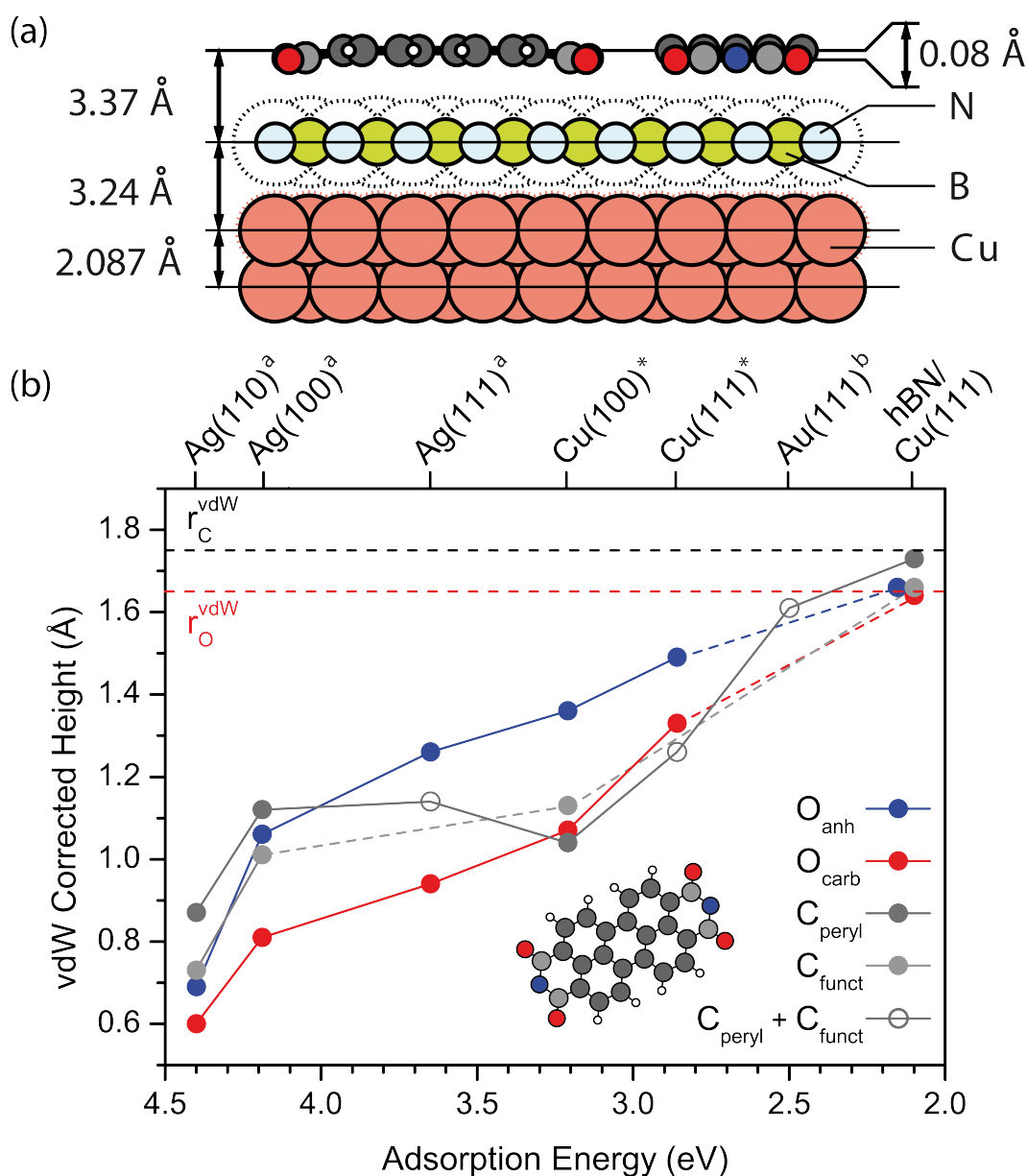
Figure 6.4: *a) Side view model of PTCDA/hBN/Cu(111) along the short and long molecular axes. The vertical distances between the layers are given. The vertical distortion of the PTCDA molecule is enlarged by a factor of 4 for better visibility. The functional groups show a minute downward bend toward the surface relative to the perylene backbone. The vdW radii of the N and B atoms are indicated, the covalent radii of PTCDA are drawn at 75% for clarity. b) Adsorption heights of the chemically discernible species in the PTCDA molecules on different substrates, determined in XSW [45, 47, 56, 100, 102]. The adsorption heights are corrected (i.e. reduced) by the vdW radii of the respective substrate atoms (for hBN, the radius of boron is used, which is larger and positioned higher than nitrogen), and they are shown as a function of the adsorption energy E_{ads} of the PTCDA molecule on these surfaces. Data marked by "a" and "b" are taken from Refs. [47] and [215], respectively. Data marked by * was not available and horizontal data point positions are qualitatively placed according to the work function trend of the substrates [102]. For substrates, where the functional and perylene carbon atoms were not analyzed individually, averaged values are given as hollow data points. Guide lines for the eyes are included, dashed lines indicate incomplete data sets. Dashed horizontal lines indicate the vdW radii of sp^2 hybridized carbon and oxygen atoms. All radii used in this thesis and the results of the XSW experiments and the resulting values for the vertical distances are summarized in Tables G.3 and G.2 in Appendix G.*

details, see Figure 2 in Appendix A.2). This indicates that the electronic structure of PTCDA is unaltered on hBN/Cu(111) due to the lack of strong interactions with the substrate. Additionally, the UP spectra of both the monolayer and the bilayer of PTCDA on hBN/Cu(111) show no differential shifts of the orbital energies compared to the gas phase spectrum [216]. No indications for a CT from metal to molecule as it is the case for PTCDA/Cu(111) [46] were found. Finally, no reduction of the work function of hBN/Cu(111) upon PTCDA adsorption could be detected. Commonly, a reduction of the work function upon PTCDA adsorption on metals is found as a result of the push-back effect [46]. Here, the metallic states that spill into the vacuum are pushed back because of the interaction with the molecule. The absence of a change in work function for PTCDA/hBN/Cu(111) points to the low probability density of Cu states above the hBN layer, as this layer already pushes the states back and separates the metallic and molecular states. In summary, these findings show that no static CT between the molecule and the metal substrate occurs.

6.4 Conclusion

In a series of complementary experiments, the structural and electronic decoupling of PTCDA from the Cu(111) surface by a singe layer of hBN was decidedly shown. The arguments for this decoupling are the following:

   I. The lateral structure of the PTCDA domains is incommensurate and strongly resembles the structures of the bulk modifications. No sign of influence of the hBN/Cu(111) substrate can be found. This includes the azimuthal orientation of PTCDA domains. On a defect free hBN layer, the orientations of the domains are homogeneously distributed.

  II. No trapping of molecules in the moirons of the hBN/Cu(111) substrate was observed.

 III. The molecules from the first layer of PTCDA desorb completely and intact. The adsorption energy of the first layer amounts to only (2.10 ± 0.09) eV.

 IV. The vertical distance of the PTCDA molecule from the hBN layer amounts to (3.37 ± 0.03) Å, which constitutes an extreme case. The vdW corrected heights of the atoms in the PTCDA molecule even exceed that of the physisorbed PTCDA/Au(111) which is in accordance with the low adsorption energy.

  V. The molecule remains essentially flat on the surface. The minute downwards shift of the oxygen atoms of 0.08 Å is a result of attractive local vdW interactions as the adsorption heights of both oxygen and carbon amount to the sum of the vdW radii of the involved atoms.

 VI. No indications for a static CT between PTCDA and the substrate was found in UPS.

VII. In XPS, a resemblance between PTCDA/hBN/Cu(111) and PTCDA multilayers was found, whereas the spectra of PTCDA monolayers on metals differ significantly.

VIII. Upon PTCDA adsorption, no change in work function of the hBN/Cu(111) substrate as a result of the push-back effect was observed which points to the absence of spilled-out Cu states at the PTCDA/hBN interface.

While the evidence for the decoupling of the PTCDA molecule from the metal is exhaustive, the completeness of the hBN layer is essential. If defects are present in the hBN layer, PTCDA molecules are able to pin to the bare Cu(111) surface at those defects. This leads to a preferential orientation of the PTCDA domains. Presumably, the direct contact between molecule and metal also has an impact on the electronic structure of the molecule.

7 The optical properties of PTCDA on hBN/Cu(111)

The optical properties of PTCDA on hBN/Cu(111) were investigated using FL and Raman spectroscopy. The goal of these investigations was to find out whether a single layer of hBN suffices to decouple the molecules from the metal substrate so that FL from the molecules can be observed and to determine the changes of the optical properties of PTCDA compared to other substrates. For this, the optical properties of PTCDA/Cu(111) have been investigated, too, since a comparison between the two allows to draw direct conclusions about the ability of hBN to decouple molecules from the metal substrate. Most results have been published in Appendix A.3. They will be summarized here briefly and supplemented with a more in-depth comparison with published literature regarding both, the FL and the Raman modes.

7.1 Literature Overview

Schneider et al. investigated the photoluminescence of the α- and β-phase of thick PTCDA layers (30 monolayers) on Ag(111) [44]. For both phases, the pure electronic 0-0 transition (in accordance with the terminology by Leonhard et al. [217] called "Y") was found at 16,000 cm^{-1}. Several vibronic modes summarized into one broad effective mode are located at 800 - 1,200 cm^{-1} below the Y mode. A third, low energy emission occurs between 13,500 and 14,000 cm^{-1} and is associated with excimer emission and thus termed "E" [44].

Stallberg et al. [58] found qualitatively equivalent results for 18 ML PTCDA on Ag(111) with Y located at 15,040 cm^{-1} and E at 13,746 cm^{-1}. The same positions of Y and E were found for a PTCDA multilayer (9 ML) on Au(111) [58]. At coverages smaller than 9 ML on Ag(111) and 4 ML on Au(111) neither Y nor E were observed. However, in the second PTCDA layer on either metal surface a mode denoted as "M" at 16,980 cm^{-1} and 17,304 cm^{-1}, respectively, was observed which persisted also at higher coverages, then coexisting with the Y and E modes. M was assigned to luminescence from PTCDA molecules without interlayer coupling (called "monomers" by Stallberg et al. [58]) which refers to PTCDA molecules in layers that are neighboring other PTCDA molecules on one side and the vacuum on the other side. On Ag(111), 1,373 cm^{-1} below M an additional mode ("M$_{\text{vib}}$") appears and was assigned to the vibrational progression of M. The first PTCDA layer on either metal shows no luminescence because it is quenched due to the direct contact of the molecules to the metal [23, 44, 58].

On Au(111), Stallberg et al. were not able to observe M$_{\text{vib}}$ as it was superposed by Raman bands that were present even in the submonolayer regime. This was attributed to surface enhancement

of the Raman modes on Au(111) [58]. The Raman shifts of PTCDA on a metal surface was the focus of the work by Schneider and Wagner [218, 219]. There, the Raman modes of PTCDA/Ag(111) were investigated regarding their dependence on film thickness and preparation temperature. Thick films of PTCDA have been extensively studied in regard to their Raman shifts [220–222]. These results for high coverages, as well as for PTCDA single crystals [223] will be used as a reference for the results presented in the present work.

Vibronic modes that can be probed in Raman spectroscopy are also accessible via FL spectroscopy. While they could not be resolved in FL spectra of PTCDA on metal substrates [58], they have been observed for PTCDA adsorbed on dielectric films, namely on thin films of KCl and NaCl (measured at 20 K). The 0-0 transition of PTCDA monomers on KCl was found at 20,000 cm^{-1} [53, 224] and on NaCl at 19,680 cm^{-1} [52]. Thus, the adsorption on these substrates leads to a red-shift of the spectrum in regard to the PTCDA molecule in a He droplet (0-0 transition at 20,988 cm^{-1} [225]). Both spectra show similar and well resolved vibronic modes which *(i)* points to identical excitation and relaxation channels and *(ii)* can be attributed to similar bonding situations of the molecules to the respective surfaces [165]. DFT calculations showed that the spectral red-shift of the adsorbed molecules partially (30−40%) stems from the arch-shaped distortion of the molecule discussed in Chapter 2.2 [113].

For complete monolayers on KCl and NaCl, the spectra are shifted even further to lower energies (to 19,600 cm^{-1} on KCl [53] and to 19,380 cm^{-1} and 19,120 cm^{-1} on NaCl in the Q-phase and HB*-phase, respectively [52]). The red-shift from monomer to monolayer can be attributed to exciton band formation and to non-resonant intermolecular interactions [53]. Additionally, the signals become broader so that the vibronic modes are less well resolved which is a result of finite size effects of the molecular domains [53]. The resolution of the vibronic modes on KCl, however, is much better than on NaCl which may be attributed to a higher order of the molecules, due to specific adsorption sites [224].

The FL of PTCDA on thin films of KCl and NaCl will be compared with the FL of PTCDA on a single layer of hBN. Furthermore, the efficiency of hBN for decoupling the molecule from the metal surface will be judged compared to these alkali halides.

7.2   Optical spectra of PTCDA on hBN/Cu(111) and Cu(111)

The optical spectra of PTCDA/hBN/Cu(111) and PTCDA/Cu(111) are qualitatively very similar (see Figure 2 in Appendix A.3). They can be divided into three regions:

1) sharp Raman lines are observed between 18,600 and 21,000 cm^{-1} (see section 7.3),

2) FL from ordered PTCDA is observed between 18,000 and 18,600 cm^{-1} (see section 7.4), and

3) defect luminescence of the Cu substrate as one very broad peak at 16,000−18,000 cm^{-1}.

The first reason why the broad peak at 16,000−18,000 cm^{-1} was assigned to surface defects is the strong dependency of its intensity on the sample position (see Figure 7.1b). This can be explained

by a difference in the local defect density on the Cu(111) surface. Furthermore, the energy of this luminescence agrees with the photoluminescence that has been measured for Cu nanoparticles at $15{,}380-17{,}240$ cm^{-1} [226]. Due to this similarity, it is reasonable to assume that the surface defects that cause the luminescence are protrusions of the Cu surface, which are comparable to nanoparticles adsorbed on the surface. This interpretation of the defect luminescence compliments the observations made in regard to the Raman lines of PTCDA which will be presented below.
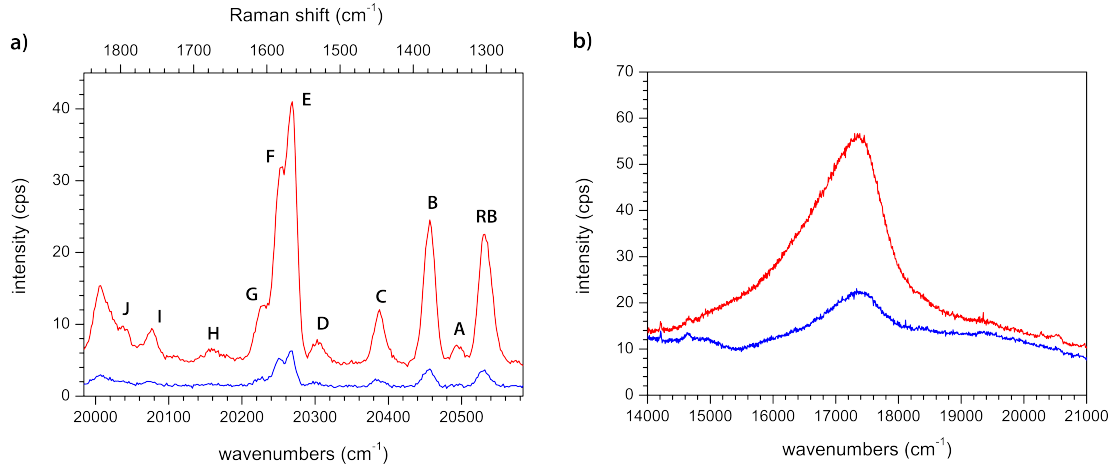
7.3 Raman Modes of PTCDA on hBN/Cu(111) and Cu(111)

Raman modes of PTCDA were observed on both, hBN/Cu(111) and Cu(111), at energies between 18,600 and 21,000 cm^{-1}. The positions of the Raman modes of PTCDA/hBN/Cu(111) are shown in Figure 7.1a and Figure 3 of Appendix A.3 where the positions of the Raman lines of PTCDA/Cu(111) are shown, too. Their exact positions are summarized in Table 7.1. The Raman modes have typically a FWHM of 17 cm^{-1} which is larger than the instrumental FWHM of the spectrometer. The ability to observe the Raman modes even at small coverages is explained by the SERS effect (cf. Chapter 3.2.2).

7.3.1 Raman Enhancement on hBN/Cu(111) and Cu(111)

The SERS effect at Cu protrusions

As explained in Chapter 3.2.2, the SERS effect on metal surfaces is the result of localized surface plasmon polaritons (SPPs) that are trapped in crevices between surface defects (protrusions) [147]. The local E field, which is caused by the localized SPPs, causes an enhancement of the Raman signal by a factor of 10^5 - 10^6. This effect is strong enough to even have an effect on molecules on an hBN layer. Thus, the Raman signal originates only from molecules that are localized in the vicinity of protrusions ("hot-spots") on the Cu(111) surface. This means that at sample positions with a high density of defects, a higher intensity of the Raman lines can be expected. Figure 7.1 shows that this is indeed the case. Figure 7.1a shows a portion of the Raman region of the spectrum ($19{,}985-20{,}585$ cm^{-1}) and Figure 7.1b shows the defect luminescence ($14{,}000-21{,}000$ cm^{-1}), both signals are shown for two different sample positions. At the position where the defect luminescence is high (i.e. where the density of defects is high), the Raman signal is enhanced by a factor of ~7.

A further indication for the presence of these Raman hot-spots on the surfaces is the apparent necessity for the ability of the molecules to migrate to these. In the first PTCDA layer on Cu(111), Raman modes were never observed after deposition at a temperature of 20 K. After deposition at 300 K, they could be observed, and on hBN/Cu(111), they were found even at low temperatures. At present, this is interpreted as follows: A certain mobility of the molecule on the surface is required to allow the molecules to move to the Raman hot-spots and, consequently, for Raman lines to be observed. This mobility is obtained on the Cu(111) surface by elevated temperatures and on the hBN/Cu(111) surface by the weak physisorptive bond between PTCDA and hBN.

Figure 7.1: *a) Raman modes of 0.80 ML PTCDA on hBN/Cu(111), recorded at two different sample positions. The Raman shifts of the modes are listed in Table 7.1. b) Defect luminescence of the clean hBN/Cu(111) surface before deposition of 0.80 ML PTCDA, recorded at two different sample positions. Red and blue spectra were measured at the sample positions, respectively. Spectra were measured at 20 K using graings with a) 1200 and b) 300 grooves per mm.*

Surface Plasmon Polaritons on flat metal surfaces

Stallberg et al. [58] have interpreted their observation of Raman lines of PTCDA/Au(111) differently. They considered the energy of the SPPs on a flat metal surface. They argued that the SPP on the Au(111) surface with an energy of $E_{\mathrm{SPP}}^{\mathrm{Au}} = 2.5$ eV could resonantly interact with the incident light, which had an energy of 2.37 eV while such a resonance was not possible for the Ag(111) surface with $E_{\mathrm{SPP}}^{\mathrm{Ag}} = 3.7$ eV and an energy of 2.43 eV of the incident light.

For comparison, the SPP of Cu(111) can be derived from the surface loss function [227] which is calculated as

$$-\mathrm{Im}(\epsilon^{-1}) = \frac{\epsilon_2}{\epsilon_1^2 + \epsilon_2^2} \, , \tag{7.1}$$

using the dielectric functions ϵ given in Ref. [228]. This results in $E_{\mathrm{SPP}}^{\mathrm{Cu}} = 2.3$ eV. The difference to the energy of the incident light of 2.698 eV is intermediate between the energy differences of incident light and SPP reported for the Ag(111) and Au(111) surfaces by Stallberg et al. [58]. However, the enhancement of the local E field by SPPs *requires* surface defects that break the translational symmetry on the surface [229]. Hence, the SERS effect is usually observed on *rough* surfaces [145]. Thus, regardless of the resonance between SPPs and incident light, an interpretation of the Raman enhancement without taking surface defects into account appears to be incomplete.

hBN as a SERS substrate

Not only noble metal surfaces exhibit a SERS effect. hBN itself has gained some interest as a SERS substrate [230]. Ling et al. [231] have shown that a chemical mechanism of the SERS effect may come into play for molecules on an hBN layer. They argued that the polar character of the B−N bond acts as a dipole parallel to the surface. In molecules that are adsorbed flat on the hBN a

dipole will thus be induced which effects the polarizability of the molecule similar to an interfacial CT.

However, to attribute the observation of the PTCDA Raman lines here to this effect would be inaccurate. First of all, the interactions between PTCDA and hBN have been shown to be very weak (see Chapter 6). Thus, an induced dipole in the PTCDA molecule that is strong enough to have such a significant impact on its polarizability seems unlikely. More importantly, the SERS effect has also been observed on the bare Cu(111) surface. Here, the SERS effect is obviously caused by the metal substrate. To dismiss this contribution of the *electromagnetic* mechanism for the much weaker *chemical* mechanism for hBN/Cu(111) is unreasonable. However, there may be *some* contribution from the hBN layer to the SERS effect. This cannot be further discerned here.

7.3.2 PTCDA Raman modes - A comparison to literature

Now, the positions of the Raman lines of PTCDA on hBN/Cu(111) and Cu(111) will be discussed in detail and compared to PTCDA in other systems (see Table 7.1). Here, only the PTCDA layers prepared at 300 K will be considered which constitute "the final state" of these systems. For temperature induced changes of the Raman lines of PTCDA/hBN/Cu(111) and PTCDA/Cu(111), see section 2.2.2 of Appendix A.3.

For an easier overview of the shifts of the Raman lines, their positions are visualized in Figure 7.2. First, only the modes A−J will be in focus (for the labeling, see Figure 7.1a). There is a systematic shift to smaller energies by ~7 cm^{-1} for PTCDA/hBN/Cu(111) compared to PTCDA/Cu(111). Meanwhile, the Raman modes of PTCDA/Cu(111) agree well with those of PTCDA/Ag(111) [219] within 0.3%. This difference between the substrate hBN/Cu(111) versus the metallic substrates Cu(111) and Ag(111) may be explained by the different bond between them and the PTCDA molecules (physisorptive vs. chemisorptive, see Chapters 2.2 and 6.3). Possibly, the CT from metal to molecule on Cu(111) and Ag(111) [46] makes the intermolecular bonds harder which results in an increase of the energies of the vibrational modes.

A validation of this assumption can be gained from a comparison with Raman modes measured for thin films [220, 221] and single crystals of PTCDA [223]. The structural and electronic investigations (see Chapter 6) have shown that PTCDA on hBN/Cu(111) rather behaves like PTCDA in multilayers or in the bulk. Thus, the same behavior can be expected for the vibrational modes. However, an unambiguous result cannot be received here. For energies <1,570 cm^{-1}, the Raman shifts of PTCDA/hBN/Cu(111) are in good agreement with the shifts for the single crystal or the thin films, comparable to the similarity between Cu(111) and Ag(111). At Raman shifts >1,570 cm^{-1}, however, the modes of PTCDA/hBN/Cu(111) are positioned consistently at smaller energies while the modes of PTCDA/Cu(111) are now virtually identical with the modes of the single crystal.

Noteworthy here are the Raman modes of the single crystal at 1,375.4 and 1,383.6 cm^{-1}. These are separate Raman modes of two internal molecular vibrations and are not the result of a Davydov splitting [223]. The high energy mode has been observed in thin films [220, 221], on Ag(111) (at 1,385 cm^{-1}) [219], and on the Cu(111) surface (at 1,386.0 cm^{-1}). The lower energy mode, on
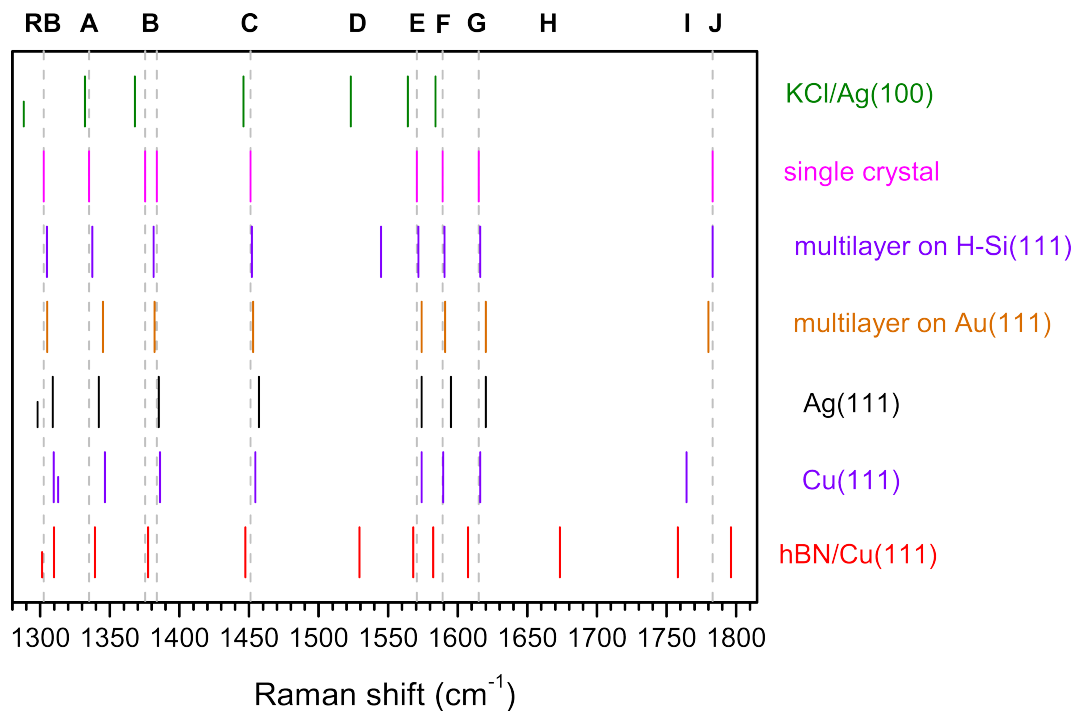
Figure 7.2: *Energetic positions of Raman modes of PTCDA on hBN/Cu(111), on Cu(111), on Ag(111) [219], in thin films on Au(111) [220], in thin films on H-passivated Si(111) [221], in single crystals [223], and on KCl/Ag(100) [114]. The data for hBN/Cu(111), Cu(111), and KCl/Ag(100) were measured in FL experiments. For values, see Table 7.1. For easier comparison, the positions of the Raman modes in single crystals are extended over the entire image in dashed gray lines. For the RB modes (~1,300 cm^{-1}) on hBN/Cu(111), Cu(111), and Ag(111), the Raman shifts of multilayers are given as longer lines, those of the monolayers are represented by shorter lines.*

the other hand, matches the Raman mode B observed for PTCDA/hBN/Cu(111) at 1,377.5 cm^{-1}. These energetic positions of Raman modes in the different systems relative to each other are not understood, yet.

To find further indications that PTCDA/hBN/Cu(111) behaves like PTCDA multilayers, the ring breathing (RB) mode of the central carbon ring of the PTCDA molecule will be discussed. This is the only mode that shows a significant energetic shift between mono- and multilayers and the largest shift between monolayers on hBN/Cu(111), Cu(111), and Ag(111) [219]. The substrate dependent shift is attributed to a change in bonding motif. The energy of the RB mode decreases when the shape of the molecule changes from the boat-shape on Cu(111) [56], over the flat molecule on hBN/Cu(111) and the saddle shape on Ag(111) [100], to the arch-like shape on KCl [232].

The RB modes of the multilayers are expected to have the same energy as a result of the identical interactions between the multilayers. Indeed, they have all been observed at 1,309 cm^{-1}. However, the RB modes of thin films [220, 221] and single crystals [223] are found at lower energies of 1,302−1,305 cm^{-1}. This discrepancy is not understood. For the two metallic substrates it might be feasible to assume that some influence of the substrates remains even in higher layers. But for hBN/Cu(111), this can be excluded as already the first layer exhibits characteristics

Table 7.1: *Raman shifts (in cm^{-1}) of PTCDA on hBN/Cu(111), Cu(111), and Ag(111) [219], of thin films of PTCDA on Au(111) [220] and H-passivated Si(111) [221], of PTCDA single crystals [223], and of PTCDA on KCl/Ag(100) [114]. Data marked with [1] was measured in FL experiments. The sample temperatures during preparation of the PTCDA films T_S, the sample temperatures during measurement T_m, the wavelength of the exiting laser λ_{ex}, and the PTCDA coverages θ are given. PTCDA/hBN/Cu(111) was deposited at 20 K and subsequently annealed at $T_S = 300$ K. The positions of the Raman modes A−J are independent of the coverage on hBN/Cu(111) and are given as averages over 8 data sets (error margins are the standard deviation). The position of the ring breathing (RB) mode is given for mono- and multilayers if possible (refers to the averaged value of 5.10 and 8.20 ML on hBN/Cu(111), to 2.55 ML on Cu(111), and to 60 ML on Ag(111)). For the single crystal, the upper Davydov components are listed. The split between the Davydov components is < 2.5 cm^{-1} [223]. The absolute errors of the Raman shifts in the literature are not known.*

Mode	hBN/Cu(111)[1]	Cu(111)[1]	Ag(111) [219]	Au(111) [220]	H-Si(111) [221]	single crystal [223]	KCl[1] [114]
T_S	300 K	300 K	400 K	300 K	300 K	n.a.	6−20 K
T_m	20 K	20 K	20 K	300 K	300 K	300 K	6−20 K
λ_{ex}	458 nm	458 nm	514 nm	488 nm	488 nm	488 nm	458 nm
θ	0.05−0.80 ML	1.00 ML	1 ML	30 nm	>100 nm	n.a.	0.02−1.00% ML
RB (mono)	1301.2 ± 1.7	1312.9	1298	n.a.	n.a.	n.a.	1288
RB (multi)	1309.8 ± 3.1	1309.5	1309	1305	1304.8	1302.3	n.a.
A	1339.2 ± 1.2	1346.5	1342	1345	1337.4	1335.0	1332
B	1377.5 ± 1.5	1386.0	1385	1382	1381.3	1375.4/1383.6	1368
C	1447.4 ± 1.7	1454.6	1457	1453	1452.1	1451.0	1446
D	1529.4 ± 0.7	−	−	−	1544.9	−	1523
E	1567.9 ± 2.5	1574.0	1574	1574	1571.6	1570.6	1564
F	1582.3 ± 2.0	1589.6	1595	1591	1590.4	1589.1	1584
G	1607.3 ± 2.0	1616.2	1620	1620	1616.2	1615.0	−
H	1673.3 ± 2.4	−	−	−	−	−	−
I	1758.0 ± 1.7	1764.3	−	−	−	−	−
J	1796.2 ± 2.2	−	−	1780	1773.7	1783.0	−

of the multilayer as explained in Chapter 6. Remarkably, it is the RB mode of the PTCDA *mono-layer* on hBN/Cu(111) that is identical to the RB mode of the single crystal. This actually matches the expectations that resulted from the investigation of the structural and electronic properties of PTCDA/hBN/Cu(111) that showed so many similarities to the bulk. A possible influence may be a difference in stacking motif in the multilayers and in the thin films (α- and β-modifications).

Figure 7.2 illustrates that most of the Raman modes measured for thin films [220, 221] and on the metallic substrates [219] are shifted to higher energies compared to single crystals [223] while the same Raman modes measured on hBN/Cu(111) and KCl/Ag(100) [114] are shifted to lower energies. This observation cannot be explained, yet. However, it may point to an influence of the polar bonds within the substrate. KCl is an ionic material, the B$-$N bonds are dipols because of the difference in electronegativities of boron and nitrogen. An interaction of the PTCDA molecule with theses dipols in the surface may cause a slight change in polarizability of the molecules which leads to the observed shifts.

7.3.3   The Raman mode of hBN

Along with the many Raman lines of PTCDA, the appearance of the characteristic Raman line of hBN at a shift of 1,370 cm^{-1} was expected. This line has been observed for exfoliated hBN on SiO$_2$/Si [233], for hBN grown from ammonia borane on Cu foils and transferred to SiC [187], and for hBN grown by molecular beam epitaxy on Ni foils [74] and Pt foils [73]. However, this Raman line was systematically *not* observed here. The reason is unclear. It may however be connected to the preparation recipe of depositing borazine molecules under vacuum on a hot metal surface which was not done in the studies listed above.

7.4   Fluorescence of PTCDA on hBN/Cu(111) and Cu(111)

In both investigated systems, PTCDA/hBN/Cu(111) and PTCDA/Cu(111), different FL peaks were observed. Their origins will be briefly summarized here and are illustrated in Figure 7.3a and b. For details on the reasoning for these assignments, see Appendix A.3.

On Cu(111), FL of the first monolayer is never observed. As expected according to the findings for other metal substrates like Ag(111) [23, 58] and Au(111) [58], the FL from the first layer of PTCDA on Cu(111) is completely quenched. This quenching is understood to be the result of the chemisorptive bond between PTCDA and the Cu(111) surface [46] (see Chapter 2.2). However, this interfacial PTCDA layer (gray in Figure 7.3b) decouples the PTCDA molecules in the higher layers from the metal substrate, just as the hBN layer (blue in Figure 7.3a) does. The PTCDA that adsorbs on these interfacial layers is the first layer in either system that is not in direct contact with the metal substrate. It acts as a separating layer (pink) between the interfacial layer and the higher, physisorbed PTCDA layers (red). In both systems, hBN/Cu(111) and Cu(111), a peak FL$_A$ is observed from the separating layer and a peak FL$_C$ from the physisorbed layers (FL spectra shown in Figure 7.3c). Only on hBN/Cu(111), a third peak FL$_B$ was observed from the separating

layer. The occurrence of these peaks depends not only on the PTCDA coverage but also on the preparation temperature. Table 7.2 gives an overview of the peak positions and the conditions under which they were observed.
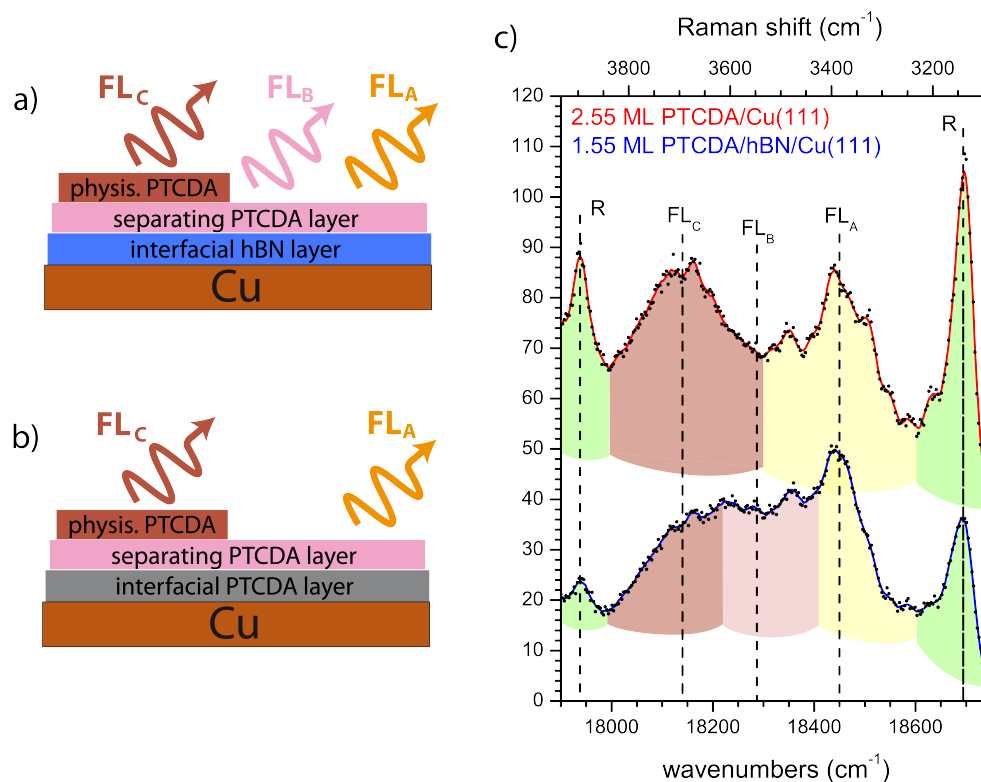
Figure 7.3: *Schematic representation of a) 2 ML PTCDA on hBN/Cu(111) and b) 3 ML PTCDA on Cu(111). FL signals that were observed from the respective layers are included as arrows. The interfacial hBN (blue) and PTCDA (gray) layers decouple the fluorescing PTCDA layers from the Cu(111) surface. The FL from the first PTCDA layer on Cu(111) (gray) is completely quenched due to the chemisorptive bond to the metal surface. FL_A and FL_C originate from the separating (pink) and physisorbed (red) PTCDA layers, respectively, on either substrate. FL_B stems from the separating PTCDA layer on hBN/Cu(111). c) Fluorescence spectra of 2.55 ML PTCDA/Cu(111) (red spectrum, prepared by deposition at 300 K) and 1.55 ML PTCDA/hBN/Cu(111) (blue spectrum, prepared by deposition at 20 K and subsequent annealing at 300 K). The spectra are smoothed (lines) and vertically shifted, original data are shown as dots. Spectra of the clean substrates were subtracted as background. All spectra were measured at 20 K using a grating of the spectrometer with 600 grooves per millimeter. Raman lines are labeled "R" and highlighted in green. FL peaks FL_A, FL_B, and FL_C are highlighted in yellow, pink, and red, respectively. FL_B was observed only on hBN/Cu(111), not on Cu(111).*

The interpretation for the presence of the FL peaks FL_A, FL_B, and FL_C in the spectra of PTCDA on hBN/Cu(111) and Cu(111) is as follows.

FL_A is observed on both, Cu(111) and hBN/Cu(111), from the second and first layer, respectively (the separating layers). It was deduced that it stems from molecules that are located at surface defects. These defects are different from the hot-spots that cause the SERS effect that were described in section 7.3. It is assumed that the defects here, that are present on Cu(111) *and* hBN/Cu(111), are atoms of another species, like carbon, that segregated from the substrate, because segregation has been observed for the Cu(111) crystal used in these

Table 7.2: *Energetic positions of the FL peaks of PTCDA on hBN/Cu(111) and on Cu(111), the coverages θ for which the respective FL peaks were observed, and the preparation temperatures needed to observe these peaks. Upper limits for the life times of the excited states τ_S derived from the FWHM of the peaks are included.*

	θ	FL_A	FL_B	FL_C
		~18,450 cm^{-1}	~18,300 cm^{-1}	~18,150 cm^{-1}
τ_S		$(4.4 \pm 0.3) \cdot 10^{-14}$ s	$(1.7 \pm 0.1) \cdot 10^{-14}$ s	$(1.6 \pm 0.1) \cdot 10^{-14}$ s
hBN/Cu(111)	≤ 1 ML	≥ 200 K	≥ 280 K	—
	>1 ML	≥ 20 K	≥ 200 K	≥ 200 K
Cu(111)	≤ 1 ML	—	—	—
	$1-2$ ML	300 K	—	—
	>2 ML	300 K	—	300 K

experiments (cf. Appendix D). These segregations locally prevented the growth of hBN so that the same kind of defects can be present on Cu(111) and hBN/Cu(111). Peak FL_A shows a temperature dependent increase of intensity and a saturation which agrees with the diffusion of molecules to the defects and the saturation of the adsorption sites at these defects.

FL_B is FL from ordered PTCDA domains on hBN/Cu(111). It can be observed for mono- and multilayers and is absent for PTCDA/Cu(111). FL_B can only be observed at elevated temperatures and after the saturation of FL_A which implies that this FL component is related to the formation of ordered domains by diffusion of molecules after the adsorption sites at defects responsible for FL_A are saturated.

FL_C is present on Cu(111) *and* on hBN/Cu(111). On the former, it appears in the third layer and higher, for the latter in the second layer and higher. Thus, FL_C is assigned to FL from ordered PTCDA in higher, physisorbed layers. It is different from the well-known FL from PTCDA multilayers [44] which was observed at 15,950 cm^{-1} on hBN/Cu(111) and at 16,100 cm^{-1} on Cu(111) (Y line).

While the observation of FL of PTCDA on hBN/Cu(111) at coverages as small as 0.1 ML shows that a single layer of hBN is able to suppress the CT between PTCDA and Cu(111), the intensities of the FL peaks remain very low. For a full monolayer, the intensities are smaller by a factor of ~10^4 compared to PTCDA on KCl/Ag(100) [164]. Furthermore, the FL peaks are very broad. This is taken as an indication of a very small life time of the excited state τ_S. Since LEED experiments showed high order in the PTCDA layers, the width of the peaks is assumed to be life time limited [135]. The life times τ_S as obtained per Eq. (3.9) are included in Table 7.2. From these, the quantum yield η can be calculated according to Eq. (3.8) using the life time of the FL of isolated PTCDA molecules of 5.5 ns [234] as the natural life time τ_r:

$$\eta = \frac{\tau_S}{\tau_r} = \frac{1.7 \cdot 10^{-14}\ \text{s}}{5.5 \cdot 10^{-9}\ \text{s}} = 3.1 \cdot 10^{-6}\ . \tag{7.2}$$

This small value for the quantum yield shows that the FL must be strongly reduced, which was observed in the experiments. Since the FL is so small, the limiting factor of the life time of the excited state is supposed to be the CT process. Since the life times of the excited state found for PTCDA on hBN/Cu(111) of $1.7 - 4.4 \cdot 10^{-14}$ s are almost identical to the life time of an electron hole [21, 22] it is now clear why the CT was not observed in photoemission spectra (see Chapter 6.3 and Appendix A.2) although the FL experiments show that a CT *does* occur. For comparison, FL experiments of PTCDA/KCl yielded life times of the excited state of ~0.35 ns [164] which, according to Eq. (7.2), corresponds to a quantum yield of 0.06. This is larger by a factor of $2 \cdot 10^5$ compared to the quantum yield of PTCDA/hBN/Cu(111). This demonstrates how much more efficient the decoupling by a KCl film is compared to an hBN layer.

Due to the small η of PTCDA on hBN/Cu(111) another molecule was considered for a possibly larger η: DBP is a Lander-type molecule and thus intrinsically adsorbs with a larger vertical distance between substrate and perylene backbone of the molecule which can improve their decoupling. Indeed, the intensity of the 0-0 transition of DBP/hBN/Cu(111) was higher than that of PTCDA/hBN/Cu(111) by a factor of 4 and the vibronic peaks of DBP were resolved. Details about the molecule and FL spectra of DBP/hBN/Cu(111) are shown in Appendix C.

7.4.1 Fluorescence of PTCDA on different substrates

As introduced in section 7.1, the FL of PTCDA has been investigated on several different substrates in other studies before. For an easy comparison, the energies of the 0-0 transitions of PTCDA on these substrates are summarized in Figure 7.4. On the basis of these data, several different aspects about the systems in focus in the present work can be discussed:

1) the energetic shift between isolated molecules at surface defects and molecules in ordered domains on hBN/Cu(111) which is observed in the spectrum as FL_A and FL_B,

2) the influence of other hBN substrates on the 0-0 transition of PTCDA,

3) the change of the FL of PTCDA on different noble metal substrates,

4) the difference between hBN, noble metals, and alkali halide films as substrates for PTCDA in FL experiments.

The FL spectra of PTCDA molecules in the different circumstances listed above can be influenced by three factors: lateral interactions between molecules in domains, the distortion motif of the molecule on the surface, and the interaction strength between molecules and the underlying surface.

On KCl/Ag(100) [53] and NaCl/Ag(100) [52], isolated molecules were prepared by depositing <1% of a monolayer at low temperatures. On these substrates, the 0-0 transitions were red-shifted
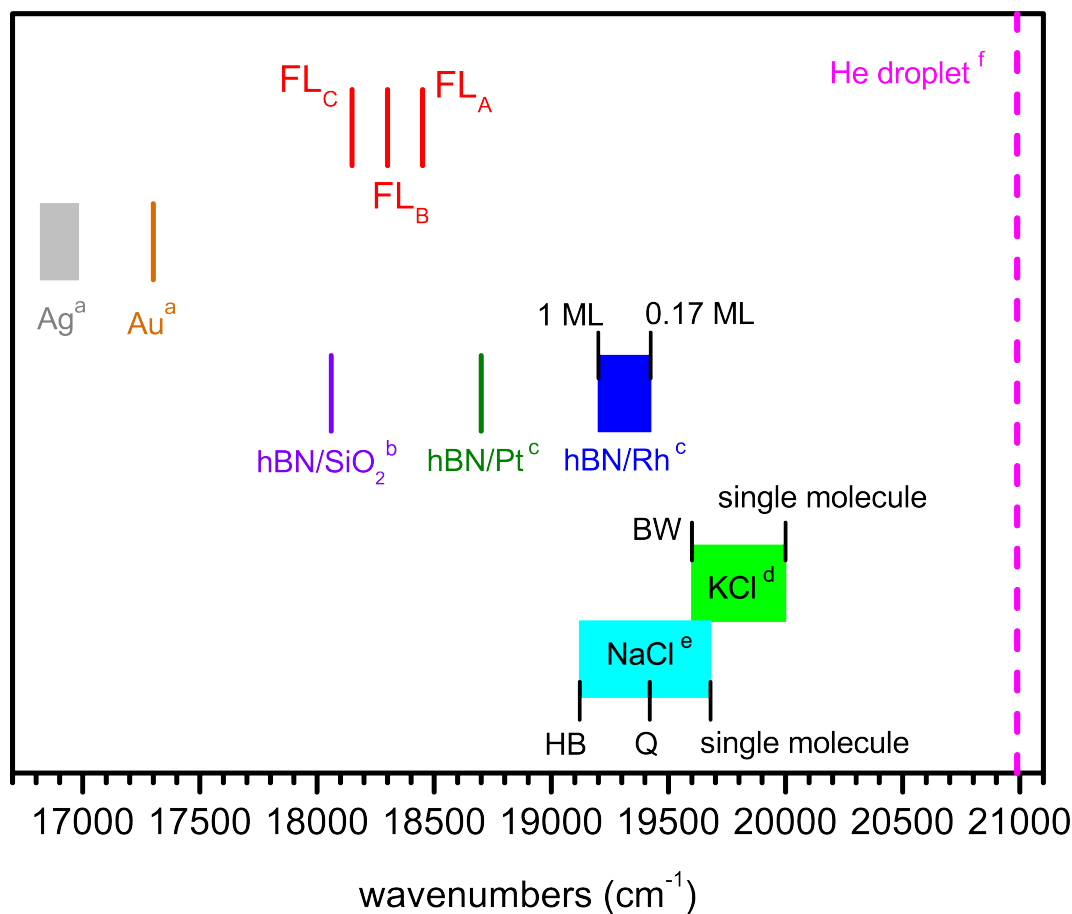
Figure 7.4: *Overview on the energies of the 0-0 transitions of PTCDA on different substrates as found in the present work and as reported in literature. Data taken from Refs. [58] (a), [126] (b), [125] (c), [53] (d), [52] (e), [225] (f). For Ag(111), hBN/Rh(111), NaCl, and KCl different coverages of PTCDA were investigated that resulted in a shift of the 0-0 transition. These are indicated by blocks.*

by 400 cm^{-1} compared to the ordered brickwall structure on KCl and by 300 cm^{-1} and 560 cm^{-1} compared to the ordered Q- and HB-phases on NaCl (see light green and light blue bars in Figure 7.4). DFT calculations showed that $60-70\%$ of the red-shift is caused by the change in lateral interactions between isolated molecules and domains [113]. The second contribution is a change in distortion motive of the PTCDA molecules when they change from isolated to aggregated. On KCl and NaCl, isolated molecules are strongly bent in an arch-shape [114]. When the molecules can interact laterally by forming a domain, an uplifting of the anhydride groups can be expected as it is also the case when an isolated molecule interacts with a step edge [114].

Isolated molecules and ordered layers

On hBN/Cu(111), isolated PTCDA molecules are those adsorbed at defects and whose FL can be observed already at a coverage of only 0.01 ML and a preparation temperature of 200 K. Their FL peak FL_A is red-shifted by 150 cm^{-1} compared to FL_B from ordered domains. The PTCDA molecule on hBN/Cu(111) is hardly distorted at all and the lateral interactions in the monolayer

are strong enough to determine the structure. Thus, a red-shift due to lateral interactions rather then a distortion of the molecule seems reasonable.

Forker et al. [125] have investigated the absorbance of PTCDA on hBN/Rh(111). At low coverages, the molecules are trapped in the pores of the buckled hBN layer while at higher coverages, the molecules form an ordered herringbone structure. Between these coverages, the 0-0 transition undergoes a red-shift by 223 cm^{-1} which is indicated in Figure 7.4. These trapped molecules can be considered as isolated molecules. The red-shifts of PTCDA of hBN/Cu(111) and on hBN/Rh(111) agree well. The larger red-shift of PTCDA/hBN/Rh(111) is interpreted as an indication for a stronger distortion of the PTCDA molecule. The vertical structure and distortion of PTCDA on hBN/Rh(111) has not been investigated. However, the trapping of the molecules as shown in STM [125] demonstrates, that the interfacial interactions are much stronger here compared to hBN/Cu(111) so that a stronger molecular distortion can be expected. This explains the larger red-shift on hBN/Rh(111) which is still smaller than the red-shift of the strongly distorted molecule on the alkali halides.

Here, it should be emphasized that FL_A of PTCDA on hBN/Cu(111) does not stem from trapped molecules in moirons of the hBN/Cu(111) substrate [174]. Most importantly, FL_A is also observed for PTCDA/Cu(111) which excludes PTCDA trapped in moirons as the origin. But secondly, STM experiments have shown that there is no preferential occupation of moirons of hBN/Cu(111) for PTCDA molecules at all (see Appendix A.2).

The influence of the substrates

Figure 7.4 shows that the energy of the 0-0 transition of PTCDA in the monolayer decreases in the order of the substrates hBN/Rh(111) (19,200 cm^{-1}), hBN/Pt(111) (18,700 cm^{-1}), hBN/Cu(111) (18,300 cm^{-1}), and hBN/SiO$_2$ (18,060 cm^{-1}). As in the previous section, intermolecular interactions and the molecular distortion will be discussed as possible explanations for the observed red-shifts.

On hBN/SiO$_2$, the PTCDA molecules order in a quadratic phase, similar as on NaCl which may be due to the preparation from an ethanolic solution instead of a preparation by CVD [126]. On the other three substrates (hBN/Rh(111), hBN/Pt(111), and hBN/Cu(111)), the PTCDA molecules order in herringbone patterns [125]. This difference in lateral structure is not expected to be the cause for the observed shifts. On NaCl/Ag(100), both a quadratic and a herringbone structure have been observed for PTCDA [111]. The HB*-phase is red-shifted by 300 cm^{-1} compared to the Q-phase [52] (cf. Figure 7.4). On the hBN-substrates, on the other hand, the *quadratic* structure is red-shifted with respect to the herringbone phase so that the molecular interactions do not seem to be the deciding factor for the different red-shifts on the hBN substrates.

Forker et al. [125] have discussed the different polarizabilities of the substrates as the cause for the spectral shift between PTCDA/hBN/Rh(111) and PTCDA/hBN/Pt(111). They concluded that, while the different polarizabilities are actually expected to cause a spectral shift, these expected shifts are much smaller (by ~75%) than those that were observed.

Interestingly, the observed changes in the 0-0 transition energy correlate with the interaction strengths between the hBN layer and the respective supportive materials. On Rh(111), hBN forms a strongly corrugated nanomesh due to strong interfacial interactions [75, 83]. The hBN layer on Pt(111) shows a weaker but significant corrugation [84, 85]. The interactions at the hBN/Cu(111) interface have been shown to be very weak in Chapter 5. hBN/SiO$_2$ was prepared by depositing exfoliated hBN [126] which can be expected to show the weakest interactions of all of these systems. This points to the molecular distortion as the deciding factor on the spectral shifts. A strong molecular distortion is caused by strong interfacial interactions between molecule and substrate. Such strong interactions can be expected for PTCDA on hBN/Rh(111) and on hBN/Pt(111) as indicated by the trapping of molecules in the pores [125]. The interfacial interactions for PTCDA on hBN/Cu(111) have been shown to be very weak (Chapter 6).

A similar interpretation may apply to the FL spectra of PTCDA on the (111) surfaces of the three noble metals where the peak positions of the FL are red-shifted in the order Cu(111), Au(111), Ag(111). Here, the PTCDA molecules in the second layer have to be considered since FL[1] from the first layer is quenched [58]. The interactions between PTCDA and the metal surfaces is strong enough to still influence the second molecular layer (the separating layer). However, since the distortion motifs and lateral interactions in the second layers have not been investigated as thoroughly as those of the first monolayers, concrete deductions regarding the specific influences of the noble metal substrates on the FL of PTCDA can not yet be drawn.

Figure 7.4 shows that a red-shift occurs with changing substrate families from noble metals, to hBN substrates, to alkali halides. While there is some overlap of these groups in the spectral positions of the 0-0 transitions of the adsorbed PTCDA layers, this trend can be clearly discerned. The significant trend here are the dipols in the substrates parallel to the surface. On the metal surfaces, the first PTCDA layer has to be considered as the substrate. While the anhydride groups carry partial negative and the perylene backbone partial positive charges, the electronic modulation of the substrate can be categorized as very weak since the electrons are delocalized over the whole molecule. In the hBN layer, the B−N bonds are clearly characterized as dipols due to the different electronegativities of the atoms, and the alkali halides are ionic materials with full charges alternating in their lattices. The electronic structures of the substrates influence the structure of the adsorbed PTCDA molecules as demonstrated by the strong distortion of the molecule due to interactions between the positively charged alkali cations and the anhydritic groups of the molecules which are partially negatively charged [113] (see Chapter 2.2). This influence extends to the energies of the electronic states of the molecule and, thus, results in the observed spectral shifts.

7.4.2   Absorbance of PTCDA/hBN/Cu(111)

All FL spectra of PTCDA in the present work were measured using a laser with an exciting wavelength of $\lambda_{ex} = 458$ nm. Additionally, attempts were made to record FL spectra with $\lambda_{ex} = 497-507$

---

[1]The FL of PTCDA/Cu(111) refers here to FL$_C$ from ordered domains.

and 532 nm. However, these experiments yielded only Raman lines but no FL. This was surprising, since these wavelengths were used to record FL and FLE (*fluorescence excitation*) spectra of PTCDA on KCl/Ag(100) and NaCl/Ag(100) [164, 235]. It was expected that the absorbance of PTCDA/hBN/Cu(111) was similar to these systems. Figure 7.5a shows FL (black) and FLE (red) spectra of 1% ML PTCDA/KCl/Ag(100) [224]. Here, the laser line at 458 nm clearly coincides with a peak in the absorbance.
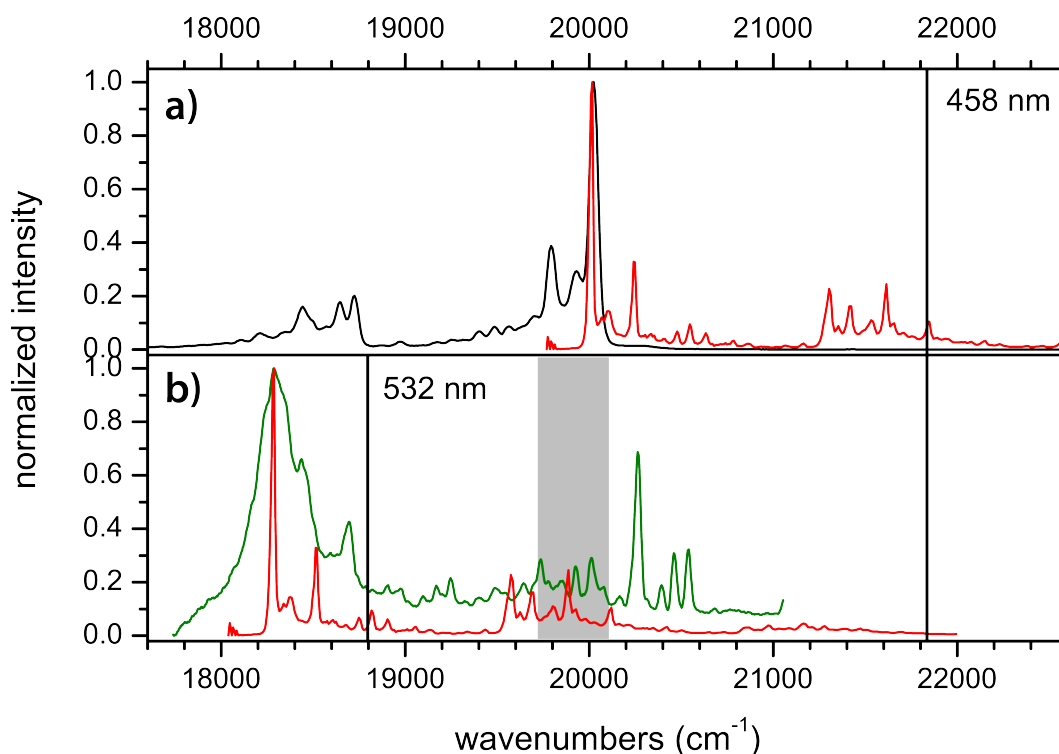
Figure 7.5: *a) FL (black) and FLE (red) spectra of 1% ML PTCDA/KCl/Ag(100). Taken from Ref. [224]. b) FL spectrum of 0.60 ML PTCDA/hBN/Cu(111) (green). For an estimation of the absorbance, the FLE spectrum from a) is shifted to the position of the FL$_B$ peak (red). The positions of the laser lines at 532 nm and 458 nm are indicated by black lines, the positions of the laser lines at 497−507 nm are represented in gray.*

The absorbance of PTCDA/hBN/Cu(111) was not measured. For an estimation, the FLE spectrum of PTCDA/KCl/Ag(100) was shifted to the position of FL$_B$ of PTCDA/hBN/Cu(111) (see Figure 7.5b). This estimation assumes no significant Stokes shift of the absorbance as is the case for PTCDA on KCl/Ag(100) [224] and no change in absorbance structure. Remarkably, the laser lines at 497−507 nm and at 532 nm coincide with absorption peaks while the laser line at 458 nm, which is the only one that yielded any FL of PTCDA on hBN/Cu(111), does not.

Since the Raman lines of PTCDA/hBN/Cu(111) showed that the vibrational modes remain the same as it has been observed in other systems (cf. section 7.3.2), the absorbance structure can be assumed to remain more or less the same for PTCDA on different substrates. Instead, it is likely that a Stokes shift occurs. The absence of or very small Stokes shifts of PTCDA on both KCl/Ag(100) [224] and NaCl/Ag(100) [52], respectively, have been assigned to the absence of trapped excitons like excimers or CT excitons [165]. The unexpected absorption behavior might indicate the presence of such trapped excitons in PTCDA/hBN/Cu(111).

7.5   Conclusion

A single layer of hBN is able to decouple PTCDA from an underlying Cu(111) surface so that FL from the first molecular layer can be observed. Here, FL from molecules adsorbed at surface defects (at ~18,450 cm^{-1}) and in ordered domains (at ~18,300 cm^{-1}) can be distinguished. Furthermore, another FL signal from the second layer and higher was observed at ~18,150 cm^{-1}. The efficiency of the decoupling, however, is small. The FL intensity is low compared to that of PTCDA molecules on alkali halide films and the life time of the excited state is small ($(1.6 - 4.4) \cdot 10^{-14}$ s), resulting in a low quantum yield.

The energy of the 0-0 transition of PTCDA on different substrates was discussed. Several trends were identified that linked the interaction strength at the PTCDA/substrate interface to the energetic shift of the transition. For the hBN substrates in particular, the comparison showed that the remaining interaction strength between the PTCDA molecules and the underlying metal substrates influences the fluorescence of the molecule.

Beside the FL, Raman lines of PTCDA on hBN/Cu(111) could be observed. Their occurance was explained by the SERS effect caused by protrusions on the Cu(111) surface because Raman lines were also observed for PTCDA/Cu(111). The Raman lines of PTCDA/hBN/Cu(111) show similarities to thin films and single crystals of PTCDA in many regards. But in several aspects, like the Raman shifts at higher energies, differences are observed.

8 Summary and Outlook

The aim of the present thesis was to show whether a single layer of the two-dimensional material hexagonal boron nitride (hBN) is able to decouple an organic molecule from an underlying metal surface so that an electronic excitation of the molecule is preserved. To demonstrate this, the fluorescence (FL) of PTCDA was investigated on an hBN/Cu(111) substrate. Cu(111) was chosen as the metallic substrate because the interactions at the hBN/Cu(111) interface were expected to be weak and the interfacial distance to be large. Both aspects were expected to increase the decoupling at this interface. PTCDA is a model molecule whose properties on various surfaces have been studied extensively. Consequently, it was chosen for the present problem as well. In particular the comparison to PTCDA/Cu(111) is of interest to determine the changes of this system caused by an hBN layer. FL spectroscopy allowed the observation of interfacial coupling of the excited state of the molecule even to a low degree, so that a charge-transfer that cannot be detected by photoemission methods due to the small life times of the excited states involved, could be observed.

This overarching question was tackled in three steps which will be summarized now.

1) The expected very weak interfacial interactions of hBN/Cu(111) were demonstrated in spot-profile analysis low energy electron diffraction (SPA-LEED) and normal incidence x-ray standing waves (XSW) experiments. The hBN layer is incommensurate to the Cu(111) surface despite a very small lattice mismatch and the domains are disordered in their azimuthal orientation. The vertical interfacial distance of (3.24 ± 0.03) Å exceeds the sum of the vdW radii of the involved atoms. A buckling of the hBN layer with an amplitude of (0.42 ± 0.05) Å was found in SPA-LEED. This buckling is small compared to the interfacial distance and stretches over a lateral distance of several nm so that the hBN layer can be seen as locally flat.

   The azimuthal orientations of the hBN domains are determined during the growth process which can be separated into three steps. The formation of hBN nuclei begins at surface defects where the desorption energy of the borazine molecules is the highest. These nuclei have an azimuthal orientation of 30° relative to the Cu(111) surface with a wide azimuthal distribution. After saturation of the surface defects, nuclei form on the Cu(111) terraces. They are aligned with the surface because they occupy the preferred adsorption sites $N_{top}B_{hcp}$ and $N_{top}B_{fcc}$. The domains that grow from these nuclei cover the majority of the surface. hBN domains that fill the gaps between larger domains which cannot coalesce grow during the last step. Their azimuthal orientation is random and they constitute the minority of hBN domains on the surface. The desorption energy of the borazine monolayer on Cu(111) terraces is only (0.495 ± 0.005) eV.

2) PTCDA on hBN/Cu(111) forms an incommensurate structure with *p2gg* symmetry, shows high azimuthal disorder in the orientation of the domains, and grows layer-by-layer for at least the first two layers. The structure shows high similarity to PTCDA in the bulk and points to considerably weaker interfacial interactions compared to either PTCDA on the metal surfaces Cu(111) and Ag(111), or on hBN/Pt(111) and hBN/Rh(110). The structural analysis is possible with LEED patterns that show a smaller degree of azimuthal disorder which is related to the hBN quality. Namely, on not completely closed hBN layers, PTCDA domains are pinned to small patches of bare Cu(111) surface from where they grow onto the hBN layer. This leads to PTCDA domains whose orientation agrees with that of PTCDA domains in the *β*-phase on Cu(111).

The vertical distance at the PTCDA/hBN interface is very large at (3.37 ± 0.03) Å and the molecule is essentially flat. The distances measured for the different atoms in the molecule match the sum of the vdW radii of the atoms involved. The adsorption energy of PTCDA on hBN/Cu(111) amounts to only (2.10 ± 0.09) eV. In UPS experiments, no indications for a static charge-transfer at the interface or a change in work function upon PTCDA adsorption were found. XPS experiments showed that the energies of the $1s$ orbitals of the carbon atoms in the PTCDA molecule on hBN/Cu(111) show more similarity to PTCDA multilayers than to PTCDA adsorbed on metal surfaces.

3) Due to the surface enhanced Raman scattering (SERS) effect caused by protrusions on the Cu(111) surface, Raman lines of PTCDA could be observed on Cu(111) and on hBN/Cu(111). The Raman shifts of PTCDA/hBN/Cu(111) show some significant similarities to those observed for thin films of PTCDA or single crystals of PTCDA which reveals that the substrate hBN/Cu(111) has little influence on the PTCDA layer and agrees with the expectation of a physisorbed system.

Measuring FL from PTCDA/hBN/Cu(111) was possible even from the first monolayer which is not the case for PTCDA/Cu(111). Three different FL peaks were observed at ~18,450 cm^{-1}, ~18,300 cm^{-1}, and ~18,150 cm^{-1}. They were assigned to FL from isolated molecules adsorbed at surface defects, likely ad-atoms of another species like carbon, from molecules in ordered domains in the first layer, and from molecules in higher layers, respectively.
While the hBN layer is able to suppress the charge-transfer, the FL intensities are low, the vibrational peaks could not be observed, the life time of the excited states in the PTCDA monolayer were estimated to be only $(1.6 - 4.4) \cdot 10^{-14}$ s, and the quantum yield amounts to only $3.1 \cdot 10^{-6}$. Thus, the efficiency of the decoupling by an hBN layer is very limited.

In conclusion, a single layer of hBN cannot be deemed sufficient to decouple PTCDA molecules from an underlying Cu(111) surface to prevent the quenching of an electronic excitation. While the charge-transfer at the interface is reduced, it is still significant enough to drastically reduce fluorescence intensities and quantum yields.
However, hBN as a decoupling layer does not need to be dismissed in general because the decoupling of another molecule, the Lander-type molecule DBP, yielded a much higher FL intensity, life time, and quantum yield than PTCDA. This can be attributed to an additional decoupling due to

the increased vertical distance between the perylene backbone of the chromophore and the hBN layer caused by the peripheral phenyl groups of the molecule.

In future work, similar systems with even more increased separation of the electronic states of the molecule and the metal should be in focus. The adsorption complex DBP/hBN/Cu(111) has not yet been investigated regarding its structural properties or a more in-depth analysis of its fluorescence. Furthermore, the use of a different metallic substrate with even more reduced interactions with the hBN layer, like Ag(111), may be of interest.

Finally, a further development of the growth model of hBN on surfaces is necessary. If the process is understood, the preparation of bilayer hBN may become possible which would significantly increase the ability of the material to decouple molecules and metals.

A Publications

A.1 "Long Vertical Distance Bonding of the Hexagonal Boron Nitride Monolayer on the Cu(111) Surface"

by Christine Brülke, Timo Heepenstrick, Niklas Humberg, Ina Krieger, Moritz Sokolowski, Simon Weiß, Frank Stefan Tautz, and Serguei Soubatch

published in: Physical Chemistry C **121**, 23964 (2017), including Supporting Information.

Long Vertical Distance Bonding of the Hexagonal Boron Nitride Monolayer on the Cu(111) Surface

Christine Brülke,[†] Timo Heepenstrick,[†] Niklas Humberg,[†] Ina Krieger,[†] Moritz Sokolowski,*[,†] Simon Weiß,[‡,§] Frank Stefan Tautz,[‡,§] and Serguei Soubatch[‡,§]

[†]Institut für Physikalische und Theoretische Chemie der Universität Bonn, Wegelerstrasse 12, 53115 Bonn, Germany
[‡]Peter Grünberg Institut (PGI-3), Forschungszentrum Jülich, 52425 Jülich, Germany
[§]Jülich Aachen Research Alliance (JARA), Fundamentals of Future Information Technology, 52425 Jülich, Germany

S *Supporting Information*

ABSTRACT: The hexagonal boron nitride (hBN) monolayer on the Cu(111) surface has recently been considered an example of an extremely weak hBN/metal interaction, as indicated, e.g., from the presence of an only electronic Moiré-like superstructure that was observed in scanning tunneling microscopy images. From these results, a large bonding distance of the hBN sheet to the topmost Cu layer can be envisaged but has not been proven so far. We report a structural analysis of the hBN/Cu(111) interface based on high resolution low energy electron diffraction and normal incidence X-ray standing wave experiments. We find that both the boron and nitrogen atoms are located at very large vertical distances of $d_B = 3.25 \pm 0.02$ Å and $d_N = 3.22 \pm 0.03$ Å with respect to the nominal position of the topmost Cu(111) layer. Significant vertical buckling and lateral distortions of the hBN layer can be excluded. These results demonstrate that the hBN monolayer on the Cu(111) surface is indeed well described by a rigid and geometrically well separated sheet.
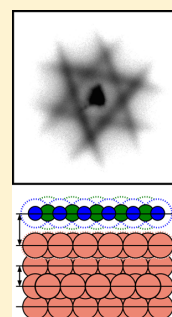
1. INTRODUCTION

Monolayers of hexagonal boron nitride (hBN) are often considered as a wide-band-gap analogue to graphene. Such monolayers are chemically robust and are of interest as ultrathin insulating interlayers for thin film devices.[1] On many metal surfaces, a monolayer of hBN can be grown in a self-terminating catalytic process by dissociation of borazine [(HBNH)$_3$] that is dosed onto the hot metal surface. The elemental type of the surface has a significant influence on the rate constant of the dissociation and also on the morphology of the resulting hBN layers. The general trend is that low reactivity of the catalytic process and more "flat" and weakly bonded hBN layers are found on the surfaces of coinage metals, e.g., Cu(111),[2] Ag(111),[3] and Ag(100),[4] whereas higher reactivity and corrugated (buckled) hBN films are characteristic for d-metal surfaces, e.g., Ni(111)[5] or Ir(111),[6] ranging to structures considered as "nanomeshes", e.g., on Rh(111).[7−9] Considering applications, Cu is an interesting substrate for hBN growth because free-standing hBN monolayers can be prepared by catalytic growth of a hBN monolayer on Cu foils that are subsequently etched away.[10] A very weak bonding of the hBN monolayer to the Cu surface is possibly an important aspect in this procedure; in addition, this weak bonding may be attractive for an electronic decoupling of molecular adsorbates on top of the hBN layer from the Cu states.[11] Here we report on the lateral geometric structure and a quantitative determination of the vertical bonding distance of the hBN monolayer with respect to the Cu(111) surface.

The properties of catalytically grown hBN monolayers on the Cu(111) surface have been studied experimentally by several groups.[5,12] Most relevant in the context of the present work are the results of Joshi et al.[2] who performed detailed scanning tunneling microscopy (STM) investigations. Due to the small lattice misfit of the hBN monolayer to the Cu(111) surface lattice, Moiré patterns are seen in the STM images. From the appearance of these at high bias voltages (>3 V), Joshi et al.[2] derived that they result from an electronic contrast and not from a geometric vertical height modulation (buckling) of the hBN layer.

The hBN/Cu(111) interface was also investigated several times by density functional theory (DFT). An important structural parameter is evidently the hBN/Cu(111) interfacial bonding distance, given by the vertical distances of the B and N atoms with respect to the topmost Cu layer. Remarkably, different authors obtained values spread over a significant range, which partially reflects differences of the specific DFT methodologies used. For instance, for the bonding distance of N at Cu on-top positions, values between 2.65 ± 0.03[13] and 3.341 ± 0.007 Å[14] were reported. Other authors reported interfacial bonding distances also falling into this interval.[15−18] One reason for the broad spread of obtained values is that small variations in the empirical corrections to the DFT accounting for the van der Waals interactions lead to large changes in the

interfacial bonding distances. This is presumably a consequence of the very weak interfacial chemical bonding which makes the van der Waals bonding rather decisive for the interfacial distance.

The hBN/Cu(111) interfacial bonding distance has not been determined *experimentally* so far, and thus, we do not have a conclusive understanding of the hBN/Cu(111) interface, yet. The purpose of the reported investigation was to fill this gap. We performed an analysis of the vertical positions of the N and B atoms versus the Cu(111) surface by the normal incidence X-ray standing wave technique (NIXSW). In addition, we report data from high resolution low energy diffraction (LEED). These show very pronounced satellite structures close to the diffraction spots of the Cu substrate. As we will demonstrate, these satellites have to be interpreted by multiple electron scattering processes. We can exclude a significant structural vertical buckling of the hBN layer related to the Moiré structure which results from the incommensurability of the hBN layer and the Cu(111) surface. From the LEED data, we also derive information on the azimuthal orientation of the hBN domains versus the Cu surface. We discuss these findings in the frame of a weak interfacial bonding leading to local variations in the bonding heights and orientations of individual hBN domains.

2. EXPERIMENTAL SECTION

The sample preparation and all experiments were carried out under ultrahigh vacuum. Our home chamber had a base pressure of 3×10^{-10} mbar. It was equipped with a low energy electron diffraction (LEED) instrument specially designed for performing spot profile analysis (SPA-LEED).[19] For a high precision calibration of the $k_{\parallel}$-axis, we used the tabulated temperature dependent Cu lattice constant.[20] In addition, the recorded data were corrected numerically for nonlinearities in the $k_{\parallel}$-axis to second order. The criterion was that the respective distances of hBN satellites to the specular (0,0) spot or to the first order spots of the Cu(111) surface were identical. This criterion is based on the origin of the satellites from multiple electron scattering that we describe below.

The Cu single crystal sample was mounted on a manipulator which allowed cooling by liquid nitrogen to 100 K and heating of the sample by a tungsten filament and electron bombardment to 1150 K. The Cu(111) crystal was prepared by repeated 30 min cycles of sputtering with Ar ions (1000 eV, 7 μA) and subsequent annealing at 1070 K for 30 min. The structural quality and chemical purity of the so prepared Cu(111) surface was checked by LEED and X-ray photoelectron spectroscopy (XPS).

Borazine [(HBNH)$_3$] was purchased from Katchem. It was filled into a small glass tube under an Ar atmosphere that was attached to a leak valve. The Ar was pumped away during several cycles while the borazine was frozen by liquid nitrogen. The borazine was then continuously held at about -4 °C in order to minimize thermal degradation. The hBN layers were prepared by dosing 2000 L of borazine via the background at a pressure of 1.5×10^{-6} mbar, while the Cu crystal was kept at a temperature of 1070−1120 K. Typically, the preparation was finished by closing the leak valve and subsequent cooling down of the sample by about 1 K s^{-1}. An ion gauge was used to measure the dosage of the borazine. Using a quadrupole mass spectrometer, the fraction pattern of the borazine was found to be identical to that published in ref 21.

Normal incidence X-ray standing wave (NIXSW) measurements were performed at the Diamond light source (beamline

I09). For details of the NIXSW method, we refer to ref 22. Hard/soft X-ray photoelectron spectroscopy (XPS)[5,23] and angular resolved photoelectron spectroscopy (ARPES)[24] were used to check the quality of the hBN layer by comparison with published data. XPS spectra recorded on the clean Cu(111) sample did not show indications for surface contaminants (e.g., carbon or sulfur). LEED images of the hBN layer taken at the synchrotron were in good agreement with those taken in our home lab. NIXSW data were recorded at 300 K. We measured photoelectrons of the N 1s and B 1s levels for the (111) reflection of the Cu substrate while scanning the photon energy around the Bragg energy of 2.972 keV. A defocused X-ray beam was used in order to minimize possible radiation damage (300 μm $\times$ 300 μm spot size). Data collection on one sample spot took about 40 min; no significant sample degradation by the X-ray beam was observed during this time. The axis of the electron analyzer was perpendicular to the direction of the incident X-ray beam and in the direction of the polarization. The crystal was tilted by 2° toward the analyzer, yielding a Bragg angle θ_B of 88°. The photoelectrons were detected in the plane of the incident and reflected X-ray beam and within a wide range of angles α with respect to the analyzer axis of $\alpha =$ 0−25°. This corresponds to emission angles with respect to the surface ranging from 2 to 27° (see inset of Figure 5, below).

Because of the wide-range angle detection of the photoelectrons, angle dependent corrections for nondipolar emission have to be included in the evaluation of the data.[25] For this purpose, the photoelectrons were recorded in angular resolved mode, and analyzed separately for 10 narrow angular slices of 2.5° width (see Table S1) . The respective yields were analyzed using the appropriate nondipolar correction parameters which were calculated for the angles α at the centers of the respective slices. The correction parameters were obtained as described in the Supporting Information and are tabulated in Table S1 there. The fits of the yield curves for extracting the coherent positions (p_c) and coherent fractions (f_c) were performed by the program Torricelli.[26] Overall, yield curves for B 1s and N 1s levels were analyzed for eight different sample spots. Averaging the extracted p_c and f_c values was done by using an error processing routine similar to the one reported in ref 27.

3. RESULTS

3.1. LEED Data. Figure 1a shows a LEED pattern of a complete monolayer hBN on the Cu(111) surface. It is consistent with that reported by Roth et al.;[24] however, due to the higher resolution, we see additional interesting details that we describe in the following. A sharp ring of intensity runs around the six first order Cu diffraction spots (see Figure 1a). The ring radius $k_{\parallel}$ is by 2.2% larger than the reciprocal lattice vectors of the Cu(111) surface (at 300 K). The ring stems from the superposition of first order diffraction spots of hexagonal hBN domains which have different azimuthal orientations with respect to the Cu(111) surface. The lattice constant of the hBN layer is thus smaller than that of the Cu(111) surface. From the full width at half-maximum (fwhm) of the intensity profile of the ring in the radial direction, we can estimate that the hBN domains have a lateral extension of at least 200 Å. For a complete hBN monolayer, we observe that narrow angular sections of the ring located close to the first order Cu spots ($\overline{\Gamma M}$ direction) gain pronounced intensity. We name these sections "arcs" in the following. Thus, for the complete hBN monolayer, most of the hBN domains are azimuthally aligned to the Cu substrate within a small azimuthal angular range of φ
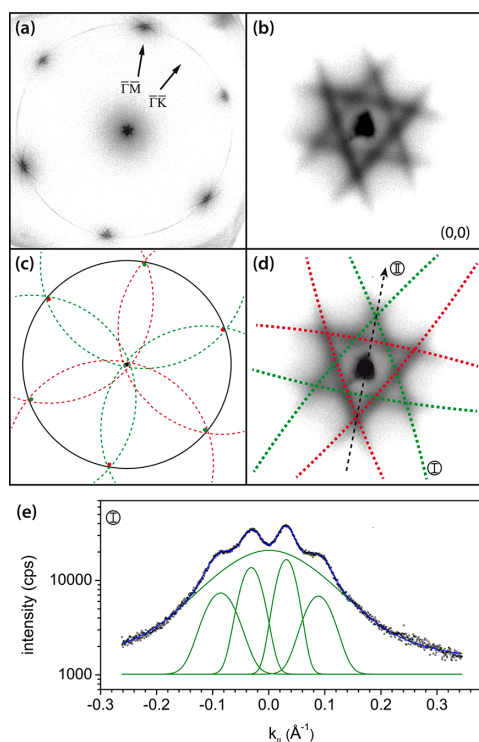
Figure 1. SPA-LEED patterns, schematic representations, and line profile of a hBN layer on Cu(111). (a) Overview. (b) Zoom-in of the central (0,0) spot which is surrounded by six arcs due to multiple electron scattering from the hBN layer and the Cu(111) substrate. (c) Schematic representation of the multiple scattering effects. The black ring represents the primary scattering signal from the hBN domains that is centered on the (0,0) spot. The dashed red and green circles represent intensities related to scattering from the hBN layer in combination with scattering from one of the six first order Cu(111) spots. The two sets of symmetry inequivalent Cu spots are marked by red and green. (d) LEED pattern from panel b superimposed with the schematic representation from panel c. (e) SPA-LEED scan along the green arc marked by (I) in panel d. The four maxima stem from the four intersection points with other arcs. The profile was fitted with four Gaussian functions for the intersection points plus a pseudo-Voigt function for the intensity distribution of the green arc along the scan direction. This function reflects the azimuthal distribution of the hBN domains and exhibits a fwhm of 4.4°. The blue curve represents the envelope. The origin of the $k_{\parallel}$ axis was positioned to the center of the scan. These patterns were recorded at an electron energy of 70.7 eV and a sample temperature of 105 K.

around the $\overline{\Gamma}\overline{M}$ direction ($\varphi = 0°$ denoting the $\overline{\Gamma}\overline{M}$ direction). A detailed profile analysis, which we will describe below, reveals that the intensity profile along the arcs has a fwhm of $\Delta\varphi$= 4.4°. We note that $\Delta\varphi$ is independent of the preparation conditions. Even very prolonged annealing or variations in the temperature of the Cu substrate during the borazine dosing (1050 and 1120 K) do not cause changes in $\Delta\varphi$.

The ring around the first order Cu spots was also observed for incomplete monolayers of hBN (~50% of the dosage required for a complete layer). There it is also not uniform but more pronounced in the $\overline{\Gamma}\overline{K}$ direction (different from the situation for complete layers, where only little intensity is found

in the $\overline{\Gamma}\overline{K}$ direction). This indicates that, for incomplete monolayers, there is a larger fraction of domains rotated by 30° with respect to the preferred orientation of the domains in the completed layer. Tentatively, we can distinguish three different types of domains: *aligned* domains (within a small angular spread around the $\varphi = 0°/\overline{\Gamma}\overline{M}$ direction), 30°-rotated domains (with a preferential orientation in the $\overline{\Gamma}\overline{K}$ direction), and domains that are homogeneously distributed in the azimuthal orientation leading to intensity that is continuously distributed along the ring in LEED. Judging from the LEED intensities, the aligned domains constitute the majority phase for complete monolayers; the respective LEED spots comprise about 90% of the total intensity.

From the ring radius ($k_{\parallel}^{hBN}$), we determine a lattice constant of the hBN layer of 2.497 ± 0.003 Å at 100 K and of 2.500 ± 0.004 Å at 300 K. These values of the lattice constant are thus by about 0.35 and 0.19% smaller than those of the hBN bulk lattice constant at the respective temperatures.[28] As said, the lattice constant of the hBN layer (a_{hBN}) is smaller than the in-plane lattice constant a_{Cu} = 2.556 Å (300 K) of the Cu(111) surface.[20] The lattice misfit m of the hBN layer to the Cu(111) surface ($m = 1 - a_{hBN}/a_{Cu}$) amounts to 2.0 ± 0.1 and 2.2 ± 0.2% at 100 and 300 K, respectively. This is compatible with the value reported by Joshi et al.,[2] who found a lattice misfit of 1.8% at 6 K from STM data. The lattice constant of a free-standing hBN monolayer was reported to be 2.488 ± 0.016 Å at 300 K,[29] which agrees with our value within 0.012 Å. Thus, the lateral structure of the hBN monolayer appears to not be significantly influenced by the underlying Cu substrate (<5%).

In the following, we consider the aligned domains. Because of the slightly different lattice constants of the hBN domains and the Cu(111) surface, a hexagonal Moiré structure results. Its lattice constant L can be calculated for a respective hBN domain from its individual rotation angle φ and the misfit m to the Cu(111) lattice according to the following formula:

$$L = \left[1 + (1 - m)^{-2} - 2(1 - m)^{-1} \cos(\varphi)\right]^{-1/2} a_{Cu}$$

Here we obtain values of L ranging from 5.7 to 11.4 nm for rotation angles φ ranging from 0 to 2.2° (at a misfit of 2.2% at 300 K). These values are in good agreement with values in the interval 5−14 nm which were observed by Joshi et al.[2] for the Moiré lattice constant of the electronic corrugation.

We now consider the prominent satellite features in the LEED pattern which are observed around the Cu spots. For instance, around the specular (0,0) spot, we see a highly symmetric star-like diffraction pattern (Figure 1b). Similar features can be seen near the first order Cu spots (see Figure 1a). The important question is whether these features result from a vertical buckling of the hBN layer resulting from the periodic change of the lateral positions of the B and N atoms with respect to the interfacial Cu atoms as described by the Moiré lattice? Or, do we have to explain them by multiple electron scattering effects between a "flat" hBN layer and the Cu(111) surface related to the electron diffraction? Even a combination of both effects may be possible. The first case would point to a vertically buckled hBN layer (similar to situations seen for hBN on other metal surfaces, e.g., Ir(111));[6] the second case would agree with the result from Joshi et al. of a structurally flat hBN layer. The answer is nontrivial, because in both cases scattered intensity is expected at $k_{\parallel}$ space positions which correspond to combinations of the reciprocal lattice vectors of the hBN layer and the Cu(111) surface.[30] This

problem of unraveling vertical buckling of a Moiré lattice from multiple electron scattering effects has been encountered in other similar situations before.[31] The ambiguity is a consequence of the fact that the diffraction pattern of a Moiré lattice is obtained by a convolution of the respective diffraction patterns of the overlayer (here the hBN layer) and the substrate (here the Cu(111) surface). The same convolution is, however, generated when, due to multiple scattering, subsequent scattering processes at the hBN layer and the Cu(111) surface contribute. In both cases, the diffraction spots correspond to reciprocal lattice vectors that are given by combinations of reciprocal lattice vectors of the hBN overlayer and the substrate.

We note that *lateral* relaxations (in contrast to *vertical* buckling), sometimes also termed as *static distortion waves*,[30] of the hBN lattice with the periodicity of the Moiré lattice could also explain these additional satellites. However, we suppose that lateral relaxations in the hBN layer are only very small. This conclusion is based on the fact that there are strong covalent sp^2-type bonds within the hBN layer but only very weak bonds between the hBN layer and the Cu(111) surface. The latter aspect is supported by the large vertical interfacial bonding distance which we will report below.

Before we further expand on the question of the origin of the satellite features, we demonstrate how they can be understood in principle. For this purpose, we have illustrated the intensity contributions from waves scattered by the first order reciprocal lattice vectors of the Cu(111) surface in combination with scattering contributions by the first order reciprocal lattice vector of the hBN layer. These are depicted as red and green circles with radii $k_{\parallel}^{hBN}$ in Figure 1c and d. The radii are centered on the respective LEED spots. The two colors mark the two symmetry inequivalent groups of first order LEED spots of the Cu(111) surface. Figure 1d shows how the star-like pattern around the specular (0,0) spot is composed by the superposition of six arcs belonging to circles centered on the six first order Cu spots. Due to the limited width of the azimuthal distribution of the hBN domains, the intensity is only present on small sections of the indicated circles ("arcs"). Figure 1e shows a line scan along an arc. The two maxima and two shoulders of this scan correspond to the four intersection points with four other arcs (see Figure 1d). The broad intensity distribution along the arc directly monitors the azimuthal distribution of the hBN domains. We fitted this distribution by a pseudo-Voigt function (∼40% Lorentzian contribution) with a fwhm of $\Delta\varphi = 4.4°$. Fully analogous interpretations apply to the diffraction features close to the first order Cu spots (Figure 1a). For an illustration, we refer to Figure S1 in the Supporting Information. They can be explained by arcs due to scattering by the hBN layer that are centered on second and third order spots of the Cu(111) surface.

We now come back to the origin of these satellite features. We first demonstrate that multiple scattering is relevant and explains the satellites. For this purpose, we consider the intensities of the satellite features in relation to those of the contributing (parental) Cu spots. The six first order Cu spots split into two interdigitated groups of three spots (marked by red and green color in Figure 1c) with inequivalent intensities. This is a consequence of the 3-fold symmetry of the Cu(111) surface in combination with scattering contributions from deeper Cu layers. This effect is characteristic for LEED images of all fcc(111) surfaces. The intensity ratio between these two groups changes with electron energy due to the energy

dependence of the multiple scattering effects.[32] We found that the intensities of the respective arcs are proportional to those of the contributing Cu spot. This can be seen from the scans taken across the specular (0,0) spot shown in Figure 2.
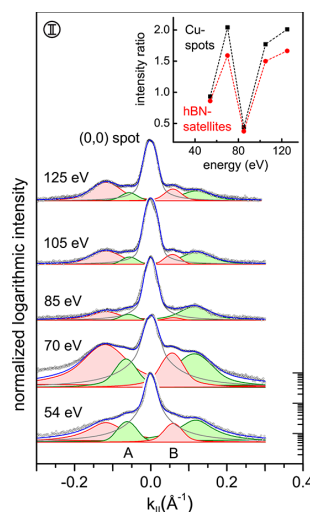
Figure 2. SPA-LEED scans along the dashed black line (II) in Figure 1d for varying electron energies. Each scan is centered on the (0,0) spot and normalized by the peak intensity of the (0,0) spot. In addition, it crosses arcs caused by scattering at the hBN layer (cf. Figure 1d). This leads to four satellites which are marked by the same colors as used in Figure 1d. The central (0,0) spot and the four hBN related satellites have been fitted by pseudo-Voigt functions for the determination of the integrated intensities. The blue curve is the respective envelope of the fitted peaks. The scans are vertically shifted for clarity. The sample temperature was between 120 and 160 K. The inset shows the variation of the intensity ratios of the two satellites closest to the (0,0) spot (A and B) and of the corresponding parental first order spots of the Cu(111) surface (cf. Figure 1c) with the electron energy. The good agreement of the ratios with electron energy indicates that the hBN satellites originate from multiple scattering of the electrons at the Cu(111) surface and the hBN layer.

The scans are not symmetric, because the intensities on the red and green colored arcs that contribute to the scan differ. In order to evaluate the intensities quantitatively, we have fitted all scans for different energies by a sum of pseudo-Voigt functions. In particular, we have evaluated the integrated intensities (I_B, I_A) of the two innermost peaks on the left and right of the central (0,0) spot in Figure 2. These are marked by A and B. They correspond to intersection points of a green and a red arc with the scan direction, respectively (cf. Figure 1d). Importantly, the ratio I_B/I_A agrees with that of the two groups of the related first order Cu spots (I_{red}/I_{green}). The latter intensities were read from energy dependent LEED patterns, corresponding to that shown in Figure 1. The computed ratios are displayed as a function of the electron energy in the inset of Figure 2. We find a good agreement of the two ratios which holds for different electron energies, although the ratios themselves vary. We thus deduce that the intensity ratio of the first order Cu spots determines the ratio of intensities of the respective hBN arcs. This is a strong indication that the satellites result from two subsequent scattering processes: one occurring at the Cu surface and one within the hBN layer.

We also consider the alternative that the intensity of the satellites is a consequence of the vertical buckling of the hBN layer. In this case, the scattering from the buckled hBN layer is described as a single scattering process related to the lateral wavelength of the Moirè lattice. The two innermost satellites on both sides of the central (0,0) spot (see Figure 2) would be interpreted as the first order diffraction spots of the Moiré lattice. (No second order spots would be expected for a purely sinusoidal buckling.) Intensity variations related to the Cu spots would not be expected, because a scattering process at the Cu surface cannot contribute to the small scattering vectors given by the relative positons of the inner satellites with respect to the (0,0) spot (i.e., $k_{\parallel} = 0.064$ Å).

A situation of this kind was considered in detail by Horn-von Hoegen et al. for Ge films on the Si(111) surface.[33] Here intensity of the satellites is calculated in the kinematic approximation for LEED which neglects multiple scattering effects. For the most simple situation of a sinusoidal buckling, one finds that the relative intensity of the satellites with respect to that of the (0,0) spot scales with the square of the momentum transfer k_z perpendicular to the surface: $I_S/I_{(0,0)} = A/4 \cdot k_z^2$.[33] Hereby, A denotes the amplitude of the surface buckling; k_z can be calculated directly from the electron energy.[19] The above equation is valid in the limit of small k_z values or, equivalently, at small electron energies.[33] Evidently, it fails to describe our profiles, since it would predict these to be symmetric with respect to the central (0,0) spot, which is not the case (see Figure 2). Nevertheless, we can use the relative intensities evaluated form our profiles to give an upper estimate for the buckling amplitude. This estimation neglects the role of multiple electron scattering and assigns the satellite intensity entirely to the vertical buckling. In order to come closest to the range of validity of the above equation, we evaluated our LEED scan taken at the lowest electron energy (54 eV) (Figure 2). From the fitted peak areas, we estimated the ratio of the integrated intensities of the first order satellites with respect to the intensity of the (0,0) spot at $I_S/I_{(0,0)} \approx 5\%$. According to the above equation, this corresponds to a buckling amplitude A of 0.05 Å. Because of the neglect of the multiple electron scattering contributions, we consider this value as an upper limit of A.

3.2. XPS Results. Parts a and b of Figure 3 display soft and hard X-ray photoemission spectra of the N 1s and B 1s levels measured at low and high photon energies, respectively. The binding energies determined from the soft X-ray spectra are 397.97 ± 0.03 eV for the N 1s level and 190.35 ± 0.01 eV for the B 1s level. These values are both in good agreement with results reported in the literature for hBN films grown on copper foil[23,34,35] as well as on Cu(100), Cu(110), and Cu(111), respectively,[35] whereby the deviation of the binding energies is of ±0.5 eV at most. Both peaks exhibit the same profile with a small asymmetry due to a smooth tail on the high binding energy side.

From both types of XPS spectra, we can identify only *one* chemical component of N and B. This is in contrast to the situation described for hBN on Ir(111),[6] where different chemical components are seen. In particular, comparing the spectra that were measured when the photon energy was scanned across the Bragg energy did not reveal any significant changes in the spectral shape due to the varying intensity contributions of possible different chemical species of N or B located at different vertical positions. This is again in contrast to the situation for hBN on Ir(111).[6] For the determination of the
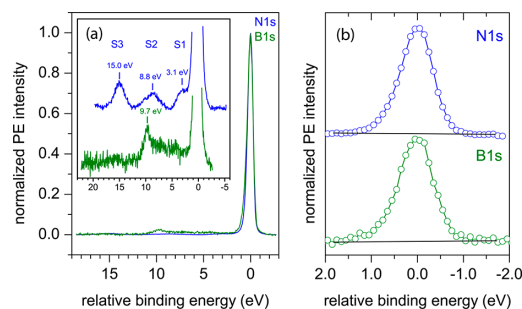

Figure 3. Normalized soft and hard XPS spectra of the B 1s and N 1s level, centered at the respective maxima of the peaks. (a) Soft XPS spectra measured at photon energies of 500 eV (N 1s) and 290 eV (B 1s), respectively. The absolute positions of the maxima (soft XPS) are at binding energies of 397.97 ± 0.15 eV (N 1s) and 190.35 ± 0.15 eV (B 1s). The inset shows a zoom-in on the satellite peaks on the high binding energy side. (b) XPS spectra measured at a photon energy of 2.962 keV, i.e., 10 eV below the Bragg energy. The full curves are splines serving as guide lines for the eye. Both spectra exhibit a fwhm of 0.85 eV and are slightly asymmetric with a broader half width on the high binding energy side. The black lines indicate a respective fitted linear background which was subtracted when the integrated intensity was determined for the NIXSW analysis.

photoelectron yields, it was thus sufficient to subtract a linear background from the N 1s and B 1s spectra and to integrate the peak area (see Figure 3b).

We include some comments on the satellite structures of the peaks seen in soft X-ray photoemission spectra which are displayed in the inset in Figure 3a. The spectrum for N 1s contains three satellites (S1−S3) located at higher binding energies that are shifted by 3.1, 8.8, and 15.0 eV with respect to the main peak. The spectrum of B 1s shows only one prominent satellite at 9.7 eV and a band of intensity between this peak and the main peak. We suppose that these satellites result from *inter*band excitations between occupied and unoccupied states of the hBN layer. The existence of the satellite S2 (8.8 eV) has been previously discussed for hBN/Ni(111) by Preobrajenski et al.[5] The authors stated that this feature is indicative for the hBN energy gap (5.5 eV), which is reflected in the onset of the satellite.

3.3. NIXSW Results. Figure 4 shows representative photoelectron yield curves of the B 1s and N 1s signal, and the reflectivity as a function of the photon energy for the slice of emission angles α between 20.0 and 22.5°. In addition, the corresponding fits according to the NIXSW theory are shown as solid lines. The fits describe the experimental curves well for the slice underlying the data of Figure 4 and for all other slices of emission angles. The similar shapes of the yield curves for B and N immediately indicate similar coherent positions for both types of atoms.

Figure 5 shows the variations of the coherent fractions f_c and positions p_c as a function of the emission angle α. We observe variations (trends) of f_c and p_c as a function of α. This is surprising, because for a flat layer one expects constant values, independent of α. If the nondipolar (ND) correction parameters which depend on α (see Table S1 in the Supporting Information) are not included in the analysis at all, we find even larger variations of f_c and p_c. In particular, the f_c values vary more strongly and come out with too large unphysical values (e.g., 1.1−1.25 for N 1s). The variations and also the impact of
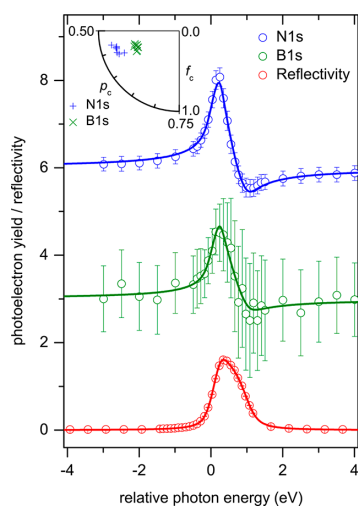
Figure 4. Reflectivity of the Cu(111) surface (red/bottom), photoelectron yields of the B 1s photoemission signal (green/middle), and N 1s photoemission signal (blue/top) as a function of the photon energy relative to the Bragg energy. The here displayed photoemission data were recorded for emission angles between α = 20.0 and 22.5°. The points are the experimental values; the lines are fits according to theory. The error bars represent the statistical error of the photoemission yield data. The spectra are shifted vertically by an offset of 3 for clarity. The inset shows the relevant quadrant of the Argand diagram plotted with the f_c and p_c values for all evaluated data sets. The Argand diagram presents the f_c and p_c values in the complex plane by the complex number $f_c \exp(i2\pi p_c/d_{Cu(111)})$.
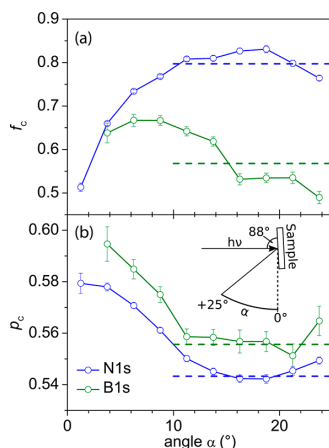
Figure 5. Coherent fractions f_c (a) and positions p_c (b) obtained for the N 1s and B 1s signals as a function of the emission angle α (see inset). Nondipolar correction parameters depending on α were included in the fit. The plotted values are the mean values calculated for each angle α from eight data sets for the N 1s and B 1s signals. The dashed lines represent average values computed from all values measured for $\alpha \geq 10°$.

the ND corrections are much smaller for the p_c than for the f_c values. The latter is typical: ND corrections have a smaller effect on the fitted p_c values, and the uncertainties in the ND parameters thus cause only small systematic errors. The fact that some variations persist here, although ND correction

parameters have been included in the evaluation, may indicate that there are angular dependent details in the experiment that are not sufficiently described by the NIXSW theory, yet. However, the details of this aspect go beyond the scope of this work and have to be left to future investigations. We further find that the coherent fractions of the B 1s signal are systematically by about 25% smaller than those of the N 1s signal (see Figure 5b). This is remarkable and will be discussed further below.

The averaged f_c and p_c values are summarized in Table 1. Because of the above-noted variation of f_c and p_c, we have

Table 1. Coherent Fractions f_c and Positions p_c for the N 1s and B 1s Photoelectron Signals Obtained after Averaging over the Angular Dependent f_c and p_c Values and the Independent Data Sets[a]

	N 1s	B 1s
f_c	0.80 ± 0.04	0.57 ± 0.02
p_c	0.54 ± 0.01	0.56 ± 0.01
d_c (Å)	3.22 ± 0.03	3.25 ± 0.02

[a]The vertical distances d_c to the top-most Cu(111) plane were calculated as $d_c = d_{(111)}^{Cu}(1 + p_c)$, whereby $d_{(111)}^{Cu}$ = 2.087 Å is the lattice constant at 300 K.[20]

computed the averaged values of f_c and p_c only from data measured at emission angles α above 10°. The reasoning behind this is that in this range the variations of the p_c values are small (<2%), and in addition, systematic errors are reduced due to the much higher counting rates that are recorded at these larger emission angles. These average values are indicated in Figure 5 by the horizontal lines.

From the coherent positions, the vertical distances d_c from the plane of the topmost Cu (111) layer are computed as $d_c = d_{(111)}^{Cu}(1 + p_c)$, whereby we use $d_{(111)}^{Cu}$ = 2.087 Å.[20] We obtain d_c(N) = 3.22 ± 0.03 Å and d_c(B) = 3.25 ± 0.02 Å. Here we assume that the topmost Cu layer is at the position of the topmost extended (111) Bragg plane (which serves as the reference plane for NIXSW results). The clean Cu(111) surface is nearly bulk terminated, because only a very small relaxation of the surface layer of −0.7 to −0.8%, corresponding to an inward shift of 0.02 Å, was found.[36,37] Considering the weak bonding of the hBN to the Cu surface, a significant relaxation from the Bragg plane is thus unlikely, and the assumption made above that the d_c values from the NIXSW analysis can be interpreted as vertical distances from the topmost Cu(111) layer is justified. The averaged vertical height of the B atoms is by $\Delta d_{B/N} = d_c(B) - d_c(N) = 0.03$ Å larger compared to that of the N atoms. Although $\Delta d_{B/N}$ is of the order of the error bars of the d_c values, we suppose that this vertical height difference is real, because this difference is found systematically for all p_c values taken at different emission angles α (see Figure 5b).

4. DISCUSSION

4.1. Vertical Bonding Height. Figure 6 shows a structure model based on our results. From the large vertical bonding distances of the N and B atoms with respect to the Cu surface, it can be concluded that interactions between both the N and B atoms and the Cu(111) surface are weak. This is also indicated by the nonoverlapping van der Waals (vdW) spheres shown in Figure 6. It is instructive to compare the averaged bonding height ($\bar{d}_c = (d(N) + d_c(B))/2 = 3.24$ Å) with that of the perylene core of the planar molecule 3,4,9,10-perylenetetra-
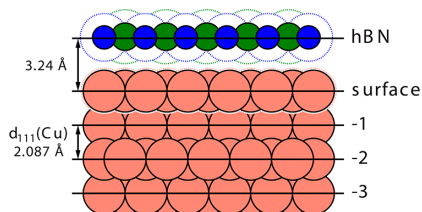
Figure 6. Hardsphere model of the hBN/Cu(111) interface (side view along the $[11\bar{2}]$ direction). The radii of the full spheres correspond to the covalent radii $r_{cov}^B = 0.84$ Å and $r_{cov}^N = 0.71$ Å[47] and the metallic radius $r_{met}^{Cu} = 1.28$ Å,[48] respectively. In addition, the van der Waals spheres of the B, N, and Cu are indicated by the dotted spheres. The respective radii are $r_{vdW}^B = 1.65$ Å, $r_{vdW}^N = 1.46$ Å, and $r_{vdW}^{Cu} = 1.40$ Å.[39] The vertical height of the B atoms is by 0.03 Å above that of the N atoms. The full line indicates the average vertical position $\bar{d}_c$ of the B and N atoms of 3.24 Å above the topmost Cu(111) layer.

carboxylic acid dianhydride (PTCDA), which has been measured by NIXSW on different surfaces. We consider the perylene core as a model for a planar flake of a π conjugated material. PTCDA is chemically bonded on the Cu(111) surface. The vertical bonding height of the perylene core was determined at 2.66 Å[27] which is much smaller than $\bar{d}_c$ for hBN on Cu(111). PTCDA on the Au(111) surface is weakly bonded. There, the perylene core is at a height of 3.27 Å.[38] This height exceeds that of hBN on Cu(111) by only 0.03 Å. Considering the significantly larger size of the vdW radius of Au compared to that of Cu (1.66 Å/1.40 Å[39]), the bonding height of hBN on Cu(111) thus has to be considered as large, and the bond is identified as weak and likely physisorptive. The assumption made above that lateral relaxations within the hBN layer are absent appears thus retrospectively verified.

Farwick zum Hagen et al.[6] reported the bonding distance for a hBN layer on the Ir(111) surface. They found a strongly buckled hBN layer with chemisorbed valleys at a distance of 2.22 Å embedded in a flat physisorbed plane at 3.72 Å distance. This latter value exceeds the value reported here for hBN on Cu(111) considerably (by 0.48 Å). This is presumably due to compressive stress in the hBN layer on Ir(111) which results from the strong bonding to the Ir(111) surface in the valleys. This causes a displacement of the hBN areas in between these valleys vertically away from the surface, leading to the large bonding height of 3.72 Å.

4.2. Azimuthal Orientation. One of the most interesting questions arising from our structural results is, what determines the azimuthal orientation of the hBN layer versus the Cu(111) surface? Before we expand on this aspect, we compare our results to those reported in the literature for hBN layers on other (111) metal surfaces. For hBN on Ag(111) (misfit 15%),[3] the bonding is likely even weaker than that for hBN/Cu, because the azimuthal orientation of the hBN domains is arbitrary and yields a uniform ring in the LEED pattern. Some similarity of hBN/Cu(111) exists for hBN on Pt(111) (misfit 11%),[40] for which a similar LEED pattern with arc-type elongated hBN spots was reported. Interestingly, on Pt(111), exchange of the borazine by B-trichloroborazine leads to additional hBN domains rotated by 30° with respect to those of the majority phase.[40] On Pd(111), a minority phase rotated by 30° is also observed for hBN layers prepared from borazine.[41] These results are similar to our finding of 30° rotated domains at low coverages. Other examples of hBN on (111) metal

surfaces differ considerably from the present situation on Cu(111), because stronger chemical interactions between the metal and the hBN sheet induce a periodic structural modulation. This leads to Moiré lattices with identical lattice points; in other words, the hBN lattice is commensurate to the lattice of the metal surface in higher order. This case is encountered, e.g., on Ir(111),[6] Ru(001),[42] and Rh(111).[8] The respective LEED patterns show distinct Moiré spots around the first order spots in all cases. On Ni(111), the situation is exceptional because the small lattice misfit causes a commensurate structure.[43] In all of these examples, the azimuthal orientation of the hBN layer is a consequence of the energy gain related to the coincidence of lattice points of the hBN layer and the underlying metal surface.

For hBN on Cu(111), the situation is significantly different. The unit cell of the hBN layer is incommensurate with respect to that of the Cu(111) surface. This also includes the absence of any coincidence of lattice points in reciprocal space, which would yield an interfacial energy gain (i.e., if the structure was of the point-on-line or line-on-line type).[30] Such coincidence, indeed, explains the azimuthal orientation of many epitaxial layers of organic molecules on metal surface with super-structures that are not commensurate to the underlying metal surface.[30] Thus, from the lateral structure of the hBN layer alone, an energetically favorable azimuthal orientation—as seen on Cu(111)—cannot be explained. We note that for incommensurate layers of rare gas atoms on metal surfaces lateral relaxations of the gas atoms from their ideal positions have been identified as a mechanism of interfacial energy gain and azimuthal orientation.[44] However, for the hBN domains on Cu(111), we consider this as not appropriate, because weak forces across the interface are counteracted by much stronger lateral forces within the hBN layer related to the covalent intralayer bonding. Therefore, we alternatively interpret the azimuthal orientation as a consequence of the growth mechanism and the related kinetics of the hBN domains.

We suggest that the orientation of the hBN domains is selected when the domains are still very small, and due to the small misfit, all N and B atoms can be located very close to their favorable adsorption sites on the Cu surface. This way, a few favorable orientations are selected. Felter et al. have recently observed the growth of the hBN domain on Cu(111) by low energy electron microscopy.[45] These data indeed indicate that the orientation of the domains is maintained from the beginning of their nucleation up to the point of domain coalescence and formation of a completed hBN layer. This is in agreement with our own (unpublished) STM data which show individual separated domains of hBN for incomplete layers. This scenario thus supports the described picture of kinetically, but not energetically, determined domain orientations. It is further consistent with our observation that there exists some probability for the growth of by 30° rotated domains. The growth of these possibly starts at some specific surface defects different from the growth of domains in the 0° orientation. In this regard, the growth of hBN layers differs considerably from that of epitaxial layers of organic molecules, because for the latter the intralayer bonds are reversible, and an optimization of the orientation under energetic aspects remains possible at later stages of the domain growth. Differently, for the hBN domains, the intralayer bonds are covalent and nonreversible. Because a concerted rotation of complete domains is kinetically impossible, the domain orientation that is realized in the nucleation process is maintained during later growth stages.

4.3. Coherent Fractions. We finally comment on the coherent fractions f_c of the N 1s and B 1s signals (see Table 1). The coherent fractions principally bear information on the vertical distribution of the atoms, and thus potentially also on a possible buckling of the hBN layer. For an unbuckled ideally flat layer, we expect f_c of 1.0 of both the N and B atoms. Buckling on any length scale would lead to values below 1.0, whereby an increase in the buckling amplitude lowers the coherent fractions.[22] This correlation was used, e.g., for a quantitative determination of the buckling amplitude of graphene layers on Ir(111), using the "egg box model".[46] The name of this model refers to the fact that the buckling yields a layer with a structure similar to that of an egg box. Because other effects, e.g., signal contributions in the NIXSW yield curves from a second chemically not separated species, may also lower the f_c, this approach gives only an upper limit for the buckling amplitude. However, unprecise ND correction parameters can also lead to systematic errors of f_c. Our own experiments indicate that f_c values are typically overestimated and, therefore, the derived buckling amplitudes can be underestimated. As noted, this is different from the situation for the coherent positions that are commonly quite robust with respect to small variations in the ND corrections. For the f_c of the Cu 2p signal of the substrate, we found a value of about 1.05, which is thus 5% above the physically reasonable limit of 1.0. A reasonable limit for a downward correction of the measured f_c of the hBN layer for accounting for the systematic errors related to the ND corrections should thus be given by 5%.

We find that the coherent fraction of the B 1s signal ($f_c(B) = 0.57$) is by about 25% smaller than that of the N 1s signal ($f_c(N) = 0.80$) (see Figure 5). This is unexpected, because a layer of hBN, either flat or buckled, should yield identical f_c values of B and N. Presumably, there exists a mechanism—or a combination of different mechanisms—that specifically reduces the f_c of B. We discuss three possibilities: (i) There are additional disordered residual fragments which contain more B than N on the surface which are not resolved as separated peaks in the photoelectron spectra and which contribute additionally by a coherent or incoherent signal. (ii) The spatial distribution of the s orbital of B is larger compared to that of N and thus yields intrinsically a reduced respective f_c value. (iii) The B atoms undergo stronger static and/or dynamic displacements from their average height. This could also include a split vertical position of the B atoms above and below their average height. We estimate that a vertical displacement of 50% of the B atoms below and 50% above the average height by 0.27 Å produces a reduction of the coherent fraction from 0.80 ($f_c(N)$) to the value 0.57 ($f_c(B)$). At present, we cannot decide further on these possibilities on the basis of our experimental data, and in the following, we thus limit our discussion to the coherent fraction of the N atoms.

From the egg box model,[46] using $f_c(N) = 0.80$, we estimate a buckling amplitude A of 0.35 Å (peak-to-peak corrugation 0.70 Å).[27] This value is definitely not compatible with our analysis of the LEED data, which gave an upper limit of 0.05 Å for A. It is also incompatible with the STM results of Joshi et al.[2] Thus, the fact that the f_c of N is significantly below 1.0 has to be explained differently here. We suppose that the hBN layer is not significantly buckled but that there exists some variation in the vertical bonding heights when passing from one hBN domain to the other. Assuming a Gaussian distribution of the vertical bonding height of different domains, we calculate from $f_c(N) = $

0.80 a fwhm $\Delta z = 0.50$ Å of this distribution (see formula C.7 in ref. 27). We suppose that this variation of the vertical bonding distance is a consequence of the weak interfacial interaction leading to a broad minimum in the interfacial interaction energy. This broad minimum in the interaction potential is also found in the DFT calculations, e.g., in ref 15. One may envisage that the variation in the bonding height (Δz) of individual domains is correlated with the spread ($\Delta\varphi$) in the azimuthal orientation of the hBN domains. For example, a stronger deviation of the domain from the $\bar{\Gamma}\bar{M}$ direction could be related to a larger bonding height. Possibly surface defects also play a role here. These could be steps of the Cu(111) surface which are overgrown by the hBN layer. This aspect indicates that the structural quality of the clean Cu(111) at the start of the growth is relevant for the hBN layer properties.

5. CONCLUSIONS

We found that the catalytically grown hBN monolayer on the Cu(111) surface exhibits a very large vertical bonding distance ($\bar{d}_c = 3.24 \pm 0.03$ Å) to the underlying Cu(111) surface. The difference between the N and B atoms is marginal; the B atoms are displaced by 0.03 Å farther into the vacuum. We find no indications for a significant vertical buckling of the hBN layer resulting from the misfit of the hBN lattice to the underlying Cu(111) surface and the related formation of a Moiré lattice. The characteristic satellites observed in high resolution LEED patterns can be interpreted by multiple scattering of the electrons. There are indications that the vertical bonding distances of different hBN domains scatter around the average value $\bar{d}_c$, possibly in conjunction with a spread in the azimuthal orientations. All of these results speak for a very weak hBN/Cu(111) interaction and motivate the model of a rigid hBN layer on top of the Cu surface.

■ ASSOCIATED CONTENT

Ⓢ Supporting Information

The Supporting Information is available free of charge on the ACS Publications website at DOI: 10.1021/acs.jpcc.7b06107.

> Additional details on the nondipolar correction parameters used for the evaluation of the NIXSW data and additional LEED patterns of higher order spots (PDF)

■ AUTHOR INFORMATION

Corresponding Author

*E-mail: sokolowski@pc.uni-bonn.de.

ORCID Ⓞ

Moritz Sokolowski: 0000-0001-5991-3910

Notes

The authors declare no competing financial interest.

program. Financial support by the DFG under project So407/6-3 is acknowledged.

■ REFERENCES

(1) Xu, M.; Liang, T.; Shi, M.; Chen, H. Graphene-Like Two-Dimensional Materials. *Chem. Rev.* **2013**, *113*, 3766−3798.

(2) Joshi, S.; Ecija, D.; Koitz, R.; Iannuzzi, M.; Seitsonen, A. P.; Hutter, J.; Sachdev, H.; Vijayaraghavan, S.; Bischoff, F.; Seufert, K.; et al. Boron Nitride on Cu(111): An Electronically Corrugated Monolayer. *Nano Lett.* **2012**, *12*, 5821−5828.

(3) Müller, F.; Hüfner, S.; Sachdev, H.; Laskowski, R.; Blaha, P.; Schwarz, K. Epitaxial Growth of Hexagonal Boron Nitride on Ag(111). *Phys. Rev. B: Condens. Matter Mater. Phys.* **2010**, *82*, 113406.

(4) Müller, F.; Grandthyll, S. Monolayer Formation of Hexagonal Boron Nitride on Ag(001). *Surf. Sci.* **2013**, *617*, 207−210.

(5) Preobrajenski, A. B.; Vinogradov, A. S.; Mårtensson, N. Ni 3d−BN π Hybridization at the hBN/Ni(111) Interface Observed with Core-Level Spectroscopies. *Phys. Rev. B: Condens. Matter Mater. Phys.* **2004**, *70*, 165404.

(6) Farwick zum Hagen, F. H.; Zimmermann, D. M.; Silva, C. C.; Schlueter, C.; Atodiresei, N.; Jolie, W.; Martínez-Galera, A. J.; Dombrowski, D.; Schröder, U. A.; Will, M.; et al. Structure and Growth of Hexagonal Boron Nitride on Ir(111). *ACS Nano* **2016**, *10*, 11012−11026.

(7) Laskowski, R.; Blaha, P.; Gallauner, T.; Schwarz, K. Single-Layer Model of the Hexagonal Boron Nitride Nanomesh on the Rh(111) Surface. *Phys. Rev. Lett.* **2007**, *98*, 106802.

(8) Corso, M.; Auwärter, W.; Muntwiler, M.; Tamai, A.; Greber, T.; Osterwalder, J. Boron Nitride Nanomesh. *Science* **2004**, *303*, 217−220.

(9) Preobrajenski, A. B.; Nesterov, M. A.; Ng, M. L.; Vinogradov, A. S.; Mårtensson, N. Monolayer h-BN on Lattice-Mismatched Metal Surfaces: On the Formation of the Nanomesh. *Chem. Phys. Lett.* **2007**, *446*, 119−123.

(10) Song, L.; Ci, L.; Lu, H.; Sorokin, P. B.; Jin, C.; Ni, J.; Kvashnin, A. G.; Kvashnin, D. G.; Lou, J.; Yakobson, B. I.; et al. Large Scale Growth and Characterization of Atomic Hexagonal Boron Nitride Layers. *Nano Lett.* **2010**, *10*, 3209−3215.

(11) Schulz, F.; Drost, R.; Hämäläinen, S. K.; Liljeroth, P. Templated Self-Assembly and Local Doping of Molecules on Epitaxial Hexagonal Boron Nitride. *ACS Nano* **2013**, *7*, 11121−11128.

(12) Auwärter, W.; Kreutz, T. J.; Greber, T.; Osterwalder, J. XPD and STM Investigation of Hexagonal Boron Nitride on Ni(111). *Surf. Sci.* **1999**, *429*, 229−236.

(13) Lyalin, A.; Nakayama, A.; Uosaki, K.; Taketsugu, T. Adsorption and Catalytic Activation of the Molecular Oxygen on the Metal Supported h-BN. *Top. Catal.* **2014**, *57*, 1032−1041.

(14) Feigelson, B. N.; Bermudez, V. M.; Hite, J. K.; Robinson, Z. R.; Wheeler, V. D.; Sridhara, K.; Hernandez, S. C. Growth and Spectroscopic Characterization of Monolayer and Few-Layer Hexagonal Boron Nitride on Metal Substrates. *Nanoscale* **2015**, *7*, 3694−3702.

(15) Laskowski, R.; Blaha, P.; Schwarz, K. Bonding of Hexagonal BN to Transition Metal Surfaces: An *Ab Initio* Density-Functional Theory Study. *Phys. Rev. B: Condens. Matter Mater. Phys.* **2008**, *78*, 045409.

(16) Lin, S.; Huang, J.; Gao, X. A Cu(111) Supported h-BN Nanosheet: A Potential Low-Cost and High-Performance Catalyst for CO Oxidation. *Phys. Chem. Chem. Phys.* **2015**, *17*, 22097−22105.

(17) Gómez Díaz, J.; Ding, Y.; Koitz, R.; Seitsonen, A. P.; Iannuzzi, M.; Hutter, J. Hexagonal Boron Nitride on Transition Metal Surfaces. *Theor. Chem. Acc.* **2013**, *132*, 1350.

(18) Koitz, R.; Seitsonen, A. P.; Iannuzzi, M.; Hutter, J. Structural and Electronic Properties of a Large-Scale Moire Pattern of Hexagonal Boron Nitride on Cu(111) Studied with Density Functional Theory. *Nanoscale* **2013**, *5*, 5589−5595.

(19) Horn-von Hoegen, M. Growth of Semiconductor Layers Studied by Spot Profile Analysing Low Energy Electron Diffraction − Part I. *Z. Kristallogr. - Cryst. Mater.* **1999**, *214*, 684−721.

(20) Straumanis, M. E.; Yu, L. S. Lattice Parameters, Densities, Expansion Coefficients and Perfection of Structure of Cu and of Cu−

In α Phase. *Acta Crystallogr., Sect. A: Cryst. Phys., Diffr., Theor. Gen. Crystallogr.* **1969**, *25*, 676−682.

(21) http://webbook.nist.gov/cgi/cbook.cgi?Formula=N3B3H6&NoIon=on&Units=SI.

(22) Zegenhagen, J.; Kazimirov, A. *The X-Ray Standing Wave Technique - Principles and Applications*; World Scientific: Hackensack, NJ, 2013.

(23) Preobrajenski, A. B.; Vinogradov, A. S.; Mårtensson, N. Monolayer of h-BN Chemisorbed on Cu(111) and Ni(111): The Role of the Transition Metal 3d States. *Surf. Sci.* **2005**, *582*, 21−30.

(24) Roth, S.; Matsui, F.; Greber, T.; Osterwalder, J. Chemical Vapor Deposition and Characterization of Aligned and Incommensurate Graphene/Hexagonal Boron Nitride Heterostack on Cu(111). *Nano Lett.* **2013**, *13*, 2668−2675.

(25) Vartanyants, I.; Lee, T.-L.; Thiess, S.; Zegenhagen, J. Non-Dipole Effects in X-Ray Standing Wave Photoelectron Spectroscopy Experiments. *Nucl. Instrum. Methods Phys. Res., Sect. A* **2005**, *547*, 196−207.

(26) Torricelli, an XSW Data Analysis and Simulation Program Written by G. Mercurio and F. C. Bocquet. Copies can be obtained from f.bocquet@fz-juelich.de.

(27) Weiß, S.; Krieger, I.; Heepenstrick, T.; Soubatch, S.; Sokolowski, M.; Tautz, F. S. Determination of the Adsorption Geometry of PTCDA on the Cu(100) Surface. *Phys. Rev. B: Condens. Matter Phys.* **2017**, *96*, 075414.

(28) Paszkowicz, W.; Pelka, J. B.; Knapp, M.; Szyszko, T.; Podsiadlo, S. Lattice Parameters and Anisotropic Thermal Expansion of Hexagonal Boron Nitride in the 10−297.5 K Temperature Range. *Appl. Phys. A: Mater. Sci. Process.* **2002**, *75*, 431−435.

(29) Mahvash, F.; Paradis, E.; Drouin, D.; Szkopek, T.; Siaj, M. Space-Charge Limited Transport in Large-Area Monolayer Hexagonal Boron Nitride. *Nano Lett.* **2015**, *15*, 2263−2268.

(30) Meissner, M.; Sojka, F.; Matthes, L.; Bechstedt, F.; Feng, X. L.; Müllen, K.; Mannsfeld, S. C. B.; Forker, R.; Fritz, T. Flexible 2d Crystals of Polycyclic Aromatics Stabilized by Static Distortion Waves. *ACS Nano* **2016**, *10*, 6474−6483.

(31) Meissner, M.; Gruenewald, M.; Sojka, F.; Udhardt, C.; Forker, R.; Fritz, T. Highly Ordered Growth of PTCDA on Epitaxial Bilayer Graphene. *Surf. Sci.* **2012**, *606*, 1709−1715.

(32) Van Hove, M. A.; Weinberg, W. H.; Chan, C.-M. *Low-Energy Electron Diffraction, Experiment, Theory and Surface Structure Determination*; Springer: Berlin, 1986.

(33) Horn-von Hoegen, M.; Alfalou, A.; Pietsch, H.; Müller, B. H.; Henzler, M. Formation of Interfacial Dislocation Network in Surfactant-Mediated Growth of Ge on Si(111) Investigated by SPA-LEED. *Surf. Sci.* **1993**, *298*, 29−42.

(34) Bresnehan, M. S.; Hollander, M. J.; Wetherington, M.; LaBella, M.; Trumbull, K. A.; Cavalero, R.; Snyder, D. W.; Robinson, J. A. Integration of Hexagonal Boron Nitride with Quasi-Freestanding Epitaxial Graphene: Toward Wafer-Scale, High-Performance Devices. *ACS Nano* **2012**, *6*, 5234−5241.

(35) Hite, J. K.; Robinson, Z. R.; Eddy, C. R.; Feigelson, B. N. Electron Backscatter Diffraction Study of Hexagonal Boron Nitride Growth on Cu Single-Crystal Substrates. *ACS Appl. Mater. Interfaces* **2015**, *7*, 15200−15205.

(36) Lindgren, S. Å.; Walldén, L.; Rundgren, J.; Westrin, P. Low-Energy Electron Diffraction from Cu(111): Subthreshold Effect and Energy-Dependent Inner Potential; Surface Relaxation and Metric Distances between Spectra. *Phys. Rev. B: Condens. Matter Mater. Phys.* **1984**, *29*, 576−588.

(37) Prieto, J. E.; Rath, C.; Müller, S.; Miranda, R.; Heinz, K. A Structural Analysis of the Co(0001) Surface and the Early Stages of the Epitaxial Growth of Cu on It. *Surf. Sci.* **1998**, *401*, 248−260.

(38) Henze, S. K. M.; Bauer, O.; Lee, T. L.; Sokolowski, M.; Tautz, F. S. Vertical Bonding Distances of PTCDA on Au(111) and Ag(111): Relation to the Bonding Type. *Surf. Sci.* **2007**, *601*, 1566−1573.

(39) Bondi, A. van der Waals Volumes and Radii. *J. Phys. Chem.* **1964**, *68*, 441−451.

Article

(40) Müller, F.; Stöwe, K.; Sachdev, H. Symmetry Versus Commensurability: Epitaxial Growth of Hexagonal Boron Nitride on Pt(111) from B-Trichloroborazine (ClBNH)$_3$. *Chem. Mater.* **2005**, *17*, 3464−3467.

(41) Morscher, M.; Corso, M.; Greber, T.; Osterwalder, J. Formation of Single Layer h-BN on Pd(111). *Surf. Sci.* **2006**, *600*, 3280−3284.

(42) Goriachko, A.; He; Knapp, M.; Over, H.; Corso, M.; Brugger, T.; Berner, S.; Osterwalder, J.; Greber, T. Self-Assembly of a Hexagonal Boron Nitride Nanomesh on Ru(0001). *Langmuir* **2007**, *23*, 2928−2931.

(43) Nagashima, A.; Tejima, N.; Gamou, Y.; Kawai, T.; Oshima, C. Electronic Dispersion Relations of Monolayer Hexagonal Boron Nitride Formed on the Ni(111) Surface. *Phys. Rev. B: Condens. Matter Mater. Phys.* **1995**, *51*, 4606−4613.

(44) Novaco, A. D.; McTague, J. P. Orientational Epitaxy - Orientational Ordering of Incommensurate Structures. *Phys. Rev. Lett.* **1977**, *38*, 1286−1289.

(45) Felter, J.; Franke, M.; Kumpf, C. In-Situ LEEM Investigation on the Growth of Hexagonal Boron Nitride on Metal Surfaces. *Verhandlungen der Deutschen Physikalischen Gesellschaft (IV)* **2017**, *52/2*, 418.

(46) Runte, S.; Lazic, P.; Vo-Van, C.; Coraux, J.; Zegenhagen, J.; Busse, C. Graphene Buckles under Stress: An X-Ray Standing Wave and Scanning Tunneling Microscopy Study. *Phys. Rev. B: Condens. Matter Mater. Phys.* **2014**, *89*, 155427.

(47) Cordero, B.; Gomez, V.; Platero-Prats, A. E.; Reves, M.; Echeverria, J.; Cremades, E.; Barragan, F.; Alvarez, S. Covalent Radii Revisited. *Dalton Transactions* **2008**, 2832−2838.

(48) Tromel, M.; Hubner, S. Metallic Radii and Ionic Radii. *Z. Kristallogr. - Cryst. Mater.* **2000**, *215*, 429−432.

Supporting Information

Long Vertical Distance Bonding of the Hexagonal Boron Nitride Monolayer
on the Cu(111) Surface

Christine Brülke,[1] Timo Heepenstrick,[1] Niklas Humberg,[1] Ina Krieger,[1]

Moritz Sokolowski,[1]*

*[1] Institut für Physikalische und Theoretische Chemie der Universität Bonn,
Wegelerstrasse 12, 53115 Bonn, Germany*

Simon Weiß,[2,3] Frank Stefan Tautz,[2,3] Serguei Soubatch[2,3]

[2]Peter Grünberg Institut (PGI-3), Forschungszentrum Jülich, 52425 Jülich, Germany

*[3]Jülich Aachen Research Alliance (JARA), Fundamentals of Future Information Technology,
52425 Jülich, Germany*

* Corresponding author: sokolowski@pc.uni-bonn.de

1. Additional information concerning the nondipolar corrections

The nondipolar (ND) correction parameters were calculated using the program Torricelli.[1]

We note that the corrections for nonnormal incidence of the X-ray beam which were included into the Torricelli program very recently were not used in our evaluation.[2] According to our experience, the effect on the present results would be within their error limits.

The ND contributions cause that, for the used experimental geometry, the reflected X-ray wave contributes stronger to the photoelectron yield than the incident X-ray wave. As a consequence, the photoelectron yield function Y is modified and is given by:[3]

$$Y = 1 + S_R R + 2|S_I|\sqrt{R} f_c \cos(\phi - 2\pi p_c + \Psi).$$

Here $S_R, |S_I|$, and Ψ are the ND correction parameters. These parameters can be written as functions of the two independent correction parameters Q and Δ:

$$S_R = \frac{1+Q}{1-Q},$$

$$|S_I| = \frac{\sqrt{1 + Q^2 \tan^2(\Delta)}}{1-Q},$$

$$\Psi = \arctan\left(Q \tan(\Delta)\right).$$

The values of Q and Δ can be calculated:

$$Q = \frac{\gamma}{3} \cos(\theta_p),$$

$$\Delta = \delta_d - \delta_p.$$

Here γ is one of the angular distribution parameters given in ref. [4], which amount to $\gamma_{N1s} = 1.10527$ and $\gamma_{B1s} = 1.17698$. The angle θ_p corresponds to the angle between the direction of the incident wave and the direction of the emitted electrons. δ_d and δ_p denote the partial phase shifts of the asymptotic p and d waves. The values for δ_d and δ_p were calculated by use of the NIST Electron Elastic-Scattering Cross-Section Database[5] and amount to $\delta_p(N1s) = 0.87501$, $\delta_d(N1s) = 0.63863$, $\delta_p(B1s) = 0.65998$ and $\delta_d(N1s) = 0.49623$. These values can be considered as constant within the small photon energy intervals and were calculated at

S2

the Bragg energy. We calculated: $\Delta_{N1s} = -0.23638$, $\Delta_{B1s} = -0.16959$. Values calculated for Q, S_R, $|S_I|$, and Ψ are summarized in Table S1.

Table S1: Values used for the nondipolar correction parameters Q, S_R, $|S_I|$, and Ψ as a function of the emission angle α for both N1s and B1s levels.

| angular slice α_{min} - α_{max} (°)	N1s				B1s			
	Q	S_R	$\|S_I\|$	Ψ	Q	S_R	$\|S_I\|$	Ψ
0 - 2.5	0.00804	1.01620	1.00810	-0.00194	0.00856	1.01727	1.00863	-0.00141
2.5 - 5.0	0.02410	1.04938	1.02471	-0.00580	0.02566	1.05267	1.02635	-0.00424
5.0 - 7.5	0.04011	1.08357	1.04183	-0.00966	0.04271	1.08924	1.04464	-0.00706
7.5 - 10.0	0.05605	1.11875	1.05947	-0.01350	0.05968	1.12694	1.06352	-0.00986
10.0 - 12.5	0.07188	1.15488	1.07760	-0.01731	0.07654	1.16577	1.08297	-0.01265
12.5 - 15.0	0.08757	1.19195	1.09622	-0.02109	0.09325	1.20569	1.10297	-0.01541
15.0 - 17.5	0.10310	1.22989	1.11529	-0.02483	0.10978	1.24665	1.12351	-0.01814
17.5 - 20.0	0.11843	1.26867	1.13480	-0.02852	0.12611	1.28862	1.14456	-0.02083
20.0 - 22.5	0.13353	1.30822	1.15471	-0.03215	0.14219	1.33154	1.16609	-0.02349
22.5 - 25.0	0.14838	1.34847	1.17498	-0.03573	0.15801	1.37533	1.18807	-0.0261

2. Additional LEED patterns
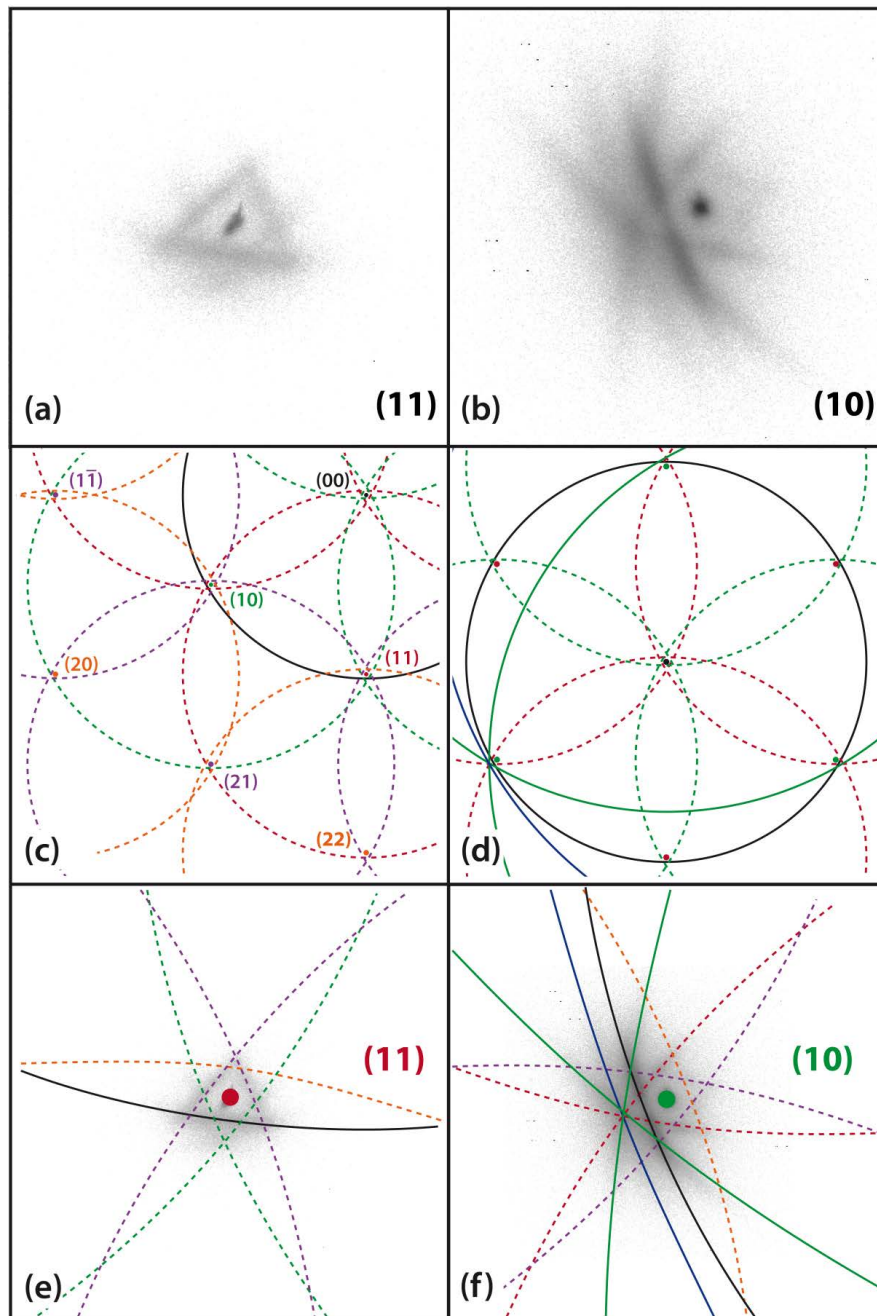
Figure S1

Figure S1: SPA-LEED patterns and schematic representations of the first order Cu spots and the satellite structure of the hBN layer on Cu(111). (**a**) and (**b**): Zoom-in LEED patterns of two symmetry inequivalent first order Cu (11) and (10) spots surrounded by arcs due to multiple electron scattering from the hBN layer and the Cu(111) substrate. (**c**) and (**d**): Overview of a schematic representation of the multiple scattering effects. The black ring represents the primary scattering signal from the hBN domains that is centered on the (0,0) spot. The dashed rings of different colors represent intensities related to *first* order scattering from the hBN layer in combination with scattering from Cu(111) spots of different orders: first order (red/green), second order (violet), and third order (orange). The solid green and blue circles (in (d)) represent intensities related to *second* order scattering from the hBN layer in combination with scattering from symmetry inequivalent first order Cu(111) spots. (**e**) and (**f**)**:** Zoom-in LEED patterns from (a) and (b) superimposed with the schematic representation from panels (c) and (d) in order to illustrate the composition of the pattern by the different multiple scattering contributions. The sample temperature was 105 K, the electron energy 70.7 eV.

(1) Torricelli is an XSW Data Analysis and Simulation Program Written by G.Mercurio and F.C. Bocquet. Copies can be obtained from f.bocquet@fz-juelich.de.

(2) van Straaten, G.; Franke, M.; Bocquet, F. C.; Tautz, F. S.; Kumpf, C. Non-Dipolar Effects in Photoelectron-Based Normal Incidence X-Ray Standing Wave Experiments. *J. Electron. Spectrosc. Relat. Phenom.* **2017**, *in press*.

(3) Vartanyants, I. A.; Zegenhagen, J. Photoelectric Scattering from an X-Ray Interference Field. *Solid State Commun.* **1999**, *113*, 299-320.

(4) Trzhaskovskaya, M. B.; Nefedov, V. I.; Yarzhemsky, V. G. Photoelectron Angular Distribution Parameters for Elements Z=1 to Z=54 in the Photoelectron Energy Range 100–5000 eV. *At. Data Nucl. Data Tables* **2001**, *77*, 97-159.

(5) Jablonski, A.; Salvat, F.; Powell, C. J. *Nist Electron Electron Elastic-Scattering Cross-Section Database, Version 3.2, Srd 64*, National Institute of Standards and Technology, Gaithersburg, MD: 2010.

A.2 "Quantitative analysis of the electronic decoupling of an organic semiconductor molecule at a metal interface by a monolayer of hexagonal boron nitride"

by Christine Brülke, Timo Heepenstrick, Ina Krieger, Beatrice Wolff, Xiaosheng Yang, Ali Shamsaddinlou, Simon Weiß, François C. Bocquet, F. Stefan Tautz, Serguei Soubatch, and Moritz Sokolowski

Quantitative analysis of the electronic decoupling of an organic semiconductor molecule at a metal interface by a monolayer of hexagonal boron nitride

Christine Brülke,[1] Timo Heepenstrick,[1] Ina Krieger,[1] Beatrice Wolff,[1] Xiaosheng Yang,[2,3] Ali Shamsaddinlou,[2,3]
Simon Weiß,[2,3] François C. Bocquet,[2,3] F. Stefan Tautz,[2,3] Serguei Soubatch,[2,3] and Moritz Sokolowski[1]

[1]*Institut für Physikalische und Theoretische Chemie, Universität Bonn, Wegelerstrasse 12, 53115 Bonn, Germany*
[2]*Forschungszentrum Jülich, Peter Grünberg Institut (PGI-3), 52425 Jülich, Germany*
[3]*Jülich Aachen Research Alliance (JARA), Fundamentals of Future Information Technology, 52425 Jülich, Germany*

The adsorption geometry, the electronic properties, and the adsorption energy of the prototype organic molecule 3,4,9,10-perylene tetracarboxylic dianhydride (PTCDA) on a monolayer of hexagonal boron nitride (hBN) grown on the Cu(111) surface were determined experimentally. The perylene core is at a large height of 3.37 Å and only a minute downward displacement of the functional anhydride groups (0.07 Å) occurs, yielding adsorption heights that agree with the sum of the involved van der Waals radii. Thus, already a single hBN layer leads to a decoupled (physisorbed) molecule, contrary to the situation on the bare Cu(111) surface.

Wide band gap two-dimensional materials (2DMs) [1,2], as, for instance, hexagonal boron nitride (hBN), are of interest as interfacial layers for separating the electronic states of adjacent conducting or semiconducting materials [3]. The appeal of hBN is given by the possibility to grow hBN mono- and multilayers [4] on many metallic substrates by chemical vapor deposition of borazine [5–7]. The hBN layer of monoatomic thickness is particularly interesting as it represents the ultimate case of a thin interfacial barrier. In short, the hBN monolayer constitutes a π bonded honeycomb net with alternating boron and nitrogen atoms [8]. It is known that multilayer sheets of hBN constitute a good electrical insulator with a wide band gap [9]. But how do these properties scale down to the single hBN monolayer and how well does this still separate the electronic states located at its two interfaces? This aspect appears to be important for the understanding and optimization of electronic thin film devices based on monoatomic hBN layers or similar other 2DMs in general. Obviously, an experimental clarification requires monitoring the electronic properties on the hBN layer at the microscopic level. One approach is to use the adsorption of an organic molecule as a probe. Investigations of this kind have been made by comparing the submolecular contrast in scanning tunneling microscopy (STM) images to that expected for the unperturbed molecular orbitals [10,11]. Here, we go further and measure the electronic *and* structural response of an organic molecule on an hBN/metal surface. Furthermore, we quantify the remaining interfacial bonding by the adsorption energy.

The Cu(111) surface lends itself to this purpose because, for building devices, hBN layers are commonly grown on Cu foils [12,13]. In a preceding experiment we have already determined the distance of the hBN layer to the underlying topmost Cu(111) layer [14]. The large value of 3.24 Å exceeds the sum of the van der Waals (vdW) radii of the interfacial atoms significantly [$(r_N^{vdW} + r_{Cu}^{vdW}) = 2.86$ Å and $(r_B^{vdW} + r_{Cu}^{vdW}) = 3.05$ Å] and identifies the bonding between the hBN layer and the Cu(111) surface as very weak. The analysis also

revealed no signs of a vertical long-range modulation of the hBN layer caused by its misfit to the Cu(111) surface [14]. We therefore consider it as perfectly flat in the following. As a consequence of the large interfacial hBN/Cu(111) distance and its band gap of 5–6 eV [15], the probability density of metal states should be strongly reduced at the hBN/vacuum interface. In conclusion, a molecule placed onto this surface should show negligible features for electronic and structural modifications due to interactions of molecular and metallic states, and thus its properties should be very close to those expected for a *physisorbed* molecule. However, quantitative information is desirable here, not at least because recent observations point in different directions: On the one hand, an electronic corrugation due to the misfit to the Cu(111) substrate is present on the hBN/Cu(111) surface [16] and reveals itself by a template effect on the adsorption of molecules [11,17–19]. Furthermore, a "catalytic transparency" of hBN on Cu(111) has been stated [20,21], which indicates a "leaking" of the metal states through the hBN that enables borazine dissociation on a closed hBN layer. On the other hand, STM images show small perturbations of the molecular states on the hBN/Cu(111) surface indicating efficient decoupling [17].

We use the semiconductor model molecule 3,4,9,10-perylene tetracarboxylic dianhydride [PTCDA, cf. Fig. 1(d)] in order to take advantage of the fact that the structural and electronic details of adsorbed PTCDA molecules have been documented for a wide range of different metal surfaces [22–25]. The height of the perylene core above the surface is dependent on the substrate due to varying strengths in bonding and interactions with metallic states, as seen by the energetic shifts of the PTCDA valence orbitals [26–29]. In addition, characteristic vertical displacements of the functional anhydride groups out of the molecular plane of the otherwise planar molecule occur. The pattern and size of these structural distortions bear information about the bonding of the molecule to the surface. For example, on the bare Cu(111) surface, the distortion of the anhydride groups encompasses

A.2 Quantitative analysis of the electronic decoupling of an organic semiconductor molecule at a metal interface by a monolayer of hexagonal boron nitride
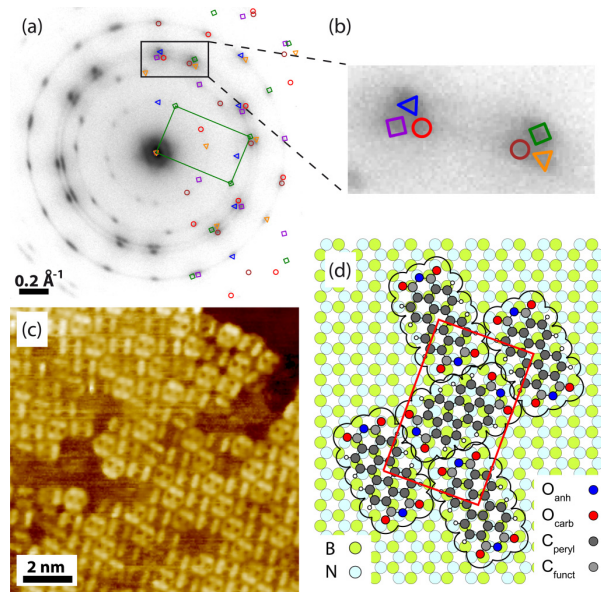
111

FIG. 1. (a) Overview LEED pattern of one monolayer PTCDA on hBN/Cu(111) with superimposed calculated spot positions and reciprocal unit cell (green). Different colors refer to six symmetry equivalent domains. The pattern was recorded at an electron energy of 30.4 eV and a sample temperature T of 110 K. (b) Zoom-in of the detail marked in (a). (c) STM image of PTCDA molecules on hBN/Cu(111) arranged in a herringbone pattern. The image was recorded at $U_{bias} = +1.5$ V and $I = 500$ pA at $T = 300$ K. (d) Corresponding hard-sphere model of the unit cell. The covalent atom radii in the molecules are drawn at 75% of their sizes for clarity. The envelope of the vdW spheres and the unit cell of the PTCDA lattice (red) are indicated.

FIG. 2. (a) XPS data for the C 1s level of PTCDA on different surfaces. Contributions from the different C atoms have been fitted and are indicated by different colors; red: different C atoms of the perylene core; blue: functional carbon atoms; dashed: respective satellites; dashed gray: nonassigned satellites. For details of the assignment, see Ref. [23] [Ag(100) spectra taken from Refs. [23,34]; Cu(100) spectrum taken from Ref. [24]]. (b) UPS data of the bare hBN/Cu(111) interface (black curve), and the PTCDA monolayer and bilayer on hBN/Cu(111) (red curves). The spectra are angle integrated over an emission angle between 8° and 25°, and were normalized by the height of the Fermi edge. A zoom of the Fermi edge is shown. Spectra were measured using He IIα radiation in 45° incidence. For comparison, a gas phase spectrum of PTCDA is shown (blue curve, taken from Ref. [35]; the spectrum was aligned at the HOMO position).

a vertical shift of the central O atom (O_{anh}) by 0.23 Å with respect to the perylene core in the direction away from the surface, while the carboxylic O atoms (O_{carb}) and the functional C atoms (C_{funct}) stay approximately at the height of the perylene core (C_{peryl}). [See Fig. 1(d) for the nomenclature.] This indicates a chemical interaction that is dominantly located on the perylene core [25]. Here, we use these effects as a delicate probe to test the coupling of leaking Cu states at the hBN/vacuum interface with molecular orbitals.

Figure 1 comprises structural data on a PTCDA monolayer adsorbed on the hBN/Cu(111) heterostructure. The low-energy electron diffraction (LEED) image reveals the formation of ordered domains. The PTCDA lattice is found to be incommensurate with respect to the hBN lattice. The lattice parameters can be identified from the spot positions in the LEED image with high precision, as it was done, e.g., for PTCDA on the Ag(111) surface before [30]. They were determined with an accuracy of 0.5% and agree within 3% with those of PTCDA layers in the β modification of the bulk crystal [31]. The achieved fit of calculated and measured LEED spot positions is shown in the zoom-in displayed in Fig. 1(b). Notably, the spots are not sharp, but smeared out azimuthally. This is due to the imperfect azimuthal order of the hBN domains [14] that is imprinted on the PTCDA layer. The STM image [Fig. 1(c)] gives further insight into

the structure: There are two molecules per unit cell forming the well-known herringbone arrangement stabilized by hydrogen bonds [Fig. 1(d)] that is seen for PTCDA on many surfaces [32]. But STM also reveals a high density of domain boundaries involving the azimuthal rotation of individual or groups of molecules. STM imaging was only successful for tunneling into unoccupied states and the obtained submolecular contrast resembles the lowest unoccupied orbital (LUMO) [33]. The observed incommensurate structure and the bulklike lateral packing point to a very weak interaction of PTCDA with hBN, leading to an only small lateral corrugation of the interaction potential. However, the possibility to draw a tunnel current from the PTCDA layer indicates that some, at least very weak, coupling to metallic states must still exist here.

Figure 2(a) displays C 1s x-ray photoelectron spectroscopy (XPS) data taken for PTCDA on hBN/Cu(111) in comparison to spectra for a multilayer and for PTCDA monolayers on the bare Cu(100) and Ag(100) surfaces. The important observation from these spectra concerns the energetic shift of the peak related to the four C_{funct} atoms with respect to the position of the main peak stemming from the 20 central C_{peryl} atoms. While on hBN and for the PTCDA multilayers the C_{funct} peak is located at a binding energy 4 eV below the C_{peryl} peak, it is shifted by 1.5 eV towards the latter on the metal surfaces. This differential shift marks the chemical bonding of the PTCDA to the metal surfaces and has been discussed in detail [26].

Concurrently, the very good agreement of PTCDA/hBN and the multilayer spectra identifies the bonding situation on hBN as similar to that between PTCDA multilayers.

Commonly, the coupling of PTCDA to metallic states leads to shifts in the frontier orbitals [26,27]. A significant downward shift of the LUMO to or even below the Fermi energy and small upward shifts of the HOMO (highest occupied orbital) and the "HOMO-1 band" (which consists of four individual orbitals [36]) are typical [26]. Quite differently, at the hBN/Cu(111) surface, the energetic distances between the frontier orbitals are not altered with respect to those seen for gas phase spectra. This is illustrated by the ultraviolet photoemission spectra (UPS) displayed in Fig. 2(b). The binding energies and partially also the relative intensities of the well-resolved HOMO and the unresolved groups of lower-lying orbitals of the gas phase spectrum [35] are well reproduced in both the spectra of a PTCDA mono- and bilayer on hBN. On bare Cu(111), the LUMO is filled due to hybridization with Cu states and found at a binding energy of 0.8 eV [27]. In contrast, for hBN/Cu(111), we see a continuous intensity related to metal states ($E_{\mathrm{Bind}} \leqslant 2$ eV) with no indications for a contribution of a former LUMO which excludes any charge transfer from the metal to the molecule. Work-function changes derived from the cutoffs in UPS data compliment the finding of an absent metal-molecule coupling: A negative change of the work function ($\Delta\Phi = -0.5$ eV) upon deposition of the hBN layer on the Cu(111) surface shows that hBN suppresses the spill-out of the Cu states. Upon PTCDA deposition on hBN/Cu(111), we find *no* significant further reduction of the work function (-0.05 eV $< \Delta\Phi < 0$ eV) caused by a possible pushback of the metallic states, which is typically encountered for PTCDA adsorption on metal surfaces [27]. This is compatible with a low probability density of Cu states at the PTCDA/hBN interface. In summary, we deduce the following: A PTCDA monolayer on hBN displays the structural and electronic signatures which are expected for a *physisorbed* molecule. Thus, the final question is whether this conclusion can be corroborated by the structural parameters of the adsorption complex.

To this end, we have determined the vertical heights of chemically and thus electron spectroscopically discernible atoms with respect to the hBN layer by the normal incidence x-ray standing wave (NIXSW) technique [40]. The data analysis was performed by the program TORRICELLI [41] and included necessary nondipolar corrections (cf. Ref. [14]). Table I summarizes the results. The underlying electron yield curves, respective fits, and the corresponding Argand diagram are shown in Fig. 3. The vertical position of the hBN layer covered by PTCDA was also determined in this experiment by NIXSW in the same manner as reported earlier for the bare hBN/Cu(111) heterostructure [14]. The obtained positions were identical within the error in both experiments, which means that PTCDA does not change the height of hBN. The theoretical fits to the experimental NIXSW curves of PTCDA are good, and the coherent fractions, which are between 0.60 and 0.85, are in agreement with our expectation based on results from other similar NIXSW experiments [22–25].

For the perylene core we find a vertical height of $d_{\mathrm{c}}^{\mathrm{hBN}}(\mathrm{C}_{\mathrm{peryl}}) = 3.37$ Å above the hBN layer. This is the largest adsorption height which has been reported so far for

TABLE I. Coherent fractions f_{c} (describing the height distribution) and coherent positions p_{c} of four chemically inequivalent atoms of the PTCDA molecule and derived respective vertical distances $d_{\mathrm{c}}^{\mathrm{Cu}}$ and $d_{\mathrm{c}}^{\mathrm{hBN}}$ with respect to the topmost Cu(111) and hBN layer, respectively. $d_{\mathrm{c}}^{\mathrm{Cu}}$ and $d_{\mathrm{c}}^{\mathrm{hBN}}$ were calculated as $d_{\mathrm{c}}^{\mathrm{Cu}} = (n + p_{\mathrm{c}}) \cdot d_{(111)}^{\mathrm{Cu}}$ and $d_{\mathrm{c}}^{\mathrm{hBN}} = d_{\mathrm{c}}^{\mathrm{Cu}} - d^{\mathrm{hBN}}$, with $n = 3$, $d_{(111)}^{\mathrm{Cu}} = 2.087$ Å [37], and $d^{\mathrm{hBN}} = 3.24(3)$ Å [14]. $n = 3$ is derived because other values give unreasonable distances.

	f_{c}	p_{c}	$d_{\mathrm{c}}^{\mathrm{Cu}}$ (Å)	$d_{\mathrm{c}}^{\mathrm{hBN}}$ (Å)
$\mathrm{O}_{\mathrm{carb}}$	0.59(1)	0.128(3)	6.528(6)	3.29(3)
$\mathrm{O}_{\mathrm{anh}}$	0.64(2)	0.135(4)	6.543(8)	3.30(3)
$\mathrm{C}_{\mathrm{funct}}$	0.83(5)	0.137(9)	6.547(19)	3.31(4)
$\mathrm{C}_{\mathrm{peryl}}$	0.85(2)	0.169(3)	6.614(6)	3.37(3)

the perylene core of PTCDA on any surface [22–25,42]. This distance is well fitted by the sum of the vdW spheres of B and C ($r_{\mathrm{B}}^{\mathrm{vdW}} = 1.65$ Å, $r_{\mathrm{C}}^{\mathrm{vdW}} = 1.75$ Å [39]). We refer to B, and not to N, to describe the hBN surface, because B exhibits a slightly larger vdW radius and because B is
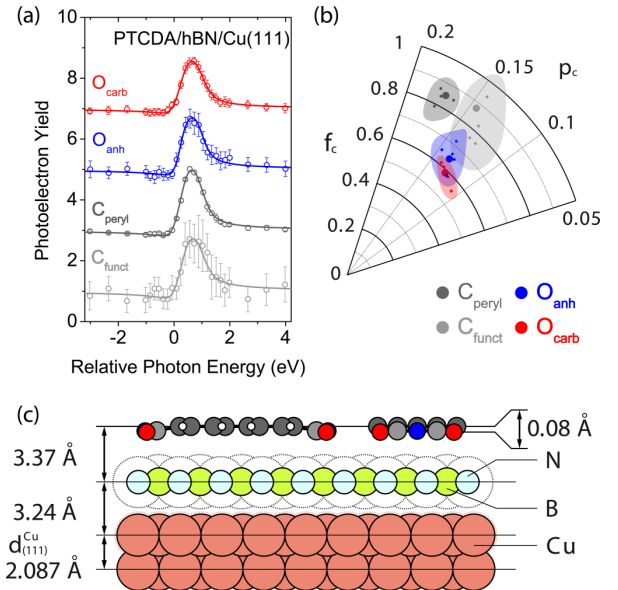
FIG. 3. (a) Electron yield curves from NIXSW data (angle integrated) for $\mathrm{O}_{\mathrm{carb}}$, $\mathrm{O}_{\mathrm{anh}}$, $\mathrm{C}_{\mathrm{funct}}$, and $\mathrm{C}_{\mathrm{peryl}}$ (vertically shifted). Photon energies are given relative to the Bragg energy of Cu(111). (b) Argand diagram showing the results of all data sets and the respective averaged values (heavy symbols). Shaded areas mark the envelope of the error bars of the data sets. The O $1s$/C $1s$ level was evaluated on five/four different positions on the sample. Note that the coherent position of the $\mathrm{C}_{\mathrm{peryl}}$ signal is by ∼0.03 larger than those of the other three species, which are about the same. (c) Side views of PTCDA/hBN/Cu(111) along the short and long molecular axes. The vertical distances within the PTCDA molecule are enlarged by a factor of 4 and the covalent radii of PTCDA are drawn at 75% of their sizes in order to better show the very small downwards bending of the terminal anhydride groups. For the hBN layer the vdW spheres are indicated.

A.2 Quantitative analysis of the electronic decoupling of an organic semiconductor molecule at a metal interface by a monolayer of hexagonal boron nitride

113

FIG. 4. Adsorption heights of chemically discernible groups in PTCDA on various surfaces as determined by NIXSW [22–25] corrected (i.e., reduced) by the vdW radii of the respective surface atoms vs the adsorption energies E_{ads} (data marked by "a" and "b" taken from Ref. [23] and Ref. [38], respectively). For Cu(100) and Cu(111) (marked by $*$) E_{ads} values are not available and horizontal data point positions are only qualitatively placed according to the work-function trend [24]. The data illustrate the trend of the bonding height from stronger chemisorptive bonding (left) to weak physisorptive bonding (right). The vdW radii were taken from Ref. [39]: $r_{Ag}^{vdW} = 1.72$ Å, $r_{Cu}^{vdW} = 1.40$ Å, $r_{Au}^{vdW} = 1.66$ Å. For the hBN substrate the boron radius was used, because it is larger ($r_{B}^{vdW} = 1.65$ Å; $r_{N}^{vdW} = 1.46$ Å) and because B is located by 0.03 Å higher than N [14]. For Ag(111), Cu(111), and Au(111), th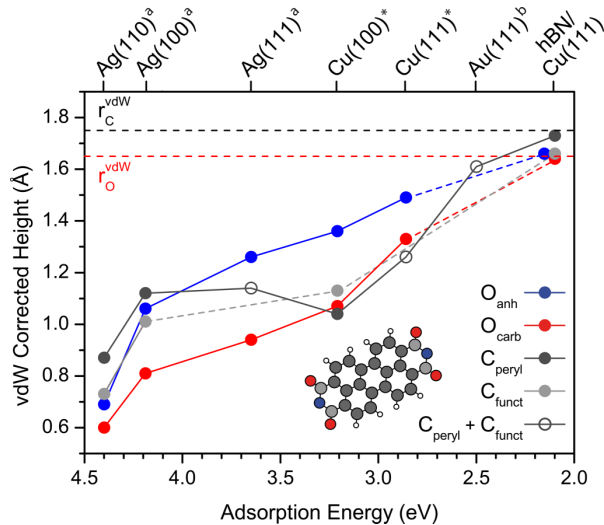e positions of C_{peryl} and C_{funct} were not analyzed individually. Thus, averaged values for all C atoms ($C_{peryl} + C_{funct}$) are shown there. For the Au(111) surface the position of the O atoms could not be determined for experimental reasons [22]. The lines linking the data points are guides for the eye. Dashed lines indicate incomplete data. The horizontal dashed lines mark the vdW radii of carbon and oxygen. The value $r_{C}^{vdW} = 1.75$ Å is valid for sp^2 hybridized carbon in perylene, in the direction perpendicular to the molecular plane [39]. The value $r_{O}^{vdW} = 1.65$ Å is the average of 1.6 and 1.7 Å, the range covering the generally found radii for sp^2 hybridized oxygen parallel to its double-bond axis [39].

positioned by 0.03 Å higher than N [14]. The agreement with the vdW radii also holds true within error for the atoms in the terminal anhydride groups (O_{carb}, O_{anh}, C_{funct}). We have illustrated this in Fig. 4. There we have also included available data for PTCDA on different metal surfaces for comparison. The bonding heights are given as corrected bonding heights, meaning that we have subtracted the vdW radii of the respective surface atoms. The corrected bonding heights can thus be directly compared to the vdW radii of

the respective atoms of PTCDA. We have ordered the metal surfaces from left to right with increasing work functions, which marks to some degree the trend of decreasing strength of the chemisorptive interaction [24]. This order is further justified by the adsorption energies (E_{ads}) given on the x axis where they are available. For the present system we have determined E_{ads} from the desorption energy that was measured by thermal desorption spectroscopy [43–46] as described in the Supplemental Material (SM) [47]. For estimating the contribution of the intermolecular interactions to E_{ads} we used data available for the PTCDA/Ag(100) system [48,49].

The situation on hBN falls on an extreme. For comparison, on the Au(111) surface, for which the bonding is considered physisorptive, a height of the perylene core of 3.27 Å was obtained [22]. The large bonding height of the perylene core on hBN/Cu(111) is remarkable and identifies the interaction of the PTCDA molecule with this surface as extremely weak. It is mirrored by a decrease of E_{ads} to a small value of 2.10 ± 0.09 eV which is by 0.4 eV smaller than that on Au(111) (see SM for details). Indeed, the only indication for the presence of the interface imprinted on the structure of the PTCDA molecule is a very minute downward shift of the peripheral anhydride groups including both types of oxygen atoms O_{carb}, O_{anh} and the functional carbon atoms C_{funct}. The averaged downward shift with respect to the perylene core amounts to 0.07 Å (the largest downward shift is that of O_{carb} by 0.08 Å). The molecule is thus *not* fully planar. However, we interpret this not as a consequence of a chemical interaction. Instead, it must be due to the attractive local vdW interactions of the O atoms with the surface, and/or an electrostatic interaction of the partially negatively charged O atoms with image charges in the Cu substrate. Apparently, the C_{funct} atoms follow the oxygen atoms in their move.

In conclusion, the hBN layer suppresses the Cu wave functions at the hBN/vacuum interface, such that adsorption has little influence on structural and electronic, i.e., the ground state, properties of PTCDA. It remains to be proven in how far this is also true for excited state properties, e.g., lifetimes of electronic excitations. In hindsight the template effect of hBN/Cu(111) on molecular adsorption noted at the beginning must be due to a very small local variation of the adsorption energy that is compatible with a physisorptive bonding.

Note added. Recently, we became aware of two publications that are interesting in the context of the present work. A similar study of a molecule on hBN/Cu(111) was reported [50]; for PTCDA adsorbed on hBN multilayers an adsorption energy of 2.46 eV and a vertical distance of 3.1 Å were found from calculations by density functional theory [51].

[1] K. S. Novoselov, A. Mishchenko, A. Carvalho, and A. H. Castro Neto, 2D materials and van der Waals heterostructures, Science **353**, 461 (2016).

[2] A. C. Ferrari, F. Bonaccorso, V. Fal'ko, K. S. Novoselov, S. Roche, P. Bøggild, S. Borini, F. H. L. Koppens, V. Palermo, N. Pugno, J. A. Garrido, R. Sordan, A. Bianco, L. Ballerini,

M. Prato, E. Lidorikis, J. Kivioja, C. Marinelli, T. Ryhänen, A. Morpurgo *et al.*, Science and technology roadmap for graphene, related two-dimensional crystals, and hybrid systems, Nanoscale **7**, 4598 (2015).

[3] T. Niu and A. Li, From two-dimensional materials to heterostructures, Prog. Surf. Sci. **90**, 21 (2015).

[4] M. Xu, T. Liang, M. Shi, and H. Chen, Graphene-like two-dimensional materials, Chem. Rev. **113**, 3766 (2013).

[5] A. Nagashima, N. Tejima, Y. Gamou, T. Kawai, and C. Oshima, Electronic Structure of Monolayer Hexagonal Boron Nitride Physisorbed on Metal Surfaces, Phys. Rev. Lett. **75**, 3918 (1995).

[6] A. B. Preobrajenski, S. A. Krasnikov, A. S. Vinogradov, M. L. Ng, T. Käämbre, A. A. Cafolla, and N. Mårtensson, Adsorption-induced gap states of *h*-BN on metal surfaces, Phys. Rev. B **77**, 085421 (2008).

[7] A. B. Preobrajenski, M. A. Nesterov, M. L. Ng, A. S. Vinogradov, and N. Mårtensson, Monolayer h-BN on lattice-mismatched metal surfaces: On the formation of the nanomesh, Chem. Phys. Lett. **446**, 119 (2007).

[8] C. Tan *et al.*, Recent advances in ultrathin two-dimensional nanomaterials, Chem. Rev. **117**, 6225 (2017).

[9] J. J. Jia, T. A. Callcott, E. L. Shirley, J. A. Carlisle, L. J. Terminello, A. Asfaw, D. L. Ederer, F. J. Himpsel, and R. C. C. Perera, Resonant Inelastic X-Ray Scattering in Hexagonal Boron Nitride Observed by Soft-X-Ray Fluorescence Spectroscopy, Phys. Rev. Lett. **76**, 4054 (1996).

[10] H. T. Zhou, J. H. Mao, G. Li, Y. L. Wang, X. L. Feng, S. X. Du, K. Müllen, and H.-J. Gao, Direct imaging of intrinsic molecular orbitals using two-dimensional, epitaxially-grown, nanostructured graphene for study of single molecule and interactions, Appl. Phys. Lett. **99**, 153101 (2011).

[11] S. Berner *et al.*, Boron nitride nanomesh: Functionality from a corrugated monolayer, Angew. Chem., Int. Ed. **46**, 5115 (2007).

[12] K. K. Kim *et al.*, Synthesis of monolayer hexagonal boron nitride on Cu foil using chemical vapor deposition, Nano Lett. **12**, 161 (2011).

[13] R. Y. Tay, M. H. Griep, G. Mallick, S. H. Tsang, R. S. Singh, T. Tumlin, E. H. T. Teo, and S. P. Karna, Growth of large single-crystalline two-dimensional boron nitride hexagons on electropolished copper, Nano Lett. **14**, 839 (2014).

[14] C. Brülke, T. Heepenstrick, N. Humberg, I. Krieger, M. Sokolowski, S. Weiß, F. S. Tautz, and S. Soubatch, Long vertical distance bonding of the hexagonal boron nitride monolayer on the Cu(111) surface, J. Phys. Chem. C **121**, 23964 (2017).

[15] J. Sławińska, I. Zasada, and Z. Klusek, Energy gap tuning in graphene on hexagonal boron nitride bilayer system, Phys. Rev. B **81**, 155433 (2010).

[16] S. Joshi *et al.*, Boron nitride on Cu(111): An electronically corrugated monolayer, Nano Lett. **12**, 5821 (2012).

[17] F. Schulz, R. Drost, S. K. Hämäläinen, and P. Liljeroth, Templated self-assembly and local doping of molecules on epitaxial hexagonal boron nitride, ACS Nano **7**, 11121. (2013).

[18] J. I. Urgel, M. Schwarz, M. Garnica, D. Stassen, D. Bonifazi, D. Ecija, J. V. Barth, and W. Auwärter, Controlling coordination reactions and assembly on a Cu(111) supported boron nitride monolayer, J. Am. Chem. Soc. **137**, 2420 (2015).

[19] C.-A. Palma, S. Joshi, T. Hoh, D. Ecija, J. V. Barth, and W. Auwärter, Two-level spatial modulation of vibronic conduc-

tance in conjugated oligophenylenes on boron nitride, Nano Lett. **15**, 2242 (2015).

[20] M. Wang, M. Kim, D. Odkhuu, N. Park, J. Lee, W.-J. Jang, S.-J. Kahng, R. S. Ruoff, Y. J. Song, and S. Lee, Catalytic transparency of hexagonal boron nitride on copper for chemical vapor deposition growth of large-area and high-quality graphene, ACS Nano **8**, 5478 (2014).

[21] S. K. Jang, J. Youn, Y. J. Song, and S. Lee, Synthesis and characterization of hexagonal boron nitride as a gate dielectric, Sci. Rep. **6**, 30449 (2016).

[22] S. K. M. Henze, O. Bauer, T.-L. Lee, M. Sokolowski, and F. S. Tautz, Vertical bonding distances of PTCDA on Au(111) and Ag(111): Relation to the bonding type, Surf. Sci. **601**, 1566 (2007).

[23] O. Bauer, G. Mercurio, M. Willenbockel, W. Reckien, C. H. Schmitz, B. Fiedler, S. Soubatch, T. Bredow, F. S. Tautz, and M. Sokolowski, Role of functional groups in surface bonding of planar π-conjugated molecules, Phys. Rev. B **86**, 235431 (2012).

[24] S. Weiß, I. Krieger, T. Heepenstrick, S. Soubatch, M. Sokolowski, and F. S. Tautz, Determination of the adsorption geometry of PTCDA on the Cu(100) surface, Phys. Rev. B **96**, 075414 (2017).

[25] A. Gerlach, S. Sellner, F. Schreiber, N. Koch, and J. Zegenhagen, Substrate-dependent bonding distances of PTCDA: A comparative x-ray standing-wave study on Cu(111) and Ag(111), Phys. Rev. B **75**, 045401 (2007).

[26] Y. Zou, L. Kilian, A. Schöll, Th. Schmidt, R. Fink, and E. Umbach, Chemical bonding of PTCDA on Ag surfaces and the formation of interface states, Surf. Sci. **600**, 1240 (2006).

[27] S. Duhm, A. Gerlach, I. Salzmann, B. Bröker, R. L. Johnson, F. Schreiber, and N. Koch, PTCDA on Au(111), Ag(111) and Cu(111): Correlation of interface charge transfer to bonding distance, Org. Electron. **9**, 111 (2008).

[28] A. Hauschild, R. Temirov, S. Soubatch, O. Bauer, A. Schöll, B. C. C. Cowie, T.-L. Lee, F. S. Tautz, and M. Sokolowski, Normal-incidence x-ray standing-wave determination of the adsorption geometry of PTCDA on Ag(111): Comparison of the ordered room-temperature and disordered low-temperature phases, Phys. Rev. B **81**, 125432 (2010).

[29] L. Kilian, A. Hauschild, R. Temirov, S. Soubatch, A. Schöll, A. Bendounan, F. Reinert, T.-L. Lee, F. S. Tautz, M. Sokolowski, and E. Umbach, Role of Intermolecular Interactions on the Electronic and Geometric Structure of a Large π-Conjugated Molecule Adsorbed on a Metal Surface, Phys. Rev. Lett. **100**, 136103 (2008).

[30] L. Kilian, E. Umbach, and M. Sokolowski, Molecular beam epitaxy of organic films investigated by high resolution low energy electron diffraction (SPA-LEED): 3,4,9,10-perylenetetracarboxylicacid-dianhydride (PTCDA) on Ag(111), Surf. Sci. **573**, 359 (2004).

[31] T. Ogawa, K. Kuwamoto, S. Isoda, T. Kobayashi, and N. Karl, 3,4:9,10-Perylenetetracarboxylic dianhydride (PTCDA) by electron crystallography, Acta Crystallogr., Sect. B **55**, 123 (1999).

[32] F. S. Tautz, Structure and bonding of large aromatic molecules on noble metal surfaces: The example of PTCDA, Prog. Surf. Sci. **82**, 479 (2007).

[33] M. Rohlfing, R. Temirov, and F. S. Tautz, Adsorption structure and scanning tunneling data of a prototype organic-inorganic

A.2 Quantitative analysis of the electronic decoupling of an organic semiconductor molecule at a metal interface by a monolayer of hexagonal boron nitride

115

interface: PTCDA on Ag(111), Phys. Rev. B **76**, 115421 (2007).

[34] O. Bauer, Surface bonding of a functionalized aromatic molecule: Adsorption configurations of PTCDA on coinage metal surfaces, Ph.D. thesis, University of Bonn, 2014.

[35] N. Dori, M. Menon, L. Kilian, M. Sokolowski, L. Kronik, and E. Umbach, Valence electronic structure of gas-phase 3,4,9,10-perylene tetracarboxylic acid dianhydride: Experiment and theory, Phys. Rev. B **73**, 195208 (2006).

[36] P. Puschnig *et al.*, Energy ordering of molecular orbitals, J. Phys. Chem. Lett. **8**, 208 (2017).

[37] M. E. Straumanis and L. S. Yu, Lattice parameters, densities, expansion coefficients and perfection of structure of Cu and of Cu-In α phase, Acta Crystallogr., Sect. A **25**, 676 (1969).

[38] C. Wagner, N. Fournier, F. S. Tautz, and R. Temirov, Measurement of the Binding Energies of the Organic-Metal Perylene-Teracarboxylic-Dianhydride/Au(111) Bonds by Molecular Manipulation Using an Atomic Force Microscope, Phys. Rev. Lett. **109**, 076102 (2012).

[39] A. Bondi, van der Waals volumes and radii, J. Phys. Chem. **68**, 441 (1964).

[40] J. Zegenhagen and A. Kazimirov, *The X-Ray Standing Wave Technique - Principles and Applications* (World Scientific, Singapore, 2013).

[41] F. C. Bocquet, G. Mercurio, M. Franke, G. van Straaten, S. Weiß, S. Soubatch, C. Kumpf, and F. S. Tautz, Torricelli: A software to determine atomic spatial distributions from normal incidence x-ray standing wave data, Comput. Phys. Commun. **235**, 502 (2019).

[42] X. Yang, I. Krieger, D. Lüftner, S. Weiß, T. Heepenstrick, M. Hollerer, P. Hurdax, G. Koller, M. Sokolowski, P. Puschnig, M. G. Ramsey, F. S. Tautz, and S. Soubatch, On the decoupling of molecules at metal surfaces, Chem. Commun. **54**, 9039 (2018).

[43] P. Feulner and D. Menzel, Simple ways to improve flash desorption measurements from single-crystal surfaces, J. Vac. Sci. Technol. **17**, 662 (1980).

[44] H. Schlichting and D. Menzel, High resolution, wide range, thermal desorption spectrometry of rare gas layers: sticking, desorption kinetics, layer growth, phase transitions, and exchange processes, Surf. Sci. **272**, 27 (1992).

[45] B. Lehner, M. Hohage, and P. Zeppenfeld, The influence of long-range lateral interactions on the thermodynamics and kinetics of thermal desorption, Chem. Phys. Lett. **379**, 568 (2003).

[46] T. Wagner, H. Karacuban, and R. Möller, Analysis of complex thermal desorption spectra: PTCDA on copper, Surf. Sci. **603**, 482 (2009).

[47] See Supplemental Material at http://link.aps.org/supplemental/10.1103/PhysRevB.99.121404 for the experimental determination of the adsorption energy of PTCDA on hBN/Cu(111).

[48] J. Ikonomov, O. Bauer, and M. Sokolowski, Highly ordered thin films of perylene-3,4,9,10-tetracarboxylic acid dianhydride (PTCDA) on Ag(100), Surf. Sci. **602**, 2061 (2008).

[49] J. Ikonomov, C. H. Schmitz, and M. Sokolowski, Diffusion-limited island decay of PTCDA on Ag(100): Determination of the intermolecular interaction, Phys. Rev. B **81**, 195428 (2010).

[50] M. Schwarz, D. A. Duncan, M. Garnica, J. Ducke, P. S. Deimel, P. K. Thakur, T.-L. Lee, F. Allegretti, and W. Auwärter, Quantitative determination of a model organic/insulator/metal interface structure, Nanoscale **10**, 21971 (2018).

[51] J. Kerfoot, V. V. Korolkov, A. S. Nizovtsev, R. Jones, T. Taniguchi, K. Watanabe, I. Lesanovsky, B. Olmos, N. A. Besley, E. Besley, and P. H. Beton, Substrate-induced shifts and screening in the fluorescence spectra of supramolecular adsorbed organic monolayers, J. Chem. Phys. **149**, 054701 (2018).

Supplemental Material

Electronic decoupling of an organic semiconductor molecule at a metal interface by a monolayer of hexagonal boron nitride

Christine Brülke,[1] Timo Heepenstrick,[1] Ina Krieger,[1] Beatrice Wolff,[1] Xiaosheng Yang,[2,3] Ali Shamsaddinlou,[2,3]
Simon Weiß,[2,3] François C. Bocquet,[2,3] F. Stefan Tautz,[2,3] Serguei Soubatch,[2,3] and Moritz Sokolowski[1]

[1]*Universität Bonn, Institut für Physikalische und Theoretische Chemie, Wegelerstr. 12, 53115 Bonn, Germany*
[2]*Forschungszentrum Jülich, Peter Grünberg Institut (PGI-3), 52425 Jülich, Germany*
[3]*Jülich Aachen Research Alliance (JARA), Fundamentals of Future Information Technology, 52425 Jülich, Germany*

THERMAL DESORPTION SPECTRA OF PTCDA ON HBN/CU(111)

Fig. 1(a) gives an overview on a series of temperature programmed desorption (TPD) spectra of PTCDA films of different thicknesses. We monitored the desorption rate $(-\frac{\mathrm{d}\theta}{\mathrm{d}t})$ at the mass-to-charge ratio $m/z = 392$ amu, using a quadrupole mass spectrometer equipped with a Feulner cup [1]. The spectra show two peaks: a high temperature peak which saturates and which corresponds to the first PTCDA layer adsorbed directly on the hBN/Cu(111) surface, called monolayer in the following, and a non-saturating peak at lower temperatures corresponding to further layers on top of the monolayer, called multilayers in the following. The integrated areas under the TPD spectra resemble the total quantities of desorbing molecules. We find that these numbers are proportional to the deposited amounts of molecules which we determined by integrating the flux from the deposition source over time. This revealed that the sticking coefficient is constant and that PTCDA desorbs intact and completely from the hBN/Cu(111) surface. This situation thus differs from that found on the more reactive metal surfaces, e.g. Ag(111) [2] or Ag(100) [3], where the stronger bonding to the surface causes the disintegration of the PTCDA molecules upon heating. In the following, the coverages (θ) or film thicknesses are calibrated in numbers of monolayers (ML).

The multilayer peak shows a zero-order desorption behavior with a common leading edge of spectra belonging to different film thicknesses and a sharp declining edge. Such a zero-order desorption is typical for multilayer films and corresponds to desorption from a non-depleting reservoir of molecules. Quantitatively, the spectra are described by the *Polanyi-Wigner* equation:

$$-\frac{\mathrm{d}\theta}{\mathrm{d}t} = k_m\,\theta^m \exp\left(-\frac{E_{\mathrm{des}}}{k_{\mathrm{B}}T}\right), \qquad (1)$$

where m denotes the order (here $m = 0$), k_m the pre-exponential factor (attempt frequency), and k_{B} the Boltzmann constant. We used a 20 ML spectrum of good statistics to determine the desorption energy $E_{\mathrm{des}}^{\mathrm{mult}}$ of the multilayers by fitting its leading edge (after subtraction of the background on the low temperature side)

by eq. (1). The fit is shown in Fig. 1(b) and yields $E_{\mathrm{des}}^{\mathrm{mult}} = 2.13 \pm 0.05$ eV. This is in good agreement with the value of 2.20 ± 0.20 eV determined by Wagner et al. from multilayer desorption spectra of PTCDA on Cu(111) [4]. For the pre-eponential factor k_m we obtained a value of $(3 \pm 1) \times 10^{19}$ s^{-1} which is again in good agreement with Wagner's value $(4 \times 10^{19}$ s$^{-1})$ [4].

DESORPTION ENERGY OF PTCDA ON HBN/CU(111)

The monolayer desorption peak (Fig. 1(a)) also shows zero-order desorption characteristics with a common leading edge for varying coverages below one monolayer. We explain this desorption behavior by desorption from a two dimensional gas phase which coexists with a condensed phase of PTCDA islands on the surface. The desorption hence involves two consecutive steps: transition of a molecule from an island into the two dimensional gas phase on the surface and desorption from this gas phase into the vacuum. The islands constitute a reservoir that feeds the gas phase and grants its constant density. This makes the desorption rate independent from the coverage and a zero-order desorption kinetics is obtained for the leading edge of the monolayer desorption peak [6]. However, compared to the multilayer desorption peak, the maximum of the monolayer peak is rounded. This is understandable because, at the end of the monolayer desorption process, the islands have vanished and the density of the gas phase is not maintained further which leads to a crossover to a first-order desorption process.

For the determination of the desorption energy of the monolayer $E_{\mathrm{des}}^{\mathrm{mono}}$ we evaluated the monolayer desorption peaks according to a zero-order desorption kinetics. However, due to the smaller statistics and the above noted rounding of the peak, the monolayer peaks do not permit to perform reliable fits to their leading edges as it was possible for the multilayer peaks. Thus, we used a more robust method for the evaluation. It is motivated by the procedure used for the analysis of TPD spectra of PTCDA on Cu(111) by Wagner et al. [4] and is based on the reasonable assumption that the prefactors k_m of the multilayer and monolayer desorption are identical. This presumes that the microscopic desorption processes

A.2 *Quantitative analysis of the electronic decoupling of an organic semiconductor molecule at a metal interface by a monolayer of hexagonal boron nitride*
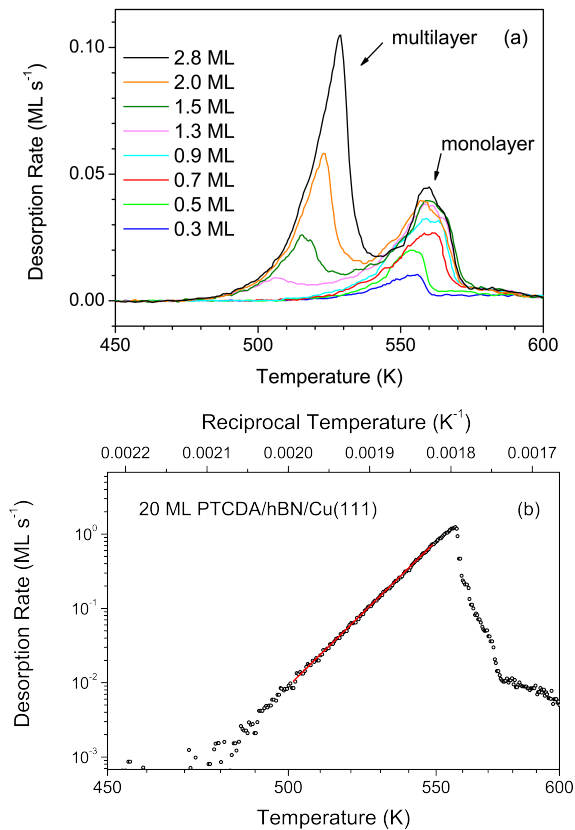
117

2

FIG. 1. (a) TPD spectra of PTCDA for different initial coverages given in number of monolayers (ML). The high temperature peak corresponds to the first layer (monolayer) adsorbed directly on the hBN/Cu(111) surface. The low temperature peak stems from the desorption of the further layers, i.e.those from the second one onward. The heating rate was 1 Ks^{-1}. (b) Arrhenius plot of the leading desorption edge of a TPD spectrum of 20 ML (reversed $1/T$ axis, *Menzel-Schlichting* plot [5]) with fitted desorption rate according to eq. (1).

monolayer, i.e. for $-d\,\theta_{multi}/d\,t(T_1) = -d\,\theta_{mono}/d\,t(T_2)$, the following equation holds:

$$\frac{E_{des}^{multi}}{T_1} = \frac{E_{des}^{mono}}{T_2}. \qquad (2)$$

Fig. 2 illustrates how we determined pairs of temperatures T_1 and T_2 from the spectra. Hereby, the desorption rate was chosen at a level that ensures that the rounding of the monolayer peak does not play a role for the shape of its leading edge. Using eq. (2) and $E_{des}^{mult} = 2.13$ eV we calculate $E_{des}^{mono} = T_2/T_1 \times 2.13$ eV and obtain $E_{des}^{mono} = 2.30 \pm 0.07$ eV. We note that an hypothetic inequality of the prefactors of the mono- and multilayer desorption by one order of magnitude would change the deduced value of E_{des}^{mono} by only ~ 0.1 eV. This makes our analysis and conclusions robust.
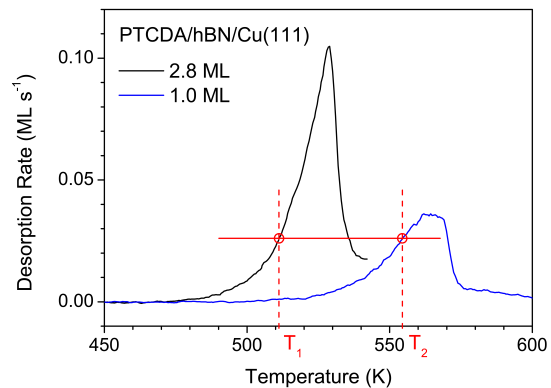
FIG. 2. Determination of the desorption energy of the monolayer from its leading edge. The horizontal line marks two temperatures T_1 and T_2 where the desorption rates of the multi- and the monolayer are identical.

of the individual molecules into the gas phase are alike in both situations. The desorption proceeds either from a two-dimensional gas phase on the hBN/Cu(111) surface (monolayer desorption) or from a two-dimensional gas phase on top of completed PTCDA layers (multilayer desorption). Because of the weak bonding of the molecule to both surfaces (a result derived from the data below and those of the main paper) and the planar adsorption geometry of the molecule on both surfaces we can expect that the partition functions of both the initial and the transition state ($Z_{initial}$ and Z_{trans}) are comparable for the two desorption processes. Thus identical prefactors ($k_m \propto Z_{trans}/Z_{initial}$ [4]) are plausible. Under this premise, eq. (1) implies that for two temperatures T_1 and T_2 which yield equal desorption rates of the multi- and

ADSORPTION ENERGIES OF PTCDA ON HBN/CU(111) AND ON DIFFERENT METAL SURFACES

For the interpretation of vertical bonding distances of PTCDA molecules in ordered layers on different surfaces which are given in the main paper the adsorption energy E_{ads} in the limit of a complete layer is the appropriate quantity. It describes the energy per molecule that is required for lifting the entire (rigid) adsorbate layer vertically from the surface into the vacuum.

We describe how we derive E_{ads} from the experimental E_{des} value of PTCDA on hBN/Cu(111). We note ahead that we assume that the desorption from the surface proceeds without a significant activation barrier. This is

TABLE I. Adsorption energies (E_{ads}) of PTCDA for ordered monolayers on different surfaces.

surface	E_{ads} (eV)	reference
hBN/Cu(111)	2.10 ± 0.09	this work
Au(111)	2.50 ± 0.10	[8]
Ag(111)	3.65	[9]
Ag(100)	4.19	[9]
Ag(110)	4.40	[9]

plausible for a weakly bonded molecule as in our case and is also indicated by the absence of an activated adsorption that would lead to a sticking factor below one. As a consequence, the desorption energies are equivalent to the adsorption energies of the reversed process. In our case, the experimental value of E_{des} describes the desorption energy of an individual molecule out of a completed layer (island) into the vacuum. Therefore E_{des} exceeds E_{ads} by the energy that is needed to break the attractive bonds of the molecule to its nearest neighbor molecules. Here, we have attractive hydrogen bond-like intermolecular interactions between the terminal anhydride groups and the hydrogen terminated sides of the perylene cores of neighboring molecules (see Fig. 1(d) of the main paper). Evidently, the value of E_{des} measured in the zero-coverage limit would better resemble E_{ads}. However, its direct determination from the TPD spectra is beyond the statistical significance of our data.

Hence, we use an alternative approach to estimate E_{ads} from E_{des} based on knowledge about the interaction energies (E_{NN}) between nearest neighbor molecules in the layer. This comes from an experiment on the ordered structure of PTCDA on the Ag(100) surface [7]. There we determined the interaction energy E_{NN} for a pair of molecules from the decay of PTCDA islands into the surrounding two dimensional gas phase by time. We obtained $E_{NN} = 102 \pm 10$ meV. This implies a total interaction energy of a molecule with its four nearest neighbor molecules of $4 \times E_{NN}/2 = 204 \pm 20$ meV. Transferring this value to the PTCDA layer on hBN/Cu(111) requires some caution: First off all, the stronger chemisorptive bonding of PTCDA to the Ag(100) surface alters the electronic and geometric structure of the molecule and consequently the intermolecular interactions. And secondly, the intermolecular arrangement differs slightly for the two systems. PTCDA on Ag(100) forms a commensurate quadratic structure [7], whereas on hBN/Cu(111), the intermolecular arrangement corresponds to that within PTCDA crystals (see the main paper). However, as the intermolecular interaction energy amounts to only about 10% of the desorption energy, we can conclude that the difference between the two systems will cause an only small systematic error of the value of E_{ads}. Hence, we deduce $E_{ads} = E_{des}^{mono} - (0.204 \pm 0.020)$ eV $= 2.10 \pm 0.09$ eV.

Tab. I compares values of E_{ads} for PTCDA on hBN/Cu(111) and on other surfaces. The values for the three canonical Ag surface were determined by density functional theory, because experimental values are not available [9]. The value for the adsorption energy of PTCDA on Au(111) refers to an isolated molecule. It was determined from a lift-off experiment performed on PTCDA molecules using an atomic force microscope (AFM) [8]. Strictly speaking, this value is not identical to the considered E_{ads} of a molecule as a part of a complete layer. However, for a weakly bonded system, as PTCDA/Au(111), we expect the impact of the intermolecular bonding on the molecule substrate interaction to be small, and therefore the adsorption energy of an isolated molecule to be very similar to that of a molecule integrated in a complete layer. This justifies to include the given value measured by AFM into our comparison. We note that this similarity is, however, not granted for stronger chemisorptive interfacial bonding. Tab. I lists the values of the adsorption energies we used to compile Fig. 4 of the main paper. As noted, no data of this kind was available for PTCDA on the Cu(111) or Cu(100) surface.

[1] P. Feulner and D. Menzel, "Simple ways to improve flash desorption measurements from single-crystal surfaces," Journal of Vacuum Science & Technology **17**, 662 (1980).

[2] L. Kilian, E. Umbach, and M. Sokolowski, "Molecular beam epitaxy of organic films investigated by high resolution low energy electron diffraction (SPA-LEED): 3,4,9,10-perylenetetracarboxylicacid-dianhydride (PTCDA) on Ag(111)," Surface Science **573**, 359 (2004).

[3] J. Ikonomov, O. Bauer, and M. Sokolowski, "Highly ordered thin films of perylene-3,4,9,10-tetracarboxylic acid dianhydride (PTCDA) on Ag(100)," Surface Science **602**, 2061 (2008).

[4] Th. Wagner, H. Karacuban, and R. Möller, "Analysis of complex thermal desorption spectra: PTCDA on copper," Surface Science **603**, 482 (2009).

[5] H. Schlichting and D. Menzel, "High-resolution, wide-range, thermal-desorption spectrometry of rare-gas layers - sticking, desorption-kinetics, layer growth, phase-transitions, and exchange processes," Surface Science **272**, 27 (1992).

[6] B. Lehner, M. Hohage, and P. Zeppenfeld, "The influence of long-range lateral interactions on the thermodynamics and kinetics of thermal desorption," Chemical Physics Letters **379**, 568 (2003).

[7] J. Ikonomov, C. H. Schmitz, and M. Sokolowski, "Diffusion-limited island decay of PTCDA on Ag(100): Determination of the intermolecular interaction," Physical Review B **81**, 195428 (2010).

[8] C. Wagner, N. Fournier, F. S. Tautz, and R. Temirov, "Measurement of the Binding Energies of the Organic-Metal Perylene-Teracarboxylic-Dianhydride/Au(111) Bonds by Molecular Manipulation Using an Atomic Force Microscope," Physical Review Letters **109**, 076102

A.2 Quantitative analysis of the electronic decoupling of an organic semiconductor molecule at a metal interface by a monolayer of hexagonal boron nitride

119

4

(2012).

[9] O. Bauer, G. Mercurio, M. Willenbockel, W. Reckien, C. H. Schmitz, B. Fiedler, S. Soubatch, T. Bredow, F. S. Tautz, and M. Sokolowski, "Role of functional groups in

surface bonding of planar π-conjugated molecules," Physical Review B **86**, 235431 (2012).

A.3 "The influence of an interfacial hBN layer on the fluorescence of an organic molecule"

by Christine Brülke, Oliver Bauer, and Moritz Sokolowski

published in: Beilstein Journal of Nanotechnology **11**, 1663 (2020).

BEILSTEIN JOURNAL OF NANOTECHNOLOGY

The influence of an interfacial hBN layer on the fluorescence of an organic molecule

Christine Brülke, Oliver Bauer and Moritz M. Sokolowski[*]

Abstract

We investigated the ability of a single layer of hexagonal boron nitride (hBN) to decouple the excited state of the organic molecule 3,4,9,10-perylene tetracarboxylic dianhydride (PTCDA) from the supporting Cu(111) surface by Raman and fluorescence (FL) spectroscopy. The Raman fingerprint-type spectrum of PTCDA served as a monitor for the presence of molecules on the surface. Several broad and weak FL lines between 18,150 and 18,450 cm^{-1} can be detected, already from the first monolayer onward. In contrast, FL from PTCDA on a bare Cu(111) surface is present only from the second PTCDA layer onward. Hence, a single layer of hBN decouples PTCDA from the metal substrate to an extent that a weak radiative FL decay of the optical excitation can occur. The different FL lines can be ascribed to different environments of the adsorption sites, namely molecules adsorbed at surface defects, in large ordered domains, and located in the second layer.

Introduction

In recent years, two-dimensional materials (2DMs) have been established as a highly interesting field of studies, both in regard to their fundamental physical properties as well as their potential for technical applications [1]. Specifically, the use of 2DMs in layered heterostructures has been promoted [2,3]. Here, one challenge lies in the understanding of not only the processes in the individual materials, but also of those that occur at the interfaces between layers of different materials.

Advantageously, some 2DMs can be grown directly on metal substrates by chemical vapor deposition [2]. This is, for example, exploited when a 2DM interfacial layer is inserted between the metallic electrode and a functional organic layer of an organic electronic device, such as an organic light emitting diode [3]. The purpose of the interfacial layer is to achieve a separation or "decoupling" of the two adjacent layers. Here, the term decoupling refers to the spatial separation of the electronic
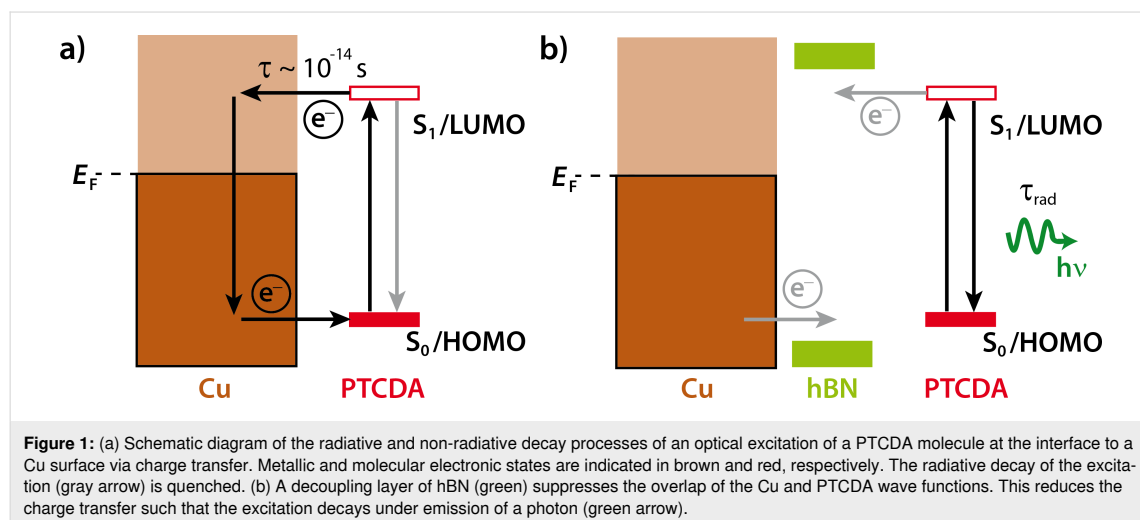
states of the molecules and those of the underlying metal, which leads to unperturbed molecular properties [4]. A scientifically relevant question is to which extent decoupling of the organic molecules from a metal electrode is achieved when a 2DM layer in the limit of a single interfacial layer, for example, a monolayer of hexagonal boron nitride (hBN), is used.

Such a decoupling is achieved when the wave functions of the metal are spatially separated from those of the molecule leading to a reduced overlap. The overlap of molecular and metallic wave functions has, in particular, an impact on excited molecular states. For fluorescent molecules, this is observed as a strongly reduced quantum yield of the fluorescence (FL) due to non-radiant decay processes via the metal states. This phenomenon is generally referred to as "quenching" [5]. When the decoupling is not efficient, a fast and non-radiative decay of the excitation of the molecule via the metallic states prevails. Therefore, the probing of the FL of a molecule located at the outer surface of a 2DM layer grown on a metal characterizes the degree of electronic coupling of the molecular and metallic states.

For completeness, we note that quenching of an electronic excitation of a molecule in the first layers on a metal surface can be the result of interfacial charge transfer (CT) [5] or of energy transfer [6]. Here, CT is in our focus since energy transfer, although additionally present, varies less abruptly on the scale of single layers [7]. A simple energy diagram of the CT process of a fluorescent molecule across interfaces is depicted in Figure 1. As an example, we use the sample system of this work, namely, 3,4,9,10-perylene tetracarboxylic dianhydride (PTCDA) on a layer of hBN on Cu(111). Here, we consider an S_1 excitation which involves mainly a HOMO/LUMO (highest occupied and lowest unoccupied molecular orbital) electronic excitation. Rapid CT leads to a delocalization of the excited electron from the LUMO into unoccupied metallic states and/or a filling of the HOMO by an electron from the metal. We note that the HOMO and LUMO for the chemisorbed molecule differ from those of the gas phase molecule. Thus, the LUMO that is drawn in Figure 1a is not identical to the LUMO in the gas phase. For a second molecular layer, even without significant overlap of the wave functions of metal and molecule, quenching is also possible, because the CT may occur from the second layer to the metal via states in the first layer [5].

In principle, the hybridization of molecular and metallic states and the dynamical CT in the excited state can be probed by photoemission spectroscopy (PES). In particular, core hole clock spectroscopy has been used to measure the time constant of dynamical CT in the valence band states as a function of the lifetime of the core hole, which is typically of the order of 10^{-14} s [8,9]. However, this technique is insensitive to a CT process of a considerably longer time constant. A technique for detecting CT processes with a longer time constant is FL spectroscopy, in which the CT process competes with the radiative fluorescent decay of the excitation. It constitutes an alternative and non-radiative decay channel for the excited state. Typically, the FL lifetime of the excited state S_1 is of the order of ca. 10^{-9} s [5]. Hence, a CT process with a time constant that is not significantly larger will reduce the FL yield (see Figure 1). Thus, even a very small overlap of states becomes evident in the experiment as it causes a reduction of the FL yield (i.e., quenching). The degree of quenching may vary and, hence, lead to different branching ratios between the radiative and non-radiative channels. In order to obtain high FL yields of molecules on metallic substrates, thin interfacial films of consider-

Figure 1: (a) Schematic diagram of the radiative and non-radiative decay processes of an optical excitation of a PTCDA molecule at the interface to a Cu surface via charge transfer. Metallic and molecular electronic states are indicated in brown and red, respectively. The radiative decay of the excitation (gray arrow) is quenched. (b) A decoupling layer of hBN (green) suppresses the overlap of the Cu and PTCDA wave functions. This reduces the charge transfer such that the excitation decays under emission of a photon (green arrow).

able thickness (5–10 monolayers) of alkali halides have been used in our lab [10]. In contrast, experiments on the light emission from molecules induced by scanning tunneling microscopy (STM-LE) required thin alkali halide films of two monolayers thickness in order to support tunneling [11-13].

A single layer or films of hBN are attractive for decoupling a molecule from an underlying metal substrate as hBN exhibits a wide bandgap of 5.9 eV [14]. Perspectively, it could also provide a substrate for STM-LE experiments. Furthermore, it is of interest due to its mechanical [15], chemical [16], and thermal [17] stability, the easy synthesis of hBN monolayers on Cu foils for usage in devices [18], and, finally, the wide structural variety of hBN monolayers depending on the underlying metal substrate [19].

To investigate the decoupling of an organic molecule from a metal substrate by a monolayer of hBN we chose PTCDA and the Cu(111) surface. PTCDA serves as a planar model molecule for investigations of organic layers on surfaces [20-23]. Monolayers of hBN on Cu(111) have been investigated by several groups and are, hence, rather well understood [24-29]. In particular, we found that hBN on Cu(111) forms a flat layer at a relatively large vertical distance from the Cu(111) top layer of 3.24 Å using an X-ray standing-waves analysis [30]. This large distance is, in principle, in agreement with the results reported independently by Schwarz and co-workers [31]. Large distances of the molecule with respect to the hBN and the metal interface are expected to be beneficial for the decoupling because the metal wave functions decrease exponentially into the vacuum.

We have previously shown that the bonding situation between PTCDA and hBN/Cu(111) is weak and physisorptive [32] as opposed to the chemisorptive bond between PTCDA and Cu(111) [33]. Ultraviolet photoelectron spectroscopy (UPS) experiments showed that on the Cu(111) surface the chemical bonding leads to a filling of the LUMO [33]. In contrast, on hBN/Cu(111), the differential energies of the PTCDA orbitals remain unaltered in comparison to those of PTCDA in the gas phase, which points to a more physisorptive bonding to the hBN/Cu(111) surface [32]. The HOMO of PTCDA is found at ca. 2.6 eV [32]. Hence, we can expect that both the LUMO and the HOMO are placed within the bandgap of hBN, as indicated in Figure 1b. This is in agreement with the findings by Martínez-Galera et al. for PTCDA/hBN/Rh(110) [34]. From scanning tunneling spectroscopy (STS) experiments, the authors concluded that the coupling is only weak. They deduced further that the CT (in the ground state) between molecule and substrate, if present at all, is small. These differences between PTCDA/hBN/Cu(111) and PTCDA/Cu(111) are also mirrored

by their vertical molecular structures. The hybridization of the electronic states of PTCDA and Cu leads to a distortion of the molecule where the oxygen atoms are pushed away from the substrate and out of the molecular plane [35]. On hBN/Cu(111), the molecule remains essentially flat and at a very large vertical distance from the hBN layer of 3.37 Å [32]. In contrast, on Cu(111) the vertical distance of the perylene core from the Cu(111) surface is only 2.66 Å [35]. This again points to a difference in the bonding character on the two surfaces.

Several studies have probed the influence of the adsorption on metal-supported hBN layers on the electronic structure of large organic molecules, namely their frontier orbitals, by PES [36] or STS [37,38]. However, to the best of our knowledge, there have been no studies on the FL of monolayers of molecules on metal-supported hBN layers, yet. Kerfoot et al. [22] studied the FL of PTCDA and perylene-3,4,9,10-tetracarboxylic-3,4,9,10-diimide (PTCDI) on an exfoliated hBN monolayer that was transferred onto SiO_2. Forker et al. [23] investigated the optical absorption properties of PTCDA on hBN/Rh(111) and hBN/Pt(111).

Here, we report a direct comparison of FL spectra of PTCDA/hBN/Cu(111) and PTCDA/Cu(111), which allows for a relative determination of the efficiency of the hBN layer to decouple the excited states of PTCDA from Cu(111). For PTCDA on Ag(111) and Au(111) [39], it has been shown that FL can only be observed from the second and third molecular layer onward. The excitation of the first layers is completely quenched by the metal substrates as described above. In UPS experiments, a partial filling of the LUMO of PTCDA was found on Ag(111), but not on Au(111) [33]. Thus, the quenching on Ag(111) is directly understood by the static charge transfer seen in UPS. The quenching on Au(111), not as evident from UPS, demonstrates the sensitivity of FL spectroscopy to an overlap of wave functions of excited states. Accordingly, the same behavior as on Ag(111) can be expected on Cu(111), where a filling of the LUMO has been found, too [33]. In addition, for multilayer PTCDA films we can compare the first, interfacial PTCDA layer with a hBN layer regarding their abilities to decouple the next PTCDA layer from the Cu(111) substrate.

In this contribution, we will discuss Raman modes and several different FL lines of PTCDA that were observed on both hBN/Cu(111) and Cu(111). For an effective comparison, the structures and the growth modes of the PTCDA layers are relevant. Details of the structural investigation of the two surfaces, including low-energy electron diffraction (LEED) patterns, are given in Appendix A. Since the interpretation of the optical data requires this knowledge, we summarize some details ahead here. PTCDA forms ordered structures and follows a layer-by-

layer growth for at least the first three layers on Cu(111) and the first two layers on hBN/Cu(111). We are able to distinguish PTCDA/hBN/Cu(111) from PTCDA/Cu(111), as well as the monolayer and multilayers of PTCDA on Cu(111) and hBN/Cu(111) by differences in the respective LEED patterns.

Experimental

All experiments were carried out in an ultrahigh-vacuum chamber with a base pressure of 2.3×10^{-10} mbar. The Cu(111) sample could be heated up to 1100 K via a tungsten filament and electron bombardment and cooled down to 20 K by using liquid helium.

The hBN layer was grown by dosing the precursor borazine [$(HBNH)_3$] into the chamber while the sample was held at 1010 K. Borazine was purchased from Katchem spol. s r. o., Czech Republic (http://www.katchem.cz). It was kept in a glass tube connected to the chamber via a dosing valve at constantly -5 °C. Prior to the hBN preparation, it was cleaned by three cycles of freezing the liquid borazine using liquid N_2 and pumping away the gas phase above the frozen borazine. The composition of the gas phase in the borazine source was monitored by a quadrupole mass spectrometer (QMS). It was considered suitable for hBN preparation when the signals for H_2 (a product of the decomposition of borazine that is known to occur even when stored at low temperatures, *m/z* 2) and borazine (*m/z* 80) showed a ratio of approximately 1:1.

The clean Cu(111) surface was prepared by consecutive steps of sputtering for 30 min with Ar^+ ions (1000 eV, 4 µA) and annealing at 1010 K for 30 min. After the last sputtering cycle, the Cu(111) sample was heated to 1010 K and ca. 2000 L borazine were dosed (1.5×10^{-6} mbar via the background for 30 min) onto the sample held at 1010 K. After stopping the borazine dosing, the sample was cooled down with 1 K·s⁻¹. The structural quality of the bare Cu(111) surface, the hBN layers, and the PTCDA layers was checked by LEED. We used a SPA-LEED instrument as described in [30]. An additional annealing step between the last sputter cycle and the borazine deposition was omitted here in order to prevent segregation of chemical impurities from the Cu bulk to the surface, which we otherwise occasionally observed as additional LEED spots. The criteria for a good hBN layer were a sharp continuous ring of intensity with a radius that is 2% larger than the distance of the first-order Cu spots from the specular spot and the appearance of a clear star-like pattern of satellites around the specular spot caused by multiple electron scattering as reported in [30].

PTCDA was evaporated from a glass crucible. The molecular flux was also monitored by the QMS at *m/z* 392, which corresponds to the mass of the non-fractured PTCDA molecule. The flux was typically one monolayer per minute. During deposition, the sample was held at a constant temperature. PTCDA layers on Cu(111) were prepared by keeping the sample at a temperature of either 20 or 300 K during deposition. PTCDA layers on hBN/Cu(111) were prepared by deposition at a sample temperature of 20 K and subsequent annealing. The sample was annealed in iterative steps of heating, holding at a constant temperature for 3 min, and cooling down again to 20 K for a measurement. The annealing temperatures were in the range of 100–400 K and are specified below. In the following, one monolayer (ML) of PTCDA refers to a single layer of close-packed, flat-lying PTCDA molecules. After every experiment, the exact coverage was determined by a thermally programmed desorption (TPD) experiment with a margin of error of ±0.05 ML. The calibration for PTCDA/hBN/Cu(111) was derived from the TPD data shown in [32]. Since the packing densities of PTCDA on hBN/Cu(111) and on Cu(111) are within a few percent of each other (see Appendix A), this calibration is also valid for PTCDA/Cu(111) within the noted margin of error.

For the optical experiments, the sample was transferred into a glass tube, standing out from the end of the chamber. In the glass tube, the sample was illuminated by a focused laser beam at an incident angle of approximately 45° with respect to the surface normal. The diameter of the laser spot on the sample was about 0.5 mm. The fluorescence and Raman scattered light from the sample was collected and parallelized by an achromatic lens and focused by a second achromatic lens onto the entrance slit of the spectrometer. The spectrometer (Acton, Spectra Pro 2300i, $f = 0.3$ m) was operated with three different gratings (300, 600, and 1200 grooves per millimeter, yielding a resolution of 48, 24, and 12 cm⁻¹, respectively). It was equipped with a nitrogen-cooled CCD camera, operated at -110 °C. In order to block external stray light from entering the spectrometer, the glass tube, the lenses and the entrance slit of the spectrometer were enclosed by a black box. If not specified otherwise, we used an optically pumped cw semiconductor laser (Coherent Sapphire LP UBB CDRH) with a wavelength of 458 nm (photon energy of 2.698 eV or 21,816 cm⁻¹) and $P = 50$ mW. To block the laser light from entering the spectrometer, a long-pass filter (cut-off at 475 nm) was positioned in front of the entrance slit of the spectrometer. All spectra were recorded at a sample temperature of 20 K with an exposure time of 2 s, 50 accumulations, and a slit width of the spectrometer of 0.1 mm.

Results and Discussion
1 Overview of the spectra
Figure 2 shows overview spectra of 1.55 ML PTCDA on Cu(111) (red spectrum) and 0.50 ML PTCDA on hBN/Cu(111)

(blue spectrum). PTCDA on Cu(111) was deposited at a sample temperature of 300 K and the LEED pattern confirmed the formation of a second layer (see Appendix A). PTCDA on hBN/Cu(111) was deposited at a sample temperature of 20 K and subsequently annealed at 300 K. The FL spectrum shown here is identical to the FL spectrum of PTCDA deposited at a sample temperature of 300 K, which showed the LEED pattern in Figure 8b (see below in Appendix A), revealing an ordered structure. Hence, we conclude that the blue FL spectrum shown in Figure 2, which is, as it will become clear, relevant for the comparison with PTCDA/Cu(111), also stems from an ordered PTCDA layer on hBN/Cu(111).
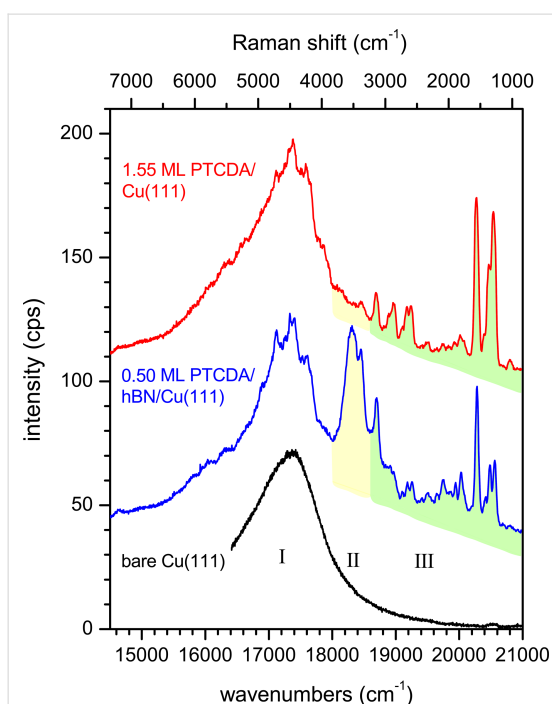
Figure 2: Overview spectra of 1.55 ML PTCDA on Cu(111) (red), of 0.50 ML PTCDA on hBN/Cu(111) (blue), and of the clean Cu(111) surface (black). For preparation details, see text. We distinguish three regions I, II, and III. The sharp lines marked in green are Raman modes (region III). The features marked in yellow are assigned to fluorescence (region II). The broadest feature on the low-energy side is due to defect luminescence of the Cu substrate (region I). All spectra were measured at 20 K using a grating with 300 grooves per millimeter. The spectra are shifted vertically for clarity.

For the discussion of the spectra, we consider three regions (I–III). At first glance, two of these regions appear qualitatively rather equal for both substrates: On the low-energy side below 18,000 cm^{-1} (region I) a broad luminescence can be observed and on the high-energy side above 18,600 cm^{-1} (region III), there is a set of sharp peaks. However, the two spectra differ significantly between 18,000 and 18,600 cm^{-1} (region II) due to

broad FL peaks (highlighted in yellow) present for hBN/Cu(111), but absent for PTCDA/Cu(111).

We tentatively assign the broad peak in region I to a radiative decay of interband transitions from the Cu substrate, as it can also be observed on the clean substrates (Cu(111) and hBN/Cu(111)) before PTCDA deposition when all other features are absent (see Figure 2, black spectrum). An enhancement of radiative interband transitions has been reported for Cu nanoparticles [40]. We thus speculate that surface defects (protrusions) play a role here. This is in agreement with our observation that the intensity of this "defect luminescence" in region I depends on the exact position of the spot of the excitation light on the sample. It will not be in the focus of this work. The sharp peaks in region III are identified as Raman lines from PTCDA (highlighted in green). The Raman lines were additionally identified by using a dye laser with tunable wavelength [20] (497–507 nm). These peaks shift according to the wavelength of the laser (see Appendix B). Notably, some Raman peaks are superposed in the region of the defect luminescence of the Cu(111) surface (region I), too.

2 Raman modes
First, we will discuss the Raman lines. The peaks in the spectrum between 21,000 and 18,600 cm^{-1} in Figure 2 exhibit Raman shifts that correspond to the energies of the vibrational modes of PTCDA adsorbed on surfaces observed before [41,42]. The vibronic modes of PTCDA that can be observed in Raman spectroscopy are A_g, B_{1g}, B_{2g}, and B_{3g} modes, with the most prominent modes being A_g modes between 1,250 and 1,650 cm^{-1} [41-43]. The spectral positions of most of these modes are about constant for PTCDA adsorbed on different substrates [41] or for different film thicknesses [42]. An interesting exception was observed for PTCDA on Ag(111) [42] for the breathing mode of the central carbon ring at ca. 1,300 cm^{-1}. In the following, we will refer to it as ring breathing (RB) mode. On Ag(111), two different adsorption states of PTCDA were observed. Both states are bonded chemisorptively to the surface [44]. The RB mode of PTCDA deposited at a low temperature (LT) of 180 K exhibits a Raman shift of 1,310 cm^{-1}. This is higher in energy by 13 cm^{-1} compared to the Raman shift (1,297 cm^{-1}) for the RB mode of a layer at room temperature (RT) [42]. The special role of this RB mode will be discussed in further detail below.

2.1 Surface-enhanced Raman scattering
The fact that the Raman modes of a small quantity of molecules can be observed here at all is attributed to surface-enhanced Raman scattering (SERS) [45]. This effect is most commonly observed on rough surfaces of noble metals [45] or at metal nanostructures [46], and it is utilized in surface-enhanced

Raman spectroscopy [47]. There are two explanations for it, namely, a chemical mechanism and an electromagnetic mechanism, which is thought to be the dominant contribution to the enhancement. The chemical mechanism is related to the specific chemical surface bonding of the investigated system. At its heart, a CT between the molecule and the substrate occurs due to the chemisorptive bonding, which leads to a change in the polarizability of the molecule and thus to an enhancement of the Raman signal. It is also possible that electronic excitations of the adsorbed molecule allow for a resonance Raman effect, which causes an additional enhancement [46]. According to the electromagnetic mechanism, on a rough surface, surface plasmon polaritons (SPPs) can also be excited by the incident light. The surface plasmons are located in the vicinity of surface defects, such as protrusions. The field enhancement at these defects leads to an enhancement of the Raman scattering [48]. Subsequently, the scattered light can be enhanced in the same manner. The electromagnetic mechanism may be responsible for an enhancement of the signal by a factor of 10^5–10^6 [48]. The contribution of the chemical mechanism is generally much smaller, causing an enhancement by a factor of not more than 10^2–10^3 [46].

Recently, hBN has gained interest as a SERS substrate [49]. In a comparative study on 2DMs on SiO$_2$ it was shown that hBN had an enhancement effect on the Raman modes of adsorbed copper phthalocyanine molecules [50]. The effect was explained by the polar character of the B–N bonds, which induced a dipole in the adsorbed molecule. The resulting interfacial dipole–dipole interactions are thought to have a similar effect on the polarizability of the adsorbed molecule as a CT.

Regarding the Raman enhancement effect of a noble metal surface, we mention a recent study by Stallberg et al. [39], which investigated optical spectra of PTCDA on Ag(111) and Au(111). They found Raman modes of PTCDA on the Au(111) surface, but not on the Ag(111) surface. This observation was discussed in view of the different energies of the SPPs of the two surfaces. Stallberg et al. used photon energies of 2.37 eV on Au(111) and 2.43 eV on Ag(111) and concluded that only the SPP of Au(111) located at $E_{\text{SPP}}^{\text{Au}}$ = 2.5 eV can resonantly interact with the incident light, leading to an enhancement of the Raman modes. The SPP on the Ag(111) surface has an energy of $E_{\text{SPP}}^{\text{Ag}}$ = 3.7 eV. Hence, a resonance was considered less probable, yielding no enhancement of Raman modes. This model should evidently encompass that the coupling to the SPPs requires a rough surface or local protrusions on the surface due to defects that break the translational symmetry. For comparison, we note that the energy of the SPP of Cu(111), which is calculated from the condition $-\text{Im}(\varepsilon^{-1}) = \varepsilon_2 / (\varepsilon_1^2 + \varepsilon_2^2)$ [51] using the dielectric functions given in [52], is obtained at a

value of $E_{\text{SPP}}^{\text{Cu}}$ = 2.3 eV. Our excitation energy was 2.698 eV. From our experiment we have indeed evidence that SERS is related to surface defects. This will be discussed in Section 2.3.

2.2 Raman modes of PTCDA on hBN/Cu(111) and Cu(111)

Figure 3a and Figure 3b show region III of the spectra of PTCDA on hBN/Cu(111) and Cu(111) for Raman shifts of 1,240 to 1,660 cm^{-1} in detail. All Raman shifts are also summarized in Table 1. Some values are given as averages for different coverages as no trends as a function of the coverage were found (see caption). First, we discuss spectra of PTCDA on hBN/Cu(111) and Cu(111), which were both stable under annealing at 300 K (cf. Figure 3a) and, hence, represent the final state. Kinetic effects do not play a role here. In Section 2.2.2, we focus on temperature-dependent effects (cf. Figure 3b).

2.2.1 The final state – 300 K spectra: Figure 3a shows Raman modes of PTCDA/hBN/Cu(111) after deposition at 20 K and subsequent annealing at 300 K (blue), and of PTCDA/Cu(111) after deposition at 300 K (red). The positions of the Raman modes of 1 ML PTCDA/Ag(111) measured by Schneider and Wagner [42,53], which was deposited at a sample temperature of 400 K, are indicated by green vertical bars for comparison. It is apparent from Figure 3a that the modes of PTCDA/hBN/Cu(111) are systematically shifted to smaller energies by about 7 cm^{-1} compared to PTCDA/Cu(111). In contrast, the modes of PTCDA/Ag(111) [53] agree well with the modes of PTCDA/Cu(111) within 0.3%. An exception is the RB mode. This mode will be discussed separately below. The shift of the other modes to higher vibrational energies seen in comparison of hBN/Cu(111) and the metal surfaces Cu(111) and Ag(111) can be linked to the different bonding of PTCDA to the surfaces. In UPS experiments [33], a chemisorptive interaction of the metal surfaces with the PTCDA molecule was found, leading to a (partial) filling of the former LUMO on Ag(111) and Cu(111). On PTCDA/hBN/Cu(111), no such chemisorptive bonding was observed in UPS [32]. We suppose that the energy of the vibrational modes recorded here are influenced by molecule–substrate interactions. The chemisorptive bond to the metal surface makes the intermolecular bonds harder, which causes the respective vibrational modes to increase in energy. For Raman shifts below 1,500 cm^{-1}, this interpretation is also supported by the closer agreement of the Raman modes on hBN/Cu(111) with those measured for PTCDA single crystals [55] (see Table 1). However, for modes above 1,570 cm^{-1}, the situation is reversed and not yet understood.

As mentioned before, the significance of the RB mode has been reported for PTCDA/Ag(111) [53]. The energy of this mode in-
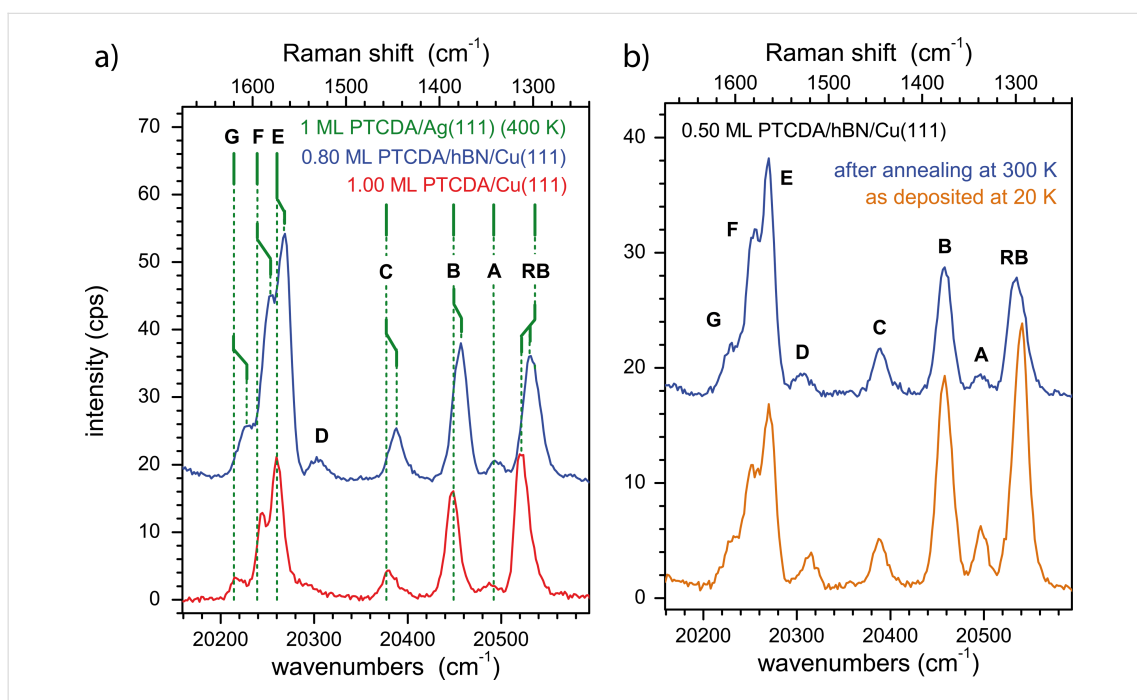
Figure 3: Zoom-in on the high-energy region (III) of the spectra. (a) 0.80 ML PTCDA/hBN/Cu(111) after deposition at 20 K and subsequent annealing at 300 K (blue) and 1.00 ML PTCDA/Cu(111) after deposition at 300 K (red). The positions of the Raman modes of 1 ML PTCDA/Ag(111) [53] are indicated in green. (b) 0.50 ML PTCDA/hBN/Cu(111) after deposition at 20 K (orange) and after subsequent annealing at 300 K (blue). All spectra were measured at 20 K using a grating with 1200 grooves per millimeter. Labels of the peaks refer to Table 1, the peaks H–K are not shown here.

Table 1: Raman shifts (in cm^{-1}) of PTCDA on hBN/Cu(111) and Cu(111), prepared at sample temperatures T_S (for details on the preparation, see text). Data were measured at 20 K. The values for PTCDA/hBN/Cu(111) are averaged for different film thicknesses (eight datasets with coverages between 0.05 and 0.80 ML for both 20 and 300 K). The error margins given are the standard deviation. The values for PTCDA/Cu(111) refer to coverages of 1.20 ML for T_S = 20 K and 1.00 ML for T_S = 300 K. For comparison, the Raman shifts of 1 ML PTCDA/Ag(111) measured by Schneider et al. [53], the vibrational energies of PTCDA/KCl/Ag(100) measured by Paulheim et al. in FL experiments [54], and the Raman shifts of the PTCDA single crystal measured by Tenne et al. [55] are listed. The ring breathing (RB) mode of the central carbon ring of PTCDA is the only mode that changes as a function of film thickness. The values for the RB mode of multilayers (RB_{multi}) refer to 5.10 ML and 8.20 ML PTCDA/hBN/Cu(111) (averaged values), 3.44 ML PTCDA/Cu(111) for T_S = 20 K, 2.55 ML PTCDA/Cu(111) for T_S = 300 K, and 60 ML PTCDA/Ag(111) [53]. The modes of PTCDA/Cu(111) with T_S = 20 K are intrinsically very small and often not observed. Those modes are listed as "n.o.".

mode	hBN/Cu(111)	hBN/Cu(111)	Cu(111)	Cu(111)	Ag(111) [53]	KCl [54]	PTCDA single crystal [55][a]
T_S	20 K	300 K	20 K	300 K	400 K	<20 K	
RB_{mono}	1296.7 ± 1.6	1301.2 ± 1.7	1304.0	1312.9	1298	1288	—
RB_{multi}	1301.8 ± 3.8	1309.8 ± 3.1	1300.0	1309.5	1309	—	1302.3
A	1339.4 ± 1.5	1339.2 ± 1.2	n.o.	1346.5	1342	1332	1335.0
B	1378.0 ± 1.0	1377.5 ± 1.5	1383.8	1386.0	1385	1368	1375.4/1383.6
C	1447.8 ± 1.5	1447.4 ± 1.7	n.o.	1454.6	1457	1446	1451.0
D	1522.4 ± 2.1	1529.4 ± 0.7	n.o.	n.o.	—	1523	—
E	1566.6 ± 1.9	1567.9 ± 2.5	1571.4	1574.0	1574	1564	1570.6
F	1582.7 ± 3.7	1582.3 ± 2.0	n.o.	1589.6	1595	1584	1589.1
G	1606.7 ± 1.7	1607.3 ± 2.0	n.o.	1616.2	1620	—	1615.0
H	1674.3 ± 0.7	1673.3 ± 2.4	n.o.	n.o.	—	—	—
I	1757.8 ± 1.8	1758.0 ± 1.7	n.o.	1764.3	—	—	—
J	1795.0 ± 1.3	1796.2 ± 2.2	n.o.	n.o.	—	—	1783.0
K	1820.4 ± 1.2	1825.9 ± 1.3	n.o.	1833.7	—	—	—

[a]Only the upper Davydov components are listed.

creases for PTCDA on different substrates, going from KCl films on Ag(100) (1,288 cm^{-1}, derived from FL spectra) [54], to Ag(111) (1,298 cm^{-1}) [53], hBN/Cu(111) (1,301 cm^{-1}, derived from FL spectra), and Cu(111) (1,313 cm^{-1}, derived from FL spectra), contrary to the other modes. This trend neither conforms with the strength of the (chemisorptive) bond to the substrate surface [33], nor with the bonding distance, or the amount of molecular distortion [32,35,56,57]. However, in some way it reflects the change in the distortion motif of the PTCDA molecule. On KCl/Ag(100), the PTCDA molecule is bend like an arch with all of the oxygen atoms pulled towards the surface [57]. On Ag(111), the molecule is saddle-shaped with only the carboxylic oxygen atoms pulled downwards out of the molecular plane towards the surface [56]. On Cu(111), the opposite is found. The oxygen atoms are pushed away from the surface, upwards out of the molecular plane, leading to a boat shape [35]. On hBN/Cu(111), the PTCDA molecule is nearly undistorted and hence planar [32]. It was surmised that the PTCDA molecule is bonded to the Ag(111) surface (and the KCl surface [57]) via the carboxylic oxygen atoms, while on Cu(111), the bonding proceeds primarily via the perylene core [58]. We hence suggest that the bonding via the perylene core on Cu(111) leads to a reduced flexibility of the intramolecular bonds of the core (including the central carbon ring), which causes the higher Raman shift of the RB mode. The flat, saddle-, and arch-like shapes of the molecule on hBN/Cu(111), Ag(111), and KCl/Ag(100) lead to smaller Raman shifts of the RB mode of 12 cm^{-1}, 15 cm^{-1}, and 25 cm^{-1}, respectively. The special sensitivity of the RB mode to the interfacial bonding was also seen in high-resolution electron loss spectra [59].

We also compare with PTCDA multilayers. The Raman shifts of the multilayers was found at similar energies on all three substrates, that is, at 1,309.8 cm^{-1} for multilayers of PTCDA/hBN/Cu(111), at 1,309.5 cm^{-1} for 2.55 ML PTCDA/Cu(111), and at 1,309 cm^{-1} for 60 ML PTCDA/Ag(111) [53]. This is in agreement with an identical interaction between the PTCDA multilayers as it is expected. The energy of the RB mode for the multilayers is between that of the monolayer on hBN/Cu(111) (1,301.2 cm^{-1}) and the monolayer on Cu(111) (1,312.9 cm^{-1}). Actually, it is rather close to the value seen on Cu(111) within 3 cm^{-1} (see Table 1). This may indicate that intermolecular interactions between adjacent layers in a multilayer also have a significant impact on the vibrational properties and cannot be neglected. We note that these values are slightly larger than those measured for PTCDA single crystals [55] or thick films [43].

2.2.2 Temperature induced changes in the Raman spectra: The unique behavior of the RB mode can also be seen in its dependency on the preparation temperature both for PTCDA/

hBN/Cu(111) and PTCDA/Cu(111). We compare spectra recorded directly after deposition at 20 K with those after annealing at 300 K (on hBN/Cu(111)) (Figure 3b) or with those after deposition at 300 K (on Cu(111)) (spectra not shown). For PTCDA deposited onto Cu(111) at 20 K, no Raman peaks could be observed at all in the sub-monolayer regime, and even for multilayers, the intensities of the Raman modes did not exceed two counts per second. (These are the modes given in Table 1.) At higher temperatures, the RB mode shifts to higher energies by 4 and 9 cm^{-1} for PTCDA on hBN/Cu(111) and Cu(111), respectively; the other modes remain unchanged (±0.4%, cf. Table 1).

This reflects the situation of PTCDA/Ag(111) [42] where the only significant temperature-dependent shift (by 10 cm^{-1}) was also observed for the RB mode. In that study, the shift of the RB mode was originally attributed to be of chemical origin due to different bonding to the Ag(111) substrate present only in the monolayer but not for the multilayers. However, this interpretation appears less possible for the monolayers considered here. Hence, we recall a later study [56] that revealed the existence of a chemisorbed LT state of the monolayer in which the PTCDA molecule is positioned at a similar distance (±5%, regarding the perylene core) from the surface as the RT state but is significantly more distorted than the RT state (maximum height difference of atoms of 0.31 Å compared to 0.20 Å) [56]. In addition, the LT state is present as a disordered phase, while the RT state forms highly ordered domains [44]. This is accompanied by a change in the valence band structure as seen, for example, in UPS [44]. Thus, instead of a multilayer/monolayer effect, the above described differences in the Raman shifts may also be caused by the intermolecular interactions and a modification in the interfacial bonding in the ordered domains of the RT state, which form upon annealing at room temperature. We propose that, in particular, the effect of intermolecular interactions is also relevant for the monolayer of PTCDA on hBN/Cu(111), whereas on Cu(111) concomitant changes in the interfacial bonding may play a role, too. The increased temperature induces the formation of ordered domains (observed in LEED). The intermolecular interactions in the domains then cause a change in the structure and charge distribution within the molecule. This in turn increases the vibrational energies, in particular of the RB mode located on the perylene core.

2.3 The role of surface defects for SERS

For both PTCDA/hBN/Cu(111) and PTCDA/Cu(111), the overall intensities of the Raman modes are of the same order, which implies that both surfaces cause a similar degree of Raman enhancement. However, we refrain from making a statement about the SERS effectiveness of hBN on Cu(111) for the following reason: In our experiments, the Raman intensities on

either hBN/Cu(111) or Cu(111) were both found to be highly dependent on the exact position of the incident laser beam on the sample (varying by a factor of up to ca. 7). This indicates that the specific local surface quality, for example, the surface roughness at the spot where the Raman scattering occurred, influences the intensity of the Raman modes. Hence, we cannot draw quantitative conclusions here. Nevertheless, we gain some insight into this aspect from an experiment we conducted at low temperatures, which we describe in the following.

As mentioned in the previous section, in the sub-monolayer regime of PTCDA/Cu(111) deposited at 20 K no Raman peaks could be observed at all, and even for multilayers their intensities were very small (spectra not shown). For PTCDA on hBN/Cu(111) the situation is drastically different. Figure 3b shows the Raman modes of PTCDA (0.50 ML) after deposition at 20 K (orange) and after subsequent annealing at 300 K (blue). For both preparations, the Raman modes are clearly present and of a similar intensity.

We discuss two possible explanations for these different kinds of behavior after deposition at 20 K: (i) The dipole–dipole interaction between hBN and PTCDA enhances the Raman signal. In this process, the underlying copper would not be involved [50]. (ii) The Raman modes of PTCDA are strongly enhanced at specific adsorption sites, which we refer to as "hot spots". On Cu(111), the molecules can reach these hot spots only by temperature-induced diffusion. Whereas, after deposition at 20 K, the molecules stay statistically distributed on the surface, and only a small fraction is located at these sites where the SERS effect occurs. On hBN/Cu(111), the significantly smaller interaction between PTCDA and the hBN surface compared to Cu(111) and a consequently smaller corrugation of the bonding potential lead to a much higher mobility, which allows for a diffusion to the hot spots even at low temperatures of 20 K.

We propose the second interpretation to be relevant. Our arguments are the following: Firstly, we have shown in a previous work [32] that the interaction between PTCDA and hBN/Cu(111) is of a physisorptive nature, which makes a strong SERS effect due to dipole–dipole interactions at the interface [50] unlikely. Secondly, the strong dependence of the Raman intensity on the sample position (see above) conforms with the interpretation of a SERS effect related to local hot spots. However, the details of the related adsorption sites remains unclear.

Since the SERS effect is primarily observed on rough/nanostructured rather than on flat metal surfaces [45], the SERS effect is expected to be larger for molecules located in proximity to surface defects. Thus, at surface positions with a higher defect density, the Raman intensities are expected to be higher.

The relevance of the defect density in the present case is corroborated by our observation that at positions where the Raman intensity was high, the defect luminescence of the substrate (see region I in Figure 2) was also higher. In a theoretical study, García-Vidal and Pendry investigated the enhancement due to the SERS effect as a function of the roughness on a surface [48]. They found that on an inhomogeneously rough surface, the Raman spectrum is dominated by the enhanced signals from molecules located at features that exhibit a maximum in roughness. We can support this interpretation by results from a previous experiment. We observed by light microscopy that Ag(100) samples that had been prepared in a similar manner as the Cu(111) surface used here and that yielded a high-quality LEED pattern indicating the presence of long-range ordered and large, defect-free terraces, actually show variations in their surface morphology on a micrometer scale [60]. We propose that the defect-rich regions exhibit a large step density due to impurities and/or grain boundaries. Consequently, we assume that the hot spots are related to an inhomogeneous mesoscopic roughness of the Cu(111) surface, which is remnant after sputtering and annealing.

In conclusion, the Raman lines of PTCDA/hBN/Cu(111) and PTCDA/Cu(111) observed between 18,600 and 21,000 cm^{-1} are in accordance with the characteristic fingerprint of the molecule. They can be used as a monitor for its presence on the surfaces. Coverages cannot be determined quantitatively from the intensities of the Raman modes, since these depend on the sample positions, which we assign to a correlation with the local roughness due to structural defects of the surface. Note that we systematically did not observe the characteristic Raman line of hBN at approximately 1,370 cm^{-1} that was observed for hBN on SiO_2/Si [61], on Cu foils [62], and on other metal foils [63,64] for our samples of hBN/Cu(111). This is an obvious discrepancy, which we cannot explain based on our current data. It may, however, be related to the specific interface between hBN and the single crystalline Cu substrate.

3 Fluorescence
3.1 PTCDA/hBN/Cu(111)
We turn to the FL, which can be observed in region II of Figure 2, between 18,000 and 18,600 cm^{-1}. We note ahead that we did not observe vibronic bands related to the FL peaks as it is the case, for example, for PTCDA on KCl [65].
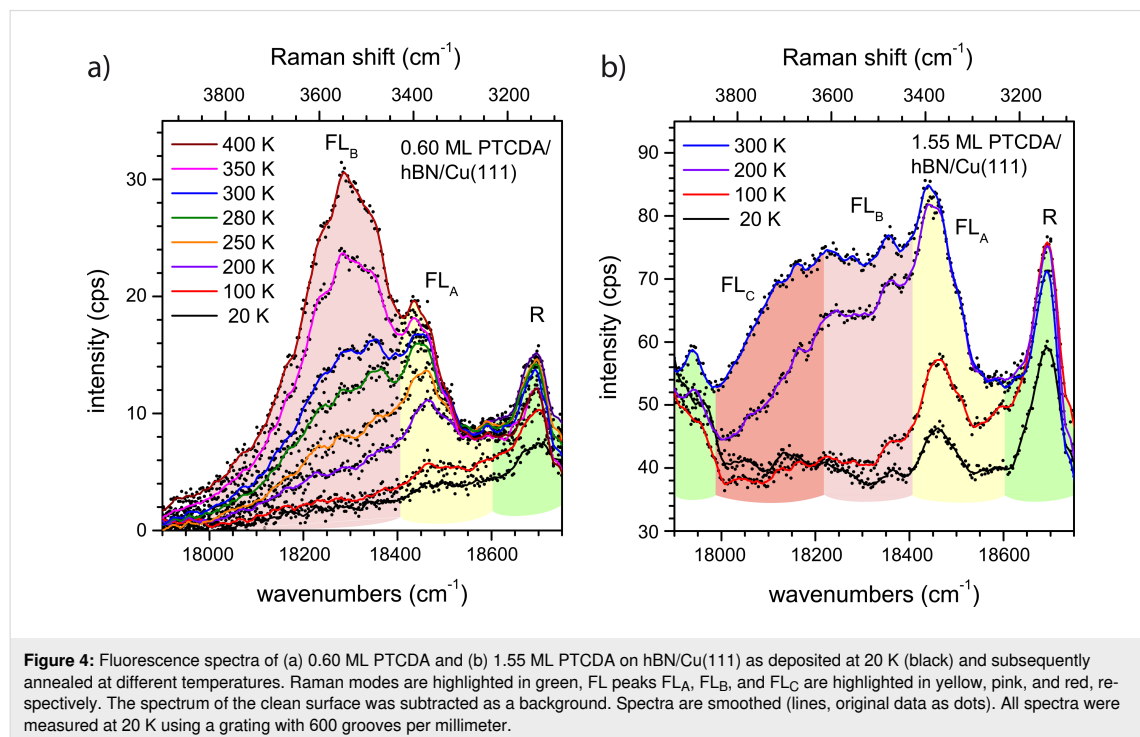
First, we consider which experimental conditions led to the observation of FL peaks. Figure 4a shows a zoom-in on region II of the spectrum of 0.60 ML PTCDA on hBN/Cu(111) as deposited at a sample temperature of 20 K, and after a series of subsequent annealing steps at temperatures between 100 and 400 K. The peak on the high-energy side of the spectrum

(marked in green and labeled "R") is a Raman mode. This mode has also been observed for PTCDA/Ag(111) [53]. Furthermore, its change in intensity as a function of the annealing temperature agreed with that of other Raman modes. The behavior of the two other peaks depicted in Figure 4a (marked in yellow and pink) was quantitatively different. We assign these peaks to the FL of PTCDA molecules and will refer to them as FL_A (at ca. 18,450 cm^{-1}) and FL_B (at ca. 18,300 cm^{-1}). Both peaks appear after annealing at temperatures above ca. 200 K (FL_A) and ca. 280 K (FL_B).

We take this finding as an indication that the FL of PTCDA on hBN/Cu(111) depends on the structural order of the molecules on the surface that is established by annealing. We explain the existence of two FL peaks by the presence of two structurally different "phases" of PTCDA. Since all optical measurements were carried out at a sample temperature of 20 K, the temperature-induced structural ordering upon annealing that led to the FL peaks is irreversible. The broad FL peaks are superimposed with several sharp Raman lines, which lead to modulations of the peaks. There are two important differences between the FL_A and FL_B peaks: FL_B is significantly broader than FL_A (by a factor of ca. three, which we will discuss in detail in the Section Final Discussion). In addition, the intensity of FL_A saturates, while that of FL_B does not. Notably, the intensity of FL_A saturates upon annealing at 280 K, which is the temperature that is

required for FL_B to be observed at all. This behavior was found for layers within a range of sub-monolayer coverages (between 0.10 and 0.80 ML).

For further insight, we refer to a temperature-dependent series of spectra at a higher coverage of 1.55 ML PTCDA on hBN/Cu(111), shown in Figure 4b. We observe the same Raman line as for the 0.60 ML spectrum, as well as FL_A and FL_B. However, there are a few important differences compared to the spectra in Figure 4a: (i) FL_A can be observed in the spectrum immediately after deposition at 20 K; (ii) FL_B appears in the spectrum already after annealing at 200 K (not at 280 K); and (iii) additional FL intensity at lower energies (ca. 18,150 cm^{-1}) appears, which we assign to a third peak FL_C. The appearance of FL_A at low temperatures leads us to the conclusion that the attributed "phase A" of PTCDA/hBN/Cu(111) forms directly at higher coverages, while at lower coverages its formation requires annealing. Hence, we assign FL_A to PTCDA molecules at surface defects. In a sub-monolayer, the molecules can reach these defects via diffusion, which has to be temperature-induced. For a higher coverage, the sites at defects are already populated during the deposition, even at low temperatures. A saturation of the sites at defects leads to the observed intensity saturation of the corresponding FL_A peak. We note in this context that the surface defects connected to FL_A are not identical to the hot spots mentioned above, which support the SERS

Figure 4: Fluorescence spectra of (a) 0.60 ML PTCDA and (b) 1.55 ML PTCDA on hBN/Cu(111) as deposited at 20 K (black) and subsequently annealed at different temperatures. Raman modes are highlighted in green, FL peaks FL_A, FL_B, and FL_C are highlighted in yellow, pink, and red, respectively. The spectrum of the clean surface was subtracted as a background. Spectra are smoothed (lines, original data as dots). All spectra were measured at 20 K using a grating with 600 grooves per millimeter.

effect, as we will discuss below. After the saturation of the defects, the temperature-induced formation of a second "phase B" occurs leading to the peak FL_B.

We also observed the FL_B peak on hBN/Cu(111) after deposition at 300 K for coverages of 1–3 ML. For all these experiments, we observed the LEED pattern that is characteristic of ordered domains of PTCDA/hBN/Cu(111) (see Appendix A). Thus, we conclude that FL_B stems from these ordered PTCDA domains in the first layer on hBN. The formation of ordered domains is not possible at a sample temperature of 20 K during deposition. It requires a certain threshold temperature (ca. 280 K). This explains why FL_B can only be observed after annealing or deposition at or above this temperature.

The energetic difference between FL_A and FL_B amounts to ca. 150 cm^{-1}. We compare this to the energetic shift reported by Forker et al. who investigated PTCDA on hBN/Rh(111) [23]. They found that PTCDA molecules on hBN/Rh(111) are trapped in the pores of the hBN superstructure, which leads to isolated monomers on the surface. Annealing leads to the formation of ordered domains and a redshift of the spectrum by 223 cm^{-1} (27.6 meV) [23]. The molecules trapped in pores on hBN/Rh(111) can be compared with isolated molecules located at defects on hBN/Cu(111). However, please note that we do not consider trapped PTCDA molecules but isolated molecules to be the origin of FL_A. This will be discussed in further detail in Section 3.3 in relation with further information from FL experiments. An energetic shift of the same order has also been observed for the FL of isolated molecules and that of ordered domains of PTCDA on NaCl [10]. Here, two different structures of ordered domains of PTCDA were observed (a herringbone and a quadratic structure) the S_0/S_1 transitions of which are redshifted relative to the isolated molecules by 560 cm^{-1} and 300 cm^{-1}, respectively.

For a comparison of FL_B of PTCDA domains on hBN/Cu(111) at 18,300 cm^{-1}, we refer to optical data taken for ordered monolayers of PTCDA on a monolayer of hBN grown on other substrates. The respective values are given in Table 2. Note that only PTCDA/hBN/SiO$_2$ was investigated by FL spectroscopy

while for PTCDA/hBN/Pt(111) and PTCDA/hBN/Rh(111) absorption spectra were measured. We cannot explain the differences of the S_0/S_1 transition energies, yet. However, we observe a trend of higher transition energies from hBN/SiO$_2$ to hBN/Cu(111) to hBN/Pt(111) to hBN/Rh(111). This is the direction of increasing interactions between the hBN layer and the supporting metal substrate, as indicated by the increasing amplitude of the buckling of the hBN layers [30,66]. We note that Forker et al. [23] could exclude a dominant role of the dielectric properties of the metal substrates for the transition energies.

The peak FL_C (cf. Figure 4b) shows the same behavior as FL_B at a coverage of 1.55 ML. It is as broad as FL_B and appears after annealing at 200 K. However, it is not present at a coverage of 0.60 ML. Thus, it does not stem from PTCDA directly adsorbed on hBN, but from ordered PTCDA domains in a second layer. However, this is different from the FL emission (Y), which is present in bulk-like PTCDA layers and was reported, for example, in [67]. Indeed, we observed the broad Y line and its vibronic progression Y' for higher coverages of 4–5 ML at 15,950 and 14,700 cm^{-1}, respectively. This is in agreement with the line positions measured in [67] within 50 cm^{-1} and 300 cm^{-1}, respectively.

In summary, for PTCDA/hBN/Cu(111) three FL peaks can be observed. FL_A (ca. 18,450 cm^{-1}) is present in the first layer and stems from molecules at surface defects. To enable the molecules to reach these defects, a temperature-induced diffusion is necessary at sub-monolayer coverage. FL_B (ca. 18,300 cm^{-1}) stems from ordered domains in the first PTCDA layer. It can only form under deposition at a sample temperature above ca. 280 K, or after annealing at this temperature. FL_C (ca. 18,150 cm^{-1}) is assigned to the FL from ordered PTCDA domains in the second or higher layers.

3.2 Comparison with PTCDA/Cu(111)

Figure 5a shows the FL spectra of PTCDA/hBN/Cu(111), prepared by deposition at 20 K and subsequent annealing at 300 K and of PTCDA/Cu(111), prepared by deposition at 300 K, both with varying coverages. We will list the important observations

Table 2: Spectral positions of the S_0/S_1 transition of PTCDA domains in the first monolayer on hBN on SiO$_2$ [22], Cu(111), Pt(111) [23], and Rh(111) [23]. PTCDA on hBN/SiO$_2$ and on hBN/Cu(111) were investigated using FL spectroscopy. The results for PTCDA on hBN/Pt(111) and hBN/Rh(111) were gained in absorption experiments.

hBN/SiO$_2$ [22]	hBN/Cu(111)	hBN/Pt(111) [23]	hBN/Rh(111) [23]
2.234 eV	2.26 eV	2.31 eV	2.38 eV
18,060 cm^{-1}	18,300 cm^{-1}	18,700 cm^{-1}	19,200 cm^{-1}

for these spectra: (i) There is no fluorescence at all for a full monolayer of PTCDA on bare Cu(111) while on hBN/Cu(111) FL can be observed for a coverage as low as 0.10 ML. (ii) In the second monolayer of PTCDA on bare Cu(111), an FL peak appears at 18,450 cm^{-1}, which corresponds to FL_A. (iii) In the third PTCDA layer on Cu(111), there is an FL peak at

Figure 5: (a) Fluorescence spectra of PTCDA on hBN/Cu(111) (left, blue spectra, prepared by deposition at 20 K and subsequent annealing at 300 K) and PTCDA/Cu(111) (right, red spectra, prepared by deposition at 300 K). Raman intensities are highlighted in green; FL peaks FL_A, FL_B, and FL_C are highlighted in yellow, pink, and red, respectively. There is no FL from ordered domains in the first or second layers of PTCDA/Cu(111), but from the first layer of PTCDA/hBN/Cu(111). Spectra are smoothed (lines) and vertically shifted (original data as dots). Spectra of the clean substrates were subtracted as background. All spectra were measured at 20 K using a grating with 600 grooves per millimeter. (b) Schematic representations of 2 ML PTCDA/hBN/Cu(111) and (c) 3 ML PTCDA/Cu(111) and the FL signals observed from these layers. The FL from the first PTCDA layer on Cu is quenched (gray). The interfacial hBN layer (blue) and the interfacial chemisorbed PTCDA layer (gray) decouple the fluorescing molecules from the metal. Defect-mediated FL (FL_A) is emitted from the separating PTCDA layer (pink) in both cases, FL_C originates from the physisorbed PTCDA layer (red). Only for PTCDA/hBN/Cu(111) FL occurs from PTCDA domains in the separating layer (FL_B). For details on the different PTCDA layers, see text.

18,150 cm^{-1}, which is the position of FL$_C$ observed for 1.55 ML PTCDA/hBN/Cu(111). (iv) FL$_B$ is not observed at all for PTCDA/Cu(111). The absence of FL$_B$ on Cu(111) is understood as we have assigned it to PTCDA domains on hBN/Cu(111). The other three observations have to be explained.

Ad (i): The absence of any FL of 1.00 ML PTCDA on Cu(111) confirms the complete quenching of the molecular excitation in the first layer on a metal surface as has previously been observed for the Ag(111) [5,39] and the Au(111) [39] surfaces. Ad (ii): For PTCDA/Cu(111), a sufficient decoupling to allow some FL is achieved for the second layer (1.55 ML). Thus, FL$_A$ can be observed, which we assigned to FL from molecules at defects on the hBN/Cu(111) surface. It is remarkable that the PTCDA molecules have to interact with defects in order to fluoresce, and that the same kind of FL can be observed on both substrates. For PTCDA on Cu(111), as on hBN/Cu(111), a temperature-induced process is necessary to observe FL$_A$ as PTCDA on Cu deposited at 20 K shows no FL at all (not shown). Only for PTCDA deposited at 300 K on Cu(111), we can observe the spectra shown in Figure 5. As stated in the previous section, we assume a temperature-induced diffusion process to surface defects where the PTCDA molecules are then able to fluoresce. The nature of these defects will be discussed in the next Section 3.3. Ad (iii): From our LEED experiments (see Appendix A) we know that PTCDA on Cu(111) grows layer-by-layer in the first three layers. Thus, we can assign the peak FL$_C$, which appears in the third layer, to FL from ordered PTCDA domains adsorbed on top of two completed PTCDA layers. As we will discuss now, this is in accordance with the observation of FL$_C$ from the second layer of PTCDA/hBN/Cu(111). We summarize our observations with the schematic layer models that are given in Figure 5b,c. In both cases an interfacial layer that is adsorbed on the Cu(111) surface exists. This layer decouples PTCDA molecules in higher layers, which leads to FL from these layers. The interfacial layer is either a layer of hBN or a monolayer of chemisorbed PTCDA. The next layer in both cases is formed by ordered PTCDA domains that show FL$_A$, likely from molecules at defects. In the case of PTCDA on hBN/Cu(111), an additional FL$_B$ from ordered domains is present. We call this first PTCDA layer a separating layer. In the TPD spectrum of PTCDA/hBN/Cu(111), the desorption peak of the separating layer can be distinguished from that of the multilayers (however, no separated peak for the second layer is observed) [32]. On Cu(111), the first (interfacial) layer does not desorb at all, and in the TPD spectrum, the second (separating) layer is also distinct from the multilayers [68]. The multilayers (both on hBN/Cu(111) and Cu(111)) are likely physisorbed and include the layers from the second and third layer onward. The ordered PTCDA domains in these layers are the origin of FL$_C$.

Our findings are in accord with the conclusions by Stallberg et al. who measured photoluminescence spectra of PTCDA on Ag(111) and Au(111) [39]. From coverages of 1.8 ML on Ag(111) and 2.2 ML on Au(111) onward they observed FL peaks at 17,000 cm^{-1} and 17,300 cm^{-1} (denoted by M in [39]). These were assigned to PTCDA layers separated from the metal substrate by the first interfacial PTCDA layer. This M line was distinct from that of the bulk-like FL emission from thick films, which was found at 15,000 cm^{-1} (Y line) and 13,700 cm^{-1} (E line). The M line was observed even for multilayers, co-existing with the bulk emission. Similarly, for PTCDA/Cu(111), we observed the Y line and its vibronic progression Y' of the multilayer FL for a coverage of 4.60 ML at 16,100 cm^{-1} and 14,750 cm^{-1}, respectively, while FL$_A$ and FL$_C$ were still present (not shown). The Y line was assigned to the 0–0 transition of the PTCDA bulk phase [67]. Thus, the co-existence of the Y line and FL$_A$ and FL$_C$ is consistent with the formation of bulk-like clusters at a coverage of 4.60 ML. Likewise, on hBN/Cu(111), we observed the Y and Y' lines for coverages from about 4–5 ML onward (see Section 3.1) in parallel with FL$_A$, FL$_B$, and FL$_C$. This confirms, in accordance with our LEED data, that at least two complete layers of PTCDA form on both surfaces under the given preparation conditions.

3.3 FL at defect positions

As stated above, we assign FL$_A$ to molecules adsorbed at surface defects. Since FL$_A$ can be observed for PTCDA/hBN/Cu(111) and PTCDA/Cu(111), we assume the same kind of defects has to be present on both surfaces. We propose that these defects are different to the metallic "hot spots" supporting SERS because FL$_A$ is shifted in energy, which is less expected for coupling to metallic protrusions. An alternative origin of these defects could be the presence of carbon containing species due to segregation from the Cu bulk. Although this interpretation is speculative, we give some background in order to aid subsequent research. When the Cu(111) crystal was annealed at a temperature above 1050 K and for a period of time longer than 30 min, we observed an additional superstructure in LEED. Although we cannot identify these segregations unambiguously, we assume carbon segregation as carbon is known to form highly ordered nanostructures on Cu(111) [69]. Indeed, we adjusted our preparation by reducing the temperature to 1010 K during borazine deposition and omitting the annealing step under vacuum before borazine deposition to avoid this segregation (see Experimental section). However, we cannot exclude a small and randomly distributed residual amount of segregated carbon species since these would be invisible in LEED. We indeed found that samples showing segregated carbon in LEED do not allow for the formation of the hBN layer. Presumably, due to the extended carbon coverage, there is not enough bare Cu surface left for supporting the catalytic growth of hBN. Ac-

cordingly, on a surface with a small amount of carbon, growth defects in the hBN layer at positions where carbon is present may be expected. Thus, we consider carbon species in direct contact with the bare Cu that lead to similar or even identical defects on both surfaces (hBN/Cu(111) and bare Cu(111)), which, in turn, promote identical FL signals of PTCDA molecules. Note that these carbon-related defects are different from the defects that cause the SERS effect. The hot spots that lead to an enhancement of Raman signals are caused by structural defects of the Cu crystal, such as surface roughness, and not by a different chemical species.

Besides FL_A, no further FL can be observed for 1.55 ML PTCDA/Cu(111) despite the fact that the LEED pattern shows well-resolved spots of ordered domains. The absence of FL from these ordered domains indicates that a single PTCDA monolayer on Cu(111) cannot decouple PTCDA in the second layer from the metal surface sufficiently enough for FL to occur. Thus, the observation of only FL_A for a coverage of 1.55 ML leads to the conclusion that the defects at which the fluorescing molecules are adsorbed also have a decoupling effect. This corroborates our deduction that the defects cannot be Cu ad-atoms.

We would like to reiterate that we exclude the possibility that the FL_A of PTCDA on hBN/Cu(111) stems from molecules trapped in the "moirons" of the hBN layer [24]. Studies on hBN/Cu(111) have shown a trapping of large organic molecules in the moirons of the electronic superstructure of hBN/Cu(111) at low molecular coverages [38]. At larger coverages, the entire surface was found to be homogeneously filled with molecules. Yet, they still showed site-dependent alterations in their electronic structure, namely a shift of the molecular frontier orbitals [38]. However, we propose that the situation of PTCDA on hBN/Cu(111) is different. First of all, as stated above, FL_A is also observed for PTCDA on Cu(111), which clearly excludes trapped PTCDA molecules on hBN as a possible origin for FL_A. Furthermore, our own STM investigations showed no signs of a preferential occupation of the moirons on the hBN/Cu(111) surface by PTCDA [32]. Also, holes in the hBN layer that would allow for a direct contact between the molecules and the bare Cu(111) surface can be excluded as the origin for FL_A because the FL of PTCDA molecules in direct contact with the metal would be fully quenched.

4 Final discussion
We found that two layers of PTCDA are necessary to decouple PTCDA molecules from the Cu(111) surface in order to observe FL from ordered domains in the third layer. The same effect can be achieved by only one single layer of hBN. On hBN/Cu(111), two FL components (FL_A and FL_B) are present for the first
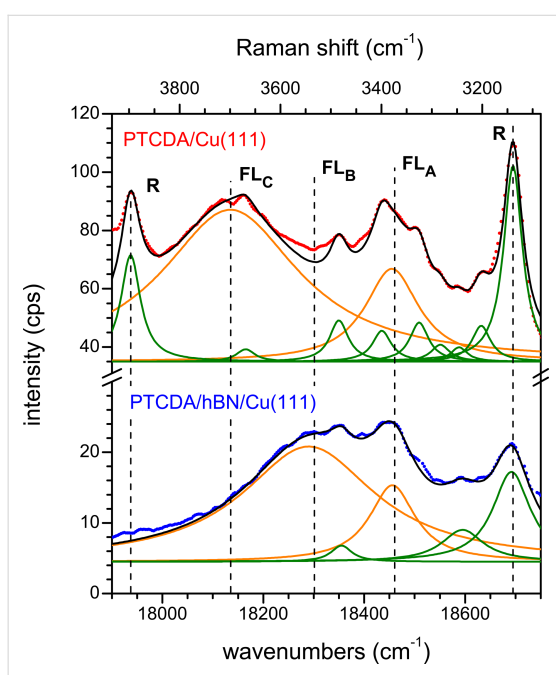
PTCDA layer, while a third one (FL_C) can only be observed from the second layer onward. On Cu(111), the FL from the first PTCDA layer is completely quenched. FL_A and FL_C are observed only from the second and third layer onward, respectively. FL_A is assigned to a defect-related FL, while both FL_B and FL_C are assigned to ordered PTCDA domains. We can exclude bulk-like crystallites on top of the monolayer as the origin of the FL_B and FL_C peaks by the following arguments: (i) The LEED patterns of PTCDA on hBN/Cu(111) and on Cu(111) identify the formation of long-range ordered structures in the second layer. (ii) LEED investigations (see Appendix A) and TPD experiments [32,68] show that PTCDA/Cu(111) and PTCDA/hBN/Cu(111) form at least three or two complete layers, respectively. (iii) The spectral positions of FL_B and FL_C are unambiguously distinct from the Y and Y' peaks of the FL of the PTCDA bulk.

We return to the question of CT across the hBN layer posed in the Introduction section. Our results indicate that the hBN layer is able to suppress the CT such that FL is observed. However, this suppression is not complete because the FL intensity is very low. In comparison to the FL of PTCDA observed on thin KCl films, we reckon that the FL on hBN/Cu(111) is smaller by a factor of ca. 10^4 [70]. However, hBN should not be dismissed as a decoupling layer altogether. In an analogue experiment, we measured the FL spectrum of 5,10,15,20-tetraphenylbisbenz[5,6]indeno[1,2,3-*cd*:1',2',3'-*lm*]perylene (DBP) on hBN/Cu(111) (not shown). (For the chemical formula and optical properties of DBP, refer to the work by Rouillé et al. [71].) Here, we observed FL at sub-monolayer coverage [72]. The FL intensity was larger by a factor of ca. 10^2 compared to the FL intensity of PTCDA on hBN/Cu(111). This can be explained by the fact that DBP is a lander-type molecule. It exhibits four peripheral phenyl groups, which function as spacers between the molecular backbone and the surface [71]. This presumably, in addition to the hBN layer and a weak interaction, supports the suppression of the CT process and allows for a higher FL intensity.

We further discuss the widths of the FL peaks on Cu(111) and hBN/Cu(111) in some detail. The large width of the FL peaks may partly be caused by disorder in the molecular domains or by a very small lifetime of the excited state. Since our LEED experiments showed the formation of ordered PTCDA domains, we assume that the main contribution for the line broadening is due to a reduced FL lifetime, τ_{FL}, and that contributions from disorder and dephasing can be neglected [73,74]. Thus, the value of τ_{FL} measured from the full width at half maximum (FWHM) of the FL peaks on the frequency scale according to FWHM = $1/2\pi\tau_{FL}$ yields a lower limit for the lifetime of the excited states. Because of the small FL yield we can assign τ_{FL}

in good order to the time constant of the CT process. Hence, τ_{FL} gives quantitative information about the efficiency of the decoupling from the metal interface. Figure 6 representatively shows region II of the optical spectra of 0.60 ML PTCDA/hBN/Cu(111) and 2.55 ML PTCDA/Cu(111). Both spectra show FL_A and FL from ordered domains as either FL_B or FL_C, respectively. The FL peaks and the Raman modes were fitted with sets of Lorentzians. The widths and positions of the narrower Raman lines were fixed during the fits. The fits were thus robust concerning the determination of the FWHM of the FL peaks. The lifetimes derived from these fits are given in Table 3. All of

them are of a similar size and of the order of 10^{-14} s. Thus, we can understand why we did not observe final-state effects in the photoemission spectra (i.e., UPS) of PTCDA/hBN/Cu(111) due to CT across the interface, that is, the signature of uncoupled molecules [32], albeit the FL experiments demonstrate that some coupling to the underlying Cu(111) surface is present. The reason is that the time constant of this coupling is only of the same order as the time constant of the photoemission process. Therefore, it has only a small or negligible impact on the spectra. These small lifetimes are in agreement with the findings by Stallberg et al. [39], who showed that the lifetimes of the excited states of PTCDA in the second layer on Ag(111) and in the third layer on Au(111) are smaller than an upper value of 4×10^{-12} s, which was given by the time resolution for their experiment. The small lifetimes also explain why the FL intensities were so low with respect to those measured, for example, for an ordered monolayer of PTCDA/KCl/Ag(100) [65].

Both the small FL intensities and the short lifetime of the excited state of PTCDA on hBN/Cu(111) show that, at least for this molecule, a single hBN layer is not sufficient to completely decouple the electronic states of the molecule and the metal. While the static CT related to the interfacial bonding is suppressed, as demonstrated by UPS [32], it is still significant for the excited state. A similar observation has been made for tetracene molecules on thin insulating layers of AlO_x on $Ni_3Al(111)$ [75]. Here, too, the luminescence was found to be quenched despite the large bandgap of AlO_x (6.5 eV) and the weak interactions at the interface due to a CT between overlapping π orbitals and the electronic states of the metal.

Conclusion

We have measured the fluorescence of PTCDA on hBN/Cu(111) and Cu(111) to determine the efficiency of the electronic decoupling of PTCDA from the Cu substrate by a single hBN layer. The observation of Raman lines served as a monitor for the presence of PTCDA on the surface. In addition, LEED patterns show the formation of ordered structures and a layer-by-layer growth for at least the first two layers on hBN/Cu(111) and the first three layers on Cu(111).

Figure 6: Fluorescence spectra of 0.60 ML PTCDA/hBN/Cu(111) (blue, bottom) and 2.55 ML PTCDA/Cu(111) (red, top). Original data (dots) are smoothed and shifted vertically. Both spectra were fitted using Lorentzian functions for the FL peaks (orange lines) and the most important Raman modes (green lines). Cumulative fits shown in black. Spectra of the clean substrates were subtracted as a background (cf. Figure 5). All spectra were measured at 20 K using a grating with 600 grooves per millimeter.

Table 3: Spectral positions of the FL peaks observed for PTCDA/hBN/Cu(111) and PTCDA/Cu(111), the species the FL peaks originate from, the FWHM of the FL peaks, and the lifetimes τ_{FL} of the respective excited states. Defect FL and physisorbed PTCDA apply for both PTCDA/hBN/Cu(111) and PTCDA/Cu(111).

	FL_A	FL_B	FL_C
FL peak position	18,450 cm^{-1}	18,300 cm^{-1}	18,150 cm^{-1}
assignment	defect related FL	PTCDA/hBN	physisorbed PTCDA
FWHM	(120 ± 10) cm^{-1}	(320 ± 16) cm^{-1}	(330 ± 15) cm^{-1}
τ_{FL}	(4.4 ± 0.3) × 10^{-14} s	(1.7 ± 0.1) × 10^{-14} s	(1.6 ± 0.1) × 10^{-14} s

The intensities of the Raman lines do not scale with the coverage, neither on hBN/Cu(111), nor on Cu(111). This clearly shows that additional aspects of the sample system, likely defects of the Cu substrate, play a role. We summarize the underlying mechanisms under the SERS effect. The small but discernibly different chemical shifts of Raman modes on the two surfaces are explained by the molecule–substrate interactions and specific bonding geometries of the molecule to the surface.

On both substrates, a broad fluorescence at ca. 18,450 cm^{-1} can be observed, which is identified as FL from molecules interacting with surface defects. This can be observed both for the first PTCDA layer on hBN/Cu(111) and the second layer of PTCDA on Cu(111). FL from the first PTCDA layer on Cu(111) is not observed. In contrast, the first PTCDA layer on hBN/Cu(111) already shows a weak FL from ordered domains at ca. 18,300 cm^{-1}.

On bare Cu(111), two interfacial layers of PTCDA are required to achieve an equivalent decoupling of the third layer as one layer of hBN on Cu(111) for the first PTCDA layer. The third layer on Cu(111) shows FL at ca. 18,150 cm^{-1}. This FL can be also observed in the second PTCDA layer on hBN/Cu(111) and is attributed in both cases to domains of physisorbed PTCDA on a separating PTCDA layer that forms on either the hBN layer or the first chemisorbed interfacial PTCDA monolayer on Cu(111).

While the charge transfer between PTCDA molecules and metal is sufficiently suppressed by a single hBN layer such that a weak fluorescence is observed, this suppression is limited. We estimate a lifetime of the excited state of ca. 10^{-14} s, which explains the very small fluorescence intensities. As a result, we find that a single layer of hBN on Cu(111) is able to decouple PTCDA molecules from the metal surface in so far as to prevent a total quenching of the fluorescence of the first molecular layer. However, a competing non-radiative channel for the decay of the excited state of the molecule remains as some charge transfer with a time constant of 10^{-14} s^{-1} is still possible. Thus, while a single layer of hBN provides a more efficient decoupling of a PTCDA layer from the Cu(111) surface than the first PTCDA layer itself, its efficiency is limited.

Appendix A: Structural Investigations
Here, we present the structural investigations of monolayer PTCDA on hBN/Cu(111) and Cu(111) by LEED.

The structure of PTCDA/Cu(111)
We begin with a summary of earlier reported results. At RT, PTCDA on the Cu(111) surface follows a layer-by-layer growth
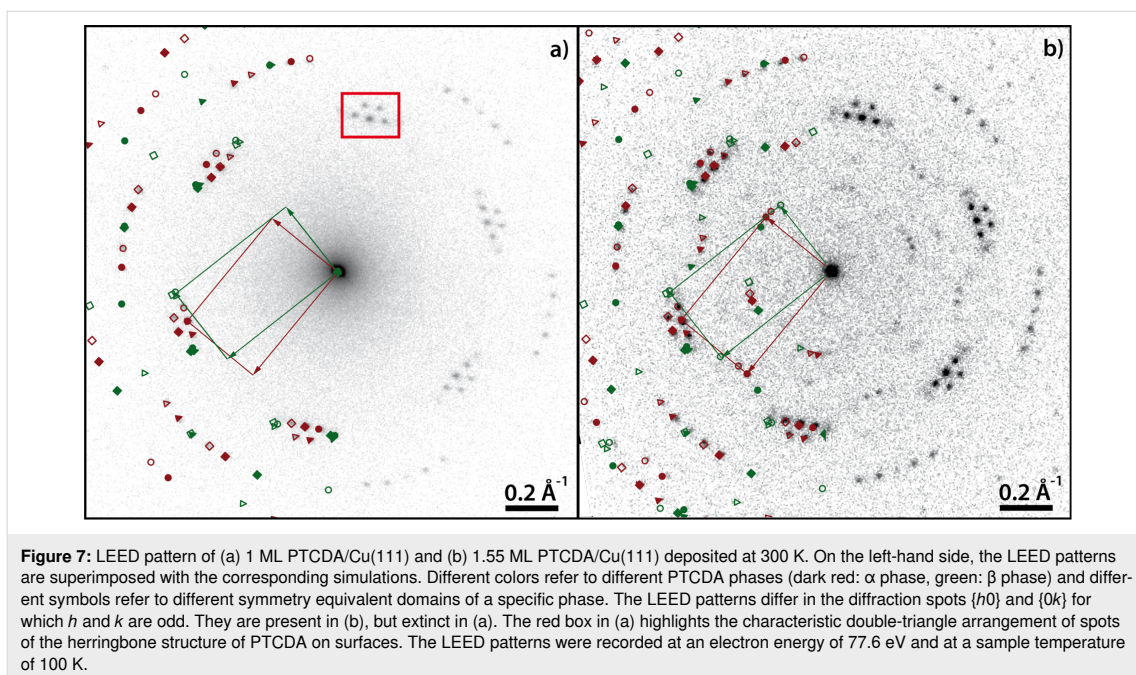
mode for the first three layers [76]. The obtained films remain unchanged under annealing at 530 K. From the fourth layer onward, the formation of nanocrystals begins. In TPD spectra, the desorption of the multilayer can be distinguished from the desorption of the second layer [68]. A desorption of the first layer was not observed due to a chemisorptive bonding to the Cu(111) surface. An STM study on the PTCDA monolayer on Cu(111) was published by Wagner et al. [77]. The authors reported two co-existing PTCDA phases, both displaying the characteristic herringbone arrangement, one commensurate, the other commensurate only in higher order.

In our experiments, PTCDA layers on Cu(111) were always grown at a sample temperature of 300 K. Experiments conducted in two different UHV chambers with different deposition rates resulted in identical LEED patterns. All LEED measurements were performed at 100 K.

Figure 7a shows the LEED pattern of a complete monolayer PTCDA/Cu(111) with sharp diffraction spots. The spots marked in dark red are explained by one single phase (α). Additionally, a second phase (β, marked in green in Figure 7) is present. From the relative spot intensities, the α phase is considered as the majority phase. The monolayer LEED pattern is fully explained by the α and β phases with no systematic differences between the LEED pattern and the simulation. There are systematic extinctions of all {$h0$} and {$0k$} spots for which h and k are odd. This points to the presence of glide planes in both phases. The structural parameters, which can be determined from the LEED pattern with small margins of error (ca. 5%), are given in Table 4. The first columns of the superstructure matrices of the α phase and the β phase exhibit elements that are integer numbers (within the margins of error). This means that both phases exhibit on-line-coincidence (OLC) [78] with the Cu(111) surface.

Both phases (α and β) exhibit a rectangular unit cell and belong to the *p2gg* space group. The differences between the two are the azimuthal orientations of the unit cell vectors relative to the Cu(111) surface vectors and the packing densities. The unit cell of the α phase is more closely aligned with the Cu surface vector **a**$_1$ (2.5°) compared to the β phase (10.3°). Furthermore, the molecules in the β phase are slightly more densely packed than in the α phase ($A_\alpha = 103\% \times A_\beta$, cf. Table 4).

The most prominent feature of the LEED pattern is the characteristic arrangement of spots forming a "double triangle" (marked by a red box in Figure 7a). This is well known for the rectangular unit cell of PTCDA molecules forming the typical herringbone motif [80,81] that can also be found in the (102) plane of the bulk material [82]. In contrast to other coinage

Figure 7: LEED pattern of (a) 1 ML PTCDA/Cu(111) and (b) 1.55 ML PTCDA/Cu(111) deposited at 300 K. On the left-hand side, the LEED patterns are superimposed with the corresponding simulations. Different colors refer to different PTCDA phases (dark red: α phase, green: β phase) and different symbols refer to different symmetry equivalent domains of a specific phase. The LEED patterns differ in the diffraction spots {h0} and {0k} for which h and k are odd. They are present in (b), but extinct in (a). The red box in (a) highlights the characteristic double-triangle arrangement of spots of the herringbone structure of PTCDA on surfaces. The LEED patterns were recorded at an electron energy of 77.6 eV and at a sample temperature of 100 K.

Table 4: Structural results of PTCDA/Cu(111) according to the structure model proposed by Wagner et al. [77] (phase '1' and '2') and as determined from our LEED experiments (α phase and β phase) and of PTCDA/hBN/Cu(111). The vectors of the unit cells, $\mathbf{b}_1$ and $\mathbf{b}_2$, the angle β between the two, and the areas of the unit cells, A, are given. φ is the enclosed angle between the vector $\mathbf{b}_1$ and the substrate lattice vector, $\mathbf{a}_1$. ρ is the packing density of the molecules. Additionally, the superstructure matrices, **M**, are given. The matrix for PTCDA/hBN/Cu(111) refers to the Cu(111) surface at 100 K. We note that the parameters of phase '1' and '2' are derived from the (higher-order) commensurate structure models given in [77] and slightly deviate from the experimental STM results (within error margins). The error for β is the experimental error of the STM data. The matrices given for phase '1' and '2' differ from those reported by Wagner et al. [77] because they refer to a symmetry-equivalent domain according to the rules given in [79].

	Cu(111) - phase '1' [77]	Cu(111) - phase '2' [77]	
$\mathbf{b}_1$ (Å)	12.8(3)	13.4(1)	
$\mathbf{b}_2$ (Å)	22.1(3)	22.0(1)	
β (°)	90(5)	92(5)	
A (Å²)	283(10)	295(3)	
φ (°)	0	11	
ρ (molecules Å⁻²)	7.07×10^{-3}	6.78×10^{-3}	
M	$\begin{pmatrix} 5 & 0 \\ 5 & 10 \end{pmatrix}$	$\begin{pmatrix} 5.75 & 1.25 \\ 3.40 & 9.80 \end{pmatrix}$	

	Cu(111) - α phase	Cu(111) - β phase	hBN/Cu(111)
$\mathbf{b}_1$ (Å)	12.4(2)	11.8(2)	12.07(3)
$\mathbf{b}_2$ (Å)	19.5(3)	19.9(5)	19.33(9)
β (°)	90.0(9)	90.0(13)	90(3)
A (Å²)	242(7)	235(10)	233(2)
φ (°)	2.5(7)	10.3(10)	9(1)
ρ (molecules Å⁻²)	8.26×10^{-3}	8.51×10^{-3}	8.85×10^{-3}
M	$\begin{pmatrix} 4.98(9) & 0.25(7) \\ 4.06(11) & 8.79(15) \end{pmatrix}$	$\begin{pmatrix} 5.01(8) & 0.95(9) \\ 3.03(15) & 8.82(20) \end{pmatrix}$	$\begin{pmatrix} 5.12(5) & 0.9(1) \\ 3.0(3) & 8.64(9) \end{pmatrix}$

metal substrates, however, where two separate triangles consisting of six diffraction spots are observed [80,83]. Here, the {11} and {20} spots coincide, leading to two triangles that are characteristically corner-connected by one spot.

The PTCDA β phase on Cu(111) found in LEED bears significant similarity to the structure '2' proposed by Wagner and co-workers [77]. Using the same rules for the matrix notations [79] for all structures shows that the matrix elements of structure '2' and of the β phase found in our work differ only slightly (only one entry differs by more than 13%). The orientations of the unit cell vector $\mathbf{b}_1$ with respect to the substrate is identical for both structures within ±1.6° (cf. Table 4). Hence, we propose that the β phase possibly corresponds to structure '2' by Wagner, although a difference in the size of the unit cell remains. Structure '1' given by Wagner, however, was not observed in our LEED experiments and differs from our α phase. Furthermore, the packing densities found for the α phase and the β phase agree well (within 2.5%) with those of the (102) planes of the PTCDA bulk phases (8.40×10^{-3} and 8.32×10^{-3} molecules Å^{-2}, respectively [82]), while the densities in structures '1' and '2' differ more significantly from these (by 14% and 21%). These differences may possibly be due to a difference in the substrate quality or preparation conditions in the two studies.

We now turn to PTCDA coverages above 1 ML. Both monolayer phases of PTCDA on Cu(111) (α and β) exist in parallel from the (sub-)monolayer to the multilayer regime. Additional deposition of PTCDA up to a coverage of 3 ML leads to additional weak spots in the LEED pattern (see Figure 7b). They can also be explained by the two PTCDA phases identified above. The spots that appear at distances of 0.3–0.6 Å^{-1} from the specular spot correspond to {*h*0} and {0*k*} spots of the α phase and the β phase for which *h* and *k* are odd and which were extinct before. No spot shifts as a function of the coverage were found. This may have two reasons. Either the molecules form only a single wetting layer on which additional molecules form clusters, or the higher layers adapt the same structure as the first layer without mismatch. Two observations point to the latter case: The intensity of the adsorbate diffraction spots increases with coverage while the relative intensity of the specular spot decreases. In addition, the {10} and {01} spots become detectable, which means that the glide planes of the adsorbate structure vanish. The glide lines in the space group *p2gg* of the PTCDA unit cell only exist if the underlying Cu(111) surface is not taken into account. For the first monolayer, this may be the case because the small periodicity of the Cu atoms compared to the PTCDA periodicity is not "felt" by the electrons scattered by a single PTCDA layer. For a second PTCDA layer, however, the periodicities in this layer and in the underlying monolayer

are identical. Both layers are shifted laterally against each other [82], which breaks the glide plane symmetry. Thus, the LEED data indicate the growth of at least two or even more complete layers of PTCDA on Cu(111). This is in accordance with the results reported in [68,76].

In summary, our LEED investigations show that PTCDA on Cu(111) forms two co-existing phases, both of them displaying on-line-coincidence to the surface with a herringbone arrangement of the molecules. Both are observed from the (sub-)monolayer regime to at least the beginning of the growth of the third layer. The adsorbate forms at least two complete layers before clusters form.

PTCDA on hBN/Cu(111)

Figure 8 shows LEED patterns of PTCDA/hBN/Cu(111) at a coverage of 2 ± 0.5 ML (Figure 8a,c) and 0.8 ± 0.2 ML (Figure 8b). All structures were grown at a sample temperature of 260 K and a deposition rate of 1 ML/min. They were observed in two different UHV chambers. LEED measurements were performed at 110 K. Note that the LEED pattern in Figure 8a has previously been published in [32]. In that study, we attributed this LEED pattern to a pure monolayer of PTCDA on hBN/Cu(111). Further analysis now leads us to the conclusion that the LEED pattern stems from a slightly higher coverage. This will be discussed in further detail below. Nonetheless, our findings presented in [32] still hold.

Commonly, two kinds of LEED patterns were observed for PTCDA/hBN/Cu(111) and were found from the sub-monolayer to the multilayer regime. The observable pattern, and thus the PTCDA structure that formed, did not depend on the PTCDA coverage, but rather on the quality of the hBN layer. The azimuthally smeared out intensity in Figure 8b,c (which was most commonly observed) points to an azimuthal disorder of the PTCDA domains on hBN/Cu(111), both in the first and in higher layers. In some cases, LEED patterns such as that given in Figure 8a were observed, which shows spots that are exceptionally not smeared out azimuthally. The radii of the rings in Figure 8b,c match the distances of the spots from the specular spot in Figure 8a.

We attribute the higher azimuthal order, which manifests in the more discrete spots, to a lower-quality hBN layer with defects or uncovered areas of Cu(111). Both may allow a pinning of PTCDA molecules to the Cu(111) surface. These molecules function as growth nuclei for PTCDA domains and determine the azimuthal orientation of these domains. Evidence for this interpretation is given by the fact that the orientation of the PTCDA domains on hBN/Cu(111) is in agreement with the orientation of PTCDA domains in the β phase on Cu(111) (within
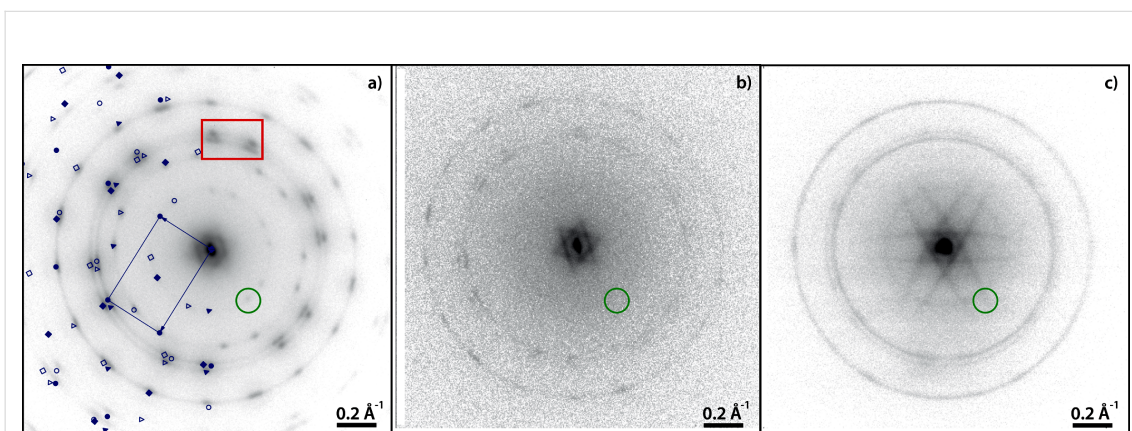
Figure 8: LEED pattern of PTCDA layers on hBN/Cu(111). (a) LEED pattern of 2 ± 0.5 ML PTCDA/hBN/Cu(111). The intensities of the LEED spots are azimuthally smeared out. The maxima in the ring intensities indicate the presence of azimuthally ordered domains. The left half of the LEED pattern is superimposed with the corresponding simulation. Different symbols refer to different symmetrically equivalent domains. This is the same LEED pattern as the one shown in [32], which we originally interpreted as a monolayer. More detailed analysis shows now that the second PTCDA layer has started to form (see main text). The red box highlights the characteristic double-triangle arrangement of spots of the herringbone structure of PTCDA on surfaces. The green ring marks a {10} diffraction spot. (b) LEED pattern of 0.8 ± 0.2 ML PTCDA/hBN/Cu(111). The LEED intensity is homogeneously distributed in rings around the specular spot. The radii of the rings match the distances of the spots in (a) from the specular spot. The green ring marks the same position as in (a). However, the rings corresponding to spot positions of {$h0$} and {$0k$} for which h or k are odd are extinct. (c) LEED pattern of 2 ± 0.5 ML PTCDA/hBN/Cu(111). The LEED intensity is homogeneously distributed in rings around the specular spot as in (b). At this higher coverage, the first-order PTCDA spots are no longer extinct. At the position of the green circle, a faint homogeneous ring can hence be observed. All LEED patterns were recorded at an electron energy of 31 ± 1 eV and at a sample temperature of 110 K.

the error margins, cf. Table 4). The comparison to PTCDA/Cu(111) shows that the β phase has a higher structural resemblance with PTCDA/hBN/Cu(111) than the majority α phase, not only with regard to the orientation, but also to the size of the unit cell (with a deviation of 0.85% of the areas of the unit cells of PTCDA/hBN/Cu(111) and the β phase).

However, in general, PTCDA domains on hBN/Cu(111) have no intrinsically preferred orientation. In Figure 8b and Figure 8c, near the specular spot, a star-like pattern caused by multiple scattering of electrons on hBN/Cu(111) [30] can be observed. Its sharpness points to the high quality of the hBN layer that leads to the homogeneous distribution of the azimuthal orientation of the PTCDA domains.

The discrete spots in Figure 8a support the determination of the structural parameters (cf. Table 4). The similarity of this LEED pattern to those of other PTCDA structures on surfaces is obvious. This includes the double-triangle arrangement of spots (marked by a red box), which makes the structural difference of PTCDA on Cu(111) and on hBN/Cu(111) apparent. Here, the double triangle is formed by six spots leading to two separated triangles. (On Cu(111), these are connected at their corners.) The structure is incommensurate to the hBN layer, and also to the underlying Cu(111) surface. This is in accordance with a weak corrugation of the PTCDA/hBN interaction potential. The

LEED pattern points to an arrangement of the molecules in the herringbone motif, as on Cu(111) [77] and other substrates [80,83]. This was also seen in STM measurements [32].
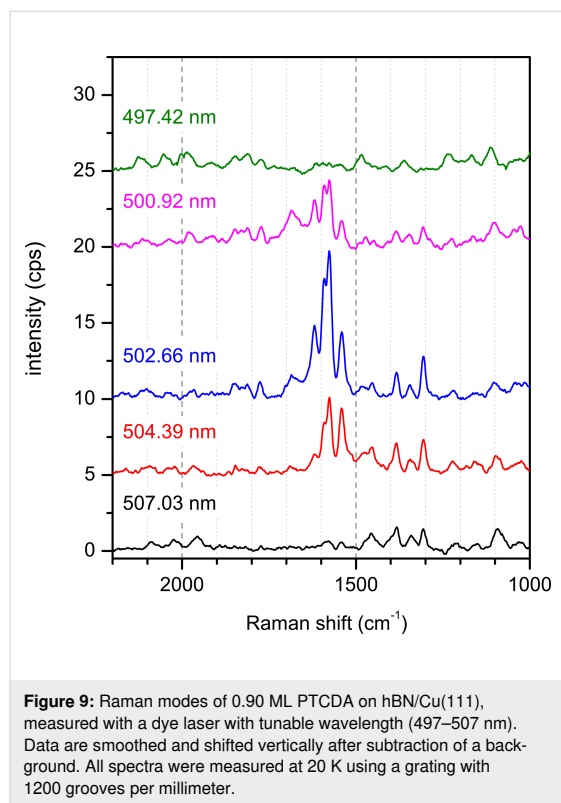
A comparison between the LEED pattern of the first PTCDA layer on hBN/Cu(111) (Figure 8b) with those of higher PTCDA layers (Figure 8a,c) shows that the diffraction spots {$h0$} and {$0k$} for which h or k are odd are extinct for the monolayer, but appear in the second layer. In Figure 8a, a discrete {10} spot is marked by a green circle. In Figure 8c, a line of a continuous ring that corresponds to the {10} spots of PTCDA is seen in the same circle. In Figure 8b, however, there is no intensity at this position in the LEED pattern. The same discussion on the extinction as for PTCDA/Cu(111) applies here (see Section "The structure of PTCDA/Cu(111)"). Furthermore, the distance of the diffraction spots from the specular spot does not change with increasing coverage. This indicates the same layer-by-layer growth mode of PTCDA on both Cu(111) and hBN/Cu(111).

In summary, monolayers of PTCDA/Cu(111) and PTCDA/hBN/Cu(111), despite their structural similarity, can be distinguished by their LEED patterns on the basis of two crucial features. On Cu(111), the "double triangle" is formed by five spots, making it a corner-connected double triangle, while on hBN/Cu(111) six spots form two distinct triangles. Furthermore, the azimuthal smearing of the spots of PTCDA on hBN/
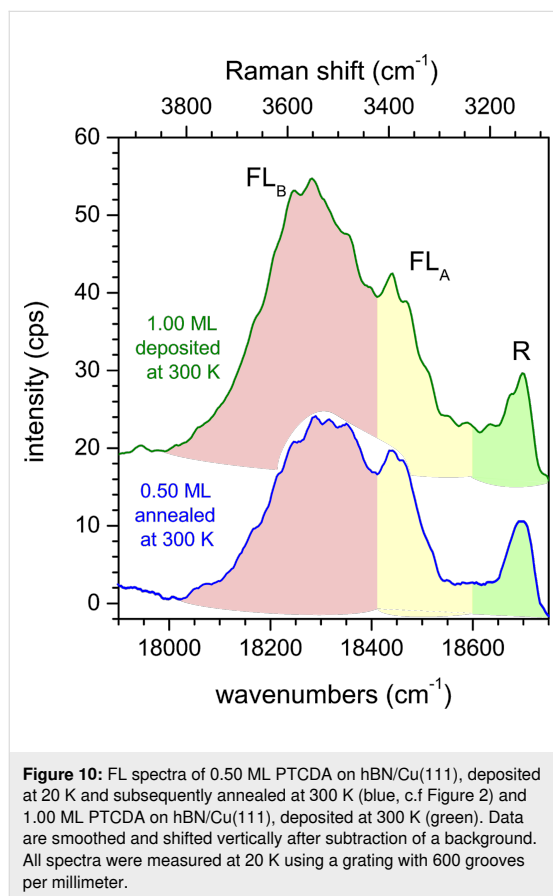
Cu(111) is specific. Additionally, LEED allows the identification of a second PTCDA layer on Cu(111) and hBN/Cu(111) due to the appearance of additional spots, which are absent in the monolayers for symmetry reasons.

Appendix B: Additional optical spectra

Here, additional optical spectra that were referred to in the main text are shown. As mentioned in Section 3.1, the Raman lines in region III of the optical spectra were identified using a dye laser with a tunable wavelength. The Raman lines shift according to the wavelength of the laser. Figure 9 shows spectra recorded with wavelengths between 497 and 507 nm as a function of the Raman shift. Here, all Raman peaks stay at the same energies as expected. Notably, the intensities of the Raman modes change as a function of wavelength. The highest intensities are observed for 458 nm, exceeding the intensities for 502.66 nm (the highest in Figure 9) by a factor of seven.

Figure 9: Raman modes of 0.90 ML PTCDA on hBN/Cu(111), measured with a dye laser with tunable wavelength (497–507 nm). Data are smoothed and shifted vertically after subtraction of a background. All spectra were measured at 20 K using a grating with 1200 grooves per millimeter.

In Section 3.1, we stated that PTCDA deposited on hBN/Cu(111) at a sample temperature of 300 K leads to the same FL as PTCDA deposited at 20 K and subsequently annealed at 300 K. Figure 10 shows spectra from PTCDA/hBN/Cu(111) prepared according to either recipe. In both cases, FL_A and FL_B are present.

Figure 10: FL spectra of 0.50 ML PTCDA on hBN/Cu(111), deposited at 20 K and subsequently annealed at 300 K (blue, c.f Figure 2) and 1.00 ML PTCDA on hBN/Cu(111), deposited at 300 K (green). Data are smoothed and shifted vertically after subtraction of a background. All spectra were measured at 20 K using a grating with 600 grooves per millimeter.

Acknowledgements

References

1. Xu, M.; Liang, T.; Shi, M.; Chen, H. *Chem. Rev.* **2013,** *113,* 3766–3798. doi:10.1021/cr300263a
2. Tan, C.; Cao, X.; Wu, X.-J.; He, Q.; Yang, J.; Zhang, X.; Chen, J.; Zhao, W.; Han, S.; Nam, G.-H.; Sindoro, M.; Zhang, H. *Chem. Rev.* **2017,** *117,* 6225–6331. doi:10.1021/acs.chemrev.6b00558
3. Novoselov, K. S.; Mishchenko, A.; Carvalho, A.; Castro Neto, A. H. *Science* **2016,** *353,* aac9439. doi:10.1126/science.aac9439
4. Yang, X.; Krieger, I.; Lüftner, D.; Weiß, S.; Heepenstrick, T.; Hollerer, M.; Hurdax, P.; Koller, G.; Sokolowski, M.; Puschnig, P.; Ramsey, M. G.; Tautz, F. S.; Soubatch, S. *Chem. Commun.* **2018,** *54,* 9039–9042. doi:10.1039/c8cc03334j
5. Gebauer, W.; Langner, A.; Schneider, M.; Sokolowski, M.; Umbach, E. *Phys. Rev. B* **2004,** *69,* 155431. doi:10.1103/physrevb.69.155431
6. Chance, R. R.; Prock, A.; Silbey, R. Molecular Fluorescence and Energy Transfer Near Interfaces. In *Advances in Chemical Physics;* Prigogine, I.; Rice, S. A., Eds.; John Wiley & Sons, Ltd, 1978; Vol. 37, pp 1–65. doi:10.1002/9780470142561.ch1

7. Campion, A.; Gallo, A. R.; Harris, C. B.; Robota, H. J.; Whitmore, P. M. *Chem. Phys. Lett.* **1980,** *73,* 447–450. doi:10.1016/0009-2614(80)80692-0

8. Neppl, S.; Bauer, U.; Menzel, D.; Feulner, P.; Shaporenko, A.; Zharnikov, M.; Kao, P.; Allara, D. L. *Chem. Phys. Lett.* **2007,** *447,* 227–231. doi:10.1016/j.cplett.2007.09.013

9. Kao, P.; Neppl, S.; Feulner, P.; Allara, D. L.; Zharnikov, M. *J. Phys. Chem. C* **2010,** *114,* 13766–13773. doi:10.1021/jp1042816

10. Müller, M.; Le Moal, E.; Scholz, R.; Sokolowski, M. *Phys. Rev. B* **2011,** *83,* 241203. doi:10.1103/physrevb.83.241203

11. Luo, Y.; Chen, G.; Zhang, Y.; Zhang, L.; Yu, Y.; Kong, F.; Tian, X.; Zhang, Y.; Shan, C.; Luo, Y.; Yang, J.; Sandoghdar, V.; Dong, Z.; Hou, J. G. *Phys. Rev. Lett.* **2019,** *122,* 233901. doi:10.1103/physrevlett.122.233901

12. Imada, H.; Miwa, K.; Imai-Imada, M.; Kawahara, S.; Kimura, K.; Kim, Y. *Phys. Rev. Lett.* **2017,** *119,* 013901. doi:10.1103/physrevlett.119.013901

13. Kimura, K.; Miwa, K.; Imada, H.; Imai-Imada, M.; Kawahara, S.; Takeya, J.; Kawai, M.; Galperin, M.; Kim, Y. *Nature* **2019,** *570,* 210–213. doi:10.1038/s41586-019-1284-2

14. Watanabe, K.; Taniguchi, T.; Kanda, H. *Nat. Mater.* **2004,** *3,* 404–409. doi:10.1038/nmat1134

15. Falin, A.; Cai, Q.; Santos, E. J. G.; Scullion, D.; Qian, D.; Zhang, R.; Yang, Z.; Huang, S.; Watanabe, K.; Taniguchi, T.; Barnett, M. R.; Chen, Y.; Ruoff, R. S.; Li, L. H. *Nat. Commun.* **2017,** *8,* 15815. doi:10.1038/ncomms15815

16. Mahvash, F.; Eissa, S.; Bordjiba, T.; Tavares, A. C.; Szkopek, T.; Siaj, M. *Sci. Rep.* **2017,** *7,* 42139. doi:10.1038/srep42139

17. Li, L. H.; Cervenka, J.; Watanabe, K.; Taniguchi, T.; Chen, Y. *ACS Nano* **2014,** *8,* 1457–1462. doi:10.1021/nn500059s

18. Lee, K. H.; Shin, H.-J.; Lee, J.; Lee, I.-y.; Kim, G.-H.; Choi, J.-Y.; Kim, S.-W. *Nano Lett.* **2012,** *12,* 714–718. doi:10.1021/nl203635v

19. Auwärter, W. *Surf. Sci. Rep.* **2019,** *74,* 1–95. doi:10.1016/j.surfrep.2018.10.001

20. Paulheim, A.; Marquardt, C.; Aldahhak, H.; Rauls, E.; Schmidt, W. G.; Sokolowski, M. *J. Phys. Chem. C* **2016,** *120,* 11926–11937. doi:10.1021/acs.jpcc.6b01956

21. Eisfeld, A.; Marquardt, C.; Paulheim, A.; Sokolowski, M. *Phys. Rev. Lett.* **2017,** *119,* 097402. doi:10.1103/physrevlett.119.097402

22. Kerfoot, J.; Korolkov, V. V.; Nizovtsev, A. S.; Jones, R.; Taniguchi, T.; Watanabe, K.; Lesanovsky, I.; Olmos, B.; Besley, N. A.; Besley, E.; Beton, P. H. *J. Chem. Phys.* **2018,** *149,* 054701. doi:10.1063/1.5041418

23. Forker, R.; Dienel, T.; Krause, A.; Gruenewald, M.; Meissner, M.; Kirchhuebel, T.; Gröning, O.; Fritz, T. *Phys. Rev. B* **2016,** *93,* 165426. doi:10.1103/physrevb.93.165426

24. Joshi, S.; Ecija, D.; Koitz, R.; Iannuzzi, M.; Seitsonen, A. P.; Hutter, J.; Sachdev, H.; Vijayaraghavan, S.; Bischoff, F.; Seufert, K.; Barth, J. V.; Auwärter, W. *Nano Lett.* **2012,** *12,* 5821–5828. doi:10.1021/nl303170m

25. Koitz, R.; Seitsonen, A. P.; Iannuzzi, M.; Hutter, J. *Nanoscale* **2013,** *5,* 5589. doi:10.1039/c3nr00709j

26. Hite, J. K.; Robinson, Z. R.; Eddy, C. R., Jr.; Feigelson, B. N. *ACS Appl. Mater. Interfaces* **2015,** *7,* 15200–15205. doi:10.1021/acsami.5b00723

27. Preobrajenski, A. B.; Vinogradov, A. S.; Mårtensson, N. *Surf. Sci.* **2005,** *582,* 21–30. doi:10.1016/j.susc.2005.02.047

28. Lyalin, A.; Nakayama, A.; Uosaki, K.; Taketsugu, T. *Top. Catal.* **2014,** *57,* 1032–1041. doi:10.1007/s11244-014-0267-7

29. Lin, S.; Huang, J.; Gao, X. *Phys. Chem. Chem. Phys.* **2015,** *17,* 22097–22105. doi:10.1039/c5cp03027g

30. Brülke, C.; Heepenstrick, T.; Humberg, N.; Krieger, I.; Sokolowski, M.; Weiß, S.; Tautz, F. S.; Soubatch, S. *J. Phys. Chem. C* **2017,** *121,* 23964–23973. doi:10.1021/acs.jpcc.7b06107

31. Schwarz, M.; Riss, A.; Garnica, M.; Ducke, J.; Deimel, P. S.; Duncan, D. A.; Thakur, P. K.; Lee, T.-L.; Seitsonen, A. P.; Barth, J. V.; Allegretti, F.; Auwärter, W. *ACS Nano* **2017,** *11,* 9151–9161. doi:10.1021/acsnano.7b04022

32. Brülke, C.; Heepenstrick, T.; Krieger, I.; Wolff, B.; Yang, X.; Shamsaddinlou, A.; Weiß, S.; Bocquet, F. C.; Tautz, F. S.; Soubatch, S.; Sokolowski, M. *Phys. Rev. B* **2019,** *99,* 121404. doi:10.1103/physrevb.99.121404

33. Duhm, S.; Gerlach, A.; Salzmann, I.; Bröker, B.; Johnson, R. L.; Schreiber, F.; Koch, N. *Org. Electron.* **2008,** *9,* 111–118. doi:10.1016/j.orgel.2007.10.004

34. Martínez-Galera, A. J.; Gómez-Rodríguez, J. M. *J. Phys. Chem. C* **2019,** *123,* 1866–1873. doi:10.1021/acs.jpcc.8b10810

35. Gerlach, A.; Sellner, S.; Schreiber, F.; Koch, N.; Zegenhagen, J. *Phys. Rev. B* **2007,** *75,* 045401. doi:10.1103/physrevb.75.045401

36. Ng, M. L.; Preobrajenski, A. B.; Zakharov, A. A.; Vinogradov, A. S.; Krasnikov, S. A.; Cafolla, A. A.; Mårtensson, N. *Phys. Rev. B* **2010,** *81,* 115449. doi:10.1103/physrevb.81.115449

37. Koslowski, S.; Rosenblatt, D.; Kabakchiev, A.; Kuhnke, K.; Kern, K.; Schlickum, U. *Beilstein J. Nanotechnol.* **2017,** *8,* 1388–1395. doi:10.3762/bjnano.8.140

38. Joshi, S.; Bischoff, F.; Koitz, R.; Ecija, D.; Seufert, K.; Seitsonen, A. P.; Hutter, J.; Diller, K.; Urgel, J. I.; Sachdev, H.; Barth, J. V.; Auwärter, W. *ACS Nano* **2014,** *8,* 430–442. doi:10.1021/nn406024m

39. Stallberg, K.; Namgalies, A.; Höfer, U. *Phys. Rev. B* **2019,** *99,* 125410. doi:10.1103/physrevb.99.125410

40. Yeshchenko, O. A.; Bondarchuk, I. S.; Losytskyy, M. Y. *J. Appl. Phys.* **2014,** *116,* 054309. doi:10.1063/1.4892432

41. Kaiser, R.; Friedrich, M.; Schmitz-Hübsch, T.; Sellam, F.; Kampen, T. U.; Leo, K.; Zahn, D. R. T. *Fresenius' J. Anal. Chem.* **1999,** *363,* 189–192. doi:10.1007/s002160051169

42. Wagner, V. *Phys. Status Solidi A* **2001,** *188,* 1297–1305. doi:10.1002/1521-396x(200112)188:4<1297::aid-pssa1297>3.0.co;2-x

43. Scholz, R.; Kobitski, A. Y.; Kampen, T. U.; Schreiber, M.; Zahn, D. R. T.; Jungnickel, G.; Elstner, M.; Sternberg, M.; Frauenheim, T. *Phys. Rev. B* **2000,** *61,* 13659–13669. doi:10.1103/physrevb.61.13659

44. Kilian, L.; Hauschild, A.; Temirov, R.; Soubatch, S.; Schöll, A.; Bendounan, A.; Reinert, F.; Lee, T.-L.; Tautz, F. S.; Sokolowski, M.; Umbach, E. *Phys. Rev. Lett.* **2008,** *100,* 136103. doi:10.1103/physrevlett.100.136103

45. Otto, A.; Mrozek, I.; Grabhorn, H.; Akemann, W. *J. Phys.: Condens. Matter* **1992,** *4,* 1143–1212. doi:10.1088/0953-8984/4/5/001

46. Schlücker, S. *Angew. Chem., Int. Ed.* **2014,** *53,* 4756–4795. doi:10.1002/anie.201205748

47. Cialla, D.; März, A.; Böhme, R.; Theil, F.; Weber, K.; Schmitt, M.; Popp, J. *Anal. Bioanal. Chem.* **2012,** *403,* 27–54. doi:10.1007/s00216-011-5631-x

48. García-Vidal, F. J.; Pendry, J. B. *Phys. Rev. Lett.* **1996,** *77,* 1163–1166. doi:10.1103/physrevlett.77.1163

49. Xia, M. *Coatings* **2018,** *8,* 137. doi:10.3390/coatings8040137

50. Ling, X.; Fang, W.; Lee, Y.-H.; Araujo, P. T.; Zhang, X.; Rodriguez-Nieva, J. F.; Lin, Y.; Zhang, J.; Kong, J.; Dresselhaus, M. S. *Nano Lett.* **2014,** *14,* 3033–3040. doi:10.1021/nl404610c

51. Ehrenreich, H.; Philipp, H. R. *Phys. Rev.* **1962,** *128,* 1622–1629.
doi:10.1103/physrev.128.1622

52. Babar, S.; Weaver, J. H. *Appl. Opt.* **2015,** *54,* 477.
doi:10.1364/ao.54.000477

53. Schneider, M. Vibronische und optische Eigenschaften ultradünner
organischer Filme am Beispiel PTCDA/Ag(111). Ph.D. Thesis,
Universität Würzburg, Würzburg, 2002.

54. Paulheim, A.; Marquardt, C.; Sokolowski, M.; Hochheim, M.;
Bredow, T.; Aldahhak, H.; Rauls, E.; Schmidt, W. G.
Phys. Chem. Chem. Phys. **2016,** *18,* 32891–32902.
doi:10.1039/c6cp05661j

55. Tenne, D. A.; Park, S.; Kampen, T. U.; Das, A.; Scholz, R.;
Zahn, D. R. T. *Phys. Rev. B* **2000,** *61,* 14564–14569.
doi:10.1103/physrevb.61.14564

56. Hauschild, A.; Temirov, R.; Soubatch, S.; Bauer, O.; Schöll, A.;
Cowie, B. C. C.; Lee, T.-L.; Tautz, F. S.; Sokolowski, M. *Phys. Rev. B*
2010, *81,* 125432. doi:10.1103/physrevb.81.125432

57. Hochheim, M.; Paulheim, A.; Sokolowski, M.; Bredow, T.
J. Phys. Chem. C **2016,** *120,* 24240–24249.
doi:10.1021/acs.jpcc.6b08540

58. Bauer, O. Surface bonding of a functionalized aromatic molecule:
Adsorption configurations of PTCDA on coinage metal surfaces. Ph.D.
Thesis, Universität Bonn, Bonn, 2014.

59. Tautz, F. S.; Eremtchenko, M.; Schaefer, J. A.; Sokolowski, M.;
Shklover, V.; Umbach, E. *Phys. Rev. B* **2002,** *65,* 125405.
doi:10.1103/physrevb.65.125405

60. Marquardt, C.; Paulheim, A.; Rohbohm, N.; Merkel, R.; Sokolowski, M.
Rev. Sci. Instrum. **2017,** *88,* 083702. doi:10.1063/1.4997953

61. Gorbachev, R. V.; Riaz, I.; Nair, R. R.; Jalil, R.; Britnell, L.; Belle, B. D.;
Hill, E. W.; Novoselov, K. S.; Watanabe, K.; Taniguchi, T.; Geim, A. K.;
Blake, P. *Small* **2011,** *7,* 465–468. doi:10.1002/smll.201001628

62. Bresnehan, M. S.; Hollander, M. J.; Wetherington, M.; LaBella, M.;
Trumbull, K. A.; Cavalero, R.; Snyder, D. W.; Robinson, J. A.
ACS Nano **2012,** *6,* 5234–5241. doi:10.1021/nn300996t

63. Nakhaie, S.; Wofford, J. M.; Schumann, T.; Jahn, U.; Ramsteiner, M.;
Hanke, M.; Lopes, J. M. J.; Riechert, H. *Appl. Phys. Lett.* **2015,** *106,*
213108. doi:10.1063/1.4921921

64. Xu, Z.; Tian, H.; Khanaki, A.; Zheng, R.; Suja, M.; Liu, J. *Sci. Rep.*
2017, *7,* 43100. doi:10.1038/srep43100

65. Müller, M.; Paulheim, A.; Eisfeld, A.; Sokolowski, M. *J. Chem. Phys.*
2013, *139,* 044302. doi:10.1063/1.4813521

66. Preobrajenski, A. B.; Nesterov, M. A.; Ng, M. L.; Vinogradov, A. S.;
Mårtensson, N. *Chem. Phys. Lett.* **2007,** *446,* 119–123.
doi:10.1016/j.cplett.2007.08.028

67. Schneider, M.; Umbach, E.; Sokolowski, M. *Chem. Phys.* **2006,** *325,*
185–192. doi:10.1016/j.chemphys.2005.08.059

68. Wagner, T.; Karacuban, H.; Möller, R. *Surf. Sci.* **2009,** *603,* 482–490.
doi:10.1016/j.susc.2008.12.007

69. Han, Q.; Shan, H.; Deng, J.; Zhao, A.; Wang, B.; Hou, J. G. *Nanoscale*
2014, *6,* 7934–7939. doi:10.1039/c4nr00017j

70. Wolff, B. Determination of the desorption energy of PTCDA on
hBN/Cu(111) by thermal desorption spectroscopy. Master's Thesis,
Universität Bonn, Bonn, 2019.

71. Rouillé, G.; Kirchhuebel, T.; Rink, M.; Gruenewald, M.; Kröger, J.;
Forker, R.; Fritz, T. *Phys. Chem. Chem. Phys.* **2015,** *17,* 30404–30416.
doi:10.1039/c5cp03761a

72. Wolff, B. Dynamics of Open Quantum Systems. Master's Thesis,
Universität Bonn, Bonn, 2019.

73. Valeur, B. *Molecular Fluorescence,* 1st ed.; Wiley-VCH: Weinheim,
Germany, 2002.

74. Ambrose, W. P.; Basché, T.; Moerner, W. E. *J. Chem. Phys.* **1991,** *95,*
7150–7163. doi:10.1063/1.461392

75. Langner, A.; Su, Y.; Sokolowski, M. *Phys. Rev. B* **2006,** *74,* 045428.
doi:10.1103/physrevb.74.045428

76. Wagner, T.; Bannani, A.; Bobisch, C.; Karacuban, H.; Stöhr, M.;
Gabriel, M.; Möller, R. *Org. Electron.* **2004,** *5,* 35–43.
doi:10.1016/j.orgel.2003.12.001

77. Wagner, T.; Bannani, A.; Bobisch, C.; Karacuban, H.; Möller, R.
J. Phys.: Condens. Matter **2007,** *19,* 056009.
doi:10.1088/0953-8984/19/5/056009

78. Forker, R.; Meissner, M.; Fritz, T. *Soft Matter* **2017,** *13,* 1748–1758.
doi:10.1039/c6sm02688e

79. Barlow, S. M.; Raval, R. *Surf. Sci. Rep.* **2003,** *50,* 201–341.
doi:10.1016/s0167-5729(03)00015-3

80. Glöckler, K.; Seidel, C.; Soukopp, A.; Sokolowski, M.; Umbach, E.;
Böhringer, M.; Berndt, R.; Schneider, W.-D. *Surf. Sci.* **1998,** *405,* 1–20.
doi:10.1016/s0039-6028(97)00888-1

81. Kilian, L.; Umbach, E.; Sokolowski, M. *Surf. Sci.* **2006,** *600,*
2633–2643. doi:10.1016/j.susc.2006.03.049

82. Ogawa, T.; Kuwamoto, K.; Isoda, S.; Kobayashi, T.; Karl, N.
Acta Crystallogr., Sect. B: Struct. Sci. **1999,** *55,* 123–130.
doi:10.1107/s0108768198009872

83. Mannsfeld, S.; Toerker, M.; Schmitz-Hübsch, T.; Sellam, F.; Fritz, T.;
Leo, K. *Org. Electron.* **2001,** *2,* 121–134.
doi:10.1016/s1566-1199(01)00018-0

B The Buckling of hBN on Cu(111) investigated by SPA-LEED

In Chapter 5.2.1, the possible origins of the satellite structure in the LEED pattern of hBN/Cu(111) were identified to be either a long-range buckling of the hBN layer or multiple scattering. It has already been shown that multiple scattering is indeed a contributing factor to the satellite structure (see Appendix A.1). However, the presence of multiple scattering does not exclude the presence of a buckling of the hBN layer which would cause a portion of the intensity of the satellite structure observed in LEED. Here, additional SPA-LEED experiments performed at low energies are described that were used to investigate the possible contribution of a buckling of the hBN layer to the satellite structure.

B.1 Theoretical Background

To find the energies where the contribution from multiple scattering of the first order Cu diffraction spots is eliminated from the LEED pattern, the Ewald construction is used (cf. Figure 3.1). When the radius of the Ewald sphere is small enough (cf. Eq. (3.3)) that it no longer intersects with the first order diffraction rods of the Cu(111) surface (with a lattice vector of $a_{Cu} = 2.556$ Å [76]), multiple scattering is no longer possible. This is achieved at an electron energy of $E_{kin} = 30.8$ eV or lower. This is illustrated in Figure B.1. Here, the diffraction rods are depicted on the scale of the Cu(111) surface with two different Ewald spheres corresponding to electron energies of 37.1 eV and 30.8 eV. At the lower energy the Ewald sphere no longer intersects with the first order diffraction rods so that a multiple scattering process is impossible.

B.1.1 Simple kinematic approximation

For the determination of the corrugation of the hBN layer via SPA-LEED, some approximations have to be applied. The model used here is based on the work by Horn-von Hoegen et al. [186] who investigated the buckling of a thick film (18 ML) of Ge on Si(111). For a flat layer, the intensity I of the diffraction spots is proportional to the square modulus of the structure form factor F:

$$I \sim |F|^2 = \left| \sum_n e^{i\vec{k}\vec{r}_n} \right|^2 . \tag{B.1}$$
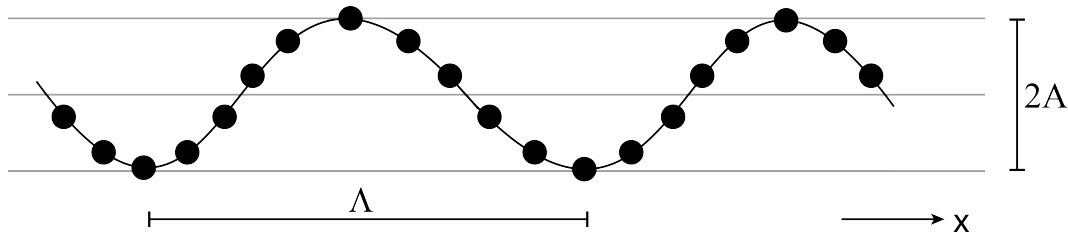
In a simple kinematic approximation, the model of a sinosoidal buckling is employed (see Figure B.2). Accordingly, F can be described as
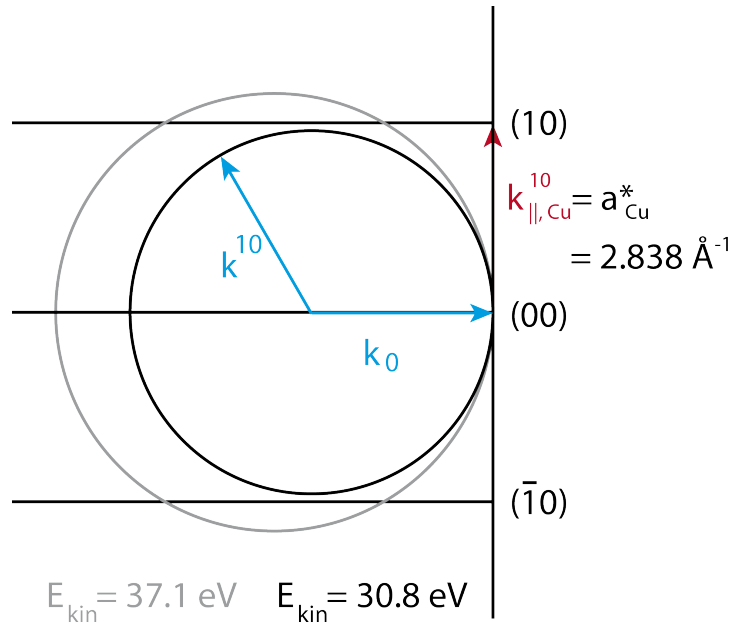
Figure B.1: *First order diffraction rods of the Cu(111) surface with Ewald spheres for electron energies of 37.1 eV (gray) and 30.8 eV (black). The Ewald sphere for the higher energy intersects with the diffraction rods. This results not only in the appearance of the respective spots in the LEED pattern but also allows multiple scattering processes to occur. For the lower energy, where the Ewald sphere no longer intersects with the diffraction rods, neither is possible.*

$$F(\vec{k}) = \sum_n e^{i(k_x,\ k_z)(n \cdot a_{hBN},\ A \cdot \sin(2\pi \frac{n \cdot a_{hBN}}{\Lambda}))} \ , \tag{B.2}$$

with a_{hBN} as the lattice constant of the adsorbed hBN layer, A as the amplitude of its buckling, and Λ as the lattice constant of the buckling of the layer. This model assumes that scattering occurs solely due to the adsorbed layer (i.e. hBN) and that the underlying Cu bulk does not play a role. This approach of modeling the sample by a single layer was legitimate for Horn-von Hoegen who investigated thick films (18 ML) [186]. Here, however, the neglect of the underlying substrate poses a problem that will be discussed further below.

Figure B.2: *Model of a sinosoidal buckling of atoms in one dimension, as employed for the kinematic approximation of the electron diffraction, here. A is the amplitude of the buckling, Λ is the lattice constant of the buckled superstructure.*

A first estimation of the buckling from LEED measurements at higher energies (see Appendix A.1) delivered an upper limit for the amplitude of 0.05 Å. At such a small buckling $k_z \cdot A < 1$ holds

(e.g., at $E_{kin} = 30$ eV, $k_z \cdot A = 0.28$). Thus, by approximating the z-component with a Taylor series, Eq. (B.2) delivers

$$F(\vec{k}) = \sum_n e^{ik_x \cdot n \cdot a_{hBN}} \cdot \left(1 + ik_z \cdot A \cdot \sin(2\pi \frac{n \cdot a_{hBN}}{\Lambda}) + ...\right) \tag{B.3}$$

$$F(\vec{k}) = \sum_n e^{ik_x \cdot n \cdot a_{hBN}} + \sum_n e^{ik_x \cdot n \cdot a_{hBN}} \cdot ik_z \cdot A \cdot \sin(2\pi \frac{n \cdot a_{hBN}}{\Lambda}) . \tag{B.4}$$

The first term in Eq. (B.4) describes the flat hBN layer since it is equivalent to Eq. (B.1) without the vertical component. The second term describes the buckling and, using the lattice vector of the buckled superstructure $G_\Lambda^x = \frac{2\pi}{\Lambda}$, can be expressed as

$$- \frac{k_z \cdot A}{2} \cdot \sum_n e^{ik_x \cdot n \cdot a_{hBN}} \cdot \left(e^{i\frac{2\pi}{\Lambda} \cdot n \cdot a_{hBN}} - e^{-i\frac{2\pi}{\Lambda} \cdot n \cdot a_{hBN}}\right) \tag{B.5}$$

$$= -\frac{k_z \cdot A}{2} \cdot \sum_n e^{i(k_x + G_\Lambda^x) \cdot n \cdot a_{hBN}} - e^{-i(k_x - G_\Lambda^x) \cdot n \cdot a_{hBN}} . \tag{B.6}$$

From Eq. (B.6) it becomes clear that

(i) spots from the buckled superstructure are only expected at positions $H \cdot \vec{a}^* + G_\Lambda^x$ and $H \cdot \vec{a}^* - G_\Lambda^x$, with $H \in \mathbb{Z}$ and

(ii) the intensities of the superstructures spots are proportional to $\left(\frac{k_z \cdot A}{2}\right)^2$.

Conclusion *(i)* agrees with the LEED patterns observed for hBN/Cu(111) where satellite structures are found around the specular spot and the Cu first order spots. Conclusion *(ii)* shows the relationship of the degree of buckling of the hBN layer with its amplitude A and the intensities of the spots from this buckled superstructure, i.e. the intensities of the lines of the satellite structures.

B.1.2 Determination of the LEED intensities of the buckled superstructure

As explained in the previous section, the LEED intensities of the spots of the buckled superstructure can be used to determine its buckling. In order to measure these intensities, line profiles across the (00) spot and the surrounding satellite structures (cf. inset in Figure B.5) were recorded at electron energies of $11-30$ eV. To extract the intensities, these line profiles were fitted using Pseudo-Voigt functions. The intensities of the satellites (I_S) and of the (00) spot (I_0) were extracted from the fits as the areas of the respective peaks. I_S is the average of the areas of the functions that were used to describe both satellites (A and B in Figure B.5) in all three high-symmetry directions. The other two maxima (A' and B') do not have to be considered here, since they are merely the cross sections of two satellite lines. For I_0, the average value of the areas of the Pseudo-Voigt functions that describe the (00) spot in the three high-symmetry directions were used. The integration of the line profiles is legitimate since the widths of the peaks were approximately constant in the perpendicular direction.

In the following, the intensity ratio r will be employed for the determination of A in order to account for variations in the electron current on the sample:

$$r = \frac{I_S}{I_0} \, . \tag{B.7}$$

B.1.3 Challenges regarding the buckling of hBN/Cu(111)

In the simple kinematic approximation, there are two significant factors that make the specific situation of hBN/Cu(111) more complicated than that of Ge on Si(111) which was investigated by Horn-von Hoegen et al. [186].

1. In the study by Horn-von Hoegen et al. [186], corrugated films with a thickness of 18 ML where investigated. At this high coverage, the surface was viewed as a row of columns of atoms that rigidly follow the same amplitude of corrugation. For hBN/Cu(111), however, there is only a single layer of adsorbate. Consequently, the (00) spot contains a significant contribution from the Cu bulk which cannot be neglected here.

2. The intensities of the superstructure spots are azimuthally smeared out, which is not included in the radial line scans across the (00) spot. Thus, some amount of intensity from the superstructure is not included when the integrated intensities of the spot profiles are computed as described above.

The approaches to solve these two problems will be discussed in sections B.3.2 and B.3.1, respectively.

B.2 Technical Adjustments

The SPA-LEED instruments used for the experiments in this thesis theoretically allow electron energies E_{kin} of $0.1-1000$ eV [236]. However, for the given set-up, measuring a LEED pattern was only possible for energies of 20 eV or higher. To achieve LEED measurements at even lower energies here, a bias voltage was applied to the sample to decelerate the electrons in front of the sample surface. This was done by connecting a self-build voltage divider to the sample via the port that is usually used to ground the sample. A circuit diagram of the voltage divider is shown in Figure B.3a.

For measurements at energies of $11-20$ eV, E_{kin} was fixed at 20 eV and the bias voltage was continually increased from 0 to 9 V in steps of 1 V. To ensure that the bias voltage applied to the sample had no unexpected impact on the spot profiles, control measurements were conducted and no influences were found. For example, a measurement conducted with E_{kin} = 25 eV delivered the same profile as a measurement conducted with E_{kin} = 30 eV and a bias voltage of 5 V.

The range of voltages that is accessible to the entrance lens of the SPA-LEED instrument E_L is $0-110\%$ of E_{kin} set in the SPA-LEED controls [237]. Thus, by fixing E_{kin} at 20 eV the voltage range
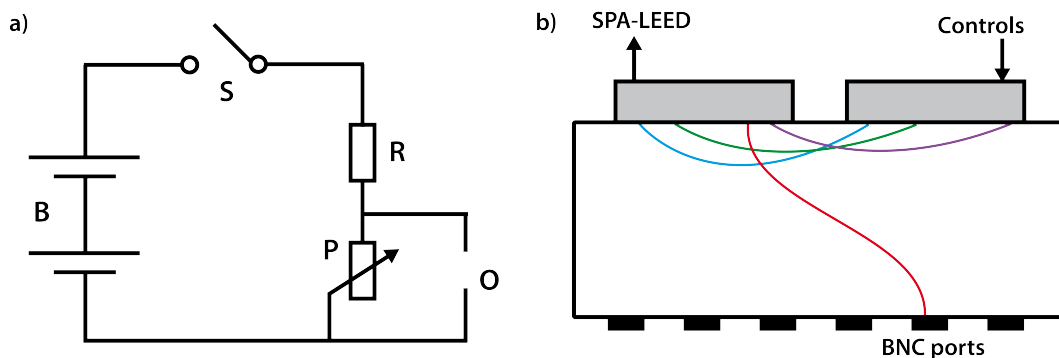
Figure B.3: *a) Circuit diagram of the self-built voltage dividers 1 and 2 used for applying a bias voltage to the sample (1) and for externally controlling the entrance lens of the SPA-LEED instrument (2). They contain a switch S, batteries B as a power source (for the voltage divider 1, two 9 V batteries were used, and for the voltage divider 2 two 30 V batteries), a potentiometer P and a resistance R (40 kΩ in 1 and 100 kΩ in 2). Via a BNC cable the voltage dividers were connected to the sample and the bypass device (see b)) at the output O. b) Schematic of the home-build bypass device for the external voltage control of individual elements of the SPA-LEED instrument. The bypass device is connected to the SPA-LEED controls and the instrument. Inside, the individual connections are split up. The wire that connects to the entrance lens at the instrument is then connected to a BNC port (red). All other wires (represented by the blue, green, and violet lines) are directly connected to the cable that leads into the SPA-LEED controls. Thus, all controls with the exception of the entrance lens remain directly connected to the instrument. E_L can be controlled via the BNC port using voltage divider 2 described in a).*

for E_L was limited and no longer allowed a sufficient adjustment that would yield a good LEED pattern.

Consequently, the voltage setting of E_L was decoupled from the SPA-LEED controls and operated externally. The individual wires that connect the SPA-LEED instruments with the controls were split up using a home-build device for this specific purpose. All wires with the exception of the one connecting to the entrance lens were reconnected to the SPA-LEED controls via a bypass as shown in Figure B.3b. The wire of the entrance lens was connected to a separate port where another voltage divider was used to control E_L with voltages of $0-49$ V.

B.3   The Buckling of hBN on Cu(111)

Figures B.4a and b show the (00) spot and the surrounding satellite structure measured at 23 eV and 15 eV, respectively. As explained in section B.1, satellite lines below an energy of 30 eV cannot stem from multiple scattering as this contribution is eliminated at this low energy. Consequently, since they are still present, the hBN layer must have a superstructure due to a buckling that causes these lines.

To determine the intensities of the (00) spot and the satellite lines at low energies, a series of profiles was measured at energies between 11 and 30 eV in the three high-symmetry directions of the surface. One of these directions is indicated by the blue arrow in Figure B.4a. The other high symmetry directions are separated from this one by 120°. A set of profiles measured in the direction of the blue arrow is shown in Figure B.5. All profiles were fitted with sets of five Pseudo-Voigt
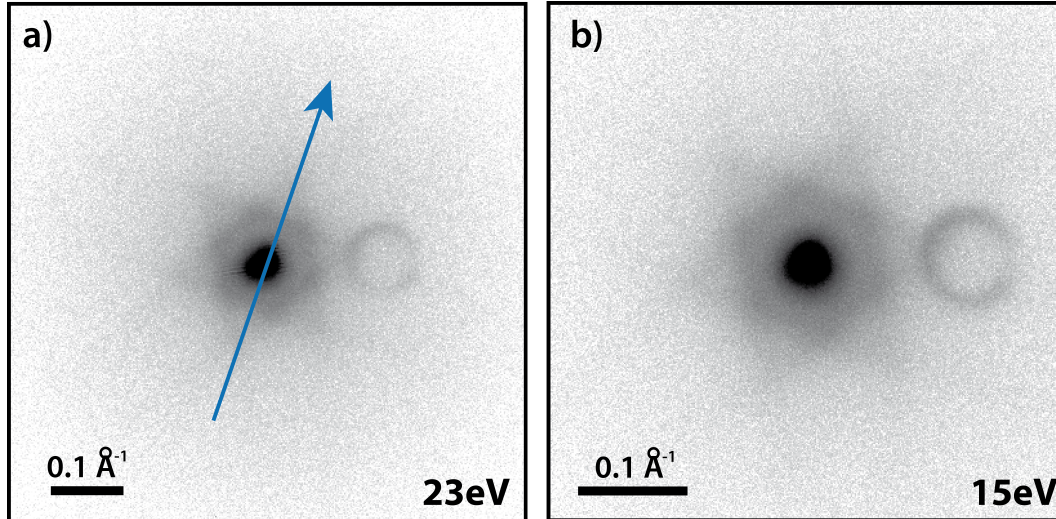
Figure B.4: *Specular spot of hBN/Cu(111) measured with a) 23 eV and b) 15 eV. The satellite structure remains clearly visible at these low energies. Thus, the remaining intensity seen here stems from a buckling of the hBN layer. The ring on the right side of the satellite structure is an artifact of the lenses of the SPA-LEED instrument that appeared at energies of 29 eV and below and is not due to the bias voltage applied to the sample. The blue arrow indicates one of the three high-symmetry directions of the Cu(111) surface. The LEED patterns were recorded at 300 K.*

functions. The contributions of the satellite lines to the profiles are highlighted in orange. These profiles are symmetrical with respect to the center, unlike the profiles measured at energies between 54 eV and 125 eV (see Figure 2 in Appendix A.1). This is in agreement with the expectation of the elimination of the contribution from multiple scattering processes by the Cu substrate. The unequal intensities of the satellite lines are due to the multiple scattering process as explained in Chapter 5.2.1.

The highlighted areas in Figure B.5 clearly show that the intensity of the satellite structure decreases when the electron energy decreases from 30 eV to 20 eV. This is expected according to Eq. (B.6). However, contrary to this expectation, the intensities of the satellites increase again between 20 eV and 15 eV. Only when the energy is decreased from 15 eV to 11 eV, the intensity decreases again.

B.3.1　Determination of A according to Horn-von Hoegen

In accordance with the approach by Horn-von Hoegen et al. [186] and Eqs. (B.1) and (B.6), the square root of the ratio r (cf. section B.1.2) was plotted as a function of k_z. This plot is shown in Figure B.6a as black data points. As already expected from the intensities of the satellite structure observed in Figure B.5, the progression of the intensity ratios shows an oscillation with a maximum at $k_z = 3.96$ Å^{-1} (15 eV) and a minimum around $k_z = 4.90$ Å^{-1} (23 eV).

Due to the oscillation of the intensity ratios, only the data points measured at 15 eV and below are taken into consideration for the determination of the buckling since the expectation of decreasing satellite intensities with decreasing electron energy is met here. A zoom-in on these data points is shown in Figure B.6b. Additionally, theoretical values of $\frac{k_z \cdot A}{2}$ for amplitudes of $A = 0.03$ Å, 0.05 Å,
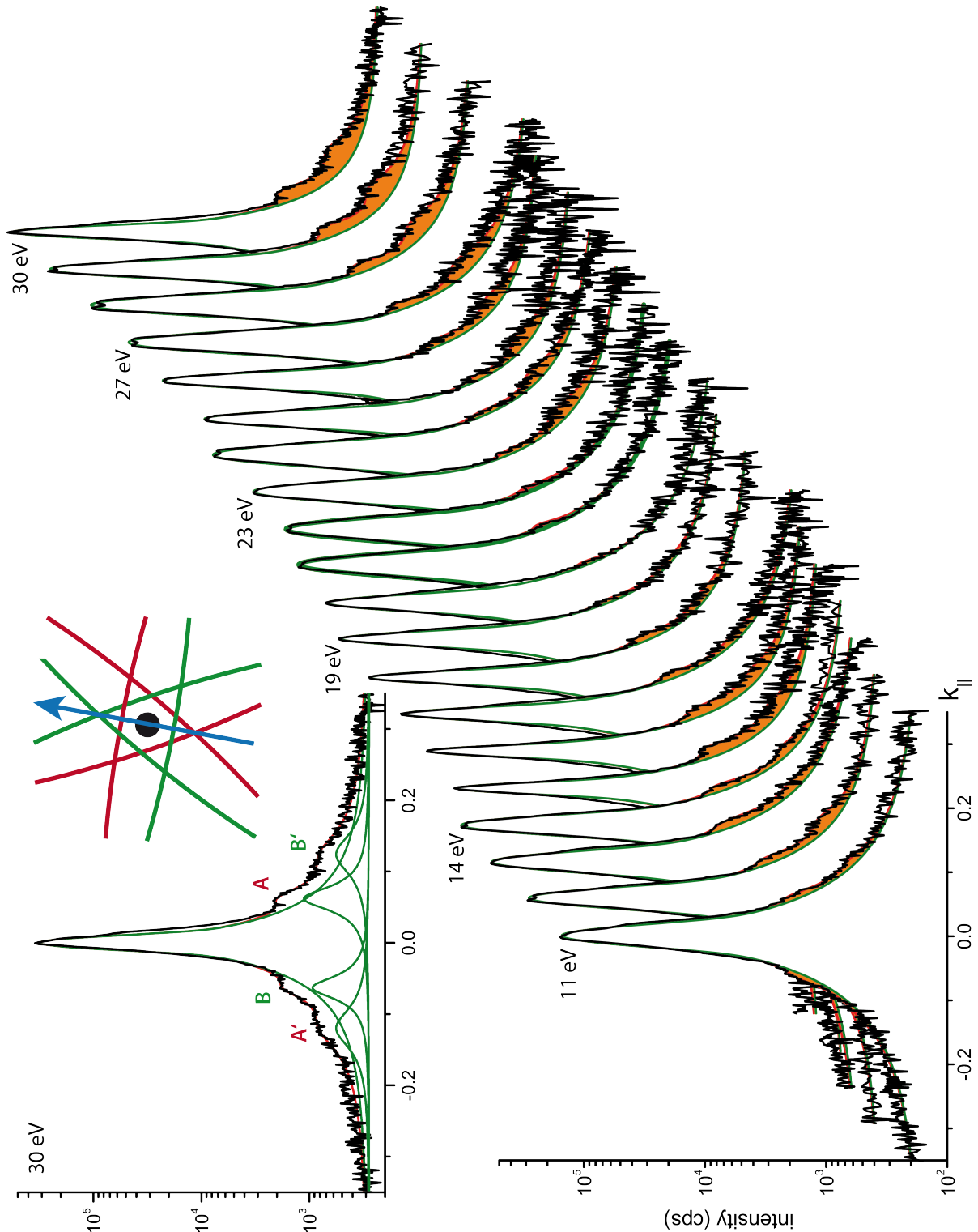
Figure B.5: *LEED spot profiles of hBN/Cu(111) across the specular spot and the surrounding satellite structure (cf. Figure B.4) measured at energies of 11−30 eV. The profiles are fitted with five Pseudo-Voigt functions each (for the specular spot, two satellite lines, and two cross sections of satellite lines). The contribution of the satellite structure to the line profiles is highlighted in orange. The profiles are symmetrical which is different compared to profiles measured at higher energies (see Figure 2 in Appendix A.1) where the contribution of the multiple scattering leads to a difference in the intensities of the different satellite lines. The inset shows the complete profile measured at 30 eV. The different peaks caused by the satellite structure are labeled. A and B refer to the lines, A' and B' refer to their cross sections. The satellite structure is schematically shown for reference. The scanning direction is indicated in blue. Going from 30 eV to lower energies, the intensity of the satellite structure decreases until an energy of 20 eV. At lower energies, the intensity increases again until 15 eV. Between 15 and 11 eV the intensity decreases again.*
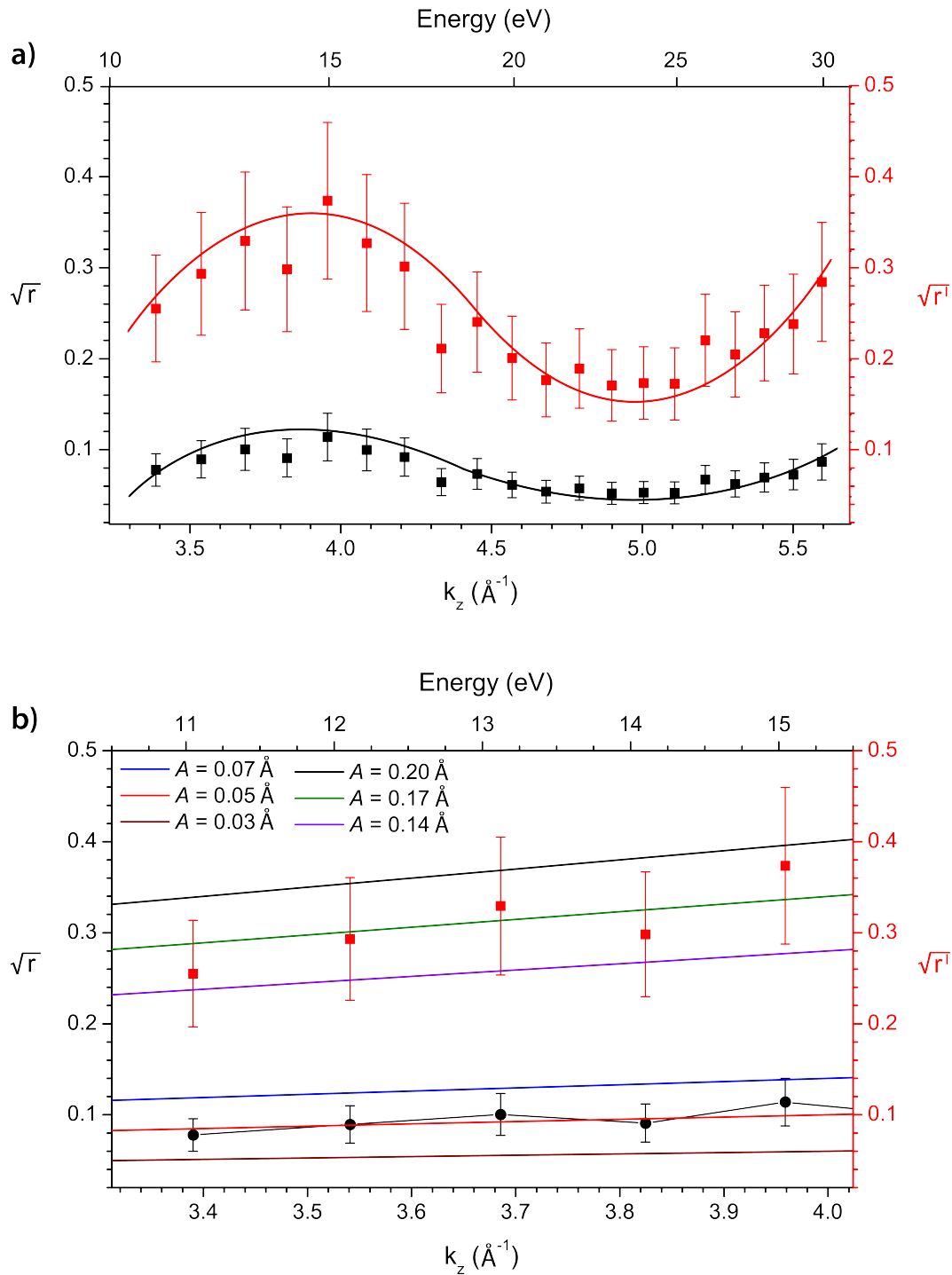
Figure B.6: *Square root of the ratio of the intensities of the satellite structure I_S of hBN/Cu(111) and the (00) spot I_0 of the LEED pattern as a function of k_z for energies of a) 11−30 eV and b) 11−15 eV. Guide lines for the eye and error bars are included. Black data points refer to the intensity ratios r as received from fits of the line profiles shown in Figure B.5, red data points refer to r′, corrected for the azimuthal smearing of the intensities - see text for details. Solid lines in b) show the theoretical values for $\frac{k_z \cdot A}{2}$ for different amplitudes of the buckling of the hBN layer. The corrected (red) data point agree best with an amplitude of 0.17 Å.*

and 0.07 Å are shown as solid lines for comparison with the experimental data. The comparison shows that the experiments give a buckling of the hBN layer of approximately (0.05 ± 0.02) Å.

However, as introduced in section B.1.3, the azimuthal smearing of the satellite intensities has to be taken into account. For this, a correction factor g is used which introduces the FWHM of the respective LEED spots in the azimuthal direction Δw. This results in a corrected intensity ratio r':

$$r' = r \cdot \frac{1}{g} = \frac{I_S}{I_0} \cdot \frac{\Delta w_S}{\Delta w_{00}} \ . \tag{B.8}$$

Δw_S can be gained from azimuthal line scans along the satellite lines as the one shown in Figure 1e in Appendix A.1. g amounts to 0.093. This means that the azimuthal spread reduces the intensity of the satellites in the line profiles by a factor of ~10. Figure B.6 also shows the square root of r' as a function of k_z as red data points. When the azimuthal smearing of the satellites is taken into account, their intensities increase which also increases the amplitude of the buckling that results from this analysis. With the correction it is determined to be 0.17 ± 0.03 Å (see Figure B.6b).

B.3.2 Applying a more elaborate layer mode for the determination of A

The model used up to now has considered a single free layer of hBN which shows the buckling caused by an underlying Cu crystal, as shown in Figure B.2. However, the model did not take into account the underling Cu crystal itself or the interface between the hBN layer and the substrate. This approach greatly simplifies the complicated situation of hBN/Cu(111).

Another approach to determine the amplitude of the buckling is to fit the ratio of intensities as a function that takes into account not only the buckling of the hBN layer (as the parameters A and Λ) but also the interfacial distance d_C and a factor s which describes the relative share of the structure factor that stems from the hBN layer as opposed to the share from the underlying Cu bulk $(1-s)$. This results in a modification of Eq. B.2 to

$$F(\vec{k}) = s \cdot \sum_n e^{i(k_x, \, k_z)(n \cdot a_{hBN}, \, d_C + A \cdot \sin(2\pi \frac{n \cdot a}{\Lambda}))} + (1-s) \cdot \sum_m e^{ik_x \cdot m \cdot a_{Cu}} \ , \tag{B.9}$$

with a_{Cu} as the lattice constant of the Cu(111) surface and m as an integer.

Figure B.7 shows the ratio r (the uncorrected intensity ratio, see Eq. B.7[1]) as a function of k_z as black data points. Additionally, a fitted curve is shown that optimized the free parameters s, A, and d_C. g was used as a free scaling factor that rigidly shifts the fitted function vertically, as demonstrated in Figure B.6. Using the program *Octave* [197] and a self-written script, which calculates the peak intensities of the satellites, the ratio r as a function of k_z was fitted in order to determine the free parameters. The results from the fit are included in the Figure. The amplitude A determines the relative height of the maxima of r at 15 eV and 30 eV while the factor s determines the position of the minima. g serves as an overall adjustment parameter.

---

[1]When r' was fitted instead of r, the results for s, A, and d_C remained the same. Only g, the fitted scaling factor, increased significantly by a factor of ~10 which is plausible.
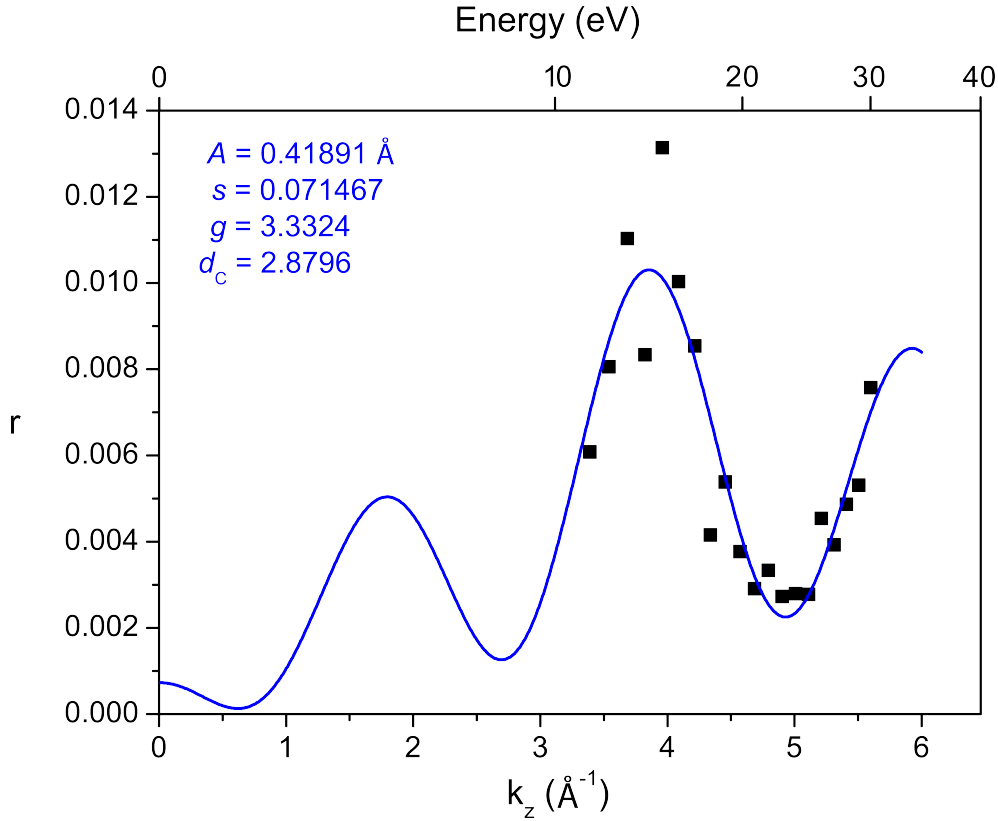
Figure B.7: *The ratio r of the satellite intensities I_S and the intensity of the (00) spot I_0 as a function of k_z as black data points. The data points were fitted with Eq. B.9 and four free parameters s, A, d_C, and g. The fit and the results for the free parameters are shown in blue.*

All reasonable fits gave an amplitude $A = (0.42 \pm 0.05)$ Å. However, the free parameter g here always had a value of ~3 which differs from the previously estimated value of g by a factor of more than 30. If g is fixed at 0.093, the data points could not be fitted. This discrepancy should, however, not be taken too serious because the absolute intensity ratio of the satellites versus the (00) spot is subject to a number of systematic uncertainties.

Furthermore, the fit gives a result of 2.8796 Å for the free parameter d_C which deviates from the value determined in XSW experiments (see Chapter 5.2.2) by 11 %. This small deviation may compensate a phase shift between the waves scattered back from the Cu(111) surface and those scattered back from the hBN layer. The result for $s = 0.07$ shows that the major contribution to the (00) spot stems from the Cu substrate. While the fit delivers an amplitude for the buckling of the hBN layer in the same order of magnitude as the more simplified analysis in section B.3.1 (0.17 $\pm$ 0.03 Å), this result is at present not so robust due to the larger number of free parameters and the limited amount of data points.

However, the fit is able to demonstrate the origin for the oscillation of the intensity ratios which was not expected in the model used in section B.3.1. In the fit, the oscillation is caused by the factor s which describes the ratio of the structure factors of the hBN layer and the Cu bulk. Thus, the oscillation of the intensities observed in Figure B.6 stems from the interference of the electrons diffracted from the hBN layer with those diffracted at the Cu bulk.

B.4 Conclusions

In this chapter, the buckling of an hBN layer on Cu(111) was investigated by SPA-LEED. The observation of the satellite structure below an energy of E_{kin} = 30.8 eV shows that a buckling of the hBN layer is a contributing factor to this structure.

The ratio of the intensities of the (00) spot and the satellites at these low energies oscillates. This oscillation is caused by the interference of electrons diffracted at the hBN layer and at the Cu bulk, respectively. This shows that the Cu bulk significantly contributed to the LEED pattern. However, this contribution cannot be quantified here so that the amplitude of the buckling of the hBN layer is estimated based on a simplified kinematic model. In this estimation the amplitude of the buckling amounts to (0.42 ± 0.05) Å.

C Optical Properties of DBP on hBN/Cu(111)

It has been shown that a single layer of hBN is not suitable to fully decouple PTCDA molecules from an underlying Cu(111) substrate. Although the observation of FL was possible, the intensities are very low and the life times of the excited states are small. However, this does not mean, that hBN can never act as an appropriate insulator to decouple organic molecules from metal surfaces. For this purpose, DBP can be considered.

Its molecular structure is shown in Figure C.1. The peripheral phenyl groups of the molecule lift the perylene backbone off of the surface, increasing the distance at the hBN/molecule interface. This is expected to further decouple the molecule, leading to higher intensity of FL signals and a longer life time of the excited state. In the following, the FL of DBP/hBN/Cu(111)[1] will be described and compared to DBP/KCl/Ag(100) [171] and to PTCDA/hBN/Cu(111).
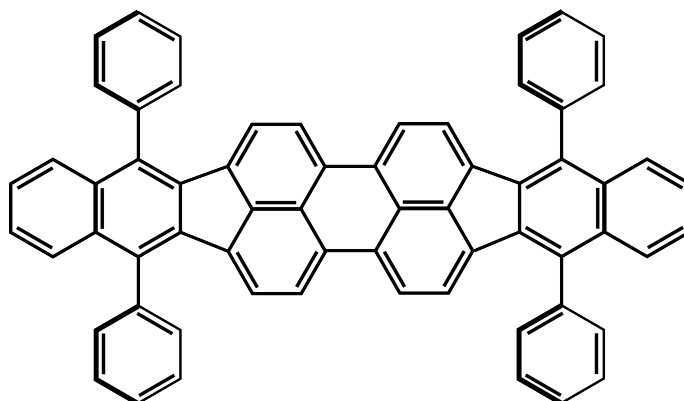

Figure C.1: *Structural formula of DBP [238]. The peripheral phenyl groups are rotated around the single C−C bond. On a surface, the phenyl groups act as spacers between the perylene backbone of the molecule and the surface.*

C.0.1 Fluorescence of DBP on hBN/Cu(111)

Figure C.2a shows the normalized FL spectra of 0.01% ML DBP/KCl/Ag(100) [171] (black spectrum). The most intense peak was assigned to the 0-0 transition, the vibrational peaks at lower energies are well resolved. In different experiments the FL spectra of DBP/KCl/Ag(100) were shifted or were composed of several shifted spectra. Currently, the interpretation of this observation is that the DBP molecules adsorb at different surface sites. These different environments then result in different shifts of the FL [171]. For example, the spectrum in Figure C.2a shows a shoulder on the high energy side of the 0-0 peak. This peak is the 0-0 transition of DBP molecules

---

[1]The FL data of DBP/hBN/Cu(111) shown in this section was obtained in collaboration with B. Wolff during the preparation of her Master's thesis.
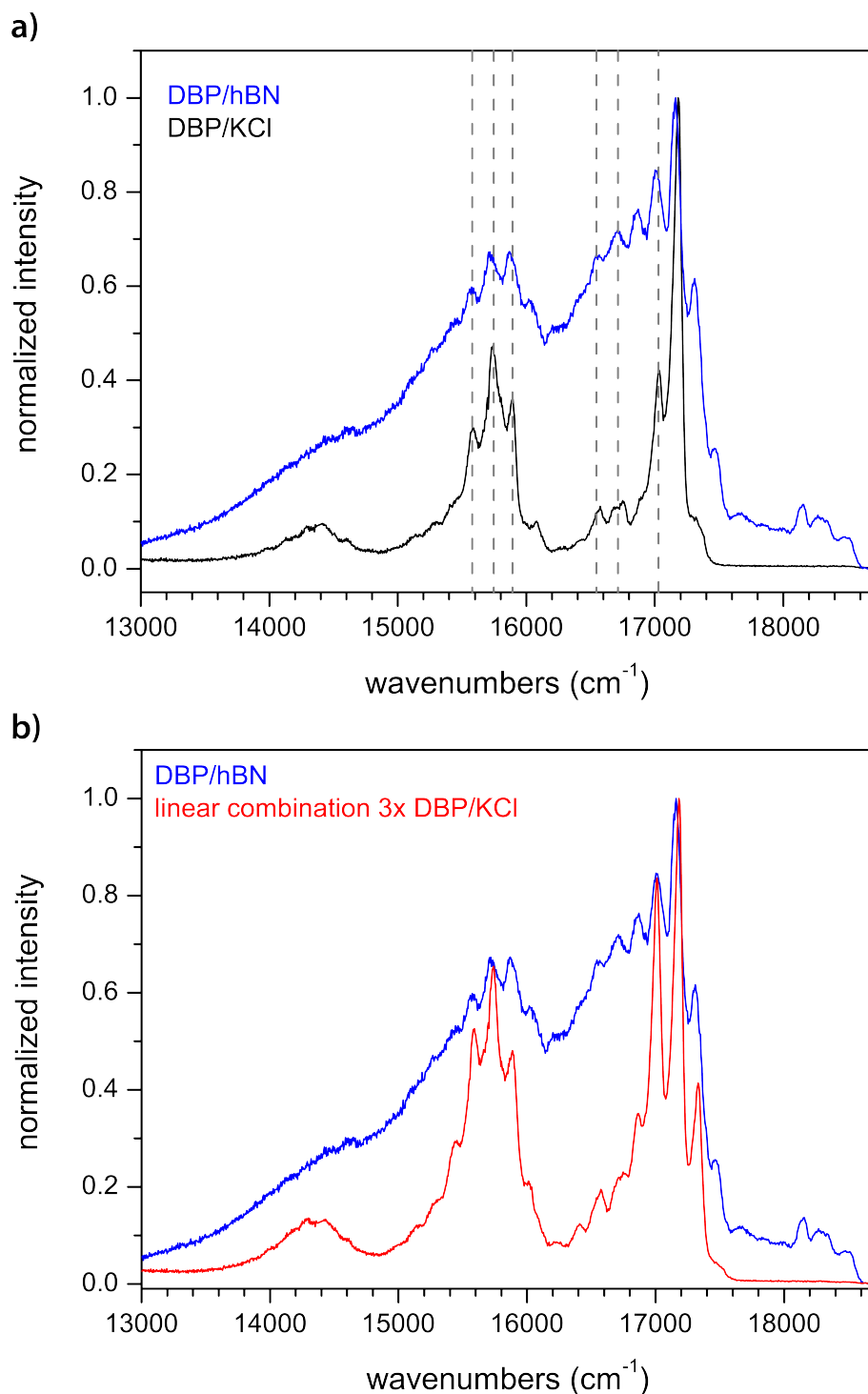
Figure C.2: *a) FL spectra of 0.25 ML DBP on hBN/Cu(111) (blue) and 0.01% ML of DBP on KCl/Ag(100) (black, taken from Ref. [171], laterally shifted for better comparison, see text for details). The intensities are normalized for a better comparison of the spectra. The blue spectrum was measured with λ_{ex} = 532 nm and P_{ex} = 10 mW for 50 seconds, using a long pass filter with cut-off at 532 nm. DBP was deposited at 20 K and heated to 70 K for 3 seconds. The black spectrum was measured with λ_{ex} = 496.4 nm and P_{ex} = 21 mW for 40 seconds. DBP was deposited at 20 K. Both spectra were measured at 20 K using gratings with 300 grooves per mm. The difference in intensity amounts to ~40% (where DBP on KCl/Ag(100) exhibits the larger intensity). b) FL spectrum of 0.25 ML DBP on hBN/Cu(111) (blue, same as in a) and a linear combination of three laterally shifted spectra of DBP/KCl/Ag(100) (the same as in a, red). These agree better than the spectra in a, which indicates that the blue spectrum of DBP/hBN/Cu(111) consists of the FL of DBP molecules at several different adsorption sites on the surface.*

adsorbed at other sites than the majority that cause the more intense lines in the spectrum. 0-0 transitions of DBP/KCl/Ag(100) were found at 17,183 cm^{-1}, 17,232 cm^{-1}, and 17,340 cm^{-1}. The spectrum shown in Figure C.2a was shifted for a better comparison to the FL spectrum of 0.25 ML DBP/hBN/Cu(111) also shown in Figure C.2a (blue spectrum). The actual position of the 0-0 transition in the DBP spectrum shown here is 17,183 cm^{-1}. The 0-0 transition of DBP/hBN/Cu(111) is positioned at 17,161 cm^{-1}. This small shift of only 22 cm^{-1} between the two substrates is a first indication for significantly reduced interactions at both interfaces because the substrates have only a minor influence on the 0-0 transition of the molecule. This is in contrast to the shifts observed for PTCDA. For example, the shift between PTCDA/hBN/Cu(111) and PTCDA/KCl/Ag(100) amounts to 1,300 cm^{-1}.

The positions of the vibrational peaks relative to the 0-0 transition of DBP/KCl/Ag(100) and DBP/hBN/Cu(111) are in good agreement as shown by the dashed lines in Figure C.2a. However, the relative intensities are rather different. The reason for this may be that the spectrum of DBP/KCl/Ag(100) mainly stems from DBP molecules at one adsorption site, while the spectrum of DBP/hBN/Cu(111) appears to be composed of contributions from molecules at several different sites on the surface. This can be seen, again, at the peak at the high energy side of the 0-0 transition. As explained above, on KCl/Ag(100) this peak had been assigned to DBP molecules at different adsorption sites [171]. The same peak is present on hBN/Cu(111), however, much more intense.

To confirm the assumption that the spectrum recorded for DBP/hBN/Cu(111) contains several spectra of different species, an attempt was made to recreate the measured spectrum by the supposition of three shifted spectra of DBP/KCl/Ag(100). This is shown in Figure C.2b (red spectrum). Some of the vibrational peaks now match in their relative intensity to the 0-0 transition. However, most features are still much lower in intensity than the measured spectrum. It appears that a very broad, red-shifted spectrum contributes to the measured spectrum of DBP/hBN/Cu(111). This broadness of the spectrum may point to disorder of the molecules on the surface.

The absolute intensities of the spectra shown in Figure C.2a amount to 355 counts per second (cps) for DBP/KCl/Ag(100) and 206 cps for DBP/hBN/Cu(111). Taking into account the difference in coverage, the different powers of the lasers, and the exposure times, the intensity of the 0-0 transition of DBP/KCl/Ag(100) is larger by a factor of ~2500 compared to DBP/hBN/Cu(111) and the FWHM is smaller by a factor of ~2. On the one hand, this again demonstrates the superior decoupling of the organic molecule by a KCl film compared to a single layer of hBN. On the other hand, the difference between the two substrates in the FL yield is significantly smaller for DBP than for PTCDA. In the following, the two molecules on hBN/Cu(111) will be compared in more detail.

C.0.2 hBN for decoupling molecules: PTCDA versus DBP

Now, the FL of DBP/hBN/Cu(111) and of PTCDA/hBN/Cu(111) will be compared. Figure C.3 shows the FL spectrum of 0.25 ML DBP/hBN/Cu(111), deposited at 20 K as already shown in Figure C.2a on an absolute intensity scale in cps (blue spectrum). The FL spectrum of 0.60 ML

PTCDA/hBN/Cu(111) is shown for comparison (green spectrum). The peaks FL_A and FL_B of PTCDA/hBN/Cu(111) are highlighted in yellow for clarity. There are two obvious differences between the two spectra. For DBP, vibronic peaks are resolved and the intensity of the 0-0 transition is higher by a factor of 4. If the difference in the power of the lasers (10 mW for DBP and 50 mW for PTCDA) and the different coverages are taken into account, an additional factor 10 can be considered to impact the intensities, yielding an actual difference by a factor of 40.
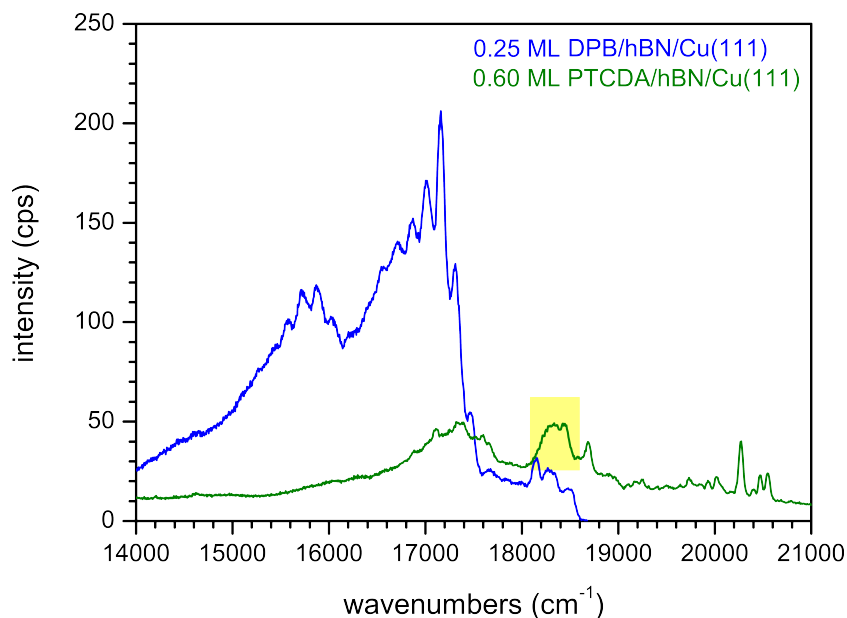
Figure C.3: *FL spectra of 0.25 ML DBP (blue) and 0.60 ML of PTCDA (green) hBN/Cu(111). The blue spectrum was measured with λ_{ex} = 532 nm and P_{ex} = 10 mW for 50 seconds, using a long pass filter with cut-off at 532 nm. DBP was deposited at 20 K and heated to 70 K for 3 seconds. The green spectrum was measured with λ_{ex} = 458 nm and P_{ex} = 50 mW for 100 seconds. PTCDA was deposited at 20 K and annealed at 300 K for 3 minutes. Both spectra were measured at 20 K using gratings with 300 grooves per mm. The FL of PTCDA is highlighted for clarity.*

These results show that, as per the expectations expressed above, the DBP molecules are indeed decoupled from the underlying Cu(111) substrate more efficiently than the PTCDA molecules. Most likely, this improved decoupling is caused by the additional spacing between the perylene backbone and the substrate due to the peripheral phenyl groups. Thus, a single layer of hBN is indeed able to decouple certain molecules from an underlying metal substrate for FL to be observed.

D Segregation of impurities from the Cu(111) crystal

For one of the Cu(111) crystals used in the experiments presented in this thesis (crystal B, see Chapter 4.2.1), segregations of impurities from the bulk were observed in LEED. If this crystal was heated to a temperature >1040 K and/or for a duration of more than 30 minutes (even at 1000 K), additional sharp spots of high order were observed in the LEED pattern.

Whenever these segregations occurred, the formation of an hBN layer was not possible. After borazine deposition following the recipe for hBN growth given in Chapter 4.2, only the LEED pattern of the impurities could be observed and there was no indication for the presence of an hBN layer. Presumably, the area of bare Cu(111) was significantly reduced so that the catalytic decomposition of borazine molecules was not possible.

The structure of the segregated material on the surface was not reproducible. Even under the same annealing conditions, different LEED patters of the segregations on Cu(111) were measured. These are shown in Figure D.1 and the preparation conditions are summarized in Table D.1.
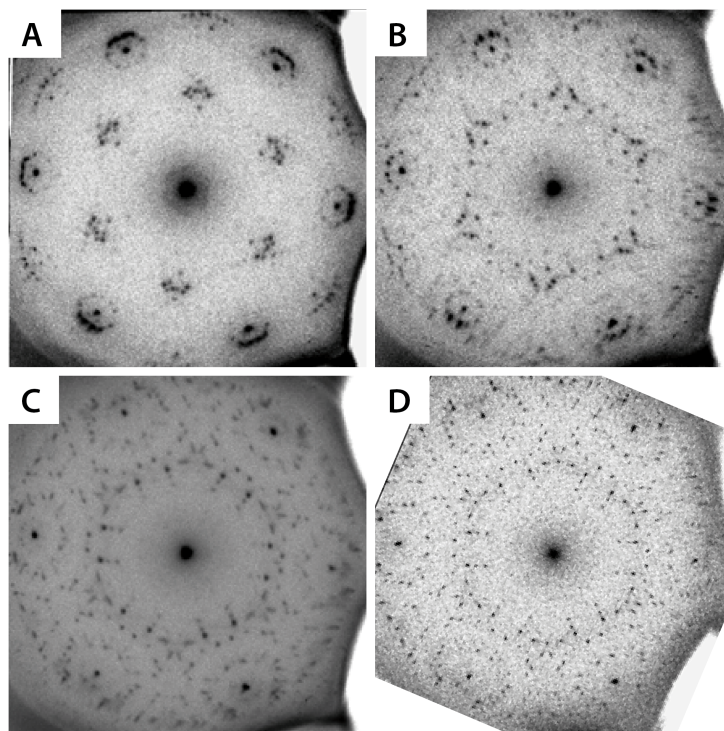
Figure D.1: *LEED patterns of the Cu(111) surface after sputtering and annealing. The preparation conditions are given in Table D.1. The LEED patterns were measured with an electron energy of 78 ± 0.1 eV at $260-280$ K.*

Table D.1: *Preparation conditions for the Cu(111) surface of crystal B that yielded the LEED patterns shown in Figure D.1. The surface was cleaned by ion bombardment from two angles ($\pm$ 45° relative to the surface normal) for a duration of $t_{\mathrm{sputtering}}$ each. Then, the sample was annealed at a temperature $T_{\mathrm{annealing}}$ for a duration of $t_{\mathrm{annealing}}$. In preparation A, borazine deposition in order to grow hBN was attempted immediately after annealing.*

preparation	$t_{\mathrm{sputtering}}$	$t_{\mathrm{annealing}}$	$T_{\mathrm{annealing}}$	
A	15	30 minutes	1040 K	borazine deposition
				at 1070 K for 30 minutes
B	5	60 minutes	1070 K	
C	15	30 minutes	1070 K	
D	15	30 minutes	1040 K	

E Attempts of the preparation of hBN on a Ag(100) surface

As introduced in the main text of this thesis, a large distance at the interfaces in a layered system of organic molecule/hBN/metal substrate increases the decoupling of the molecular electronic states from the metallic states. In a theoretical study, Laskowski et al. [55] have shown that the interactions between hBN and an Ag substrate are similarly weak as in hBN/Cu. Experimental studies of hBN/Ag(111) [87] and hBN/Ag(100) [89] have shown that the interactions appear to be even weaker. In both cases, the LEED patterns show a continuous ring of intensity whose radius matches the lattice constant of hBN. The Ag surfaces do not have any influence on either the hBN lattice constants or, unlike the Cu(111) surface, on the orientation of the hBN domains.

In an effort to find the ideal substrate for hBN to decouple PTCDA from a metal surface, attempts were made to reproduce the results by Müller et al. [89] and prepare an hBN layer on Ag(100). The even weaker interactions at the hBN/Ag(100) interface were expected to result in a similar or even larger vertical distance between the two which would enhance the ability of hBN to decouple the molecule from the metal.

However, the attempts at preparing a single layer of hBN on Ag(100) were not successful. In the following, the preparation conditions and the results of the failed attempts will be presented.

E.1 Experimental

The clean Ag(100) surface was prepared in two steps. First, contaminations were removed from the sample at room temperature by ion bombardment with Ar^+ ions at an argon pressure via the background of 2.1×10^{-5} mbar. The ions were accelerated onto the surface with 1000 eV. The ion current on the sample amounted to $4-5$ μA. The ions impacted the surface in two angles of $+/- 45°$ relative to the surface normal, for 10 minutes each. In a second step, the sample was annealed at $960-1000$ K for 1 hour in order to heal the roughened surface.

After preparation, the quality of the Ag(100) surface was verified via SPA-LEED. A well-prepared surface showed sharp spots and high spot-to-background intensity ratios. The analysis of the full-half widths of spot profiles recorded at 81 eV (corresponding to in-phase conditions for the specular spot) showed a mean domain width of 600 Å.

An hBN layer was attempted to be grown on the clean Ag(100) surface. The sample was heated up to high temperatures and borazine was let into the chamber at high doses. Since several attempts at the preparation were made, the exact conditions were varied. They are given in Table E.1. Due to the lower vapor pressure of Ag compared to Cu [76] the sample temperature during hBN

preparation was chosen to be lower than for hBN/Cu(111). When the desired dose of borazine was reached, the valve was closed and then the sample was cooled down with a rate of $1 - 2\,\mathrm{Ks^{-1}}$. If not noted otherwise, the sample was sputtered and annealed prior to dosing of the borazine.

Table E.1: *Preparation conditions for the attempts at preparing a single layer of hBN on the Ag(100) surface. The sample temperature T_S during deposition, the pressure p of borazine in the chamber (measured against the background), and the dose D of borazine are given.*

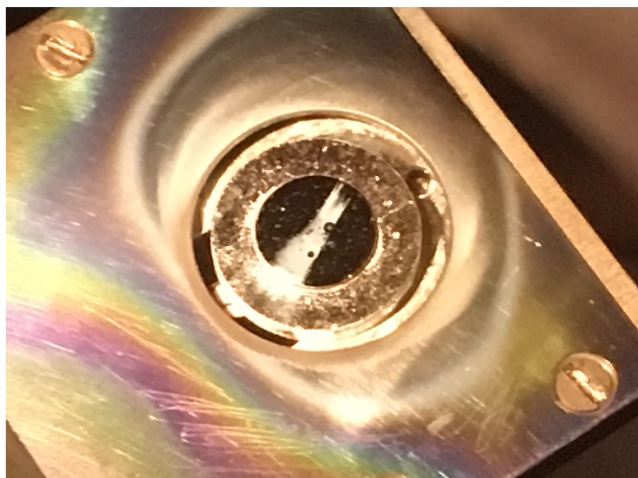| Preparation	T_S	p	D	
1	960 K	1.6×10^{-6} mbar	2880 L	
2	980 K	1.5×10^{-5} mbar	30510 L	
3	990 K	1.5×10^{-5} mbar	61020 L	sample was not cleaned before the new dose
4	980 K	1.5×10^{-5} mbar	30510 L	sample was not annealed after sputtering
5	840 K	1.5×10^{-6} mbar	2880 L	
6	865 K	1.5×10^{-5} mbar	30510 L	

E.2 Results

The conditions of preparation 1 were chosen so that the dose was larger compared to the preparation on Cu(111) by a factor of ~1.5 and by a factor of 2 compared to the dose used by Müller et al. for the preparation of hBN/Ag(100) [89]. The higher dose was chosen as a safety measure to avoid only submonolayer coverage. However, after the preparation, only the LEED pattern of the clean Ag(100) surface was observed. Subsequently, the dose was significantly increased (preparations 2 and 3) or the Ag(100) surface was not annealed after sputtering in order to increase the number of reactive sites on the surface (preparation 4). In all of these attempts, only the LEED pattern of the clean surface could be obtained.

In the next experiment (preparation 5), the sample temperature during deposition was decreased and the initial dose of only 2880 L was chosen. It was assumed that a possible high rate of sublimation of the Ag(100) surface itself might prevent the growth of the hBN layer. This, again, yielded only the LEED pattern of the clean surface.

For preparation 6, again, a low sample temperature of 865 K was chosen and the borazine dose was increased to 30510 L. These conditions caused some kind of reaction on the surface. Figure E.1 shows that the results from this experiment were visible even with the naked eye. A broad white streak had appeared on the Ag crystal. In the LEED pattern (shown in Figure E.2a), which had contained only the spots of the Ag(100) surface in the previous experiments now showed sharp, apparently disordered spots at the edges of the pattern. Moving the sample position changed the LEED pattern as shown in Figure E.2b. Sharp spot of different sizes cover the complete picture without exhibiting any kind of pattern. Furthermore, the specular spot has disappeared.

Evidently, the LEED picture in Figure E.2a was measured on the edge of the broad streak, thus showing partly the clean Ag(100) surface and partly the white material, and the LEED picture in Figure E.2b was measured directly on the streak.

Figure E.1: *Photo of the Ag(100) crystal with the broad white streak of BN.*
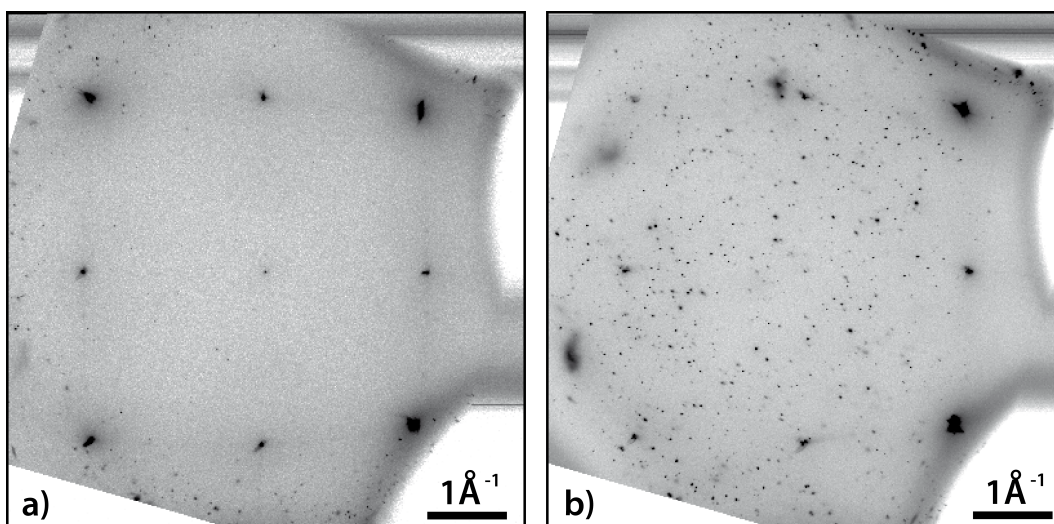
Figure E.2: *LEED patterns of the Ag(100) surface after preparation 6. The LEED patterns were measured with an electron energy of 81 eV at 290 K. Presumably, the patterns were measured a) on the edge and b) right on top of the white streak shown in Figure E.1.*

The white material that was deposited on the surface was remarkably stable. A simple preparation cycle as described in section E.1 did not remove the white substance. Subsequently, the preparation conditions for the clean Ag(100) surface were altered. First, the sputtering parameters were changed to 1200 eV (yielding an ion current on the sample of $7-8$ μA) for 60 minutes instead of 1000 eV for 20 minutes. After 8 cycles under these condition, the white streak had mostly disappeared but was still visible when the sample was viewed in a certain angle. The sharp spots in the LEED pattern remained. Then, the acceleration voltage of the Ar^+ ions was increased further up to 2000 eV (with an ion current on the sample of $9-10$ μA), the Ar pressure up to 5.0×10^{-5} mbar, and the sputtering time up to 3 hours. Yet, the sharp spots in LEED remained. It was not possible to completely remove the deposited material from the Ag(100) surface.

The nature of this white material that was deposited here is unclear. Presumably, it is some kind of BN compound. The sharp but disordered spots observed in LEED show that the streak on the surface was made up of a large number of crystallites that were tilted and rotated with respect to each other. This leads to the disorder in the LEED pattern despite a possibly high order within the small crystallites.

Based on the assumption that the white material is crystalline and the observation that it is a *very* stable compound, a possible candidate for this material is cubic boron nitride.

hBN is a single sheet of the layered hBN bulk material just as graphene is basically one sheet of graphite. However, there are more carbon-analogous modifications of boron nitride, such as nanotubes [239], wurtzitic boron nitride [240] (wBN, analogous to lonsdaleite which is known as hexagonal diamond [241]), and cubic boron nitride (cBN) [240]. This cBN has a zincblende structure and thus corresponds to diamond. Another similarity between diamond and cBN is their hardness. Indeed, the *only* material that is harder than cBN with a Vicker hardness of 5,000 kg mm^{-2} is diamond [240]. Thus, the formation of small crystallites of cBN on the Ag(100) surface may explain the observations described above.

F Borazine: Storage, handling, and cleaning

In this chapter, the handling, storage, and cleaning of borazine will be detailed. The information given here are intended as instructions for other scientist and/or students working with this chemical.

Borazine ($B_3H_6N_3$, also known as s-Triazaborane or 1,3,5,2,4,6-Triazatriborine [242]) is an inorganic compound which is isostructural and isoelectronic to benzene. It is a colorless liquid with an aromatic smell. Unlike benzene, the borazine molecule is not a true hexagon because the bond angles at the nitrogen and the boron atoms differ. The structural details of the borazine molecule are shown in Figure F.1. Another significant difference to the benzene molecule are the different electronegativities of boron and nitrogen (2.04 and 3.04 on the Pauling scale, respectively).
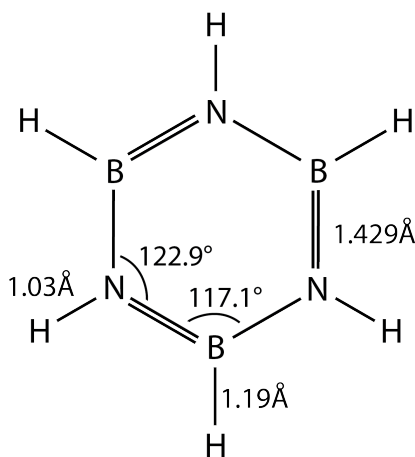
Figure F.1: *Structural formula of borazine. Three BH and three NH units alternate in a hexagonal ring. All six B−N bonds in the ring have the same length due to the delocalization of the electrons. The ring is not a true hexagon but has two different bond angles at the B and N atoms. Data taken from Refs. [71, 243].*

Borazine is a dangerous compound that has to be handled with care. The H- and P-phrases [244] which pertain here are listed in Table F.1.

The borazine used for the experiments in this thesis was bought from Katchem [245]. It was delivered in a stainless steel container under argon atmosphere equipped with two valves and KF16 flanges to allow the handling of the liquid in a closed system in accordance with P223, P231+P232, and P233. Borazine has been known to decompose to hydrogen and a polymeric BN compound over time [246]. At higher temperatures, the decomposition rate increases, but has also

Table F.1: *Hazard (H) and Precaution (P) phrases that pertain to borazine.*

H225	Highly flammable liquid and vapor.
H260	In contact with water releases flammable gases which may ignite spontaneously.
H314	Causes severe skin burns and eye damage.
H318	Causes serious eye damage.
H335	May cause respiratory irritation.
P210	Keep away from heat, hot surface, sparks, open flames and other ignition sources. - No smoking.
P211	Do not spray on an open flame or other ignition source.
P223	Do not allow contact with water.
P231 + P232	Handle under inert gas and protect from moisture.
P233	Keep container tightly closed.
P240	Ground/bond container and receiving equipment.
P241	Use explosion-proof [electrical/ventilating/lighting/.../] equipment.
P242	Use only non-sparking tools.
P243	Take precautionary measures against static discharge.
P260	Do not breathe dust/fumes/gas/mist/vapors/spray.
P280	Wear protective gloves/protective clothing/eye protection/face protection.
P301+P330+P331	IF SWALLOWED: Rinse mouth. Do NOT induce vomiting.
P303 + P361 + P353	IF ON SKIN (or hair): Take off immediately all contaminated clothing. Rinse skin with water/shower.
P304 + P340	IF INHALED: Remove person to fresh air and keep comfortable for breathing.
P305 + P351 + P338	IF IN EYES: rinse cautiously with water for several minutes. Remove contact lenses if present and easy to do – continue rinsing.
P310	Immediately call a POISON CENTER or doctor/physician.
P335+P334	Brush off loose particles from skin. Immerse in cool water/wrap in wet bandages.
P363	Wash contaminated clothing before reuse.
P403 + P235	Store in well ventilated place. Keep cool.
P405	Store locked up.

been observed over longer periods of time even when the borazine was stored at low temperatures ($-5°C$). To reduce the decomposition rate of borazine in storage, the stainless steel container was held at $-18°C$.

Due to the dangerous and unstable nature of borazine, there are several requirements to the borazine container from which the borazine is dosed into the UHV chamber. The borazine needs to be kept at a low temperature constantly, there must be a possibility to remove the decomposition products to ensure a good quality of the borazine, and there must be a way to fill the container without the borazine getting into contact with the atmosphere (P231 + P232). For this, a borazine doser was designed by M. Specht. The set-up is shown in Figure F.2.
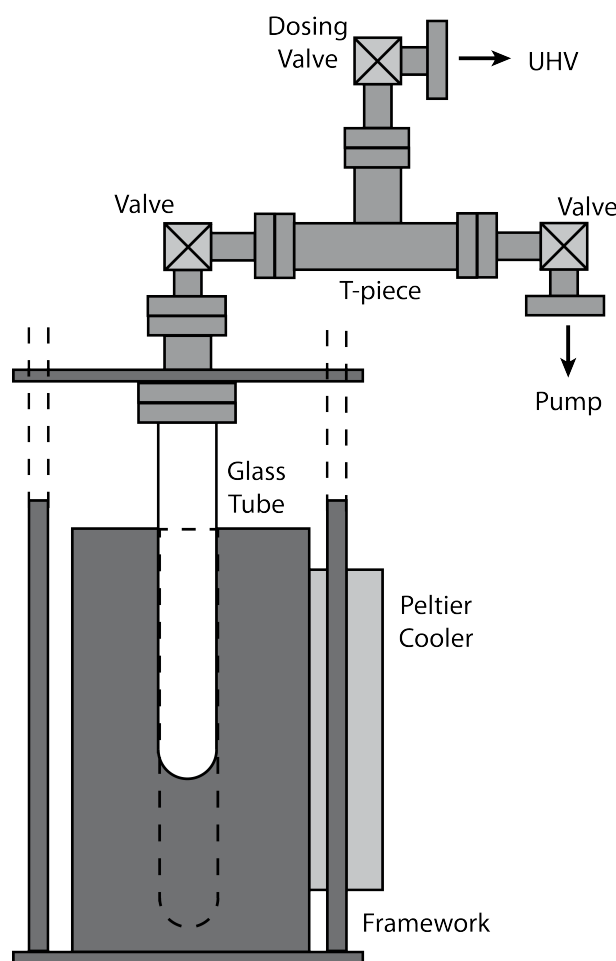
Figure F.2: *Schematic depiction of the borazine doser designed by M. Specht used in the present work. A glass tube that holds the liquid borazine is attached to a T-piece with a valve. A second valve at the T-piece allows the connection to a pump required for the filling of the doser and the cleaning of the borazine. The borazine doser is attached to the UHV chamber via a dosing valve at the T-piece through which the borazine dose can be controlled. A removable framework around the glass tube holds a Peltier cooler which is used to keep the liquid borazine at a constant temperature of $-5°C$.*

The liquid borazine is stored in a glass tube which is connected to a T-piece by a valve. The other two ends of the T-piece are connected to two other valves. One a is a dosing valve which connects the borazine doser to the UHV chamber and allows precise control of the borazine dose. The

last valve can be connected to a mobile pumping station which is required for the cleaning of the borazine which will be described below. A plate of stainless steel at the top of the glass tube allows the attachment of a framework that encloses the glass tube and holds a Peltier cooler. This is used for the cooling of the borazine down to a constant temperature of $-5°$C which slows down the decomposition rate.
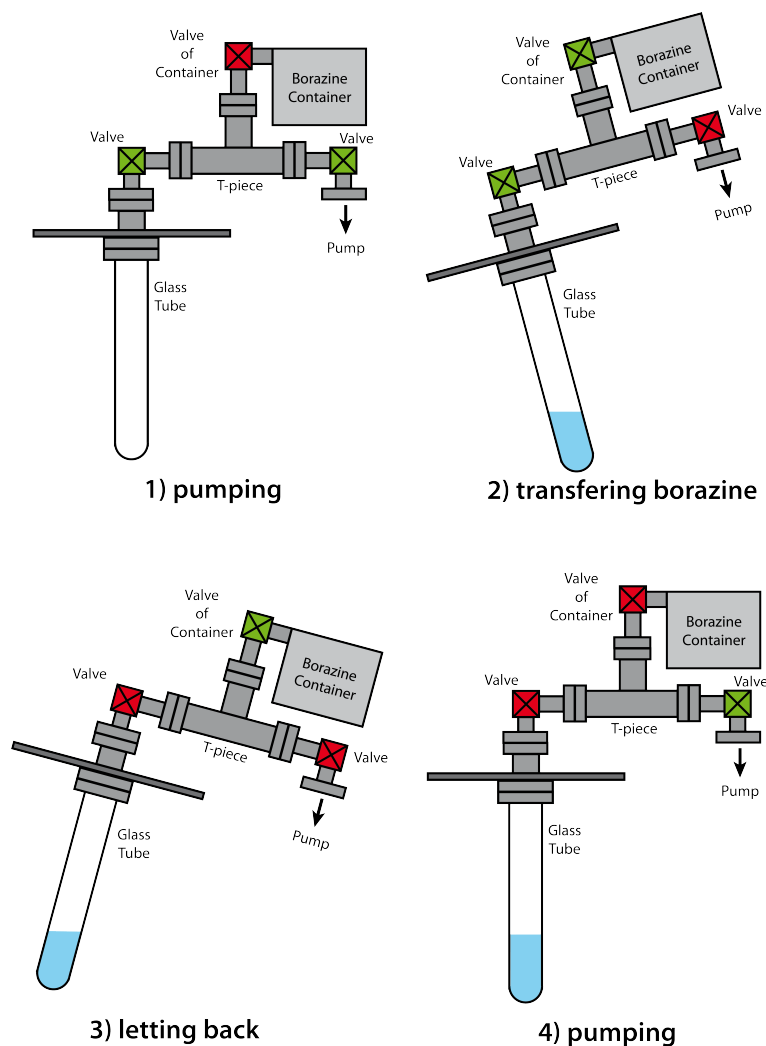
Figure F.3: *Schematic depiction of the procedure to fill liquid borazine from the stainless steel container in which it was delivered into the borazine doser shown in Figure F.2 which is attached to the UHV chamber and functions as the borazine source for the experiments in the present work. A closed valve is represented in red, an open valve in green. First, the T-piece and the glass tube are pumped to remove air and water from the borazine doser. In the next step, the borazine is transfered from the stainless steel container to the glass tube by tilting the complete set-up (the liquid borazine is represented in light blue). In the next step, with the valve to the glass tube closed, the set-up is tilted so as to pour any remaining borazine from the T-piece back into the stainless steel container. Finally, all remaining borazine gas is pumped from the T-piece.*

In the following, the filling of the borazine doser will be described. The procedure is schematically depicted in Figure F.3. This procedure is to be conducted in a fume cupboard to ensure safety. The dosing valve is removed from the T-piece and instead the stainless steel container in which

the borazine is delivered is attached. On the free valve, a rotary oil pump is connected. This valve and the valve at the glass tube are opened (the valve at the borazine container remains closed) and the borazine doser is pumped to remove air and water. Then the valve to the pump is closed and the valve at the container may be opened carefully as the gas phase above the borazine will flow into the borazine doser. By tilting the container and the borazine doser, the liquid has to be poured from the container into the glass tube. Filling it to one third is sufficient and leaves enough space for the cleaning procedure. When enough borazine is in the glass tube, the valve to the glass tube has to be closed. By appropriate tilting of the whole set-up, the remaining borazine in the T-piece should flow back into the stainless steel container. Its valve can be closed and the valve to the pump needs to be opened carefully so that the remaining gas is removed from the T-piece. The stainless steel container can be detached from the borazine doser and put into storage (at $-18°C$). The open end for the T-piece needs to be closed for the cleaning procedure.

The cleaning procedure may be done after filling the borazine doser in the fume cupboard or with the borazine doser attached to the chamber via the dosing valve. This is especially practical for regular cleaning cycles since the decomposition of borazine will occur over time. This is possible due to the removable framework which holds the Peltier cooler shown in Figure F.2.

The steps of the cleaning procedure are as follows:

1) constant pumping of the T-piece (the valve to the pump can remain open during the whole procedure),

2) freezing of the liquid borazine by putting the glass tube in liquid nitrogen,

3) opening of the valve at the glass tube so that the gas phase above the frozen borazine can be pumped away,

4) closing of the valve at the glass tube and careful heating so that the borazine melts,

5) repeat steps $2-4$ at least twice,

6) closing of the valve to the pump and removal of the mobile pumping station from the borazine doser.

The freezing of the borazine allows the pumping of the gas phase above the borazine without removing the borazine itself and melting it induces the release of solved components from the borazine, like molecular hydrogen. The heating of the glass tube can be done by using a heat gun at a low-temperature setting and at some distance from the glass tube. Too quick heating has to be avoided in oder to prevent breaking of the glass due to thermal stress. Another efficient way to thaw the borazine is using the body heat from one's hands.

Before an experiment with borazine, its quality should be checked using the QMS. Figure F.4 shows a mass spectrum of the gas phase above the borazine that was dosed into the UHV chamber to a pressure of 1.1×10^{-8} mbar against the background. Here, the ratio of hydrogen (a product of the borazine decomposition, $\frac{m}{z} = 2$) to borazine ($\frac{m}{z} = 80$) is 2.6. With such a high percentage of hydrogen in the gas phase above the borazine, the actual dose of borazine that is admitted into
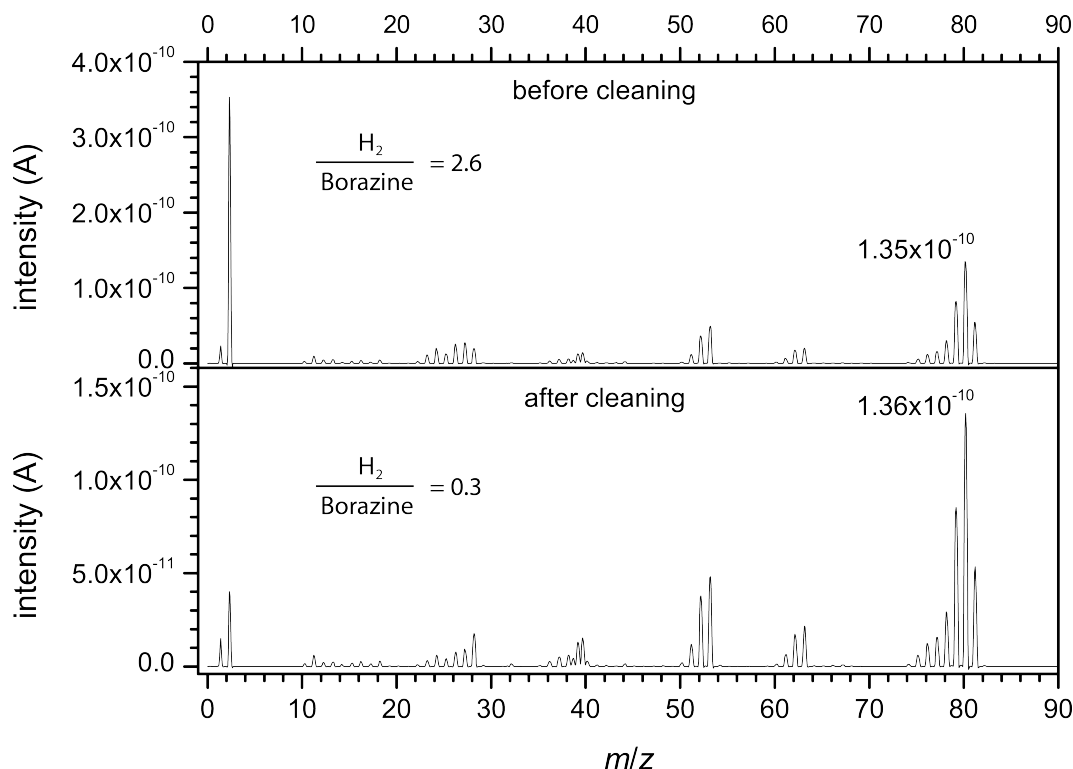
Figure F.4: *Mass spectra of the gas phase above the borazine, dosed into the UHV chamber at 1.1×10^{-8} mbar against the background before (top) and after (bottom) three cleaning cycles. The important peaks for the borazine quality are $\frac{m}{z} = 80$ for the unfractured molecule and $\frac{m}{z} = 2$ for hydrogen, a product of borazine decomposition. Before and after the cleaning cycles, the intensity of the borazine peak is the same. The hydrogen peak gets reduced by a factor of ~9. This reduces the hydrogen-borazine ratio from 2.6 to 0.3.*

the UHV chamber is smaller than what is expected from the pressure that is reached during hBN preparation. In the example shown in Figure F.4, the true amount of borazine is less than half of what is expected. Thus, before dosing the gas into the chamber for the preparation of hBN, the borazine in the doser requires cleaning. Figure F.4 also includes a mass spectrum at the same pressure after three cleaning cycles as described above. The peak of the unfractured borazine molecule at $\frac{m}{z} = 80$ has the same intensity as before the cleaning cycles. The hydrogen peak at $\frac{m}{z} = 2$, however, has significantly reduced, leaving the hydrogen-borazine ratio at only 0.3. This represents borazine in the doser in very good condition. High quality LEED patterns of hBN/Cu(111) (sharp ring and clear satellite structure) have already been achieved with a hydrogen-borazine ratio of ≈ 1.

G Tables

Here, values that were used in the main part of this thesis are summarized. Table G.1 lists the lattice mismatches between different metal surfaces and hBN. The bulk lattice constants that were used to calculate the mismatches are included. Table G.2 summarizes the XSW results for the vertical structure of PTCDA on different metal surfaces. In Table G.3, the metallic, covalent, and vdW radii used in this thesis are listed.

Furthermore, the approach to the calculation for the footprint of benzene, cyclohexane, and borazine molecules is shown in Figure G.1. Here, the footprints of the molecules are approximated as circles. The bond lengths used for this calculation and the resulting footprints are given in Table G.4. Here, the borazine molecule is approximated as a perfect hexagon.

Table G.1: *Lattice mismatches between metal(111) surfaces and the hBN monolayer. Bulk lattice constants of the metals (at 25 °C) are taken from Ref. [76]. The lattice mismatches are calculated as $m = 1 - a_{\mathrm{hBN}}/a_{\mathrm{metal}}$, using the lattice constant of hBN for the bulk of 2.505 Å at 297.5 K [77].*
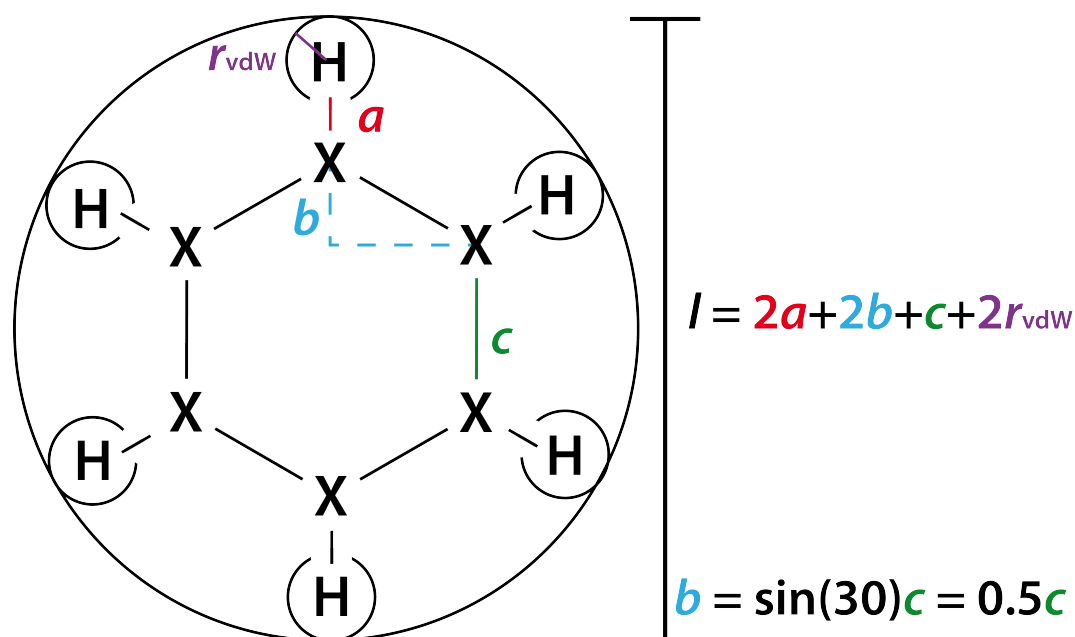
metal surface	bulk lattice constant	surface lattice constant	lattice mismatch m
Ni(111)	3.524 Å	2.492 Å	−0.5%
Ir(111)	3.839 Å	2.715 Å	7.7%
Rh(111)	3.804 Å	2.690 Å	6.9%
Pt(111)	3.923 Å	2.774 Å	9.7%
Pd(111)	3.890 Å	2.751 Å	8.9%
Ag(111)	4.086 Å	2.889 Å	13.3%
Cu(111)	3.615 Å	2.556 Å	2.0%

Table G.2: *Vertical distances d_C of the atoms in the PTCDA molecule on different noble metal surfaces as measured by XSW. Additionally, the vdW corrected heights of the atoms d_{corr} are given. These are the measured distances reduced by the vdW radii of the substrate atoms. For the vdW radii, see Table G.3.*

substrate	d_C (C total)	d_C (C peryl)	d_C (C funct)	d_C (O carb)	d_C (O anh)	Ref.
Ag(111)	2.86 ± 0.01 Å			2.66 ± 0.03 Å	2.98 ± 0.08 Å	[100]
Ag(100)	2.81 ± 0.02 Å	2.84 ± 0.02 Å	2.73 ± 0.01 Å	2.53 ± 0.02 Å	2.78 ± 0.02 Å	[47]
Ag(110)	2.56 ± 0.01 Å	2.58 ± 0.02 Å	2.45 ± 0.11 Å	2.30 ± 0.04 Å	2.38 ± 0.03 Å	[47]
Cu(111)	2.66 ± 0.02 Å			2.73 ± 0.06 Å	2.89 ± 0.06 Å	[56]
Cu(100)		2.53 ± 0.02 Å	2.44 ± 0.02 Å	2.47 ± 0.05 Å	2.76 ± 0.02 Å	[102]
Au(111)	3.27 ± 0.02 Å					[45]
	d_{corr} (C total)	d_{corr} (C peryl)	d_{corr} (C funct)	d_{corr} (O carb)	d_{corr} (O anh)	
Ag(111)	1.14 Å			0.94 Å	1.26 Å	
Ag(100)		1.12 Å	1.01 Å	0.81 Å	1.06 Å	
Ag(110)		0.87 Å	0.73 Å	0.60 Å	0.69 Å	
Cu(111)	1.26 Å			1.33 Å	1.49 Å	
Cu(100)		1.04 Å	1.13 Å	1.07 Å	1.36 Å	
Au(111)	1.61 Å					

Table G.3: *Atomic radii of different elements. Metallic radii taken from Ref. [103], covalent radii taken from Ref. [104], vdW radii taken from Ref. [101]. The covalent radius of C is valid for sp^2 hybridized C atoms in perylene. The covalent radius of O is the average of 1.6 and 1.7 Å, the range covering the generally found radii for sp^2 hybridized O atoms parallel to the double bonded axis.*

element	metallic radius	covalent radius	vdW radius
Cu	1.28 Å		1.40 Å
Ag	1.44 Å		1.72 Å
Au	1.44 Å		1.66 Å
C		0.73 Å	1.75 Å
O		0.66 Å	1.65 Å
H		0.31 Å	1.06 Å
B		0.84 Å	1.65 Å
N		0.71 Å	1.46 Å

Figure G.1: *Schematic illustration of the footprints of benzene, cyclobenzene, and borazine. The atoms X are either C, B, or N atoms. The values for the parameters a, b, and c are given in Table G.4, for the vdW radius of hydrogen r_{vdW}, see Table G.3. As per Ref. [194].*

Table G.4: *Bond lengths in the molecules benzene, cyclohexane, and borazine. a is the length of the $C-H$, $B-H$, or $N-H$ bonds, c is the length of the $C-C$ or $B-N$ bonds. The diameter of the molecules l was calculated as $l = 2 \cdot a + 2 \cdot c + 2 \cdot r_{vdW}$, where r_{vdW} is the vdW radius of hydrogen. Since the bond lengths of $B-H$ and $N-H$ are not identical, for borazine the sum of these two bond lengths is used instead of $2 \cdot a$. The footprint f of the flat lying molecules was calculated as $f = \frac{\pi}{4} \cdot l^2$.*

	a	c	l	f
benzene	1.084 Å [247]	1.392 Å [247]	12.503 Å	39.280 Å^2
cyclohexane	1.086 Å [248]	1.534 Å [248]	13.542 Å	42.545 Å^2
borazine	1.030 Å [243] (N−H)	1.429 Å [71]	7.193 Å	40.636 Å^2
	1.185 Å [243] (B−H)			

H List of Abbreviations

Chemical Abbreviations

2DM   two-dimensional material

2H-P   free-base porphine ($C_{20}H_{14}N_4$)

C_{funct} functional carbon atom of the PTCDA molecule

C_{peryl} carbon atom in the perylene backbone of the PTCDA molecule

CuPc   copper phthalocyanine ($C_{32}H_{16}CuN_8$)

DBP   5,10,15,20-tetraphenylbisbenz[5,6]indeno[1,2,3-cd : $1', 2', 3' - lm$]perylene ($C_{64}H_{36}$)

hBN   hexagonal boron nitride, here denoting the monolayer

MnPc   manganese phthalocyanine ($C_{32}H_{16}MnN_8$)

O_{anh} anhydritic oxygen atom of the PTCDA molecule

O_{carb} carboxylic oxygen atom of the PTCDA molecule

PTCDA   3,4,9,10-perylene tetracarboxylic dianhydride ($C_{24}H_8O_6$)

QDC   quaterphenylene dicarbonitrile ($C_{26}H_{16}N_2$)

TCNQ   tetracyanoquinodimethane ($C_{12}H_4N_4$)

TMDC   transition metal dichalcogenites

General Abbreviations

A, B   satellite lines in the hBN/Cu(111) LEED pattern

A', B'   cross sections of the satellite lines in the hBN/Cu(111) LEED pattern

B   batteries

CCD   charge-coupled device

CT   charge-transfer

CVD   chemical vapor deposition

DFT   density-functional theory

fcc   face-centered cubic

FL   fluorescence

FLE	fluorescence excitation
FWHM	full width at half maximum
HB	herringbone
hcp	hexagonal close-packed
HOMO	highest occupied molecular orbital
LEED	low energy electron diffraction
LEEM	low energy electron microscopy
LUMO	lowest unoccupied molecular orbital
ML	monolayer
nc-AFM	non-contact atomic force microscopy
NIXSW	normal incidence x-ray standing waves
O	output
P	potentiometer
PES	photoemission spectroscopy
pol	point-on-line
Q	quadratic
QMS	quadrupole mass spectrometer
R	resistance
RB	ring breathing mode of the PTCDA molecule
S	switch
S_0	electronic ground state of a molecule
S_1	first electronic excited state of a molecule
SERS	surface enhanced Raman scattering
SPA-LEED	spot-profile analysis low energy electron diffraction
SPP	surface plasmon polariton
STM	scanning tunneling microscopy
STS	scanning tunneling spectroscopy
TPD	temperature programmed desorption
UHV	ultra-high vacuum
UPS	ultraviolet photoemission spectroscopy
vdW	van der Waals
XPS	x-ray photoemission spectroscopy
XSW	normal incidence x-ray standing waves, see NIXSW

Variables and Parameters

$\vec{a}$	lattice vector of the unit cell of a surface
$\vec{a}^*$	reciprocal lattice vector of the unit cell of a surface
$\vec{a}_0$	distance between rows of atoms parallel to the surface
$\vec{a}_1$	lattice vector of the substrate
a_{Cu}	lattice constant of the Cu(111) unit cell
a_{Cu}^*	reciprocal lattice constant of the Cu(111) unit cell
a_{hBN}	lattice constant of an hBN layer (on a surface or free standing)
a_{hBN}^{bulk}	lattice constant of an hBN layer in the bulk
a_{metal}	lattice constant of a metal surface
a_{metal}^{hk}	distance between the lattice lines $\{hk\}$ of a metal
a_{Ni}	lattice constant of the Ni(111) unit cell
A	amplitude
A	area of a surface unit cell
α	angle between the two vectors of a unit cell
$\vec{b}$	lattice vector of the unit cell of a surface
$\vec{b}^*$	reciprocal lattice vector of the unit cell of a surface
$\vec{b}_0$	distance between rows of atoms parallel to the surface
b_1, b_2	lattice constants of the unit cell of PTCDA
β	heating rate
c	speed of light in vacuum
c_1	lattice constant of the unit cell of borazine
γ	angle between the two vectors of a unit cell
d_C	vertical interfacial distance
d_{corr}	vdW corrected vertical interfacial distance
d_{hkl}	lattice spacing or Bragg spacing between {hkl} lattice planes
D	dose
ΔE_A	activation barrier
E_{ads}	adsorption energy
E_B	binding energy of electrons
E_{Bragg}	Bragg energy
E_{des}	desorption energy
$E_{des}^{mono/multi/def}$	desorption energy of molecules adsorbed in monolayers/in multilayers/at surface defects

E_{F}	Fermi energy
E_{kin}	kinetic energy of electrons
E_{L}	voltage of the entrance lens of the SPA-LEED instrument
$E_{\mathrm{SPP}}^{\mathrm{Me}}$	energy of the surface plasmon polariton of the metal Me
ϵ	dielectric function
η	quantum yield
f	footprint of a molecule
F	structure form factor
F_{C}	coherent fraction
g	ratio of the FWHM of the satellite lines and the (00) spot in the LEED pattern of hBN/Cu(111) in the azimuthal direction
$\vec{g}$	step vector
G_{Λ}^{x}	lattice vector of the buckled superstructure in reciprocal space
h	Planck's constant
h, k	Miller indices
hν	photonic energy
H	integer number
$\Delta \mathrm{H}_{sub}$	sublimation enthalpy
I	intensity
I_0	intensity of the (00) spot in SPA-LEED
$I_{\mathrm{Cu}}^{\mathrm{A/B}}$	intensity of the Cu spot A/B in SPA-LEED
I_{S}	sample current
$I_{\mathrm{S}}^{\mathrm{A/B}}$	intensity of the satellite line A/B in SPA-LEED
I_{t}	tunnel current
$\vec{k}$	diffraction vector
$\vec{k}_{\parallel}$	component of the diffraction vector parallel to the surface
$\vec{k}^{hk}$	wave vector of electrons diffracted at $\{hk\}$ lattices
$\vec{k}_{\parallel}^{hk}$	component of the wave vector of electrons diffracted at $\{hk\}$ lattices parallel to the surface
$\vec{k}_{\perp}^{hk}$	component of the wave vector of electrons diffracted at $\{hk\}$ lattices perpendicular to the surface
$\vec{k}_0$	radius of the Ewald sphere
k$_{\mathrm{B}}$	Boltzmann's constant

k_{ads}	rate constant for the adsorption
k_{des}	rate constant for the desorption
k_{nr}	rate constant for the non-radiative decay of an excitation
k_{r}	rate constant for the radiative decay of an excitation
k_{x}	component of the wave vector in x-direction parallel to the surface
k_{z}	component of the wave vector in z-direction perpendicular to the surface
Δk_{x}	FWHM of a LEED spot
L	Moiré lattice constant
λ	wavelength of light or x-rays
λ_{el}	de Broglie wavelength of electrons
λ_{ex}	wavelength of the exciting laser
Λ	lattice constant of the buckling of the hBN layer
m	lattice mismatch
m	mass
m, n	integer number
N	number of molecules
$N_{\text{(BN)}}^{\text{hit}}$	number of particles (BN units) that hit the surface
$N_{\text{(BN)}}^{\text{stick}}$	number of particles (BN units) that stick to the surface
$\mathbf{M}$	superstructure matrix in real space
ν', ν''	vibronic states of the electronic excited/ground state
ν_0	pre-exponential factor of the *Polanyi-Wigner* equation
ν_C	phase relationship between incident and reflected x-ray wave
$\Delta\nu$	line width of an FL peak
$\Delta\nu_{\text{nat}}$	natural line width of an FL peak
p	pressure
P_C	coherent position
P_{ex}	power of the exciting laser
ϕ	angle of the azimuthal rotation of an adsorbate domain relative to the substrate
ϕ_S	impact angle during ion bombardment relative to the surface normal
Φ	work function
R	reflectivity
r	desorption rate
$\vec{r}_{\text{n}}$	position of an atom n in the surface

r	ratio of the intensities of the satellite lines and the (00) spot in SPA-LEED
r'	ratio of the intensities of the satellite lines and the (00) spot in SPA-LEED corrected with the FWHM of the spots in the azimuthal direction
r_{vdW}	vdW radius
r_{vdW}	vdW radius
ρ	packing density of molecules on the surface
s	contribution of the diffraction at the hBN layer to the (00) spot in the LEED pattern
s	sticking factor
s_0, s_1	instrument-, energy-, and direction-specific parameters for the distortion of the LEED pattern
S	scattering phase
t	time
$t_{annealing}$	annealing time
$t_{sputtering}$	time of ion bombardment
$T_{annealing}$	annealing temperature
T_G	gas temperature
T_m	surface temperature during measurement
T_{obs}	surface temperature at which LEED patterns of borazine could be observed
T_S	surface temperature
$T_{terrace}$	terrace width
$T_{transfer}$	transfer width
θ	coverage
θ_B	Bragg angle
ϑ	diffraction angle
τ_S	life time of the excited state
τ_r	natural life time of the fluorescence
U_{bias}	bias voltage
$U_{C/h}$	positions of diffraction spots of Cu/hBN in the line profile measured in SPA-LEED on the voltage scale
U_S	positions of satellite lines of hBN in the line profile measured in SPA-LEED on the voltage scale
U_x	x-axis of the line profile measured in SPA-LEED on the voltage scale
Δw	FWHM of a LEED spot in the azimuthal direction

$\Delta w_{S/00}$ FWHM of the satellite lines/the (00) spot in the LEED pattern in the azimuthal
             direction

z charge

Z collision rate

Bibliography

[1] K. S. Novoselov, A. K. Geim, S. V. Morozov, D. Jiang, M. I. Katsnelson, I. V. Grigorieva, S. V. Dubonos, and A. A. Firsov, "Two-dimensional gas of massless Dirac fermions in graphene", Nature **438**, 197 (2005).

[2] K. F. Mak, C. Lee, J. Hone, J. Shan, and T. F. Heinz, "Atomically Thin MoS_2: A New Direct-Gap Semiconductor", Physical Review Letters **105**, 136805 (2010).

[3] K. S. Novoselov, A. K. Geim, S. V. Morozov, D. Jiang, Y. Zhang, S. V. Dubonos, I. V. Grigorieva, and A. A. Firsov, "Electric Field Effect in Atomically Thin Carbon Films", Science **306**, 666 (2004).

[4] W. Choi, I. Lahiri, R. Seelaboyina, and Y. S. Kang, "Synthesis of Graphene and Its Applications: A Review", Critical Reviews in Solid State and Materials Sciences **35**, 52 (2010).

[5] K. S. Novoselov, V. I. Fal'ko, L. Colombo, P. R. Gellert, M. G. Schwab, and K. Kim, "A roadmap for graphene", Nature **490**, 192 (2012).

[6] S. Das, J. A. Robinson, M. Dubey, H. Terrones, and M. Terrones, "Beyond Graphene: Progress in Novel Two-Dimensional Materials and van der Waals Solids", Annual Review of Materials Research **45**, 1 (2015).

[7] Q. Ji, Y. Zhang, Y. Zhang, and Z. Liu, "Chemical vapour deposition of group-VIB metal dichalcogenide monolayers: engineered substrates from amorphous to single crystalline", Chemical Society Reviews **44**, 2587 (2015).

[8] J. Yang, S. Tran, J. Wu, S. Che, P. Stepanov, T. Taniguchi, K. Watanabe, H. Baek, D. Smirnov, R. Chen, and C. N. Lau, "Integer and Fractional Quantum Hall effect in Ultrahigh Quality Few-layer Black Phosphorus Transistors", Nano Letters **18**, 229 (2018).

[9] T. H. Lee, S. Y. Kim, and H. W. Jang, "Black Phosphorus: Critical Review and Potential for Water Splitting Photocatalyst", Nanomaterials **6**, 194 (2016).

[10] D. Pacilé, J. C. Meyer, Ç. Ö. Girit, and A. Zettl, "The two-dimensional phase of boron nitride: Few-atomic-layer sheets and suspended membranes", Applied Physics Letters **92**, 133107 (2008).

[11] W. Auwärter, "Hexagonal boron nitride monolayers on metal supports: Versatile templates for atoms, molecules and nanostructures", Surface Science Reports **74**, 1 (2019).

[12] K. Kalantar-zadeh, J. Tang, M. Wang, K. L. Wang, A. Shailos, K. Galatsis, R. Kojima, V. Strong, A. Lech, W. Wlodarski, and R. B. Kaner, "Synthesis of nanometre-thick MoO_3 sheets", Nanoscale **2**, 429 (2010).

[13] G. Pacchioni, "Two-Dimensional Oxides: Multifunctional Materials for Advanced Technologies", Chemistry – A European Journal **18**, 10144 (2012).

[14] C. Tan, X. Cao, X.-J. Wu, Q. He, J. Yang, X. Zhang, J. Chen, W. Zhao, S. Han, G.-H. Nam, M. Sindoro, and H. Zhang, "Recent Advances in Ultrathin Two-Dimensional Nanomaterials", Chemical Reviews **117**, 6225 (2017).

[15] M. Xu, T. Liang, M. Shi, and H. Chen, "Graphene-Like Two-Dimensional Materials", Chemical Reviews **113**, 3766 (2013).

[16] J. L. Zhang, S. Zhao, C. Han, Z. Wang, S. Zhong, S. Sun, R. Guo, X. Zhou, C. D. Gu, K. D. Yuan, Z. Li, and W. Chen, "Epitaxial Growth of Single Layer Blue Phosphorus: A New Phase of Two-Dimensional Phosphorus", Nano Letters **16**, 4903 (2016).

[17] P. Vogt, P. De Padova, C. Quaresima, J. Avila, E. Frantzeskakis, M. C. Asensio, A. Resta, B. Ealet, and G. Le Lay, "Silicene: Compelling Experimental Evidence for Graphenelike Two-Dimensional Silicon", Physical Review Letters **108**, 155501 (2012).

[18] K. S. Novoselov, A. Mishchenko, A. Carvalho, and A. H. Castro Neto, "2D materials and van der Waals heterostructures", Science **353**, 461 (2016).

[19] A. Facchetti, "Semiconductors for organic transistors", Materials Today **10**, 28 (2007).

[20] N. Thejo Kalyani and S. J. Dhoble, "Organic light emitting diodes: Energy saving lighting technology—A review", Renewable and Sustainable Energy Reviews **16**, 2696 (2012).

[21] P. Kao, S. Neppl, P. Feulner, D. L. Allara, and M. Zharnikov, "Charge Transfer Time in Alkanethiolate Self-Assembled Monolayers via Resonant Auger Electron Spectroscopy", The Journal of Physical Chemistry C **114**, 13766 (2010).

[22] S. Neppl, U. Bauer, D. Menzel, P. Feulner, A. Shaporenko, M. Zharnikov, P. Kao, and D. Allara, "Charge transfer dynamics in self-assembled monomolecular films", Chemical Physics Letters **447**, 227 (2007).

[23] W. Gebauer, A. Langner, M. Schneider, M. Sokolowski, and E. Umbach, "Luminescence quenching of ordered π-conjugated molecules near a metal surface: Quaterthiophene and PTCDA on Ag(111)", Physical Review B **69**, 155431 (2004).

[24] M. Hollerer, D. Lüftner, P. Hurdax, T. Ules, S. Soubatch, F. S. Tautz, G. Koller, P. Puschnig, M. Sterrer, and M. G. Ramsey, "Charge Transfer and Orbital Level Alignment at Inorganic/Organic Interfaces: The Role of Dielectric Interlayers", ACS Nano **11**, 6252 (2017).

[25] J. Schütte, R. Bechstein, P. Rahe, M. Rohlfing, A. Kühnle, and H. Langhals, "Imaging perylene derivatives on rutile TiO$_2$(110) by noncontact atomic force microscopy", Physical Review B **79**, 045428 (2009).

[26] L. Zhang, X. Fu, C. G. Hu, Y. Yao, Z. Y. Xu, X. T. Hu, M. Hohage, P. Zeppenfeld, and L. D. Sun, "Optical and structural properties of the pentacene/quartz (0001) interface", Physical Review B **93**, 075443 (2016).

[27] L. Zhang, X. Fu, M. Hohage, P. Zeppenfeld, and L. D. Sun, "Growth of pentacene on α-Al$_2$O$_3$ studied by *in situ* optical spectroscopy", Physical Review Materials **1**, 043401 (2017).

[28] J. Repp, G. Meyer, S. M. Stojković, A. Gourdon, and C. Joachim, "Molecules on Insulating Films: Scanning-Tunneling Microscopy Imaging of Individual Molecular Orbitals", Physical Review Letters **94**, 026803 (2005).

[29] Y. Luo, G. Chen, Y. Zhang, L. Zhang, Y. Yu, F. Kong, X. Tian, Y. Zhang, C. Shan, Y. Luo, J. Yang, V. Sandoghdar, Z. Dong, and J. G. Hou, "Electrically Driven Single-Photon Superradiance from Molecular Chains in a Plasmonic Nanocavity", Physical Review Letters **122**, 233901 (2019).

[30] H. Imada, K. Miwa, M. Imai-Imada, S. Kawahara, K. Kimura, and Y. Kim, "Single-Molecule Investigation of Energy Dynamics in a Coupled Plasmon-Exciton System", Physical Review Letters **119**, 013901 (2017).

[31] K. Kimura, K. Miwa, H. Imada, M. Imai-Imada, S. Kawahara, J. Takeya, M. Kawai, M. Galperin, and Y. Kim, "Selective triplet exciton formation in a single molecule", Nature **570**, 210 (2019).

[32] E. V. Tsiper, Z. G. Soos, W. Gao, and A. Kahn, "Electronic polarization at surfaces and thin films of organic molecular crystals: PTCDA", Chemical Physics Letters **360**, 47 (2002).

[33] X. Blase, A. Rubio, S. G. Louie, and M. L. Cohen, "Quasiparticle band structure of bulk hexagonal boron nitride and related systems", Physical Review B **51**, 6868 (1995).

[34] K. Watanabe, T. Taniguchi, and H. Kanda, "Direct-bandgap properties and evidence for ultraviolet lasing of hexagonal boron nitride single crystal", Nature Materials **3**, 404 (2004).

[35] R. Wang, X.-G. Ren, Z. Yan, L.-J. Jiang, W. E. I. Sha, and G.-C. Shan, "Graphene based functional devices: A short review", Frontiers of Physics **14**, 13603 (2019).

[36] Y. Lin and J. W. Connell, "Advances in 2D boron nitride nanostructures: nanosheets, nanoribbons, nanomeshes, and hybrids with graphene", Nanoscale **4**, 6908 (2012).

[37] A. Pakdel, Y. Bando, and D. Golberg, "Nano boron nitride flatland", Chemical Society Reviews **43**, 934 (2014).

[38] C. M. Orofeo, S. Suzuki, H. Kageshima, and H. Hibino, "Growth and low-energy electron microscopy characterization of monolayer hexagonal boron nitride on epitaxial cobalt", Nano Research **6**, 335 (2013).

[39] G. Kim, A. Jang, H. Y. Jeong, Z. Lee, D. J. Kang, and H. S. Shin, "Growth of High-Crystalline, Single-Layer Hexagonal Boron Nitride on Recyclable Platinum Foil", Nano Letters **13**, 1834 (2013).

[40] G. Giovannetti, P. A. Khomyakov, G. Brocks, P. J. Kelly, and J. van den Brink, "Substrate-induced band gap in graphene on hexagonal boron nitride: *Ab initio* density functional calculations", Physical Review B **76**, 073103 (2007).

[41] L. Wang, X. Xu, L. Zhang, R. Qiao, M. Wu, Z. Wang, S. Zhang, J. Liang, Z. Zhang, Z. Zhang, W. Chen, X. Xie, J. Zong, Y. Shan, Y. Guo, M. Willinger, H. Wu, Q. Li, W. Wang, P. Gao, S. Wu, Y. Zhang, Y. Jiang, D. Yu, E. Wang, X. Bai, Z.-J. Wang, F. Ding, and K. Liu, "Epitaxial growth of a 100-square-centimetre single-crystal hexagonal boron nitride monolayer on copper", Nature **570**, 91 (2019).

[42] K. V. Bets, N. Gupta, and B. I. Yakobson, "How the Complementarity at Vicinal Steps Enables Growth of 2D Monocrystals", Nano Letters **19**, 2027 (2019).

[43] J. S. Lee, S. H. Choi, S. J. Yun, Y. I. Kim, S. Boandoh, J.-H. Park, B. G. Shin, H. Ko, S. H. Lee, Y.-M. Kim, Y. H. Lee, K. K. Kim, and S. M. Kim, "Wafer-scale single-crystal hexagonal boron nitride film via self-collimated grain formation", Science **362**, 817 (2018).

[44] M. Schneider, E. Umbach, and M. Sokolowski, "Growth-dependent optical properties of 3,4,9,10-perylenetetracarboxylicacid-dianhydride (PTCDA) films on Ag(111)", Chemical Physics **325**, 185 (2006).

[45] S. K. M. Henze, O. Bauer, T.-L. Lee, M. Sokolowski, and F. Tautz, "Vertical bonding distances of PTCDA on Au(111) and Ag(111): Relation to the bonding type", Surface Science **601**, 1566 (2007).

[46] S. Duhm, A. Gerlach, I. Salzmann, B. Bröker, R. L. Johnson, F. Schreiber, and N. Koch, "PTCDA on Au(111), Ag(111) and Cu(111): Correlation of interface charge transfer to bonding distance", Organic Electronics **9**, 111 (2008).

[47] O. Bauer, G. Mercurio, M. Willenbockel, W. Reckien, C. H. Schmitz, B. Fiedler, S. Soubatch, T. Bredow, F. S. Tautz, and M. Sokolowski, "Role of functional groups in surface bonding of planar π-conjugated molecules", Physical Review B **86**, 235431 (2012).

[48] Y. Zou, L. Kilian, A. Schöll, T. Schmidt, R. Fink, and E. Umbach, "Chemical bonding of PTCDA on Ag surfaces and the formation of interface states", Surface Science **600**, 1240 (2006).

[49] S. Mannsfeld, M. Toerker, T. Schmitz-Hübsch, F. Sellam, T. Fritz, and K. Leo, "Combined LEED and STM study of PTCDA growth on reconstructed Au(111) and Au(100) single crystals", Organic Electronics **2**, 121 (2001).

[50] L. Kilian, E. Umbach, and M. Sokolowski, "Molecular beam epitaxy of organic films investigated by high resolution low energy electron diffraction (SPA-LEED): 3,4,9,10-perylenetetra-carboxylicacid-dianhydride (PTCDA) on Ag(111)", Surface Science **573**, 359 (2004).

[51] M. Müller, A. Langner, O. Krylova, E. Le Moal, and M. Sokolowski, "Fluorescence spectroscopy of ultrathin molecular organic films on surfaces", Applied Physics B **105**, 67 (2011).

[52] M. Müller, E. Le Moal, R. Scholz, and M. Sokolowski, "Exciton and polarization contributions to optical transition energies in an epitaxial organic monolayer on a dielectric substrate", Physical Review B **83**, 241203(R) (2011).

[53] M. Müller, A. Paulheim, A. Eisfeld, and M. Sokolowski, "Finite size line broadening and superradiance of optical transitions in two dimensional long-range ordered molecular aggregates", The Journal of Chemical Physics **139**, 044302 (2013).

[54] A. Eisfeld, C. Marquardt, A. Paulheim, and M. Sokolowski, "Superradiance from Two Dimensional Brick-Wall Aggregates of Dye Molecules: The Role of Size and Shape for the Temperature Dependence", Physical Review Letters **119**, 097402 (2017).

[55] R. Laskowski, P. Blaha, and K. Schwarz, "Bonding of hexagonal BN to transition metal surfaces: An *ab initio* density-functional theory study", Physical Review B **78**, 045409 (2008).

[56] A. Gerlach, S. Sellner, F. Schreiber, N. Koch, and J. Zegenhagen, "Substrate-dependent bonding distances of PTCDA: A comparative x-ray standing-wave study on Cu(111) and Ag(111)", Physical Review B **75**, 045401 (2007).

[57] O. Bauer, "Surface bonding of a functionalized aromatic molecule: Adsorption configurations of PTCDA on coinage metal surfaces", PhD thesis (Universität Bonn, 2014).

[58] K. Stallberg, A. Namgalies, and U. Höfer, "Photoluminescence study of the exciton dynamics at PTCDA/noble-metal interfaces", Physical Review B **99**, 125410 (2019).

[59] C. Brülke, "Strukturaufklärung epitaktischer Schichten von Lithiumchlorid und hexagonalem Bornitrid auf Metalloberflächen", MA thesis (Universität Bonn, 2015).

[60] F. Mahvash, E. Paradis, D. Drouin, T. Szkopek, and M. Siaj, "Space-Charge Limited Transport in Large-Area Monolayer Hexagonal Boron Nitride", Nano Letters **15**, 2263 (2015).

[61] D. R. Cooper, B. D'Anjou, N. Ghattamaneni, B. Harack, M. Hilke, A. Horth, N. Majlis, M. Massicotte, L. Vandsburger, E. Whiteway, and V. Yu, "Experimental Review of Graphene", ISRN Condensed Matter Physics **2012**, 501686 (2012).

[62] A. Falin, Q. Cai, E. J. G. Santos, D. Scullion, D. Qian, R. Zhang, Z. Yang, S. Huang, K. Watanabe, T. Taniguchi, M. R. Barnett, Y. Chen, R. S. Ruoff, and L. H. Li, "Mechanical properties of atomically thin boron nitride and the role of interlayer interactions", Nature Communications **8**, 15815 (2017).

[63] F. Mahvash, S. Eissa, T. Bordjiba, A. C. Tavares, T. Szkopek, and M. Siaj, "Corrosion resistance of monolayer hexagonal boron nitride on copper", Scientific Reports **7**, 42139 (2017).

[64] L. H. Li, J. Cervenka, K. Watanabe, T. Taniguchi, and Y. Chen, "Strong Oxidation Resistance of Atomically Thin Boron Nitride Nanosheets", ACS Nano **8**, 1457 (2014).

[65] R. S. Pease, "An X-ray Study of Boron Nitride", Acta Crystallographica **5**, 356 (1952).

[66] K. K. Kim, A. Hsu, X. Jia, S. M. Kim, Y. Shi, M. Hofmann, D. Nezich, J. F. Rodriguez-Nieva, M. Dresselhaus, T. Palacios, and J. Kong, "Synthesis of Monolayer Hexagonal Boron Nitride on Cu Foil Using Chemical Vapor Deposition", Nano Letters **12**, 161 (2012).

[67] N. Guo, J. Wei, L. Fan, Y. Jia, D. Liang, H. Zhu, K. Wang, and D. Wu, "Controllable growth of triangular hexagonal boron nitride domains on copper foils by an improved low-pressure chemical vapor deposition method", Nanotechnology **23**, 415605 (2012).

[68] R. Y. Tay, M. H. Griep, G. Mallick, S. H. Tsang, R. S. Singh, T. Tumlin, E. H. T. Teo, and S. P. Karna, "Growth of Large Single-Crystalline Two-Dimensional Boron Nitride Hexagons on Electropolished Copper", Nano Letters **14**, 839 (2014).

[69] S. Frueh, R. Kellett, C. Mallery, T. Molter, W. S. Willis, C. King'ondu, and S. L. Suib, "Pyrolytic Decomposition of Ammonia Borane to Boron Nitride", Inorganic Chemistry **50**, 783 (2011).

[70] F. Baitalow, J. Baumann, G. Wolf, K. Jaenicke-Rößler, and G. Leitner, "Thermal decomposition of B–N–H compounds investigated by using combined thermoanalytical methods", Thermochimica Acta **391**, 159 (2002).

[71] R. Boese, A. H. Maulitz, and P. Stellberg, "Solid-State Borazine: Does it Deserve to be Entiteled "Inorganic Benzene"?", Chemische Berichte **127**, 1887 (1994).

[72] Y. Gao, W. Ren, T. Ma, Z. Liu, Y. Zhang, W.-B. Liu, L.-P. Ma, X. Ma, and H.-M. Cheng, "Repeated and Controlled Growth of Monolayer, Bilayer and Few-Layer Hexagonal Boron Nitride on Pt Foils", ACS Nano **7**, 5199 (2013).

[73] Z. Xu, H. Tian, A. Khanaki, R. Zheng, M. Suja, and J. Liu, "Large-area growth of multilayer hexagonal boron nitride on polished cobalt foils by plasma-assisted molecular beam epitaxy", Scientific Reports **7**, 43100 (2017).

[74] S. Nakhaie, J. M. Wofford, T. Schumann, U. Jahn, M. Ramsteiner, M. Hanke, J. M. J. Lopes, and H. Riechert, "Synthesis of atomically thin hexagonal boron nitride films on nickel foils by molecular beam epitaxy", Applied Physics Letters **106**, 213108 (2015).

[75] M. Corso, W. Auwärter, M. Muntwiler, A. Tamai, T. Greber, and J. Osterwalder, "Boron Nitride Nanomesh", Science **303**, 217 (2004).

[76] D. E. Gray, ed., *American Institute of Physics Handbook*, 3rd (McGraw-Hill Inc., New York, 1972).

[77] W. Paszkowicz, J. B. Pelka, M. Knapp, T. Szyszko, and S. Podsiadlo, "Lattice parameters and anisotropic thermal expansion of hexagonal boron nitride in the 10–297.5 K temperature range", Applied Physics A **75**, 431 (2002).

[78] Y. Gamou, M. Terai, A. Nagashima, and C. Oshima, "Atomic Structural Analysis of a Monolayer Epitaxial Film of Hexagonal Boron Nitride/Ni(111) studied by LEED Intensity Analysis", Science reports of the Research Institutes, Tohoku University **A44**, 211 (1997).

[79] M. Muntwiler, W. Auwärter, F. Baumberger, M. Hoesch, T. Greber, and J. Osterwalder, "Determining adsorbate structures from substrate emission X-ray photoelectron diffraction", Surface Science **472**, 125 (2001).

[80] W. Auwärter, M. Muntwiler, J. Osterwalder, and T. Greber, "Defect lines and two-domain structure of hexagonal boron nitride films on Ni(111)", Surface Science **545**, L735 (2003).

[81] I. Shimoyama, Y. Baba, T. Sekiguchi, and K. G. Nath, "NEXAFS spectra of an epitaxial boron nitride film on Ni(111)", Journal of Electron Spectroscopy and Related Phenomena **137–140**, 573 (2004).

[82] F. H. Farwick zum Hagen, D. M. Zimmermann, C. C. Silva, C. Schlueter, N. Atodiresei, W. Jolie, A. J. Martínez-Galera, D. Dombrowski, U. A. Schröder, M. Will, P. Lazić, V. Caciuc, S. Blügel, T.-L. Lee, T. Michely, and C. Busse, "Structure and Growth of Hexagonal Boron Nitride on Ir(111)", ACS Nano **10**, 11012 (2016).

[83] R. Laskowski, P. Blaha, T. Gallauner, and K. Schwarz, "Single-Layer Model of the Hexagonal Boron Nitride Nanomesh on the Rh(111) Surface", Physical Review Letters **98**, 106802 (2007).

[84] E. Ćavar, R. Westerström, A. Mikkelsen, E. Lundgren, A. S. Vinogradov, M. L. Ng, A. B. Preobrajenski, A. A. Zakharov, and N. Mårtensson, "A single h-BN layer on Pt(111)", Surface Science **602**, 1722 (2008).

[85] A. B. Preobrajenski, M. A. Nesterov, M. L. Ng, A. S. Vinogradov, and N. Mårtensson, "Monolayer h-BN on lattice-mismatched metal surfaces: On the formation of the nanomesh", Chemical Physics Letters **446**, 119 (2007).

[86]   M. Morscher, M. Corso, T. Greber, and J. Osterwalder, "Formation of single layer h-BN on Pd(111)", Surface Science **600**, 3280 (2006).

[87]   F. Müller, S. Hüfner, H. Sachdev, R. Laskowski, P. Blaha, and K. Schwarz, "Epitaxial growth of hexagonal boron nitride on Ag(111)", Physical Review B **82**, 113406 (2010).

[88]   C. Herrmann, P. Omelchenko, and K. L. Kavanagh, "Growth of *h*-BN on copper (110) in a LEEM", Surface Science **669**, 133 (2018).

[89]   F. Müller and S. Grandthyll, "Monolayer formation of hexagonal boron nitride on Ag(001)", Surface Science **617**, 207 (2013).

[90]   T. Greber, L. Brandenberger, M. Corso, A. Tamai, and J. Osterwalder, "Single layer hexagonal boron nitride films on Ni(110)", e-Journal of Surface Science and Nanotechnology **4**, 410 (2006).

[91]   R. M. Desrosiers, D. W. Greve, and A. J. Gellman, "Nucleation of boron nitride thin films on Ni(100)", Surface Science **382**, 35 (1997).

[92]   M. Corso, T. Greber, and J. Osterwalder, "*H*-BN ON PD(110): A TUNABLE SYSTEM FOR SELF-ASSEMBLED NANOSTRUCTURES?", Surface Science **577**, L78 (2005).

[93]   J. K. Hite, Z. R. Robinson, C. R. Eddy Jr., and B. N. Feigelson, "Electron Backscatter Diffraction Study of Hexagonal Boron Nitride Growth on Cu Single-Crystal Substrates", ACS Applied Materials & Interfaces **7**, 15200 (2015).

[94]   N. A. Vinogradov, A. A. Zakharov, M. L. Ng, A. Mikkelsen, E. Lundgren, N. Mårtensson, and A. B. Preobrajenski, "One-Dimensional Corrugation of the *h*-BN Monolayer on Fe(110)", Langmuir **28**, 1775 (2012).

[95]   M. P. Allan, S. Berner, M. Corso, T. Greber, and J. Osterwalder, "Tunable self-assembly of one-dimensional nanostructures with orthogonal directions", Nanoscale Research Letters **2**, 94 (2007).

[96]   F. S. Tautz, "Structure and bonding of large aromatic molecules on noble metal surfaces: The example of PTCDA", Progress in Surface Science **82**, 479 (2007).

[97]   M. Möbus, N. Karl, and T. Kobayashi, "Structure of perylene-tetracarboxylic-dianhydride thin films on alkali halide crystal substrates", Journal of Crystal Growth **116**, 495 (1992).

[98]   T. Ogawa, K. Kuwamoto, S. Isoda, T. Kobayashi, and N. Karl, "3,4:9,10-Perylenetetracarboxylic dianhydride (PTCDA) by electron crystallography", Acta Crystallographica Section B **55**, 123 (1999).

[99]   K. Glöckler, C. Seidel, A. Soukopp, M. Sokolowski, E. Umbach, M. Böhringer, R. Berndt, and W.-D. Schneider, "Highly ordered structures and submolecular scanning tunnelling

microscopy contrast of PTCDA and DM-PBDCI monolayers on Ag(111) and Ag(110)", Surface Science **405**, 1 (1998).

[100] A. Hauschild, R. Temirov, S. Soubatch, O. Bauer, A. Schöll, B. C. C. Cowie, T.-L. Lee, F. S. Tautz, and M. Sokolowski, "Normal-incidence x-ray standing-wave determination of the adsorption geometry of PTCDA on Ag(111): Comparison of the ordered room-temperature and disordered low-temperature phases", Physical Review B **81**, 125432 (2010).

[101] A. Bondi, "van der Waals Volumes and Radii", The Journal of Physical Chemistry **68**, 441 (1964).

[102] S. Weiß, I. Krieger, T. Heepenstrick, S. Soubatch, M. Sokolowski, and F. S. Tautz, "Determination of the adsorption geometry of PTCDA on the Cu(100) surface", Physical Review B **96**, 075414 (2017).

[103] M. Trömel and S. Hübner, "Metallradien und Ionenradien", Zeitschrift für Kristallographie **215**, 429 (2000).

[104] B. Cordero, V. Gómez, A. E. Platero-Prats, M. Revés, J. Echeverría, E. Cremades, F. Barragán, and S. Alvarez, "Covalent radii revisited", Dalton Transactions, 2832 (2008).

[105] J. Ikonomov, O. Bauer, and M. Sokolowski, "Highly ordered thin films of perylene-3,4,9,10-tetracarboxylic acid dianhydride (PTCDA) on Ag(100)", Surface Science **602**, 2061 (2008).

[106] A. Schmidt, T. J. Schuerlein, G. E. Collins, and N. R. Armstrong, "Ordered Ultrathin Films of Perylenetetracarboxylic Dianhydride (PTCDA) and Dimethylperylenebis(dicarboximide) (Me-PTCDI) on Cu(100): Characterization of Structure and Surface Stoichiometry by LEED, TDMS, and XPS", The Journal of Physical Chemistry **99**, 11770 (1995).

[107] S. Gärtner, B. Fiedler, O. Bauer, A. Marele, and M. Sokolowski, "Lateral ordering of PTCDA on the clean and the oxygen pre-covered Cu(100) surface investigated by scanning tunneling microscopy and low energy electron diffraction", Beilstein Journal of Organic Chemistry **10**, 2055 (2014).

[108] O. H. Pakarinen, J. M. Mativetsky, A. Gulans, M. J. Puska, A. S. Foster, and P. Grutter, "Role of van der Waals forces in the adsorption and diffusion of organic molecules on an insulating surface", Physical Review B **80**, 085401 (2009).

[109] H. Proehl, T. Dienel, R. Nitsche, and T. Fritz, "Formation of Solid-State Excitons in Ultrathin Crystalline Films of PTCDA: From Single Molecules to Molecular Stacks", Physical Review Letters **93**, 097403 (2004).

[110] X. Yang, I. Krieger, D. Lüftner, S. Weiß, T. Heepenstrick, M. Hollerer, P. Hurdax, G. Koller, M. Sokolowski, P. Puschnig, M. G. Ramsey, F. S. Tautz, and S. Soubatch, "On the decoupling of molecules at metal surfaces", Chemical Communications **54**, 9039 (2018).

[111] E. Le Moal, M. Müller, O. Bauer, and M. Sokolowski, "Stable and metastable phases of PTCDA on epitaxial NaCl films on Ag(100)", Physical Review B **82**, 045301 (2010).

[112] M. Müller, J. Ikonomov, and M. Sokolowski, "Structure of Epitaxial Layers of KCl on Ag(100)", Surface Science **605**, 1090 (2011).

[113] M. Hochheim and T. Bredow, "Adsorption-Induced Changes of Intramolecular Optical Transitions: PTCDA/NaCl and PTCDA/KCl", Journal of Computational Chemistry **36**, 1805 (2015).

[114] A. Paulheim, C. Marquardt, M. Sokolowski, M. Hochheim, T. Bredow, H. Aldahhak, E. Rauls, and W. G. Schmidt, "Surface induced vibrational modes in the fluorescence spectra of PTCDA adsorbed on the KCl(100) and NaCl(100) surfaces", Physical Chemistry Chemical Physics **18**, 32891 (2016).

[115] M. Iannuzzi, F. Tran, R. Widmer, T. Dienel, K. Radican, Y. Ding, J. Hutter, and O. Gröning, "Site-selective adsorption of phthalocyanine on h-BN/Rh(111) nanomesh", Physical Chemistry Chemical Physics **16**, 12374 (2014).

[116] L. Liu, T. Dienel, R. Widmer, and O. Gröning, "Interplay between Energy-Level Position and Charging Effect of Manganese Phthalocyanines on an Atomically Thin Insulator", ACS Nano **9**, 10125 (2015).

[117] H. Dil, J. Lobo-Checa, R. Laskowski, P. Blaha, S. Berner, J. Osterwalder, and T. Greber, "Surface Trapping of Atoms and Molecules with Dipole Rings", Science **319**, 1824 (2008).

[118] S. Koslowski, D. Rosenblatt, A. Kabakchiev, K. Kuhnke, K. Kern, and U. Schlickum, "Adsorption and electronic properties of pentacene on thin dielectric decoupling layers", Beilstein Journal of Nanotechnology **8**, 1388 (2017).

[119] S. Berner, M. Corso, R. Widmer, O. Groening, R. Laskowski, P. Blaha, K. Schwarz, A. Goriachko, H. Over, S. Gsell, M. Schreck, H. Sachdev, T. Greber, and J. Osterwalder, "Boron Nitride Nanomesh: Functionality from a Corrugated Monolayer", Angewandte Chemie International Edition **46**, 5115 (2007).

[120] M. L. Ng, A. B. Preobrajenski, A. A. Zakharov, A. S. Vinogradov, S. A. Krasnikov, A. A. Cafolla, and N. Mårtensson, "Effect of substrate nanopatterning on the growth and structure of pentacene films", Physical Review B **81**, 115449 (2010).

[121] F. Schulz, R. Drost, S. K. Hämäläinen, and P. Liljeroth, "Templated Self-Assembly and Local Doping of Molecules on Epitaxial Hexagonal Boron Nitride", ACS Nano **7**, 11121 (2013).

[122] T. Dienel, J. Gómez-Díaz, A. P. Seitsonen, R. Widmer, M. Iannuzzi, K. Radican, H. Sachdev, K. Müllen, J. Hutter, and O. Gröning, "Dehalogenation and Coupling of a Polycyclic Hydrocarbon on an Atomically Thin Insulator", ACS Nano **8**, 6571 (2014).

[123] C. Morchutt, J. Björk, S. Krotzky, R. Gutzler, and K. Kern, "Covalent coupling via dehalo-genation on Ni(111) supported boron nitride and graphene", Chemical Communications **51**, 2440 (2015).

[124] A. J. Martínez-Galera and J. M. Gómez-Rodríguez, "Structural and Electronic Properties of 3,4,9,10-Perylene Tetracarboxylic Dianhydride on h-BN/Rh(110)", The Journal of Physical Chemistry C **123**, 1866 (2019).

[125] R. Forker, T. Dienel, A. Krause, M. Gruenewald, M. Meissner, T. Kirchhuebel, O. Grön-ing, and T. Fritz, "Optical transition energies of isolated molecular monomers and weakly interacting two-dimensional aggregates", Physical Review B **93**, 165426 (2016).

[126] J. Kerfoot, V. V. Korolkov, A. S. Nizovtsev, R. Jones, T. Taniguchi, K. Watanabe, I. Lesanovsky, B. Olmos, N. A. Besley, E. Besley, and P. H. Beton, "Substrate-induced shifts and screening in the fluorescence spectra of supramolecular adsorbed organic monolayers", The Journal of Chemical Physics **149**, 054701 (2018).

[127] C. Davisson and L. H. Germer, "Diffraction of Electrons by a Crystal of Nickel", Physical Review **30**, 705 (1927).

[128] G. Attard and C. Barnes, *Surfaces*, 1st edition (Oxford University Press, New York, 1998).

[129] K. W. Kolasinski, *Surface Science: Foundations of Catalysis and Nanoscience*, 2nd edition (John Wiley & Sons, Ltd., Weinheim, 2008).

[130] M. Horn-von Hoegen, "Growth of semiconductor layers studied by spot profile analysing low energy electron diffraction", Zeitschrift für Kristallographie **214**, 591, 684 (1999).

[131] M. Henzler and W. Göpel, *Oberflächenphysik des Festkörpers* (Vieweg+Teubner Verlag, Stuttgart, 1994).

[132] G. Ertl and J. Küppers, *Low Energy Electrons and Surface Chemistry*, 2nd edition (Wiley-VCH, Weinheim, 1985).

[133] J. Pendry, *Low Energy Electron Diffraction: The Theory and Its Application to Determination of Surface Structure* (Academic Press, London, 1974).

[134] L. de Broglie, "XXXV. A tentative theory of light quanta", The London, Edinburgh, and Dublin Philosophical Magazine and Journal of Science **47**, 446 (1924).

[135] B. Valeur, *Molecular Fluorescence*, 1st edition (Wiley-VCH, Weinheim, 2002).

[136] C. N. Banwell and E. M. McCash, *Molekülspektroskopie* (Oldenbourg, München, 1999).

[137] W. Schmidt, *Optische Spektroskopie*, 2nd edition (Wiley-VCH, Weinheim, 2000).

[138]   J. M. Hollas, *Modern Spectroscopy*, 4th edition (John Wiley & Sons, Ltd., Weinheim, 1987).

[139]   L. A. Lyon, C. D. Keating, A. P. Fox, B. E. Baker, L. He, S. R. Nicewarner, S. P. Mulvaney, and M. J. Natan, "Raman Spectroscopy", Analytical Chemistry **70**, 341R (1998).

[140]   M. Lax, "The Franck-Condon Principle and Its Application to Crystals", The Journal of Chemical Physics **20**, 1752 (1952).

[141]   P. L. Stiles, J. A. Dieringer, N. C. Shah, and R. P. Van Duyne, "Surface-Enhanced Raman Spectroscopy", Annual Review of Analytical Chemistry **1**, 601 (2008).

[142]   M. Fan, G. F. S. Andrade, and A. G. Brolo, "A review on the fabrication of substrates for surface enhanced Raman spectroscopy and their applications in analytical chemistry", Analytica Chimica Acta **693**, 7 (2011).

[143]   S. Kummer, S. Mais, and T. Basché, "Measurement of Optical Dephasing of a Single Terrylene Molecule with Nanosecond Time Resolution", The Journal of Physical Chemistry **99**, 17078 (1995).

[144]   W. P. Ambrose, T. Basché, and W. E. Moerner, "Detection and spectroscopy of single pentacene molecules in a *p*-terphenyl crystal by means of fluorescence excitation", The Journal of Chemical Physics **95**, 7150 (1991).

[145]   A. Otto, I. Mrozek, H. Grabhorn, and W. Akemann, "Surface-enhanced Raman scattering", Journal of Physics: Condensed Matter **4**, 1143 (1992).

[146]   S. Schlücker, "Surface-Enhanced Raman Spectroscopy: Concepts and Chemical Applications", Angewandte Chemie International Edition **53**, 4756 (2014).

[147]   F. J. García-Vidal and J. B. Pendry, "Collective Theory for Surface Enhanced Raman Scattering", Physical Review Letters **77**, 1163 (1996).

[148]   B. Lehner, M. Hohage, and P. Zeppenfeld, "The influence of weak adsorbate–adsorbate interactions on desorption", Chemical Physics Letters **369**, 275 (2003).

[149]   B. Lehner, M. Hohage, and P. Zeppenfeld, "Kinetic Monte Carlo simulation scheme for studying desorption processes", Surface Science **454-456**, 251 (2000).

[150]   A. M. de Jong and J. W. Niemantsverdriet, "Thermal desorption analysis: Comparative test of ten commonly applied procedures", Surface Science **233**, 355 (1990).

[151]   P. Feulner and D. Menzel, "Simple ways to improve "flash desorption" measurements from single crystal surfaces", Journal of Vacuum Science & Technology **17**, 662 (1980).

[152]   D. A. King, "Thermal desorption from metal surfaces: A review", Surface Science **47**, 384 (1975).

[153] A. Winkler, "Initial stages of organic film growth characterized by thermal desorption spectroscopy", Surface Science **643**, 124 (2016).

[154] J. W. Niemantsverdriet, K. Markert, and K. Wandelt, "The compensation effect and the manifestation of lateral interactions in thermal desorption spectroscopy", Applied Surface Science **31**, 211 (1988).

[155] J. Zegenhagen, "Surface structure determination with X-ray standing waves", Surface Science Reports **18**, 199 (1993).

[156] D. P. Woodruff, "Surface structure determination using x-ray standing waves", Reports on Progress in Physics **68**, 743 (2005).

[157] D. P. Woodruff, "Normal incidence X-ray standing wave determination of adsorbate structures", Progress in Surface Science **57**, 1 (1998).

[158] F. Reinert and S. Hüfner, "Photoemission spectroscopy—from early days to recent applications", New Journal of Physics **7**, 97 (2005).

[159] J. Zegenhagen, "Surface Structure Analysis with X-ray Standing Waves", Physica Scripta **T39**, 328 (1991).

[160] M. P. Seah, "The Quantitative Analysis of Surfaces by XPS: A Review", Surface and Interface Analysis **2**, 222 (1980).

[161] F. Schreiber, K. A. Ritley, I. A. Vartanyants, H. Dosch, J. Zegenhagen, and B. C. C. Cowie, "Non-dipolar contributions in XPS detection of X-ray standing waves", Surface Science **486**, L519 (2001).

[162] D. J. Kennedy and S. T. Manson, "Photoionization of the Noble Gases: Cross Sections and Angular Distributions", Physical Review A **5**, 227 (1972).

[163] M. E. Straumanis and L. S. Yu, "Lattice Parameters, Densities, Expansion Coefficients and Perfection of Structure of Cu and of Cu-In α phase", Acta Crystallographica Section A **25**, 676 (1969).

[164] C. Marquardt, "Optical investigations on PTCDA on KCl(100): supperradiant aggragates and single molecules", PhD thesis (Universität Bonn, 2019).

[165] M. Müller, "Optische Spektroskopie von PTCDA auf Alkalihalogenidoberflächen: vereinzelte Moleküle und Monolagen", PhD thesis (Universität Bonn, 2011).

[166] C. Marquardt, A. Paulheim, N. Rohbohm, R. Merkel, and M. Sokolowski, "A surface science compatible epifluorescence microscope for inspection of samples under ultra high vacuum and cryogenic conditions", Review of Scientific Instruments **88**, 083702 (2017).

[167] National Instruments, *LabVIEW 7 Express*, 2003.

[168] N. Humberg, "Untersuchung der Desorption von Borazin von der Cu(111)-Oberfläche mittels TPD", Protokoll zum Vertiefenden Praktikum (Universität Bonn, 2017).

[169] B. Wolff, "Determination of the desorption energy of PTCDA on hBN/Cu(111) by thermal desorption spectroscopy", MA thesis (Universität Bonn, 2019).

[170] Roper Scientific, *Winspec/32, Version 2.5.19.0*, 1996.

[171] B. Wolff, "Adsorptionsstruktur und optische Eigenschaften von DBP auf der Ag(100)- und KCl(100)-Oberfläche", BA thesis (Universität Bonn, 2016).

[172] A. B. Preobrajenski, A. S. Vinogradov, and N. Mårtensson, "Monolayer of h-BN chemisorbed on Cu(111) and Ni(111): The role of the transition metal 3d states", Surface Science **582**, 21 (2005).

[173] A. Haags, "Rastertunnelmikroskopische Untersuchungen des Wachstumsstarts von hexagonalem Bornitrid auf der Cu(111)-Oberfläche", BA thesis (Universität Bonn, 2016).

[174] S. Joshi, D. Ecija, R. Koitz, M. Iannuzzi, A. P. Seitsonen, J. Hutter, H. Sachdev, S. Vijayaraghavan, F. Bischoff, K. Seufert, J. V. Barth, and W. Auwärter, "Boron Nitride on Cu(111): An Electronically Corrugated Monolayer", Nano Letters **12**, 5821 (2012).

[175] K. Hermann, "Periodic overlayers and moiré patterns: theoretical studies of geometric properties", Journal of Physics: Condensed Matter **24**, 314210 (2012).

[176] S. Roth, F. Matsui, T. Greber, and J. Osterwalder, "Chemical Vapor Deposition and Characterization of Aligned and Incommensurate Graphene/Hexagonal Boron Nitride Heterostack on Cu(111)", Nano Letters **13**, 2668 (2013).

[177] R. Koitz, A. P. Seitsonen, M. Iannuzzi, and J. Hutter, "Structural and electronic properties of a large-scale Moiré pattern of hexagonal boron nitride on Cu(111) studied with density functional theory", Nanoscale **5**, 5589 (2013).

[178] B. N. Feigelson, V. M. Bermudez, J. K. Hite, Z. R. Robinson, V. D. Wheeler, K. Sridhara, and S. C. Hernández, "Growth and spectroscopic characterization of monolayer and few-layer hexagonal boron nitride on metal substrates", Nanoscale **7**, 3694 (2015).

[179] J. Gómez Díaz, Y. Ding, R. Koitz, A. P. Seitsonen, M. Iannuzzi, and J. Hutter, "Hexagonal boron nitride on transition metal surfaces", Theoretical Chemistry Accounts **132**, 1 (2013).

[180] S. Lin, J. Huang, and X. Gao, "A Cu(111) supported h-BN nanosheet: a potential low-cost and high-performance catalyst for CO oxidation", Physical Chemistry Chemical Physics **17**, 22097 (2015).

[181] A. Lyalin, A. Nakayama, and T. Uosaki K.and Taketsugu, "Adsorption and Catalytic Activation of the Molecular Oxygen on the Metal Supported h-BN", Topics in Catalysis **57**, 1032 (2014).

[182] P. O. Gartland, S. Berge, and B. J. Slagsvold, "Photoelectric Work Function of a Copper Single Crystal for the (100), (110), (111), and (112) Faces", Physical Review Letters **28**, 738 (1972).

[183] J. Felter, M. Raths, M. Franke, and C. Kumpf, "*IN SITU* STUDY OF TWO-DIMENSIONAL DENDRITIC GROWTH OF HEXAGONAL BORON NITRIDE", 2D Materials **6**, 045005 (2019).

[184] W. Auwärter, H. U. Suter, H. Sachdev, and T. Greber, "Synthesis of One Monolayer of Hexagonal Boron Nitride on Ni(111) from B-Trichloroborazine $(ClBNH)_3$", Chemistry of Materials **16**, 343 (2004).

[185] F. Müller, K. Stöwe, and H. Sachdev, "Symmetry versus Commensurability: Epitaxial Growth of Hexagonal Boron Nitride on Pt(111) From B-Trichloroborazine $(ClBNH)_3$", Chemistry of Materials **17**, 3464 (2005).

[186] M. Horn-von Hoegen, A. Al-Falou, H. Pietsch, B. H. Müller, and M. Henzler, "Formation of interfacial dislocation network in surfactant mediated growth of Ge on Si(111) investigated by Spa-Leed: Part I", Surface Science **298**, 29 (1993).

[187] M. S. Bresnehan, M. J. Hollander, M. Wetherington, M. LaBella, K. A. Trumbull, R. Cavalero, D. W. Snyder, and J. A. Robinson, "Integration of Hexagonal Boron Nitride with Quasi-freestanding Epitaxial Graphene: Toward Wafer-Scale, High-Performance Devices", ACS Nano **6**, 5234 (2012).

[188] S. Å. Lindgren, L. Walldén, J. Rundgren, and P. Westrin, "Low-energy electron diffraction from Cu(111): Subthreshold effect and energy-dependent inner potential; surface relaxation and metric distances between spectra", Physical Review B **29**, 576 (1984).

[189] A. Berkó and F. Solymosi, "Adsorption of nitrogen atoms on Cu(111), Rh(111) and Pt(110) surfaces", Applied Surface Science **55**, 193 (1992).

[190] M. Schwarz, A. Riss, M. Garnica, J. Ducke, P. S. Deimel, D. A. Duncan, P. Kumar Thakur, T.-L. Lee, A. P. Seitsonen, J. V. Barth, F. Allegretti, and W. Auwärter, "Corrugation in the Weakly Interacting Hexagonal-BN/Cu(111) System: Structure Determination by Combining Noncontact Atomic Force Microscopy and X-ray Standing Waves", ACS Nano **11**, 9151 (2017).

[191] C. Busse, P. Lazić, R. Djemour, J. Coraux, T. Gerber, N. Atodiresei, V. Caciuc, R. Brako, A. T. N'Diaye, S. Blügel, J. Zegenhagen, and T. Michely, "Graphene on Ir(111): Physisorption with Chemical Modulation", Physical Review Letters **107**, 036101 (2011).

[192]   C. C. Silva, M. Iannuzzi, D. A. Duncan, P. T. P. Ryan, K. T. Clarke, J. T. Küchle, J. Cai, W. Jolie, C. Schlueter, T.-L. Lee, and C. Busse, "Valleys and Hills of Graphene on Ru(0001)", The Journal of Physical Chemistry C **122**, 18554 (2018).

[193]   G. B. Grad, P. Blaha, K. Schwarz, W. Auwärter, and T. Greber, "Density functional theory investigation of the geometric and spintronic structure of h-BN/Ni(111) in view of photoemission and STM experiments", Physical Review B **68**, 085404 (2003).

[194]   M. Scheuermann, "Bestimmung der Desorptionsenergie von Borazin auf der Cu(111)-Oberfläche mit Hilfe von Temperatur-programmierter Desorption", BA thesis (Universität Bonn, 2019).

[195]   H. Schlichting, "Methoden und Mechanismen der thermischen Desorption", PhD thesis (Tecnnische Universität München, 1990).

[196]   https://webbook.nist.gov/cgi/cbook.cgi?ID=C703866&Units=SI&Mask=6EF, viewed July 23rd 2020.

[197]   J. W. Eaton et al., *GNU Ocatve, version 4.2.2*, 2018.

[198]   B. Wolff, "Calculation of Temperature Programmed Desorption Spectra", Protokoll zum Vertiefenden Praktikum (Universität Bonn, 2018).

[199]   T. J. Rockey, M. Yang, and H.-L. Dai, "Adsorption Energies, Inter-adsorbate Interactions, and the Two Binding Sites within Monolayer Benzene on Ag(111)", The Journal of Physical Chemistry B **110**, 19973 (2006).

[200]   L. E. Firment and G. A. Somorjai, "Low energy electron diffraction studies of the surfaces of molecular crystals (ice, ammonia, naphthalene, benzene)", Surface Science **84**, 275 (1979).

[201]   L. E. Firment and G. A. Somorjai, "Surface structures of normal paraffins and cyclohexane monolayers and thin crystals grown on the (111) crystal face of platinum. A low-energy electron diffraction study", The Journal of Chemical Physics **66**, 2901 (1977).

[202]   https://webbook.nist.gov/cgi/cbook.cgi?ID=C71432&Units=SI&Mask=4#Thermo-Phase, viewed July 27th 2020.

[203]   R. J. Simonson, M. T. Paffett, M. E. Jones, and B. E. Koel, "A vibrational study of borazine adsorbed on Pt(111) and Au(111) surfaces", Surface Science **254**, 29 (1991).

[204]   A. P. Farkas, P. Török, F. Solymosi, J. Kiss, and Z. Kónya, "Investigation of the adsorption properties of borazine and characterisation of boron nitride on Rh(111) by electron spectroscopic methods", Applied Surface Science **354**, 367 (2015).

[205] T. Wagner, A. Bannani, C. Bobisch, H. Karacuban, M. Stöhr, M. Gabriel, and R. Möller, "Growth of 3,4,9,10-perylenetetracarboxylic-dianhydride crystallites on noble metal surfaces", Organic Electronics **5**, 35 (2004).

[206] T. Wagner, H. Karacuban, and R. Möller, "Analysis of complex thermal desorption spectra: PTCDA on copper", Surface Science **603**, 482 (2009).

[207] T. Wagner, A. Bannani, C. Bobisch, H. Karacuban, and R. Möller, "The initial growth of PTCDA on Cu(111) studied by STM", Journal of Physics: Condensed Matter **19**, 056009 (2007).

[208] S. Joshi, F. Bischoff, R. Koitz, D. Ecija, K. Seufert, A. P. Seitsonen, J. Hutter, K. Diller, J. I. Urgel, H. Sachdev, J. V. Barth, and W. Auwärter, "Control of Molecular Organization and Energy Level Alignment by an Electronically Nanopatterned Boron Nitride Template", ACS Nano **8**, 430 (2014).

[209] C.-A. Palma, S. Joshi, T. Hoh, D. Ecija, J. V. Barth, and W. Auwärter, "Two-Level Spatial Modulation of Vibronic Conductance in Conjugated Oligophenylenes on Boron Nitride", Nano Letters **15**, 2242 (2015).

[210] A. J. Martínez-Galera and J. M. Gómez-Rodríguez, "Erratum to: Influence of metal support in-plane symmetry on the corrugation of hexagonal boron nitride and graphene monolayers", Nano Research **12**, 1217 (2019).

[211] S. M. Barlow and R. Raval, "Complex organic molecules at metal surfaces: bonding, organisation and chirality", Surface Science Reports **50**, 201 (2003).

[212] W. S. Rasband, *ImageJ*, U. S. National Institutes of Health, Bethesda, Maryland, USA, 1997-2008.

[213] N. Rohbohm, "Analysis of PTCDA domains on KCl(100) under ultra high vacuum by polarisation dependent fluorescence microscopy", MA thesis (Universität Bonn, 2018).

[214] P. Bayersdorfer, *Spot-Plotter, Version 1.2.1.4*, 2008.

[215] C. Wagner, N. Fournier, F. S. Tautz, and R. Temirov, "Measurement of the Binding Energies of the Organic-Metal Perylene-Teracarboxylic-Dianhydride/Au(111) Bonds by Molecular Manipulation Using an Atomic Force Microscope", Physical Review Letters **109**, 076102 (2012).

[216] N. Dori, M. Menon, L. Kilian, M. Sokolowski, L. Kronik, and E. Umbach, "Valence electronic structure of gas-phase 3,4,9,10-perylene tetracarboxylic acid dianhydride: Experiment and theory", Physical Review B **73**, 195208 (2006).

[217] M. Leonhardt, O. Mager, and H. Port, "Two-component optical spectra in thin PTCDA films due to the coexistence of α- and β-phase", Chemical Physics Letters **313**, 24 (1999).

[218] V. Wagner, "Raman Analysis of Ordered Organic Monolayers on Metal Surfaces", Physica Status Solidi A **188**, 1297 (2001).

[219] M. Schneider, "Vibronische und optische Eigenschaften ultradünner organischer Filme am Beispiel PTCDA/Ag(111)", PhD thesis (Universität Würzburg, 2002).

[220] R. Kaiser, M. Friedrich, T. Schitz-Hübsch, F. Sellam, T. U. Kampen, K. Leo, and D. R. T. Zahn, "Ultra-thin PTCDA layers studied by optical spectroscopy", Fresenius Journal of Analytic Chemistry **363**, 189 (1999).

[221] R. Scholz, A. Y. Kobitski, T. U. Kampen, M. Schreiber, D. R. T. Zahn, G. Jungnickel, M. Elstner, M. Sternberg, and T. Frauenheim, "Resonant Raman spectroscopy of 3,4,9,10-perylene-tetracarboxylic-dianhydride epitaxial films", Physical Review B **61**, 13659 (2000).

[222] S. Heutz, G. Salvan, S. D. Silaghi, T. S. Jones, and D. R. T. Zahn, "Raman Scattering as a Probe of Crystallinity in PTCDA and H_2Pc Single-Layer and Double-Layer Thin Film Heterostructures", The Journal of Physical Chemistry B **107**, 3782 (2003).

[223] D. A. Tenne, S. Park, T. U. Kampen, A. Das, R. Scholz, and D. R. T. Zahn, "Single crystals of the organic semiconductor perylene tetracarboxylic dianhydride studied by Raman Spectroscopy", Physical Review B **61**, 14564 (2000).

[224] M. Müller, A. Paulheim, C. Marquardt, and M. Sokolowski, "Spectroscopy of isolated PTCDA molecules on the KCl(100) surface: Vibrational spectra and azimuthal orientation", The Journal of Chemical Physics **138**, 064703 (2013).

[225] M. Wewer and F. Stienkemeier, "Laser-induced fluorescence spectroscopy of 3,4,9,10-perylenetetracarboxylic-dianhydrid in helium nanodroplets", The Journal of Chemical Physics **120**, 1239 (2004).

[226] O. A. Yeshchenko, I. S. Bondarchuk, and M. Y. Losytskyy, "Surface plasmon enhanced photoluminescence from copper nanoparticles: Influence of temperature", Journal of Applied Physics **116**, 054309 (2014).

[227] H. Ehrenreich and H. R. Philipp, "Optical Properties of Ag and Cu", Physical Review **128**, 1622 (1962).

[228] S. Babar and J. H. Weaver, "Optical constants of Cu, Ag, and Au revisited", Applied Optics **54**, 477 (2015).

[229] A. Otto, J. Billmann, J. Eickmans, U. Ertürk, and C. Pettenkofer, "The "adatom model" of SERS (Surface Enhanced Raman Scattering): The present status", Surface Science **138**, 319 (1984).

[230] M. Xia, "2D Materials-Coated Plasmonic Structures for SERS Applications", Coatings **8**, 137 (2018).

[231] X. Ling, W. Fang, Y.-H. Lee, P. T. Araujo, X. Zhang, J. F. Rodriguez-Nieva, Y. Lin, J. Zhang, J. Kong, and M. S. Dresselhaus, "Raman Enhancement Effect on Two-Dimensional Layered Materials: Graphene, h-BN and MoS$_2$", Nano Letters **14**, 3033 (2014).

[232] M. Hochheim, A. Paulheim, M. Sokolowski, and T. Bredow, "Analysis of the Vibronic Spectra of Perylene-3,4,9,10-tetracarboxylic Dianhydride Adsorbed on NaCl and KCl", The Journal of Physical Chemistry C **120**, 24240 (2016).

[233] R. V. Gorbachev, I. Riaz, R. R. Nair, R. Jalil, L. Britnell, B. D. Belle, E. W. Hill, K. S. Novoselov, K. Watanabe, T. Taniguchi, A. K. Geim, and P. Blake, "Hunting for Monolayer Boron Nitride: Optical and Raman Signatures", Small **7**, 465 (2011).

[234] O. Bünermann, "Spektroskopie von Alkali- und Erdalkaliatomen, -molekülen, Alkaliclustern und Komplexen organischer Moleküle auf Heliumnanotröpfchen", PhD thesis (University of Bielefeld, 2006).

[235] A. Paulheim, "Fluoreszenzspektroskopie an PTCDA-Molekülen auf Alkalihalogenidoberflächen: Die Rolle von Oberflächenstufen", PhD thesis (Universität Bonn, 2017).

[236] Omicron, *NG LEED/NG LEED S Technical Reference Manual*, Version 2.0, Omicron (Idsteiner Straße 78, 6532 Taunusstein, Germany, 2000).

[237] Omicron, *NG SPA: SPA-LEED Control Unit Technical Reference Manual*, Version 2.0, Omicron (Idsteiner Straße 78, 6532 Taunusstein, Germany, 1997).

[238] G. Rouillé, T. Kirchhuebel, M. Rink, M. Gruenewald, J. Kröger, R. Forker, and T. Fritz, "Identification of vibrational excitations and optical transitions of the organic electron donor tetraphenyldibenzoperiflanthene (DBP)", Physical Chemistry Chemical Physics **17**, 30404 (2015).

[239] D. Golberg, Y. Bando, C. Tang, and C. Zhi, "Boron Nitride Nanotubes", Advanced Materials **19**, 2413 (2007).

[240] P. B. Mirkarimi, K. F. McCarty, and D. L. Medlin, "Review of advances in cubic boron nitride film synthesis", Materials Science and Engineering **R21**, 47 (1997).

[241] C. Frondel and U. B. Marvin, "Lonsdaleite, a Hexagonal Polymorph of Diamond", Nature **214**, 587 (1967).

[242] https://webbook.nist.gov/cgi/cbook.cgi?Name=borazine&Units=SI, viewed August 3rd 2020.

[243] F. H. Allen and I. J. Bruno, "Bond lengths in organic and metal-organic compounds revisited: *X*—H bond lengths from neutron diffraction data", Acta Crystallographica Section B **66**, 380 (2010).

[244] https://pubchem.ncbi.nlm.nih.gov/compound/Borazine#datasheet=LCSS, viewed August 3rd 2020.

[245] K. spol. s r. o., Katchem spol. s r. o., Czech Republic, www.katchem.cz .

[246] http://www.katchem.cz/en/products?view=product&id=205, viewed August 3rd 2020.

[247] E. G. Cox, F. R. S., D. W. J. Cruickshank, and J. A. S. Smith, "The crystal structure of benzene at $-3°$C", Proceedings of the Royal Society A **247**, 1 (1958).

[248] K. B. Wiberg, V. A. Walters, and W. P. Dailey, "Infrared Intensities: Cyclohexane. A Molecular Force Field and Dipole Moment Derivatives", Journal of the American Chemical Society **107**, 4860 (1985).

Acknowledgements

Eidesstattliche Erklärung

Hiermit versichere ich an Eides statt, dass ich die Dissertation "Structural and electronic decoupling of a large organic molecule from a metal surface by a single layer of hexagonal boron nitride" persönlich, selbstständig und ohne Benutzung anderer als der angegebenen Hilfsmittel angefertigt habe, die benutzten Quellen kenntlich gemacht sind und die Arbeit nicht anderweitig als Dissertation eingereicht ist.

Als kumulative Dissertation ist die vorliegende Arbeit an den nachfolgenden Stellen veröffentlicht:

- Christine Brülke, Timo Heepenstrick, Niklas Humberg, Ina Krieger, Moritz Sokolowski, Simon Weiß, Frank Stefan Tautz, and Serguei Soubatch, "Long Vertical Distance Bonding of the Hexagonal Boron Nitride Monolayer on the Cu(111) Surface" **121** 23964 (2017).

- Christine Brülke, Timo Heepenstrick, Ina Krieger, Beatrice Wolff, Xiaosheng Yang, Ali Shamsaddinlou, Simon Weiß, François C. Bocquet, F. Stefan Tautz, Serguei Soubatch, and Moritz Sokolowski, "Quantitative analysis of the electronic decoupling of an organic semiconductor molecule at a metal interface by a monolayer of hexagonal boron nitride" **99** 12104(R) (2019).

- Christine Brülke, Oliver Bauer, and Moritz Sokolowski, "The influence of an interfacial hBN layer on the fluorescence of an organic molecule" **11** 1663 (2020).

Königswinter, Juli 2021

_____

(Christine Brülke)

Liste von Vorveröffentlichungen

C. Brülke, O. Bauer and M. Sokolowski
"The influence of an interfacial hBN layer on the fluorescence of an organic molecule"
Beilstein Journal of Nanotechnology **11**, 1663 (2020)

C. Brülke, T. Heepenstrick, I. Krieger, B. Wolff, X. Yang, A. Shamsaddinlou, S. Weiß, F. C. Bocquet, F. S. Tautz, S. Soubatch, and M. Sokolowski
"Quantitative analysis of the electronic decoupling of an organic semiconductor molecule at a metal interface by a monolayer of hexagonal boron nitride"
Physical Review B **99**, 121404(R) (2019)

S. Weiß, D. Gerbert, A. Stein, A. K. Schenk, X. Yang, C. Brülke, R. Kremring, S. Feldmann, F. C. Bocquet, M. Gille, S. Hecht, M. Sokolowski, P. Tegeder, S. Soubatch, and F. S. Tautz, "Dependence of the adsorption height of graphenelike adsorbates on their dimensionality", Physical Review B 98 075410 (2018).

C. Brülke, T. Heepenstrick, N. Humberg, I. Krieger, M. Sokolowski, S. Weiß, F. S. Tautz, Serguei Soubatch
"Long Vertical Distance Bonding of the Hexagonal Boron Nitride Monolayer on the Cu(111) Surface"
The Journal of Physical Chemistry C **121** 23964 (2017)